# ELECTRO-DEPOSITED TRANSITION METAL DICHALCOGENIDES ABSORBERS FOR PRODUCING Q-SWITCHED AND MODE-LOCKED FIBER LASERS

LEE LIAN HONG

FACULTY OF ENGINEERING

UNIVERSITI MALAYA

KUALA LUMPUR

2024

# ELECTRO-DEPOSITED TRANSITION METAL DICHALCOGENIDES ABSORBERS FOR PRODUCING Q-SWITCHED AND MODE-LOCKED FIBER LASERS

LEE LIAN HONG

THESIS SUBMITTED IN FULFILMENT OF THE REQUIREMENTS FOR THE DEGREE OF DOCTOR OF PHILOSOPHY

FACULTY OF ENGINEERING
UNIVERSITI MALAYA
KUALA LUMPUR

2024

# UNIVERSITI MALAYA
# ORIGINAL LITERARY WORK DECLARATION

Name of Candidate: **LEE LIAN HONG**

Matric No: **S2027150/1**

Name of Degree: **DOCTOR OF PHILOSOPHY (PHOTONICS)**

Title of Project Paper/Research Report/Dissertation/Thesis (“this Work”):

**ELECTRO-DEPOSITED TRANSITION METAL DICHALCOGENIDES ABSORBERS FOR PRODUCING Q-SWITCHED AND MODE-LOCKED FIBER LASERS**

Field of Study: **PHOTONICS ENGINEERING**

I do solemnly and sincerely declare that:

(1) I am the sole author/writer of this Work;
(2) This Work is original;
(3) Any use of any work in which copyright exists was done by way of fair dealing and for permitted purposes and any excerpt or extract from, or reference to or reproduction of any copyright work has been disclosed expressly and sufficiently and the title of the Work and its authorship have been acknowledged in this Work;
(4) I do not have any actual knowledge nor do I ought reasonably to know that the making of this work constitutes an infringement of any copyright work;
(5) I hereby assign all and every rights in the copyright to this Work to the Universiti Malaya (“UM”), who henceforth shall be owner of the copyright in this Work and that any reproduction or use in any form or by any means whatsoever is prohibited without the written consent of UM having been first had and obtained;
(6) I am fully aware that if in the course of making this Work I have infringed any copyright whether intentionally or otherwise, I may be subject to legal action or any other action as may be determined by UM.

Candidate’s Signature Date: 2-9-2024

Subscribed and solemnly declared before,

Witness’s Signature Date: 2-9-2024

Name:

Designation:

# ELECTRO-DEPOSITED TRANSITION METAL DICHALCOGENIDES ABSORBERS FOR PRODUCING Q-SWITCHED AND MODE-LOCKED FIBER LASERS

## ABSTRACT

This PhD research work will use two-dimensional (2D) materials especially transition metal dichalcogenides (TMD) such as $MoS_2$, $MoSe_2$ and $MoTe_2$ as saturable absorber (SA) to passively generate Q-switched and Mode-locked fiber lasers. Previously, the above mentioned TMDs based SAs were prepared using conventional methods including liquid-phase exfoliation, PVA film, drop-cast technique and mechanical exfoliation. In this research, a new method is being proposed to fabricate the mentioned TMDs and this method involves the technique of electro-deposition. This method has been applied in other research field but has not been utilized in the specific domain of Q-switched and mode-locked fiber laser. The advantage of this electro-deposition method is that it can produce a more homogeneous and more stable SA for the generation of the Q-switched and mode-locked fiber laser. The fabricated SAs will be used in the designated experiment setup to achieve Q-switched and mode-locked fiber laser by sandwiching the SAs in between two fiber ferrules. Furthermore, the characterization of the fabricated SAs is performed using field emission scanning electron microscope (FESEM), electron dispersion spectroscopy (EDS) and X-ray diffraction (XRD) to check the surface morphology of the SAs and to confirm the presence of 2D TMD materials in the fabricated SA. Moreover, the linear absorption and modulation depth are also presented for each of the fabricated SAs. Finally, this research will analyze the Q-switched and mode-locked performance of the system using the fabricated SAs. Ultrashort pulse fiber lasers operating at 1.55- and 2-micron regions with various performances are successfully achieved in this work. For instance, the prepared $MoS_2$ thin film exhibits the saturable absorption characteristic of 3.4%, when this $MoS_2$ SA was introduced into an Erbium-doped fiber laser (EDFL) cavity, a stable Q-switched pulse at 1559.4 nm was achieved by adjusting the pump power above the threshold of 51.67 mW. The pulse has a maximum repetition frequency of 89.89 kHz, minimum pulse width of 4.75 μs and maximum pulse energy of 15.03 nJ at 105.27 mW pump power. Mode-locked pulse is also obtained at 1560.8 nm when the cavity length was extended to 106 m. The repetition frequency and pulse width of the mode-locked pulse were 1.88 MHz and 1.47 ps respectively. To the best of our knowledge, this is the first time that Q-switched and mode-locked pulses have been obtained in a fiber laser based on this new electrodeposition method.

Keywords: Q-switching, Mode-locking, Saturable absorber, transition metal dichalcogenides (TMDs)

# PERALIHAN LOGAM DICHALCOGENIDE DIELEKTRO DEPOSITKAN SEBAGAI PENYERAP BOLEH TEPU (SA) UNTUK MENGHASILKAN LASER GENTIAN SUIS Q DAN MOD TERKUNCI

## ABSTRAK

Penyelidikan ini tertumpu kepada bahan dua dimensi (2D) terutamanya peralihan logam dichalcogenide (TMD) seperti $MoS_2$, $MoSe_2$ and $MoTe_2$ sebagai penyerap boleh tepu (SA) untuk menghasilkan laser gentian denyut ultra-pendek. Bahan dua dimensi (2D) yang dinyatakan di atas adalah calon yang menjanjikan untuk menunjukkan laser gentian suis-Q dan mod-terkunci. Akan tetapi, cara penyediaan penyerap boleh tepu (SA) di atas adalah menggunakan kaedah konvensional di mana ia menggunakan filem PVA, pengelupasan fasa cecair, teknik drop cast dan pengelupasan mekanikal. Kaedah ini adalah antara cara yang paling mudah untuk menyediakan SA kerana ia tidak rumit dan mudah untuk dihasilkan. Dalam penyelidikan ini, kami mencadangkan kaedah baru untuk menghasilkan TMD ini menggunakan teknik pemendapan elektro. Kaedah ini telah digunakan dalam bidang penyelidikan lain tetapi tidak dalam bidang laser gentian suis-Q dan mod-terkunci. Kelebihan kaedah pemendapan elektro ini boleh menghasilkan penyerap tepu (SAs) yang lebih homogen dan lebih stabil untuk penjanaan laser gentian suis-Q dan mod-terkunci. SA yang disediakan akan digunakan dalam persediaan eksperimen yang ditetapkan untuk mencapai laser gentian suis-Q dan mod-terkunci dengan mengapit SA di antara dua ferrule gentian. Tambahan lagi, kami juga melakukan pencirian SA yang dihasilkan dengan menggunakan mikroskop pengimbasan pancaran medan elektron (FESAM), kespektroskopan serakan elektron (EDS) dan Pemencaran Sinar-X (XRD) untuk memeriksa morfologi permukaan SA dan juga untuk mengesahkan kehadiran bahan TMD 2D dalam SA yang dihasilkan. Selain itu, penyerapan linear dan kedalaman modulasi juga dibentangkan untuk setiap SA yang difabrikasi. Akhir sekali, penyelidikan ini akan menganalisis prestasi suis-Q dan mod-terkunci melalui SA yang dihasilkan. Perbandingan prestasi akan dijalankan dan dibincangkan dalam bab berikutnya. Laser gentian nadi ultrapendek yang beroperasi pada kawasan 1.55 dan 2 mikron dengan pelbagai prestasi berjaya dicapai dalam kerja ini. Contohnya, filem nipis $MoS_2$ yang disediakan mempamerkan ciri penyerapan tepu sebanyak 3.4% dan apabila penyerap boleh tepu $MoS_2$ ini dimasukkan ke dalam rongga laser gentian doped Erbium (EDFL), denyutan suis-Q yang stabil di gelombang 1559.4 nm telah dicapai pada kuasa pam melebihi ambang 51.67 mW. Ia mempunyai deretan denyut pada kadar ulangan maksimum 89.89 kHz, lebar denyut minimum 4.75 µs dan tenaga denyut maksimum 15.03 nJ pada kuasa pam 105.27 mW. Kami juga memperolehi mod-terkunci pada 1560.8 nm apabila panjang rongga dilanjutkan kepada 106 m. Kadar pengulangan dan lebar denyut bagi mod terkunci masing-masing ialah 1.88 MHz dan 1.47 ps. Untuk pengetahuan terbaik kami, ini adalah kali pertama denyut suis-Q dan mod-terkunci diperolehi dalam laser gentian berdasarkan kaedah elektrodeposisi baru ini.

Kata kunci: suis-Q, mod-terkunci, penyerap boleh tepu (SA) , peralihan logam dichalcogenide (TMD)

# ACKNOWLEDGEMENTS

First of all, I would like to express my appreciation to my supervisors, Professor Ir. Dr. Sulaiman Wadi Harun, Prof. Ir. Ts. Dr. Tiu Zian Cheak, Prof. Dr. Hamzah Bin Arof and Dr. Tawfig Eltaif for their continuous support, patience guidance and great motivation throughout my PhD study. Their knowledge and guidance have provided great help during my research and thesis writing.

I express my gratitude to Yayasan Telekom Malaysia (YTM) for sponsoring my PhD studies and to Multimedia University for coordinating the study arrangements.

My sincere gratitude towards my lab team members Abdulkadir Mukhtar DiBlawe, Dr Anas bin Abdul Latiff, Nora Yu Chen, Izzah, Seong and Lip for their companionship, help and knowledge sharing during the research journey. Your suggestions on methods of improvement have greatly reduced the problems encountered during the research journey.

To my wife Teo Mooi Yeow and my family, thank you for your love, encouragement and support. Again, thanks to those who had helped me directly or indirectly during my research journey.

# TABLE OF CONTENTS

# LIST OF FIGURES

# LIST OF TABLES

# LIST OF SYMBOLS AND ABBREVIATIONS

| | | |
|---|---|---|
| BP | : | black phosphorus |
| EDF | : | erbium doped fiber |
| EDFA | : | erbium doped fiber amplifier |
| EDFL | : | erbium doped fiber laser |
| FWHM | : | full-wave half-maximum |
| GVD | : | group velocity dispersion |
| MoS2 | : | molybdenum disulfide |
| OSA | : | optical spectrum analyzer |
| PVA | : | polyvinyl alcohol |
| QD | : | quantum dot |
| RF | : | radio frequency |
| SA | : | saturable absorber |
| SMF | : | single mode fiber |
| SNR | : | signal-to-noise ratio |
| SPM | : | self-phase modulation |
| TBP | : | time bandwidth product |
| TDF | : | thulium doped fiber |
| TDFL | : | thulium doped fiber laser |
| TI | : | topological insulator |
| TIs | : | topological insulators |
| TMD | : | transition metal dichalcogenide |
| TMDs | : | transition metal dichalcogenides |
| TMO | : | transition metal oxide |
| TMOs | : | transition metal oxides |

WDM : wavelength division multiplexing

$\Delta\lambda 3dB$ : 3-dB spectral bandwidth

$\alpha$ : absorption coefficient

$L$ : cavity length

$vm$ : degree of light slow down in material

$D$ : dispersion

$v$ : frequency

$\beta 2$ : GVD

$DM$ : material dispersion

$\alpha ns$ : non-saturable absorption

$\lambda o$ : operating wavelength

$Po$ : output power

$Pp$ : peak power

$E$ : photon energy

$Q$ : pulse energy

$Tr$ : pulse period

$t$ : pulse width

$n$ : refractive index

$fr$ : repetition rate

$\alpha n$ : saturable absorption

$Isat$ : saturation intensity

$c$ : speed of light in material

$co$ : speed of light in vacuum

$DW$ : waveguide dispersion

$\lambda$ : wavelength

# CHAPTER 1: INTRODUCTION

## 1.1 Background

In year 2023, the Nobel Prize in Physics has been awarded to Pierre Agostine, Ferenc Krausz and Anne L'Huillier for their contributions in creating ultrafast pulses of light that can give a snapshot of changes within atoms (Agostini & DiMauro, 2004). The ultra-short pulse lasers are very useful for various applications and they can be generated via mode-locking technique. This mode-locking laser generates a coherent phase of train pules with a repetition rate in a range of MHz and a pulse width in a range of nanoseconds to picoseconds even to femtoseconds. Mode-locking refers to the requirement of phase-locking many different frequency modes of a laser cavity in order to produce a pulse train of extremely short duration rather than a continuous-wave (CW) of light. The advantage and usefulness of this mode-locked is that its capability to generate immense peak power. Due to these high pulse energy, thus it has wide variety of application ranging from micro-machining metals (Gattass & Mazur, 2008), eye surgery (Mamalis, 2011), terahertz-wave generation (Stehr et al., 2010), optical imaging (Tang et al., 2009) and supercontinuum generation (Sobon et al., 2014). Due to plenty of new findings on technologies that utilized mode-locked lasers (Fermann & Hartl, 2013; Hasan et al., 2009), it is clear that these fiber lasers will be regarded as invaluable tools for future technologies development.

This thesis deals with developments of new fabrication method for saturable absorbers (SAs) and the demonstrations of passive Q-switched and mode-locked fiber lasers operating in a range from 1.5- to 2-micron region using transition metal dichalcogenides (TMDs) materials. These fiber lasers have received great attention lately due to their low cost, low power consumption, long term robustness, and ease of long-distance transmission through a standard single mode fiber. This thesis only concentrates on 2D materials SAs especially on transition metal dichalcogenides (TMD) such as $MoS_2$, $MoTe_2$ and $MoSe_2$ as SA to generate passive Q-switched and mode-locked fiber lasers.

The reason is due to the advantages where this SAs is cheap, compact in nature, easy fabrication method and high compatibility with the fiber lasers system. In this work, a newly developed SA thin film is inserted in a laser cavity to generate mode-locking pulses trains as described in Figure 1.1. The function of this SA is to convert CW laser into an ultrashort pulse laser with high peak power.

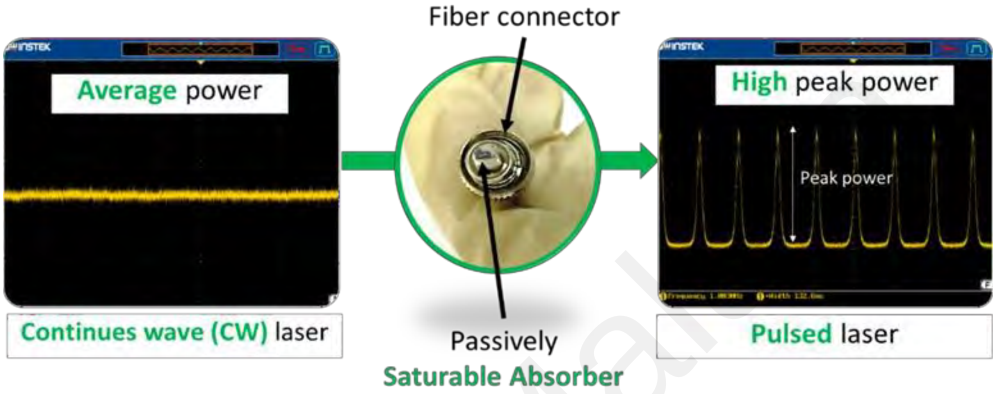

**Figure 1.1: Conversion of CW laser to pulsed laser using a passive SA device (Zhang, 2019)**

## 1.2 History of Laser

The first conceptual laser building block was established in 1916 by Albert Einstein where he proposed photons can be used to stimulate the emission of identical photons from excited atoms (Straumann & Zürich, 2013). In 1951, Townes conceptually suggested that stimulated emission at microwave frequencies can be used to oscillate in a resonant cavity to produce coherent output. Townes and Gordon successfully demonstrated the first microwave maser, directing excited ammonia molecules into a resonant cavity in 1954 which this resonant cavity oscillates at 24 GHz (Gordon et al., 1954). In 1957, Gould designed the well-known Fabry-Perot resonator (resonators mirrors) and the first word “LASER” was triggered from this design (Hecht, 2010). In 1958, Townes and Schawlow managed to publish a more details proposal about this optical maser (Schawlow & Townes, 2002). The first laser was successfully demonstrated by Maiman in 1960 at Hughes Research Labs. The ruby laser was constructed by focusing intense pump light into the ruby rod located inside the coil of a photographic flash-lamp and enclosing the assembly in a reflective cylinder (Maiman, 1960). Since then, lasers had gained a rich and complex history over the half-century. The first CW laser was successfully demonstrated at Bell Telephone Labs through the first gas laser constructed from a helium-neon gas (Javan et al., 1961).

In 1961, Snitzer demonstrated the first fiber laser using a high index neodymium-glass core in a millimeter-scale rod (Snitzer, 1961). With his continuous effort, he managed to construct the first fiber amplifier by using a spring-shaped coil of fiber that is slipped around a linear flash-lamp in 1964 (Koester & Snitzer, 1964). More than two decades later with the continuation of research and development, fiber laser technology has become more mature and finally gained more popularity. Paynes et al. manage to demonstrate a single-mode fiber laser using neodymium- doped silica glass as a gain medium in 1985 (Mears et al., 1985). Paynes constructed a neodymium-doped fiber laser ring cavity by pumping a 595 nm dye-laser. The schematic diagram is shown in Figure 1.2. The laser operated at 1078 nm with a 3-dB spectral bandwidth of 2 nm. With the maximum dye-laser power of 280 mW, it is able to produce output power of 2 mW. The progressive research and development for fiber laser keeps continues by Payne’s group (Mears et al., 1987; Reekie et al., 1986) and Desurvire (Desurvire et al., 1987) using an erbium-doped fiber for fiber laser and fiber amplifier applications at 1.55-micron region.

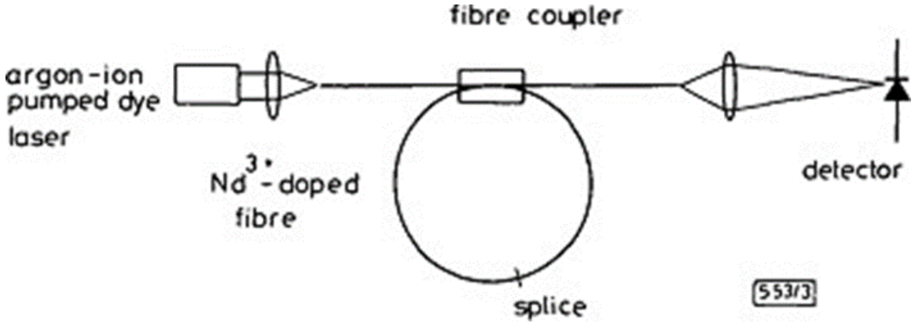

**Figure 1.2: Schematic diagram of dye-laser-pumped fiber ring cavity laser by Paynes. (Mears et al., 1985)**

In 1965, Johnson manage to demonstrate a continues-wave lasers at 2-micron region wavelength by using thulium and holmium ion as a gain medium (Johnson et al., 1965). The broad spectral bandwidth of dye lasers has led the path for ultrashort pulse laser generation. In 1964, Willis Lamb demonstrated mode-locking a laser can generate pulses limited in duration by the Fourier transform of the bandwidth (Lamb Jr, 1964).

The objective to achieve high-power applications in fiber lasers has finally realized in 2009. IPG Photonics managed to produce CW output power of 10 kW using a single-mode ytterbium-fiber oscillator amplifier. On the other hand, they manage to generate up to 50 kW for multimode fiber lasers (Gapontsev et al., 2009). In 2013, IPG Photonics manage to demonstrate the most powerful continues-wave fiber laser which produces 100 kW at 1070 nm (Shcherbakov et al., 2013). The research work on pulsed laser generation and development still ongoing progressively till this moment.

## 1.3 Motivation of the Study

As mentioned in section 1.1 above, ultrashort pulse fiber lasers are fundamental components used in many photonics system especially in industrial and medical applications as well as in scientific research (Fermann & Hartl, 2013). The prominent fiber lasers application in the industry which is very related to our daily life can be seen in machining glass for smartphone screens (Blackmon et al., 2015). Furthermore, fiber lasers are used for eye surgery in medical application (Grudinin, 2013). Moreover, in scientific research field, the research team managed to show the first proof of concept (POC) test for Project Silica (Anderson et al., 2023), a Microsoft Research project that uses the recent discoveries in ultrafast laser to store data in quartz glass and hence create a first-ever storage technology in the world. This ultrafast laser is used to encode data in quartz glass by creating layers of three-dimensional nanoscale gratings and deformations at various depths and angles (Anderson et al., 2018). Data is decoded back through the polarized light shines through the quartz glass. This latest scientific research project is used to develop a completely new storage system using femtosecond lasers where ultrafast laser is used to store data in the quartz glass. Ultrashort pulse scientific lasers can be constructed by using bulk or fiber-based components. Laser that are constructed using fibers (fiber laser) especially single-mode fibers can lead to smaller geometry size, more rugged pulsed scientific lasers, nearly zero maintenance, high peak powers, and also high intensities.

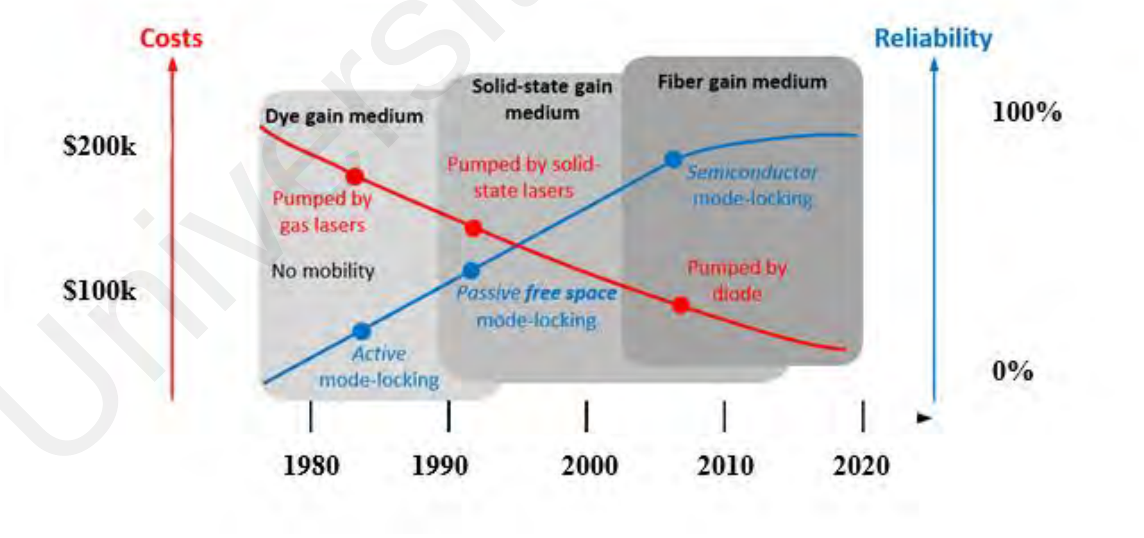

**Figure 1.3: Pulsed lasers evolution from 1980 (Wallace, 2015)**

Figure 1.3 shows the evolution of ultrashort pulse lasers development over the years. The first ultrashort pulse laser was based on a dye gain medium, this type of pulse laser was very expensive and unreliable in usage. However, ultrashort pulse laser which based on solid-state gain medium have higher reliability compared to dye laser, the cost is also more appropriate for commercial lasers (Wallace, 2015). The ultrashort pulse laser technology was shifted towards fiber laser over the past two decade. Fiber laser technology has remarkably progressed well and ultrafast lasers operating in the near-IR spectral region based on ytterbium, erbium, thulium, and holmium doped active fibers have replaced solid state lasers in many applications. The price of fiber lasers had reduced significantly due to mass production in telecommunication applications as well as in other industrial usage. Fiber lasers do not require beam alignment and high maintenance due to the nature of optical fiber itself. Fiber laser systems are significantly more compact compared to solid- state lasers since the light propagates entirely inside the optical fiber which can be coiled to have very small volume.

Saturable Absorber (SA) is often a preferred method for generating pulsed laser emission as these SAs enable a wide space of pulse parameters assessment without the need to employ costly and complex electrically- driven modulators which ultimately impose a lower limit on the pulse durations achieved directly from the laser source (Sun et al., 2009). These pulse laser devices can be broadly divided into two categories: real SA and artificial SA. Real SAs are based on materials that exhibit an intrinsic nonlinear decrease in absorption with increasing light intensity. Artificial SAs exploit nonlinear effects to mimic the action of a real SA by inducing an intensity-dependent transmission. This research work is restricted to real SAs by considering the role of emergent two-dimensional (2D) materials for this function and highlighting the benefits that these real SAs offer in terms of wideband operation, switching speed, and engineerable properties. The development and advancement of SAs technologies are almost in par with the evolution of the fiber laser itself. The first reported demonstrations of SA-based pulse generation in 1964 using a ‘reversibly bleachable’ dye (Soffer, 1964) and a colored glass filter (Bret & Gires, 1964). This SA-based pulse is generated just after four years from Maiman's successful demonstrated his first ruby laser operation (Maiman, 1960).

Figure 1.4 shows the historical evolution of the SA technologies. After the successful demonstration of lasers in the 1960s, 'reversibly bleachable' dyes were widely used in mode-locked lasers. The gain medium of this 'reversibly bleachable' dyes were also a dye, where it leads to the first demonstration of CW mode-locking (Ippen et al., 1972). From the revolution of low-loss optical fiber in 1970s, mode-locked lasers based on actively- doped fiber amplifiers emerged. This includes an early 1983 report of unstable mode-locking of a Nd:fiber laser using a dye SA (Dzhibladze et al., 1983). However, this passive method using real SAs to generate stable mode-locked in fiber systems remained challenging until the emerged of semiconductor saturable absorber mirror (SESAM) in the early 1990s (Keller et al., 1992; Zirngibl et al., 1991).

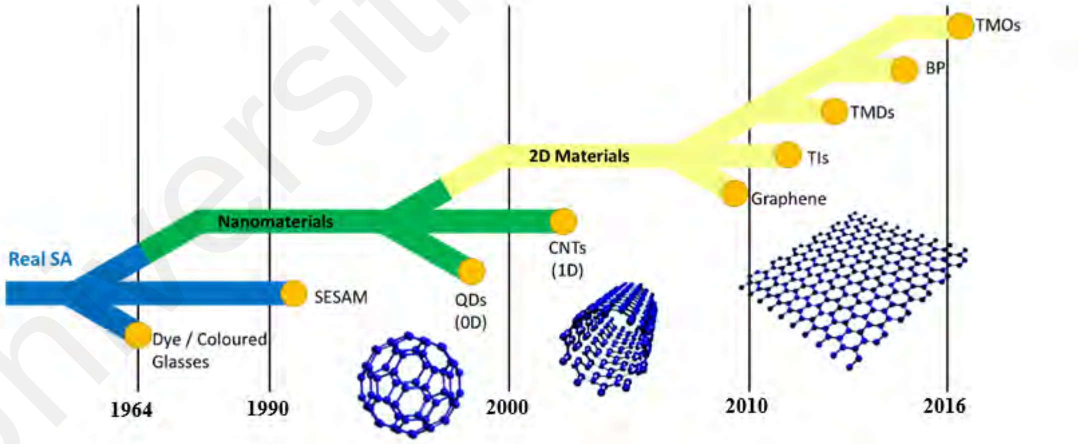

**Figure 1.4: SA evolution from 1964 (Woodward & Kelleher, 2015)**

SESAMs quickly became a highly successful technology for generating ultrafast mode-locked pulses and high-energy Q-switched emission from fiber lasers. However, SESAM is very costly and has very narrow operation bandwidth and complex fabrication method (Keller, 2003). Thus, from these limitations of SESAM, it helps the researchers to venture into other novel materials for SA application. Among these materials of particular interest are nanomaterials, where reduced dimensionality leads to strong quantum confinement, new physical phenomena and remarkable optoelectronic properties (Wang et al., 2012). Early reports of saturable absorption using colored glass filters exploited nanomaterials, where this glass filters were doped with semiconductor nanocrystals (zero- dimensional (0D) quantum dots (QDs)) such as cadmium selenide (Bret & Gires, 1964) where it modified the glass filter colour that quantum dots were explicitly engineered for the purpose of pulse generation (Guerreiro et al., 1997). After this successful pulse generation using nanocrystals, the field of nanomaterial SAs has gained attention from researchers. One dimension (1D) carbon nanotubes (CNTs) (Set et al., 2004) and two-dimension (2D) graphene (Hasan et al., 2009; Zhang et al., 2009) has emerged as promising nanomaterials exhibiting intensity-dependent absorption and sub-picosecond relaxation times (Martinez & Sun, 2013).

Graphene is a single atomic layer of carbon atoms that can be exfoliated from graphite, its 2D structure and zero band gap has enable wideband optical operation. Other 2D materials that can be used as real-SAs includes topological insulators (TIs), transition metal dichalcogenides (TMDs) and black phosphorous (BP). Transition metal oxides (TMOs) are also considered as another 2D materials which has high potential to be used as real-SAs. All of these 2D nanomaterials offer distinct, yet complementary properties (Li et al., 2015b; Woodward et al., 2015) which offer new opportunities for optical applications in fiber based systems. The possibility of combining the layers in 2D nanomaterials to form van der Waals heterostructures also offers plenty exciting opportunities for a wide range of new engineerable photonic devices (Geim & Grigorieva, 2013). This can be done through vary the potential of nanomaterial properties by their growth conditions, doping and electronic control (Lee et al., 2015). Figure 1.5 shows a recent 2D materials categories, it shows that transition metal dichalcogenides (TMD) such as $MoS_2$, $MoSe_2$ and $MoTe_2$ used in this work is categorized under 2D materials.

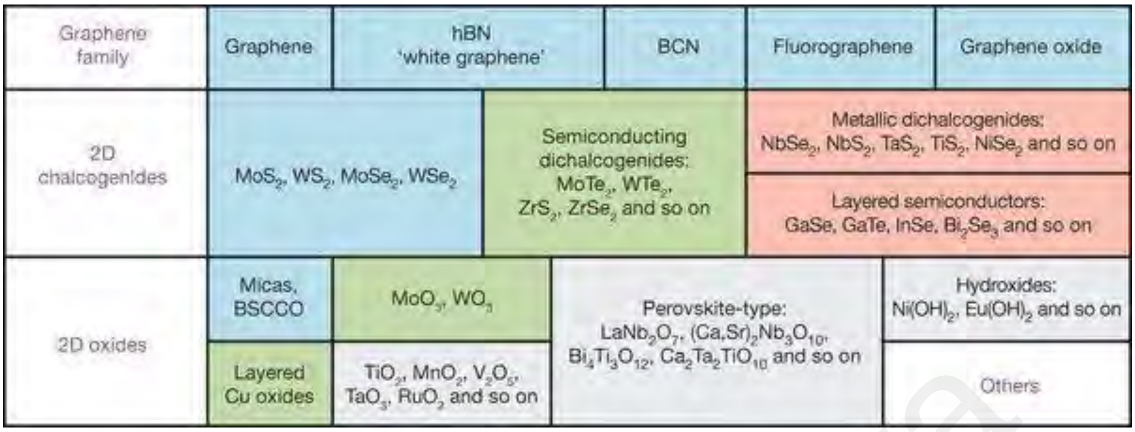

| | | | | | |
|---|---|---|---|---|---|
| Graphene family | Graphene | hBN 'white graphene' | BCN | Fluorographene | Graphene oxide |
| 2D chalcogenides | $MoS_2$, $WS_2$, $MoSe_2$, $WSe_2$ | Semiconducting dichalcogenides: $MoTe_2$, $WTe_2$, $ZrS_2$, $ZrSe_2$ and so on | Metallic dichalcogenides: $NbSe_2$, $NbS_2$, $TaS_2$, $TiS_2$, $NiSe_2$ and so on<br>Layered semiconductors: GaSe, GaTe, InSe, $Bi_2Se_3$ and so on | | |
| 2D oxides | Micas, BSCCO<br>Layered Cu oxides | $MoO_3$, $WO_3$<br>$TiO_2$, $MnO_2$, $V_2O_5$, $TaO_3$, $RuO_2$ and so on | Perovskite-type: $LaNb_2O_7$, $(Ca,Sr)_2Nb_3O_{10}$, $Bi_4Ti_3O_{12}$, $Ca_2Ta_2TiO_{10}$ and so on | Hydroxides: $Ni(OH)_2$, $Eu(OH)_2$ and so on<br>Others | |

**Figure 1.5: Current 2D materials (Geim & Grigorieva, 2013)**

## 1.4 Research Objectives

The aim of this research is to produce passively Q-switched and Mode-locked Fiber Lasers using 2D materials as SAs. We explore new method to fabricate SAs using transition metal dichalcogenides (TMD) such as $MoS_2$, $MoSe_2$ and $MoTe_2$ in this research work. In order to curb the challenges faced throughout this research journey, we have identified a few objectives as our guideline. The objectives embark as follows:

1. To fabricate Molybdenum dichalcogenides $MoS_2$, $MoSe_2$ and $MoTe_2$ as passive saturable absorbers (SAs) using the electro-deposition method and to characterize these SAs in term of their structural, crystallographic, optical and other relevant properties.
2. To validate the performances through the generation of mode-locked and Q-switch fiber laser using the above fabricated SAs

Therefore, four workflows are drafted to ensure the objectives are met as follows:

- SAs preparation and fabrication
- SAs characterization
- Experiment on ultrashort pulse fiber lasers
- Optimization of ultrashort pulse fiber parameters

## 1.5 Thesis Outline

This thesis consists of six chapters including this **chapter 1** which serves as an introduction. This chapter describes the background and history of laser. The motivation and objectives of this research work are also discussed.

**Chapter 2** provides literature reviews on various topics such as laser generation, fiber laser operating regimes, propagation properties, 2D materials, laser performance parameters and conventional fabrication methods.

**Chapter 3** discussed the saturable absorber (SA) fabrication method. Since this is a new method to prepare this TMDs materials, hence it is important to fully describe the substrate usage, mixing proportion and thin film synthetization. It is then followed by material characterization used in this research work.

**Chapter 4** shows the experimental setup for Q-switch fiber laser and hence presents all the Q-switched results obtained using different TMDs materials.

**Chapter 5** presents all the mode-locked results obtained using different TMDs materials.

**Chapter 6** present the summary of this research work and future work suggestion as an extension of the work presented in this thesis.

# CHAPTER 2: LITERATURE REVIEW

## 2.1 Introduction

With the advancement of laser technologies, ultrashort pulse lasers especially mode-locked lasers are now becoming more reliable and less complex in structure. Consumers are switching toward fiber lasers over the conventional bulk laser system in various application as fiber lasers are simpler to construct and less bulky. Semiconductor saturable absorber mirror (SESAM) (Saraceno et al., 2011) has become a highly successful technology for generating ultrafast mode-locked pulses for fiber lasers, however, most of the ultrashort pulse fiber lasers are constructed based on passive mode-locked fiber oscillators, which are then amplified in several stages to reach the desired output pulse energies. This chapter provides literature reviews on various topics on fiber lasers such as the working principal of laser generation and the fiber lasers operation regimes. Furthermore, Q-switched and mode-locked characteristic and operations are explained since it is an important parameter to generate a stable ultrashort pulse laser. The ultrashort pulse formation in the laser cavity is due to dispersion and nonlinear effect where the light propagated inside the cavity induces a self-amplitude modulation. The ultrashort pulse then travels along the optical fiber and hence its pulse dynamics is influenced by group velocity dispersion (GVD) (Rostami & Andalib, 2007) and self-phase modulation (SPM) (Verma & Garg, 2012). The harmonious interaction between GVD and SPM (Malik et al., 2008) had contributed to the generation of a solid and robust laser pulse shape. The working principle of saturable absorber (SA) is also discussed as this SA is the main contributor to provide a passive loss modulation in the laser cavity for the generation of ultrashort pulse. A two-level electronic model is used to explain the basic working principal of SA in this chapter. The material- based SA used in this research work is a 2D material, hence these 2D materials including graphene, topological insulator (TI), black phosphorus (BP) and transition metal dichalcogenide (TMD) is also included in this literature review. Subsequently, the performance of the pulse laser is measured using different parameters such as repetition rate, pulse width and pulse energy. In the last session, the conventional fabrication method is also highlighted in the literature review for the comparison of the new method proposed in this research.

## 2.2 The theory of laser generation

Laser is a device that can stimulate atoms or molecules to produce photons at certain wavelength, multiply these photons and radiate it with narrow beam. This emission only covers very limited range of visible, infrared, or ultraviolet wavelengths. Nowadays different characteristics and multiple types of lasers have been developed for different purpose of application. In other words, laser is also known as light amplification by the stimulated emission of radiation where it is generated by the interaction between light and matter (Dickey, 2018). In fact, when a particle interacts with a photon, it can absorb or emit a photon, which corresponds to a change in its energy state. This process refer to changes in the particle's quantum state or its dynamics as a result of the photon interaction which it can also affect the particle's momentum and other properties. Figure 2.1 shows the electromagnetic (EM) spectrum ranges from gamma rays, X rays, infrared to long radio waves.

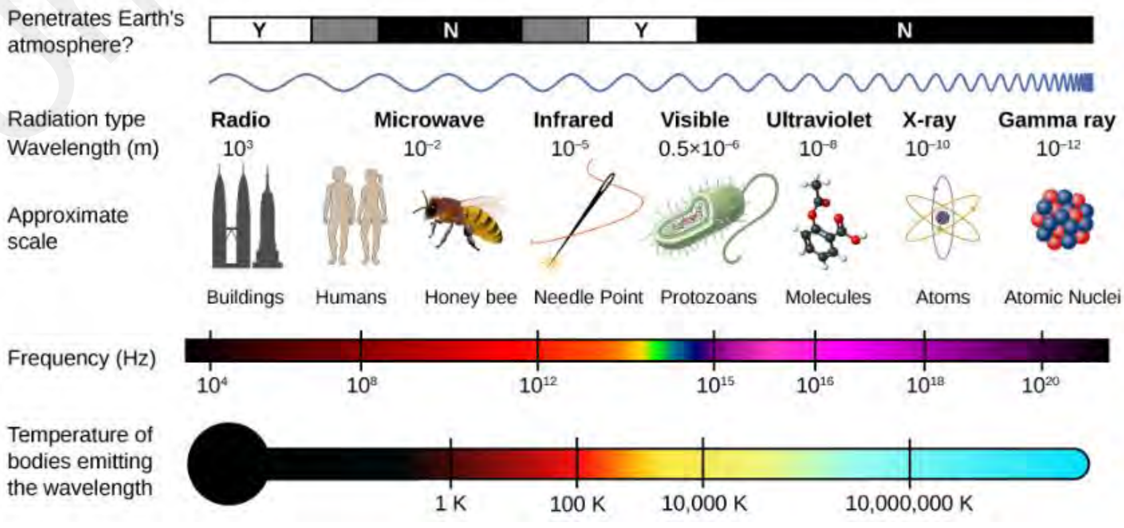

**Figure 2.1: Illustration of electromagnetic spectrum (Ling et al., 2016)**

The laser wavelengths cover the spectrum of ultraviolet (UV), visible lights, and infrared regions. The region of UV light consists of wavelengths between 180 nm and 400 nm while visible light region consists of wavelength between 380 nm to 750 nm. The material used for lasing will determine the emitted wavelength. For example, Ytterbium-doped fiber (YDF), Erbium-doped fiber (EDF) and Thulium-doped fiber (TDF) operates at wavelength of 1um, 1.55um and 2um respectively.

### 2.2.1 Basic Concepts

The interaction of radiation with an atomic system involving two energy levels as shown in Figure. 2.2. Let the ground state energy denoted as E1 and the excited state energy as E2 while N1 and N2 represent the atomic densities in the ground state and excited state respectively. If the interaction of radiation with this atomic system happens at an angular frequency as follow:

$$\omega = \frac{E_2 - E_1}{h} \qquad (2.1)$$

where h is Planck's constant with the value of $6.626 \times 10^{-34}$ J·s, it can occur in three distinct ways (Einstein, 1916). These three processes are known as stimulated absorption, stimulated emission and spontaneous emission.

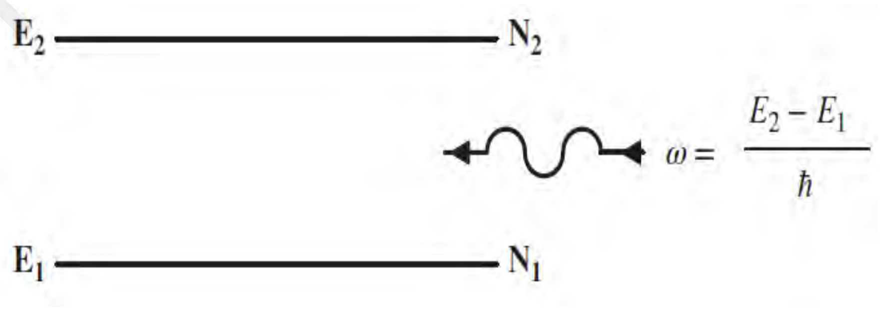

**Figure 2.2: Two-level atomic system interacting with electromagnetic radiation (Liu, 2016)**

### 2.2.2 Stimulated absorption

Figure 2.3(a) shows an atom absorbing the incident radiation and the energy from ground state $E_1$ changed to excited state energy $E_2$. It can be described also as an electron in the atoms gain energy and jump from inner orbit to outer orbit (Swader et al., 1975). In order to make this transition happen, atom requires energy corresponds this bandgap and this energy is provided by the incident electromagnetic radiation. The absorption rate is much dependent on the population density in level $E_1$ as well as on the energy spectral density per unit volume of the radiation. Albert Einstein proposed that the absorption rate of the atoms from the incident radiation per unit time per unit volume undergoes from level 1 to level 2 is given by:

$$R_{abs} = -\left(\frac{dN_1}{dt}\right) = B_{12} u_s(\omega) N_1 \qquad (2.2)$$

where $u_s(\omega)$ is the electromagnetic radiation energy spectral density per unit volume, this term represents the spectral distribution of the external field and is often depends on the frequency (ω) of the field and characterizes how much energy is available at different frequencies. $B_{12}$ is the interaction parameter or rate constant that governs the transition between energy level 1 to energy level 2. $R_{abs}$ is the rate of absorption of energy from level 1 and it's typically measured in reciprocal seconds ($s^{-1}$). The negative sign in Eq. (2.2) indicates a decrease in the population density at level 1 due to absorption. For instance, if an atomic system having the volume of 1 $m^3$ and the population of $10^{15}$ atoms make an upward transition per second after absorbing the incident radiation in that volume, hence, the absorption rate is $R_{abs} = 10^{15}/s/m^3$. This is also equivalent to $10^{15}$ photons are absorbed per second per cubic meter. Figure 2.3 (b) represents an atom already in the excited state energy $E_2$ after the absorption taken place. If the atom drops from energy $E_2$ to $E_1$, the atom will emit electromagnetic radiation typically in the form of photons and at angular frequency $\omega = (E_2 - E_1) / h$ where $h$ is the Planck constant equal to $1.0545718 \times 10^{-34}$ Js. There are 2 types of emission known as stimulated emission and spontaneous emission will be discussed in the following sections.

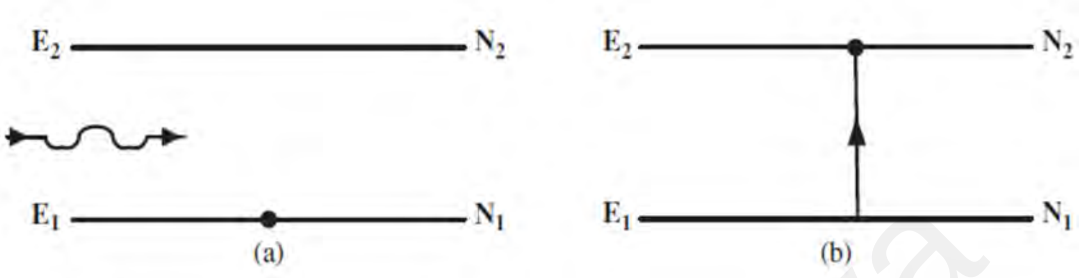

**Figure 2.3: Two-level atomic system absorbing a photon (a) Before absorption and (b) After absorption (Liu, 2016)**

### 2.2.3 Stimulated Emission

Stimulated emission is one of the fundamental principle for the operation of lasers and other optical devices. It is a process where an atom which already in the excited energy state $E_2$, is triggered to release a photon by the presence of an external photon with the same energy, frequency, phase and direction. In other words, stimulated emission occurs when an incident photon of frequency $\omega$ triggers the emission of a second photon when the atom makes a transition from the higher energy state $E_2$ to the lower energy state $E_1$ and emit another photon of frequency $\omega$ that is in phase with the incident photon. Stimulated emission is only possible with a population inversion where there are more atoms in the excited state $E_2$ than in the ground state $E_1$. Achieving population inversion is a crucial prerequisite for laser operation. Figure 2.4 shows stimulated emission amplifies light where one photon comes in and two photons leave. Hence, this creates a cascade effect, leading to the amplification of coherent light. Albert Einstein proposed that the rate of emission is proportional to the energy spectral density of radiation at frequency $\omega$ and the population density at the excited state $E_2$ (Senior & Jamro, 2009).

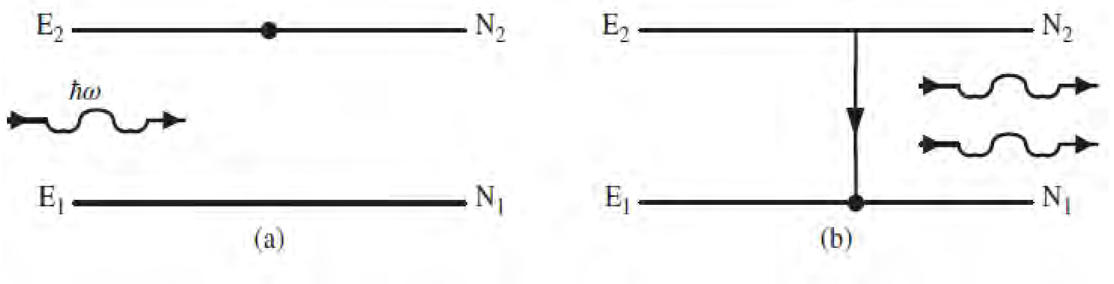

**Figure 2.4: Two-level atomic system emitting a photon due to stimulated emission (a) Before stimulated emission and (b) After stimulated emission (Liu, 2016)**

### 2.2.4 Spontaneous Emission

Spontaneous emission is another fundamental process that occurs when an atom in an excited energy state $E_2$ transitions to a lower energy state $E_1$ by emitting a photon without any external stimulation or perturbation. It is called "spontaneous" because this emission is totally random and probabilistic where the exact time of this emission cannot be predicted, and it is not dependent on the presence or influence of other photons or external triggering factors. Figure 2.5 shows the process of spontaneous emission. This spontaneous emission is responsible for the atom natural decay of excited states to their ground states and this process leads to the release of a photon which carries away the energy difference between the excited and ground states. The emitted photons in spontaneous emission have different range of frequencies and wavelengths and this is in contrast to stimulated emission where all emitted photons have the same frequency and phase. Unlike stimulated emission, spontaneous emission does not require a population inversion, in fact, it occurs even when there is a greater population in the ground state than in the excited state. For instance, white light is incoherent and non-monochromatic because there is no correlation in the times when the atoms make transitions (Wei et al., 2021).

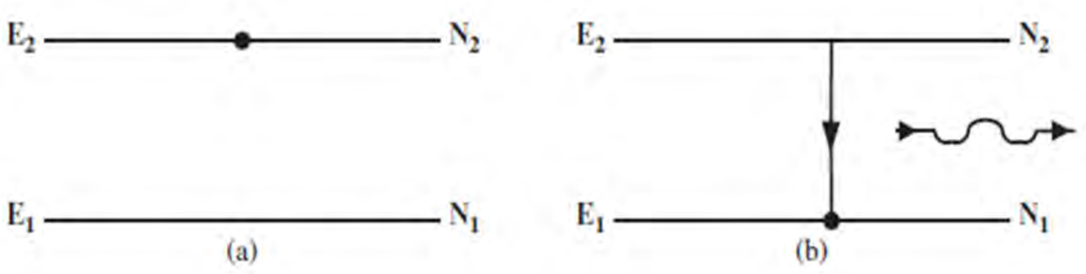

**Figure 2.5: Two-level atomic system emitting a photon due to spontaneous emission (a) before spontaneous emission and (b) after spontaneous emission (Liu, 2016)**

### 2.3 Main Operating Regimes of Fiber Lasers

Solid-state lasers, semiconductor lasers and fiber lasers are all types of lasers that they can exhibit similar operating regimes. These operating regimes are often determined by the laser's gain medium, cavity design, and the input energy it receives. The physical processes that take place in the gain medium especially the fiber core create challenges that are unique to fiber lasers mainly due to their small core dimensions compared with other active gain medium. This small core dimensions in fiber lasers resulted a high power density which leads to the generation of heat within the gain medium itself. The heat generated can cause thermal lensing which finally leads to low power output, higher beam distortion and lower beam quality. Hence, efficient thermal management is crucial to prevent overheating to maintain the laser performance. Moreover, the high-power intensity within the small fiber core can also lead to nonlinear effects such as stimulated Raman scattering and stimulated Brillouin scattering which limit the achievable laser output power, affect the beam quality and lead to unwanted spectral broadening.

In semiconductor lasers, the gain material is a thin semiconductor layer with a small cross-sectional dimension on the order of micrometers (*u*m) which are usually created using epitaxial growth techniques that allows precise control of the material properties. The length of the gain medium for semiconductor laser is very short in the range of micrometers to allow for the compact size of semiconductor lasers.

In contrast to semiconductor lasers, fiber lasers have much longer gain medium. The length of the gain medium can be the entire doped optical fiber itself, often in the order of meters or even kilometers depending on the specific cavity design and their application. This long length of gain medium in fiber lasers allows the generation of high optical powers to produce efficient laser amplification which makes them suitable for various high-power applications. The key difference between the length of gain medium in semiconductor lasers and fiber lasers contributes to different operating characteristics and performances in each type of laser itself. Semiconductor lasers are compact and efficient and well-suited for applications like optical communications, laser diodes and consumer electronics. On the other hand, fiber lasers are well-known for their high-power density, excellent beam quality and stability and the ability to efficiently generate and amplify laser pulse, making them suitable for materials processing, laser cutting and scientific research. Hence, the choice of laser type depends on the particular application and performance requirements. This following section provides a more detailed description of the three main laser regimes.

### 2.3.1 Continuous wave Operation

In continuous wave (CW) laser operation, the laser emits a constant output of photons over an extended period of time as compared to pulsed laser operation where the laser emits short bursts of high-intensity photons (Zeller & Peuser, 2000). In a CW laser, the laser medium is continuously pumped and continuously oscillates in a single or multiple longitudinal or transverse modes and the laser emits a constant, uninterrupted beam of coherent photons. The power output of a CW laser is relatively stable and consistent, hence making it suitable for a wide range of applications that requires constant power output which include materials processing such as cutting, welding and engraving, scientific research, telecommunications, medical laser surgery and dermatology and etc. The ability of this CW laser to maintain a constant output is valuable in these fields. CW lasers normally have much lower peak powers compared to pulsed lasers which can have very high peak powers for short durations. Although the overall output energy is lower, CW lasers can generate a significant amount of heat due to their continuous operation, therefore, CW lasers typically require efficient cooling systems to prevent overheating and to maintain the laser's performance.. Like all other types of lasers, the CW regime of fiber lasers follows similar physics and theory where CW fiber lasers use a gain medium to amplify the photons. This gain medium is normally an optical fiber doped with rare-earth materials such as erbium, ytterbium, praseodymium, thulium, holmium or neodymium. The choice of dopant materials determines the laser's operating wavelength. For instance, ytterbium and neodymium doped fiber laser will operates in 1um wavelength, erbium doped fiber laser operates in 1.5 um region while thulium and holmium doped fiber lasers produce 2um wavelength photons (Paschotta, 2022). CW fiber lasers require an external energy source to pump the gain medium. The pump energy is absorbed by the dopant ions in the gain medium, causing the ions to excite to higher energy levels. Hence, population inversion occurs, and this is a necessary condition for lasing as explained earlier in the stimulated emission in 2.2.3. CW fiber lasers require optical feedback to sustain its lasing operation and this action is supported by a pair of partially reflecting mirrors or by using a fiber Bragg grating as an internal reflector. This feedback mechanism causes photons to bounce back and forth within the gain medium and stimulate the emission of coherent photons. The main difference during the design and development of CW fiber is mostly associated with nonlinear scattering processes and other nonlinear processes including the optical Kerr effect, self-phase modulation, cross-phase modulation, four-wave mixing and stimulated Raman scattering. These nonlinear processes are associated with refractive index influence by high-power propagating inside the fiber core. These nonlinear effects become significant when the intensity of the light exceeds a certain threshold. Although these nonlinear effects can cause signal degradation in optical communication systems, however it can be beneficial on certain application where these nonlinear effects are harnessed for supercontinuum generation.

### 2.3.2 Q-Switched Fiber Lasers

Q-switching is a technique to generate energetic short light pulses from a laser by modulating the intracavity losses and hence controlling the Q factor (quality factor) of the laser resonator. This technique is mainly applied to generate nanosecond (ns) pulses of high energy and high peak power with low repetition rate compared to mode-locking method. In this Q-switching technique, a single solid and short pulse trains of a laser radiation can be achieved (Singh et al., 2012). The generation of the Q-switched pulses through the following procedures. First, the resonator losses are kept at a high level. Since lasing cannot happen during high losses, the input pump power that is fed into the gain medium accumulates at the resonator. The energy stored can be multiple of the saturated energy in the resonator. However, when the loss at the resonator is suddenly reduced to a small value, the energy of the laser radiation builds up very quickly in the resonator. Once the intracavity power has reached the saturation energy of the gain medium, the pulse peak is achieved when the gain equals to the resonator loss. Typically, Q-switching technique produces a short pulse fiber laser with pulse width ranges from microsecond to nanosecond and the repetition rate is in the range from 1–100 kHz in kilohertz (kHz) regime (Al-Hiti et al., 2021). Furthermore, the pulse repetition rate is always much lower than the cavity round trip time (Stumpf et al., 2010).  There are two type of Q-switching, namely active Q – switching and passive Q- switching. For active Q-switching, the losses at the resonator are modulated with an active control element typically by an acousto-optic or electro-optic modulator. The laser pulse is formed immediately after triggered by an electrical signal. Q-switched pulses are generated in a periodic form with a given pulse repetition rate and is driven by an oscillator for periodically triggering the pulse generation. The acousto-optic or electro-optic modulator is used to control the pulse repetition rate of an actively Q-switched laser. The duration of the generated pulses depends on the resonator round-trip time and also on the initial round-trip net gain.

For passive Q-switching, the losses at the resonator are automatically modulated with a variety types of saturable absorbers SAs such as SESAM, CNT and graphene. SESAMs offers very high power output with wide range of laser parameters for reliable self-starting pulse to be operated in appropriate regime (Xiao & Bass, 1997). Figure 2.6 shows the basic structure of passive Q-switch laser cavity. The operation to generate pulses are different from active Q-switching laser where the losses introduced by passive Q-switched are too high for laser process to start in the early stage. When the energy stored in the gain medium has reached a sufficiently high level, the pulse is formed in the resonator.

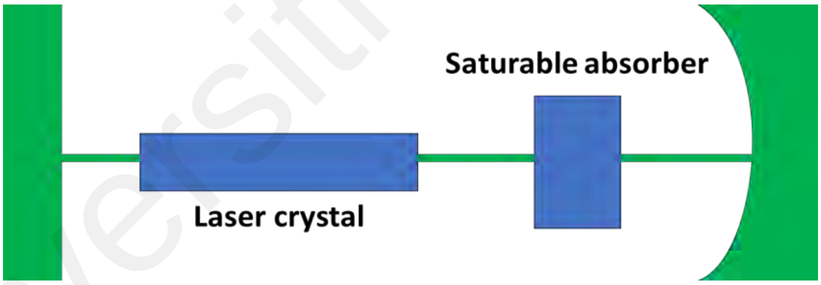

Figure 2.6: Basic structure of passive Q-switch laser cavity (Welford, 2003)

The passive Q-switched pulse generation with saturable absorber SA is shown in Figure 2.7 below. The saturable and non-saturable absorption of the SA is represented by the loss curve while the gain curve represents the population inversion for lasing to occur. The photon density or output laser intensity is represented by the pulse curve highlighted in red. When the photons are continuously supplied by the input pump, population inversion occurs where it surpasses the loss induced by the saturable absorber SA until the SA is saturated. When the SA is saturated, the loss decreases dramatically, hence allows the photons to pass through the SA. The photons emanating from the input pump coupled with the photons emitted from SA have created an abrupt and powerful peak resulting in the formation of a laser pulse with a narrow pulse width. After the release of laser pulse, the gain has decreased dramatically while the absorption loss of SA returns to its initial stage where it start to absorb photons from the input pump again. This process is repeated as long as the input pump provides continuous photons energy and eventually create a pulse train with constant repetition rate as shown in Figure 2.8.

In most cases of passive Q-switching, the pulse energy, peak power and duration are fixed, where the changes of the pump power only influence the pulse repetition rate. The pulse duration depends on the resonator round-trip time and the temporal modulation of the net gain. The temporal modulation is determined by the modulation depth of the saturable absorber SA used in the cavity. With higher modulation depth, pulses with shorter duration and higher energy is obtained.

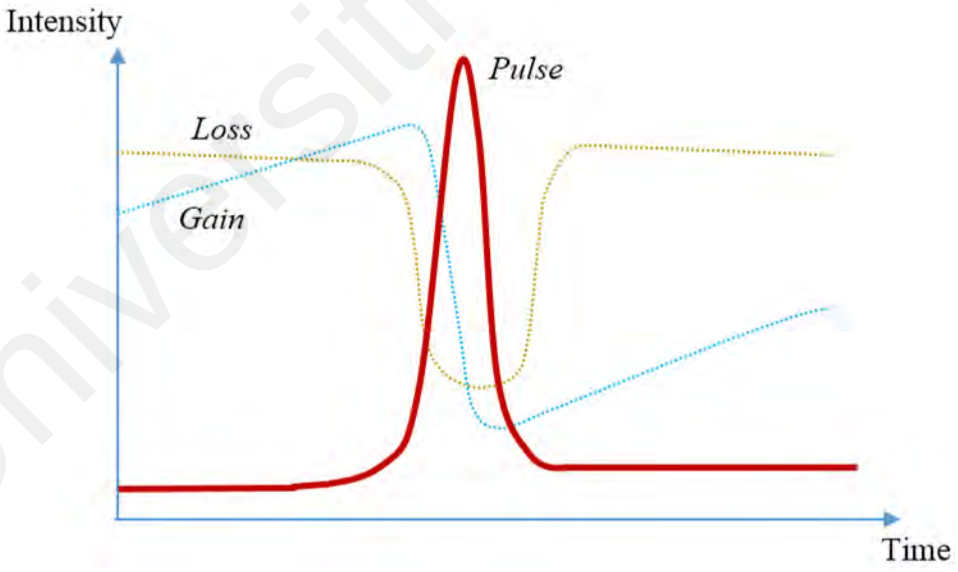

**Figure 2.7: Pulse generation process (J.-C. Diels & W. Rudolph, 2006)**

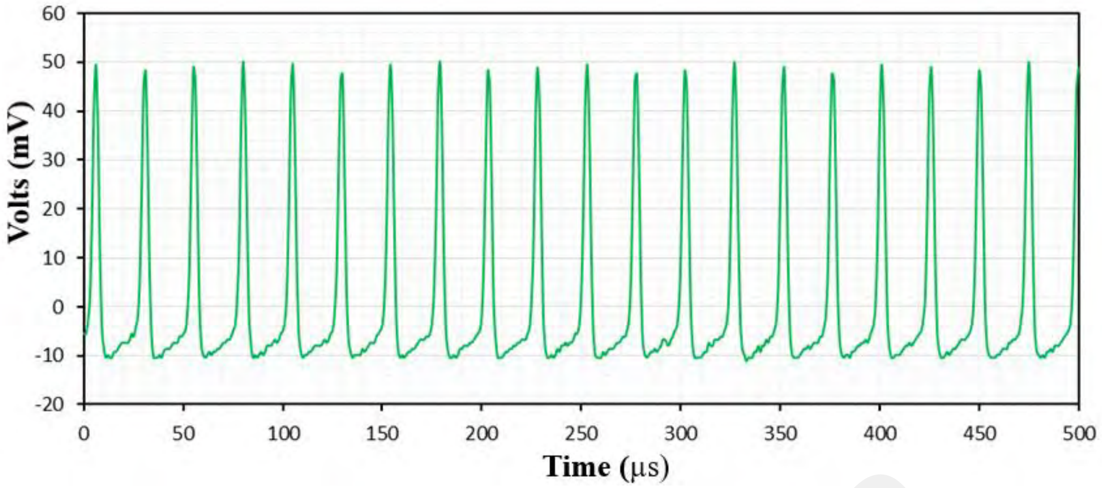

**Figure 2.8: Example of pulse train generated by a Q-switched laser (J.-C. Diels & W. Rudolph, 2006)**

In order to produce optimal performance of Q-switched pulsed laser operation, the saturable absorber SA parameters should be optimized. Among those important parameters are the saturable absorption, non-saturable absorption, saturation intensity, saturable absorber recovery time and absorption bandwidth. All of these parameters are heavily influenced by the chemical compositions and atomic arrangement of the SA material. In addition, the saturable absorption ability is much dependent on the crystal structure of the SA itself. These parameters can be described in a two-level non-linear saturable absorption profile as shown in Equation (2.3). After normalization, the saturable absorption is equivalent to modulation depth while non-saturable absorption is linear absorption expressed in percentage form (Bao et al., 2011).

$$\alpha(I) = \frac{\alpha_s}{1 + \frac{I}{I_{sat}}} + \alpha_{ns} \qquad (2.3)$$

From equation 2.3, $\alpha(I)$ is the absorption, $I$ is the input intensity, $I_{sat}$ is the saturation intensity, $\alpha_s$ is the modulation depth and $\alpha_{ns}$ is the non-saturable absorption. Moreover, the saturable absorption can be expressed as in the following equation 2.4.

$$\alpha_s = \sigma_{sg} N \qquad (2.4)$$

where the $\sigma_{sg}$ is the absorption ground cross section and N is the concentration of the SA material. The saturable absorption indicates the ratio of photons absorbed per unit distance within the SA material. When the saturable absorption coefficient is high, photons are absorbed more rapidly within a shorter distance in the SA, rather than penetrating deeper into the material. This concept can be better exemplified with the assistance of Figure 2.9 where it shows the photon intensity, $I_{v0}$ as a function of distance, x for small and large values of absorption coefficient. When the absorption coefficient is large, the photons are absorbed over relatively shorter distance and the photon intensity $I_{v0}$ decreases exponentially with the distance x within the SA.

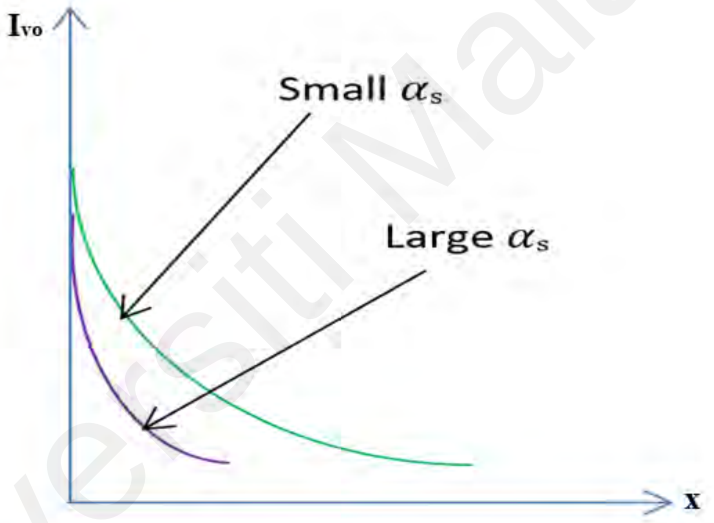

**Figure 2.9: Photon intensity, $I_{vo}$ versus distance, x for two different absorption coefficients. (Fox, 2001)**

On the other hand, non-saturable absorption consists of the loss that cannot be saturated by the saturable absorber including scattering loss, transmission loss, non-saturable defect absorption, free carrier absorption, Auger recombination, and various other mechanisms. Scattering loss may arise from factors such as the roughness of the material's surface, irregular interfaces, and lattice defects. Hence, the minimum achievable pulse width relies on the modulation depth of the saturable absorber which consists of both saturable absorption and non-saturable loss properties. To better illustrate the absorption dynamics of the saturable absorber, Figure 2.10 indicates a plot of the normalized non-linear absorption at different normalized light intensity as described in equation 2.3. Based on the figure, the optical absorption is high when light intensity produced in the laser resonator is less than the saturation intensity ($I<I_{sat}$) of the SA, thus lasing is prevented. As the light intensity $I \geqslant I_{sat}$, the absorption diminishes and the transmissivity progressively increases. Ultimately, when $I \gg I_{sat}$ the absorption becomes saturated, resulting in the resonator having a high Q-value and initiating Q-switched laser oscillation. Nonetheless, the inability to achieve 0% for nonlinear saturable absorption is due to the non-saturable loss property represented by $\alpha_{ns}$ of the saturable absorber.

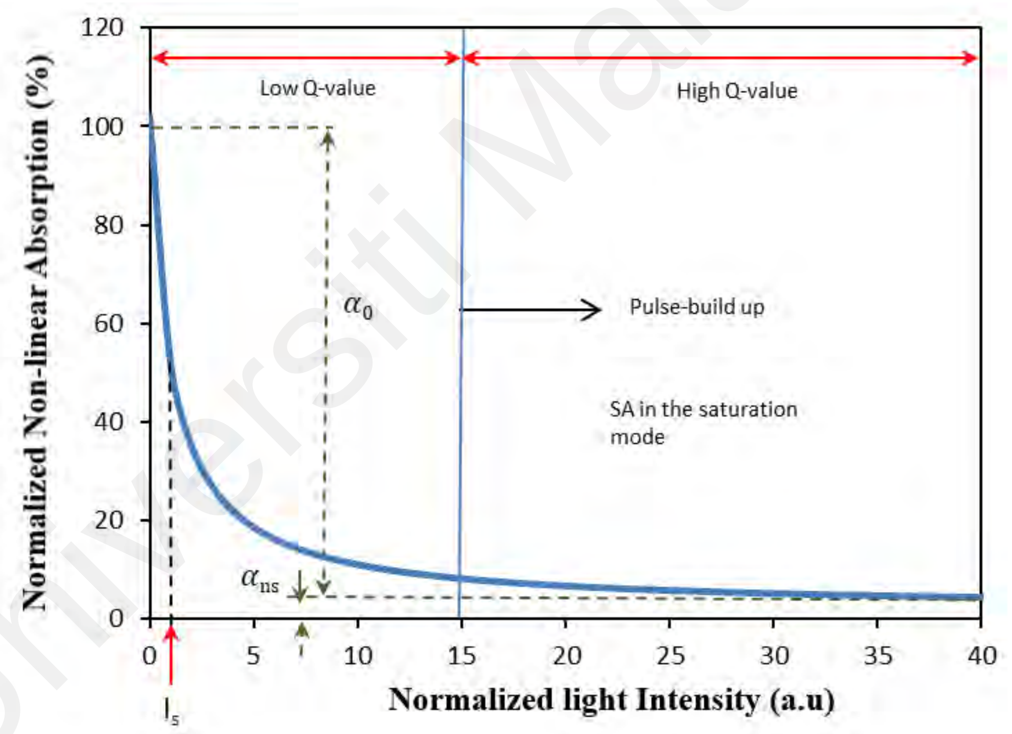

**Figure 2.10: Example of modulation depth profile of a SA (Ferreira & Paul, 2024)**

By comparison to active Q-switched fiber lasers, passive Q-switched fiber lasers have more attractive advantages of compactness, simplicity, and flexibility in design (Luo et al., 2010) while active Q-switching requires expensive and complex external driver of electro-optical or acoustic optics (AO) modulators inserted into the cavity (Kalisky, 2004). Furthermore, passive Q-switched fiber lasers have a simpler design, lower cost and able to provide stable and consistent output power compared to active Q-switch fiber lasers (Rüdiger, 2008). Passive Q-switching is suitable for very high pulse repetition rates, however, it has the disadvantage of lower pulse energy. Other than that, external pulse triggering is not possible in passive Q-switching except with an optical pulse from another source, and it may also be a disadvantage that the pulse energy and duration are independent of the pump power, which only determines the pulse repetition rate.

The typical characteristic of Q-switch technique has pulse repetition rate in the range from 1–100 kHz. Hence the typical graph obtain should match the following Figure 2.11 and Figure 2.12.

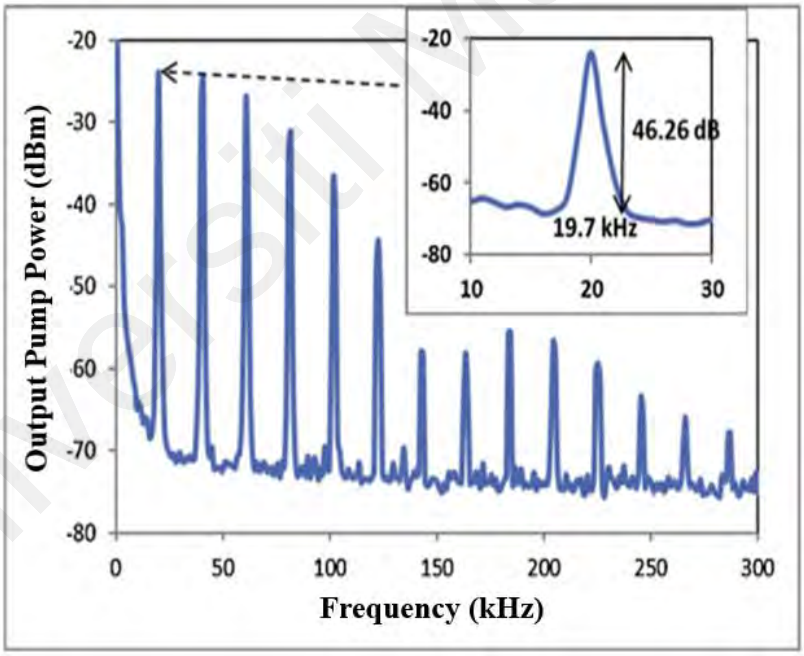

**Figure 2.11: Fundamental frequency in kHz of Q-switch at certain pump power (Mustapha et al., 2022)**

For passive Q-switching, the pulse energy, peak power and duration are fixed, where the changes of the pump power only influence the pulse repetition rate. Hence, pulse repetition rate increased with the increased pump power.

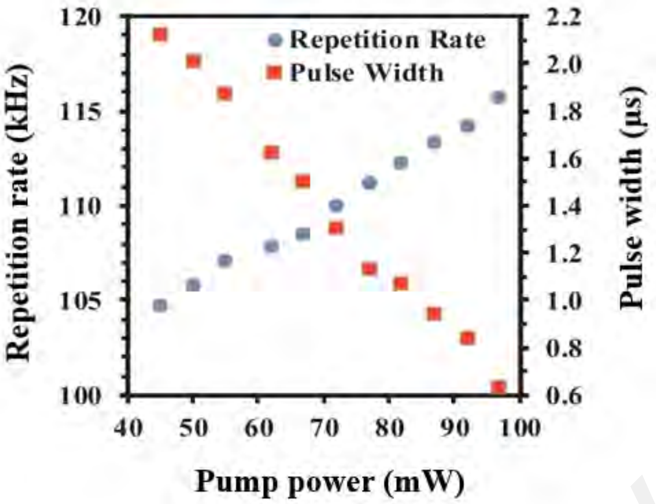

**Figure 2.12: Pulse repetition rate increased with the increased pump power (Adel, 2004)**

### 2.3.3 Mode-locked Fiber lasers

Mode-locked fiber lasers have drawn the attention of researchers due to their capacity to generate multiple crucial laser characteristics concurrently, including elevated peak power, substantial average power, relatively large pulse energy, high repetition rates and diffraction-limited beam quality. The distinct features of mode-locked fiber lasers can be seen on various traits inherent to fiber lasers and in addition to the specific characteristics associated with mode-locked lasers. Mode-locking is a technique to obtain ultrashort pulses from laser cavity and the pulse duration may vary from picoseconds (ps) to femtoseconds (fs) (Singh et al., 2012). The generation of ultra-short pulses occurs when there is a consistent phase relationship among all the longitudinal modes. This phenomenon results in a fixed phase separation between adjacent longitudinal modes which is known as "mode-locking" or "phase-locking." The establishment of a consistent phase alignment among all the modes within a laser cavity causes the continuous-wave (CW) laser to evolve into a series of pulsed emissions. The capability for multiple longitudinal modes to produce lasing simultaneously depends on the gain linewidth $\Delta vg$ and the frequency gap between these modes. Under high level of pump intensity, it is reasonable to anticipate that the number of modes M, oscillating inside the cavity is determined by the following expression:

$$M = \frac{\Delta \upsilon_g}{c/2L} = \frac{2L}{c}\Delta \upsilon_g \qquad (2.5)$$

where $c$ is the speed of light and L is the length of a linear cavity. The minimum pulse duration achievable with a specific gain linewidth $\Delta vg$ is calculated using the following formula:

$$\tau_{min} = \tau_M = \frac{2L}{cM} = \frac{1}{\upsilon_g} \qquad (2.6)$$

From Equation (2.6), it can be deduced that the shortest attainable pulse duration corresponds to the reciprocal of the gain linewidth $\Delta vg$, expressed in Hertz. Pulse radiation can be generated by enhancing the coherence of the phases among the different modes (Haus, 2000). This will result in a series of laser pulses with a high repetition rate and extremely narrow pulse widths, evenly spaced over time intervals and typically in the Megahertz range (MHz) (Fermann & Hartl, 2013; Keller, 2003).

In order to gain insight into the mode-locking process, let's commence by examining a continuous-wave (CW) laser equipped with a Fabry-Perot cavity in the frequency domain. Inside the laser cavity, the longitudinal modes are frequencies that circulate within the resonator where these modes experience greater gain than losses. These modes can function as a collection of independent oscillators and with each complete round trip through the cavity, their amplitudes will increase. While these modes oscillate independently, the laser continuously emits light. Figure 2.13 illustrates the output signal that arises from the propagation of three distinct longitudinal modes. However, when a constant phase shift exists between these different modes, the cavity generates a pulse train and the phases become locked relationship (Faubert & Chin, 1982; Trebino, 2000). Figure 2.14 shows the output signal of a mode-locked laser configuration where the mode-lock pulse originates from the propagation of three longitudinal modes with specific phase relationships. Furthermore, the mode-locking process involves setting a particular phase correlation between the various oscillating modes within the cavity.

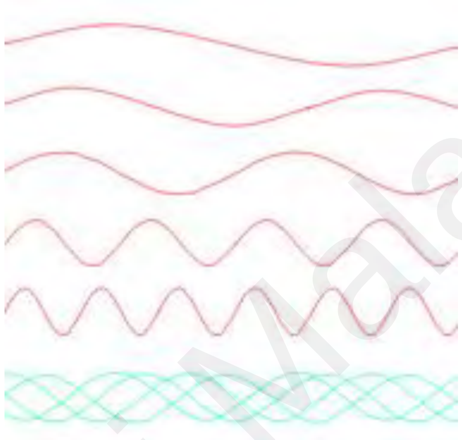

**Figure 2.13: Laser output signal worked without mode-locking mechanism (Harun & Arof, 2013)**

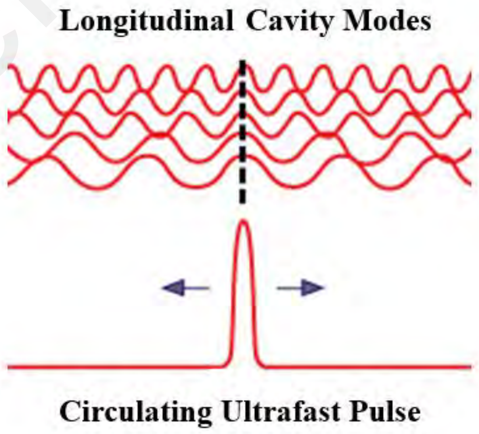

**Figure 2.14: Output of mode-locked laser signal (Harun & Arof, 2013)**

For different type of fiber laser cavity, the fundamental repetition rate of a mode-lock fiber laser is determined by its cavity length, as shown in the equations below:

Repetition rate for linear cavity:

$$f = \frac{c}{2Ln} \qquad (2.7)$$

Repetition rate for ring cavity:

$$f = \frac{c}{Ln} \qquad (2.8)$$

where L denotes the length of the cavity, c is the speed of light (3x108 $ms^{-1}$) and n is the refractive index of the medium (1.46 for silica fiber) respectively (Milonni & Eberly, 2010). As indicated by equations (2.7 & 2.8), the repetition rate f is reciprocal to the overall cavity length in passive mode-locking, hence, a shorter cavity length results in a higher pulse repetition rate.

Similar to the classification of Q-switching techniques, mode-locking methods can be categorized into two types, active mode-locking and passive mode-locking. Active mode-locking is the result of the periodic modulation of the resonator losses or the phase change of the round-trip laser cavity with modulators such as acousto-optic or electro-optic modulator, a Mach–Zehnder integrated-optic modulator, or a semiconductor electro-absorption modulator. When this modulation is synchronized with the resonator round trips, this can lead to the generation of ultrashort pulses, usually in picosecond (ps) pulse durations. Passive mode-locking is achieved with the use of saturable absorber SA which exploits the non-linear optical effects such as saturation of an SA or the use of a non-linear refractive index shift of an appropriate material (Svelto & Hanna, 2010). This mode-locking with the usage of SA allows the generation of much shorter femtosecond (fs) pulses which modulate the resonator losses much faster than an electronic modulator. This passive mode-locking method is obviously more preferable to be used to generate pulse lasers because they are more lightweight, less costly, more versatile and simpler in nature (Ismail et al., 2012). In the passive mode-locked laser as depicted in Figure 2.15, the loss modulation is accomplished using a saturable absorber, such as SESAM or other 2D materials. Using this approach allows us to generate shorter pulses compared to active mode-locking due to faster modulation loss when shorter pulses circulate in the cavity. Due to the high pulse repetition rate in mode-locked laser, hence the pulse energies obtained are very limited, normally in nanojoules (nJ) or picojoules(pJ) (Paschotta, 2008).

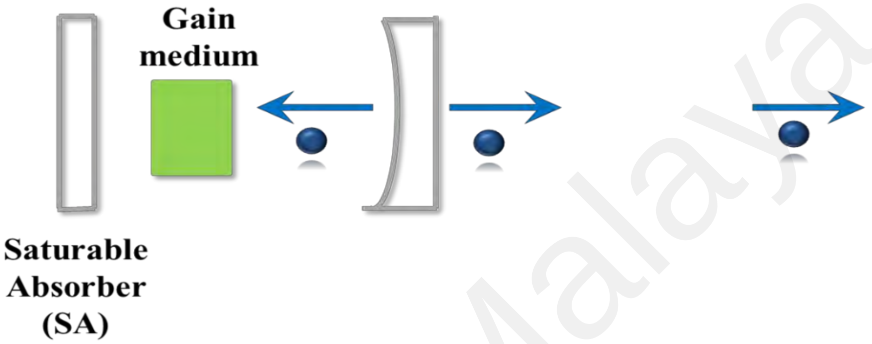

**Figure 2.15: The fundamental configuration of a passively mode-locked laser incorporating a saturable absorber mirror (Paschotta, 2008)**

Other than the pulse repetition rate, the pulse width on passive mode-locked laser is determined by a combination of factors, including the saturable absorber's pulse shaping effect and also pulse expansion due to the limited gain bandwidth. Since the pulses can be extremely short thus it is crucial to consider the impact of chromatic dispersion and optical nonlinearities inside the gain medium. As mentioned in section 2.3 above, these optical nonlinearities include Kerr-effect, self-phase modulation (SPM), cross-phase modulation (XPM), and four-wave mixing (FWM), stimulated Brillouin-scattering (SBS) and stimulated Raman-scattering (SRS). The attained pulse width can be significantly smaller by more than a factor of ten, than the recovery time of the saturable absorber. If the pulse width is not limited by higher-order dispersion, the pulse bandwidth can be a substantial portion of the gain bandwidth. Passive mode-locking simplifies the laser configuration because loss modulation synchronization occurs automatically which eliminating the need for an electronic driver. However, due to various factors, the mode-locked pulse generation process is more complex where it can be notably more challenging in order to achieve stable pulse operation.

Since mode-locked fiber lasers have ultrashort pulses, this corresponds to wide spectrum in frequency domain. Hence mode-lock fiber lasers frequency spectrum shall possess the characteristic as below Figure 2.16 and Figure 2.17.

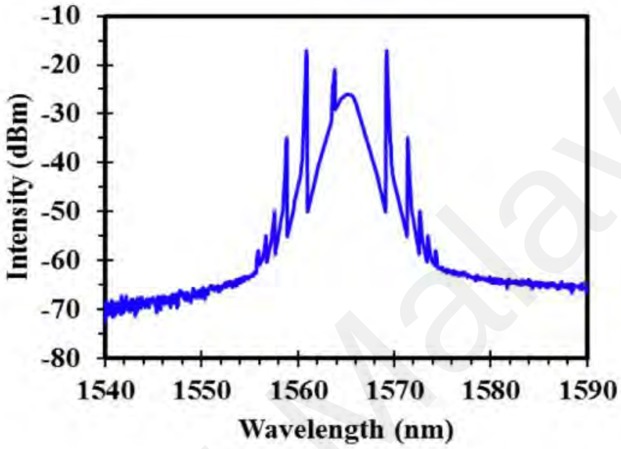

**Figure 2.16: Typical spectrum waveform generated by mode-lock fiber laser (Harun & Arof, 2013)**

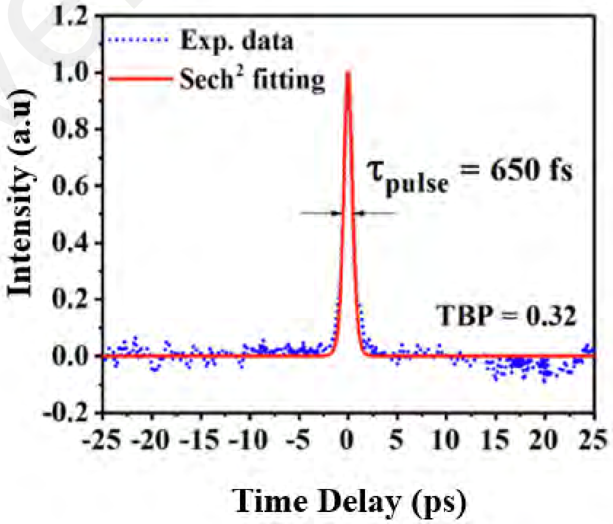

**Figure 2.17: Autocorrelation trace of the pulse generated from the mode-locked fiber laser (Harun & Arof, 2013)**

## 2.4 Propagation of Optical Pulses in a Fiber

Optical signal can be transmitted inside the fiber due to the variation in refractive index between the core and the cladding. The refractive index of the core must be higher than the cladding to enable the light to propagate in the fiber. The modal theory provides an explanation for the existence of a specific angle of incidence that facilitates the occurrence of total internal reflection (Okamoto, 2021). As light travels through the fiber, it can be regarded as an electromagnetic phenomenon and the entire propagation process is governed by Maxwell's equations associated by the electromagnetic optical fields (Agrawal, 2000). When the optical pulse propagates through an optical fiber, particularly in the linear regime, it suffers the effect of time dispersion leading to its pulse widening and potentially causing interference between the travelling signals. This interference can significantly constrain the signal's bandwidth for transmission.

In the nonlinear regime, the pulse propagation is influenced by the optical Kerr effect. Moreover, in the Nonlinear Dispersive Regime (NLDR), the propagation of pulses is simultaneously governed by Self-Phase Modulation (SPM) and Group Velocity Dispersion (GVD) (Agrawal, 2000). In the anomalous dispersion region, the SPM effect counteracts the GVD effect, resulting in a fascinating phenomenon where pulses propagate over the fiber without changing their shape. These particular pulses are referred to as solitons. In the following sections, the dispersion phenomena, non-linear effect and soliton pulses are briefly discussed.

### 2.4.1 Dispersion

Light waves travel at a constant speed *c* ($3\text{x}10^8$ $\text{ms}^{-1}$) when propagating through free space. Nevertheless, when light travels through a transmission medium from free space, the speed is reduced due to the interaction between the light's electromagnetic field and the electron cloud of the transmission medium. The extent to which light slows down in the transmission medium is expressed as the material's refractive index $n$, which is related to the speed of light in the material itself through the equation below:

$$v_m = \frac{c}{n} \qquad (2.9)$$

Since the electromagnetic field’s interaction within the transmission medium dependent upon the photon’s wavelength, hence the refractive index has the same characteristic where it also dependent on the photon’s wavelength. This characteristic is referred to as chromatic dispersion. Chromatic dispersion is also known as material dispersion and is expressed as follows:

$$D_M(\lambda) = \frac{\lambda}{n}\frac{d^2n}{d\,\lambda^2} \qquad (2.10)$$

Equation 2.10 shows that the refractive index $n$ is a function of wavelength $\lambda$. Chromatic dispersion plays a crucial role in the transmission of laser pulses. If the laser pulse consists of only one single frequency component, it will propagate through the transmission medium without distortion. However, in practical scenario, laser pulse consists of various frequencies where the shorter the pulse in the time domain, the broader the range of frequencies it covers in the frequency domain. The laser pulse with various frequency will travel at different velocities where some moving faster and others lagging behind. This results in the broadening of the pulse width. Other than chromatic dispersion, the laser pulse also encounters another form of dispersion in addition to the pulse broadening due to the optical fiber's structural characteristics known as waveguide dispersion. This can be described as follows:

$$\mathrm{Dw}(\lambda) = -\frac{n_2(\lambda)\Delta}{c\lambda}\,\mathrm{V}\,\frac{d^2(\mathrm{Vb})}{dV^2} \qquad (2.11)$$

where $n_2(\lambda)$ is the refractive index of the fiber core, Δ is the refractive index different, $b$ is the normalize propagation constant and $V$ is the normalized frequency. The overall dispersion within the fiber results from both the chromatic dispersion and waveguide dispersion:

$$D(\lambda) = D_M(\lambda) + D_W(\lambda) \tag{2.12}$$

The propagation of a laser pulse through a fiber is defined by a mode propagation constant denoted as $\beta$ and this can be further expressed as a Taylor series expansion centered around the central frequency $\omega_0$ as below equation 2.13.

$$\beta(\omega) = \frac{n(\omega)\omega}{c} = \beta_0 + \beta_1(\omega - \omega_0) + \frac{1}{2}\beta_2(\omega - \omega_0)^2 + \dots\dots \tag{2.13}$$

where

$$\beta_m = \frac{d^m\beta}{d\omega^m} \qquad \omega = \omega_0 \qquad (m = 0, 1,2,3, \dots\dots) \tag{2.14}$$

The pulse envelope travels at the group velocity $v_g = 1/\beta_1$ and the parameter $\beta_2$ is accountable for pulse broadening. $\beta_2$ is commonly known as the Group Velocity Dispersion (GVD) parameter and is related to the chromatic dispersion parameter $D$ by the following equation:

$$\beta_2 = -\frac{\lambda^2 D}{2\pi c} \tag{2.15}$$

For $\beta_2 > 0$, the laser pulse undergoes normal dispersion. However, for $\beta_2 < 0$, the laser pulse exhibits anomalous dispersion. In the normal dispersion regime, the high-frequency blue-shifted wavelength of an optical pulse travels more slowly than the low-frequency red-shifted wavelength. Conversely, in the anomalous dispersion regime, the opposite effect is observed where low-frequency wavelength propagates faster than high frequency wavelength.

Pulse broadening induced from dispersion deteriorate the initial pulse's intensity, which leads to the overlapping of two neighboring pulses. Consequently, this situation causes the receivers' error interpretation in fiber optic communication systems. However, there is a positive effect between the interaction of dispersion and Self-Phase modulation. This particular interaction leads to the creation of optical soliton in which the wave remains stable and unaltered as it propagates through the fiber.

### 2.4.2 Nonlinear Effect

Nonlinear effects and its related phenomenon occurs in any dielectric medium due to the alteration of the optical characteristics of a material system in response to the presence of sufficiently intense laser light. This phenomenon is termed "nonlinear" due to the reaction of the material system to an applied optical field relies on the strength of the optical field in a nonlinear fashion. Hence, the dielectric material exhibits characteristics of a nonlinear medium. One year after Theodore Maiman demonstrated the first working laser in 1960 (Maiman, 1960), Peter Franken's et al discovery of second-harmonic generation became a pivotal advancement in the field of nonlinear optics (Franken et al., 1961). An optical nonlinearity can be described as the way the polarization $\tilde{P}(t)$ of a material system is influenced by the intensity $\tilde{E}(t)$ of an applied optical field (Agrawal, 2000). Initially, the induced polarization exhibits a linear dependence on the field strength, which can be described as:

$$\tilde{P}(t) = \epsilon_0 \chi^{(1)} \tilde{E}(t) \tag{2.16}$$

where the proportionality constant $\chi(1)$ is known as the linear susceptibility and $\epsilon 0$ is the free space permittivity. From the equation 2.17, nonlinear effect can be express in the polarization $\tilde{P}(t)$ as a power series in the field strength $\tilde{E}(t)$.

$$\tilde{P}(t) = \epsilon_0[\chi^{(1)}\tilde{E}^1(t) + \chi^{(2)}\tilde{E}^2(t) + \chi^{(3)}\tilde{E}^3(t) + \cdots ] \qquad (2.17)$$

The terms $\chi^{(2)}$ and $\chi^{(3)}$ are referred to as the second- and third-order nonlinear optical susceptibilities, respectively. Second-order nonlinear optical interactions can only take place in non-centrosymmetric crystals which these crystals do not display inversion symmetry. Since liquids, gases, amorphous solids such as glass and many other crystals exhibit inversion symmetry thus, as a result, $\chi^{(2)}$ equals zero for these materials. Consequently, such materials cannot generate second-order nonlinear optical interactions. In contrast, third-order nonlinear optical interactions described by the $\chi^{(3)}$ susceptibility, can take place in both centrosymmetric and non-centrosymmetric media.

Nonlinear effects in optical fibers arise from either the intensity-dependent refractive index of the silica glass medium or the inelastic-scattering phenomenon. The Kerr effect is attributed to the power dependence of the refractive index. This Kerr nonlinearity includes self-phase modulation (SPM), cross-phase modulation (XPM) and four-wave mixing (FWM). In the case of the inelastic-scattering phenomenon during high power level, the silica glass medium can induce stimulated Brillouin scattering (SBS) and stimulated Raman scattering (SRS).

#### 2.4.2.1 Self-phase modulation (SPM)

In optical fiber, the refractive index is subjected to variations not only with different wavelengths but also with the intensity of the transmitted light. The interaction between light and the material's electron cloud increases nonlinearly with increasing light intensity, causing high-intensity light to travel at a slower pace than low-intensity light.

Consequently, the refractive index of the fiber rises in response to the light's intensity and can be expressed as:

$$n_{eff} = n_l + n_{nl}I \qquad (2.18)$$

where $n_{eff}$ is the effective refractive index, $n_l$ is the linear refractive index, $n_{nl}$ is the nonlinear refractive index, and $I$ is the light intensity inside the fiber.

Self-Phase Modulation (SPM) (Alfano et al., 2016; Verma & Garg, 2012) is considered as one of the most significant concerns regarding the impact of fiber nonlinearity on pulse propagation theory. In the occurrence of the SPM effect (Gu et al., 2019; Manassah, 1989), the optical pulse experiences a phase shift due to the intensity-dependent refractive index while the pulse's shape remains unaltered. The nonlinear phase constant $\phi_{nl}$ over a fiber length $L$ is expressed as:

$$\phi_{nl} = \frac{2\pi}{\lambda} n_{eff}L \qquad (2.19)$$

where $\lambda$ represents the operating wavelength of the pulse laser propagating through a fiber with an effective refractive index $n_{eff}$ along an optical path length of $L$.

Within the fiber, the intensity of the propagating light varies over time, leading to the creation of a time-varying refractive index. Consequently, the leading edge of a pulse will encounter a positive refractive index gradient ($+dn/dt$) resulting in a red shift. On the other hand, the trailing edge experiences a negative refractive index gradient ($-dn/dt$) leading to a blue shift. This time-varying change in the refractive index leads to a corresponding time-varying phase alteration, as illustrated in Figure 2.18. The optical phase changes over time in perfect synchrony with the optical signal.

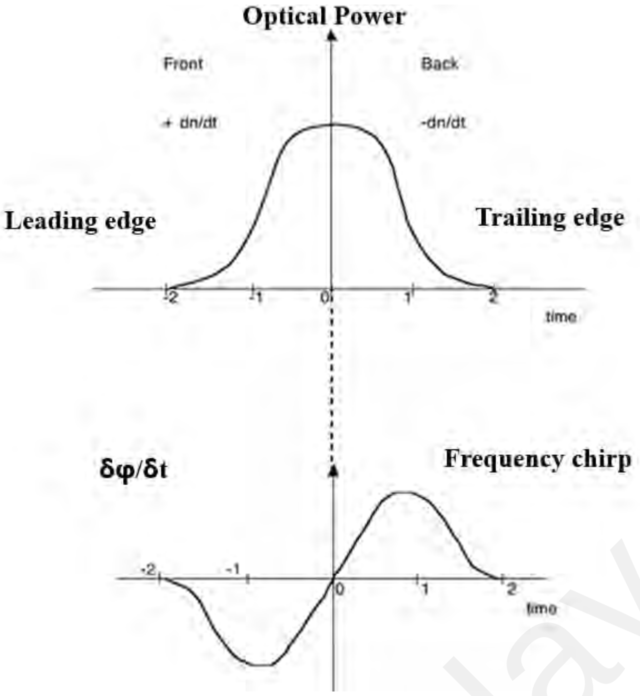

Figure 2.18: Phenomenological description of spectral broadening of pulse due to SPM. (Singh & Singh, 2007)

Since the light wavelength is temporally modulated, when the intensity varies with time the phase $\phi$ also becomes time-dependent. This time-dependent change in phase $\phi_{nl}$ is accountable for the alteration in the frequency spectrum $\omega$, which can be expressed as:

$$\delta\omega = \frac{\mathrm{d}\phi_{\mathrm{nl}}}{\mathrm{dt}} \qquad (2.20)$$

The temporal variation of $\delta\omega$ is commonly referred to as frequency chirping. This chirping phenomenon occurs along the temporal pulse profile, where $\phi_{nl}$ increases as the optical pulse interacts with the fiber over its propagation path. This signifies the creation of a new instantaneous frequency at $\omega_0 + \delta\omega(t)$ as the pulse travels within a fiber, thereby resulting in the spectral broadening of the pulse. An important application of the SPM concept is in the formation and study of optical solitons.

### 2.4.2.2 Cross-phase modulation (XPM)

Cross-Phase Modulation (XPM) (Islam et al., 1987) is a fundamental and powerful phenomenon in the domain of nonlinear optics. XPM occurs when many optical pulses of different wavelengths propagate through the same transmission medium, leading to mutual interactions that significantly alter the characteristics of these pulses. XPM has a profound influence on numerous applications with a particular emphasis on optical communication systems (Rashed et al., 2022) and plays a pivotal role in enabling advanced optical signal processing techniques (Liang et al., 2014). In this literature review, we explore into the fundamental principles of XPM's effects on optical pulses and its practical applications in modern optics and telecommunications.

XPM is a nonlinear effect that arises from the nonlinear relationship between the refractive index of the transmission medium and the intensity of incident lights. This effect becomes evident when two distinct wavelengths travel inside the same transmission medium concurrently. Understanding XPM hinges on the recognition that the refractive index of the medium undergoes changes in response to the presence of intense optical pulses. As a result, the presence of a single intense optical pulse leads to the alteration of the refractive index and subsequently causing a phase shift in other pulses that are travelling inside the same transmission medium. This phase shift causes a frequency shift which eventually results in an alteration to the wavelengths of the affected pulses. Essentially, XPM transfers optical power from one pulse to another pulse leading to the modifications in the spectral and temporal characteristics of the pulses. XPM plays a crucial role in the spectral broadening (Agrawal, 1987) of optical pulses and this has significant effect on optical communication system where multiple wavelength channels are tightly packed for high capacity data transmission. As a consequence of XPM, the wavelength spectrum of neighboring channels overlaps, resulting in a reduction in signal quality and the occurrence of cross channels interference. Hence, effective management and mitigation of XPM are essential for maintaining signal integrity in the transmission systems. Although XPM causes wavelength shifts in optical pulses, this effect can be harvest for various applications such as generating new wavelengths inside the same optical system and facilitating optical frequency combs. These frequency combs can be used in precision frequency metrology, optical clocks and high-resolution spectroscopy (Jones et al., 2000). XPM is essential for the creation and stabilization of optical solitons where solitons are waveforms that are self-sustaining, maintaining their shape and amplitude as they propagate through non-linear media. XPM contributes to the equilibrium of nonlinear effects, ensuring the stable propagation of solitons. Solitons play a crucial role in long-distance optical communication by reducing the necessity for complex dispersion compensation techniques. Moreover, XPM proves to be an invaluable tool for applications in optical signal processing. Through precise controls of the interaction between different optical pulses using XPM, signal manipulation and shaping can be achieved for various tasks, including all-optical switching and wavelength conversion.

Understanding and controlling XPM is very important in the design and operation of modern optical systems as XPM enables efficient and reliable data transmission in the continuously advancing field of telecommunications. With ongoing technological advancements, XPM will remain to be at the forefront of innovations in optical communication and signal processing, continually pushing the limits of what can be achieved in the domains of photonics and optical networking.

#### 2.4.2.3 Four-wave mixing (FWM)

Four-Wave Mixing (FWM) (Jones et al., 2000) is an optical nonlinear phenomenon that has crucial roles in various applications including optical communication, signal processing and photonics research. FWM happens when multiple optical wavelengths propagate and interact inside the nonlinear transmission medium and hence generate new wavelengths that are composed of combination of the original wavelengths (Aso et al., 1999). FWM has gained significant interest from researchers due to its potential for enabling advanced optical technologies as well as improving the performance of the existing optical systems. In this literature review study, we explore the underlying principles, mechanisms and applications of Four-Wave Mixing. FWM is a nonlinear phenomenon when multiple optical wavelengths interact with the nonlinear susceptibility of a material and can be understood through the concept of wavelength mixing, where the nonlinear medium reacts to the presence of incident optical wavelengths by generating additional wavelengths through a nonlinear interaction. These newly generated wavelengths has different frequencies compared to the original wavelengths, hence resulting in the creation of sidebands. FWM takes place via a four-wavelength interaction, where three wavelengths combine together to generate a fourth wavelength. The three input wavelengths are typically referred to as the pump wavelength, signal wavelength and idler wavelength. When these wavelengths meet specific phase-matching criteria, energy is efficiently transferred from the pump wavelength to the signal and idler wavelengths, creating new wavelengths. This wavelength mixing process enables the conversion of optical frequencies, the generation of new wavelengths and the manipulation of optical signals (Aso et al., 1999). The fundamental mechanisms of FWM involve the material's nonlinear susceptibility and the fulfillment of phase-matching conditions. The efficiency of FWM is determined by the specific characteristics of the transmission medium material including its nonlinear coefficient. Phase-matching conditions are crucial for the efficient generation of the new wavelengths. These conditions are satisfied when the phases of the pump wavelength, signal wavelength and idler wavelength are oriented in a way to allow maximum energy transfer. Phase matching can be achieved either through proper material selection, efficient waveguide design, or the introduction of chirped or dispersion-engineered optical devices. Four-Wave Mixing is applied in various optical technologies and systems across a broad spectrum of applications which include wavelength conversion, signal regeneration and amplification in optical communication systems (Aso et al., 1999; Ebnali-Heidari et al., 2009). Through FWM, it enables the conversion of signals to different wavelengths, allowing for efficient routing and transmission of data in dense wavelength-division multiplexing (DWDM) networks (Ahmed et al., 2014). In optical signal processing, FWM is used to perform logic operations, waveform shaping, and signal regeneration to enhance the capabilities of optical switches and routers. In quantum information processing, FWM is used to create entangled photon pairs for the application of quantum key distribution and quantum teleportation (Cai et al., 2015). FWM can be utilized for spectral measurement and analysis, which is then used for the purpose of characterizing optical signals, laser sources, and other optical components. FWM can be harvest to generate optical frequency combs which can be used to revolutionize precision metrology, optical clocks and spectroscopy. In nonlinear microscopy techniques like coherent anti-Stokes Raman scattering (CARS) and stimulated Raman scattering (SRS), FWM is employed to create contrast and acquire molecular information (Lefrancois et al., 2012).

Despite its numerous benefits, FWM also face some challenges including the need for precise phase matching, dispersion management and mitigation of unwanted sidebands. Scientists and engineers are consistently investigating creative solutions and materials to improve the effectiveness and versatility of FWM. The future of FWM lies in its fusion with other cutting-edge optical technologies such as photonic integrated circuits (PICs) and quantum photonics. Such integrations hold the potential to unlock new capabilities and applications in the domains of quantum communication, optical computing, and beyond. As technology continues to advance, FWM will undoubtedly remain to play a leading role of innovations in optical science and engineering, pushing the boundaries of what is achievable in the photonics and optical networking fields.

#### 2.4.2.4 Stimulated Raman scattering (SRS)

Stimulated Raman scattering (SRS) (Freudiger et al., 2014; Sirleto & Ferrara, 2020) is a fascinating and powerful spectroscopic method that enables in-depth investigation of molecular vibrations and chemical composition with exceptional sensitivity and precision. SRS is an optical nonlinear phenomenon that takes advantage of the Raman effect, where photons interact with molecular vibrations that lead to energy shifts in the scattered wavelength (Basiev et al., 1999). Due to the capability in providing detailed information on the molecular structure and kinetic behavior of a sample, SRS has gained popularity in various fields including chemistry, biology, and materials science. This literature review provide insight into the fundamentals of SRS, its applications, and its impact on scientific research (J.-X. Cheng et al., 2021; Yakovlev et al., 2009).

Stimulated Raman scattering relies on the foundational concept of the Raman effect, first discovered by Sir C.V. Raman in 1928. This effect revolves around the interaction of light wavelength with molecules of the transmission medium material, resulting in energy shifts in the scattered photons. In conventional spontaneous Raman scattering, a small portion of the scattered photons experiences energy loss, resulting in Stokes scattering, while majority of the photons remain at the same energy level, which is known as Rayleigh scattering (Seto et al., 2023). Furthermore, SRS involves a stimulated process where incident photons interact with the transmission medium material, leading to the amplification of the Raman signal and significantly enhancing its sensitivity.

In SRS, two laser beams are employed in the system, a fixed-frequency pump laser and a Stokes laser that is precisely tuned to match the vibrational frequency of the transmission medium material. When the energy difference between the pump laser and

Stoke laser precisely corresponds to the energy of the molecular vibration of transmission medium material, SRS amplification occurs and gives rise to a robust anti-Stokes signal (Choi et al., 2019). Detecting this signal provides valuable insights into the chemical composition, molecular vibrations and concentration of the transmission medium material.

SRS has discovered a wide range of applications across numerous scientific domains including chemical analysis (Li et al., 2021), biological imaging (F.-K. Lu et al., 2015) and environmental monitoring (Q. Cheng et al., 2021) . In chemical analysis, SRS enables the non-invasive and label-free analysis of chemical compounds where it is used for the identification of organic and inorganic molecules, including pharmaceuticals, polymers, and complex mixtures. Moreover, SRS can even provide detailed information on molecular structure, composition, and concentration. On biological imaging field, SRS has allowed researchers to visualize biological structures and processes at the molecular level and this has deepened our understanding of cellular processes and disease mechanisms. It is widely used for imaging lipids, proteins, and other biomolecules in live cells and tissues. On the other hand, SRS microscopy can provide insights into cell membrane dynamics, lipid droplets and cell organelles. For environmental monitoring field, SRS can be applied to monitor and analyze environmental samples where it is used for the detection and quantification of pollutants, gases, and contaminants in air, water, and soil. This information is crucial for environmental conservation and protection. In materials science, SRS is a valuable tool for studying materials and their properties. It can be used to investigate the composition and structural changes in materials such as semiconductors, catalysts, and nanoparticles. Researchers use SRS to understand how material properties evolve under various conditions.

Stimulated Raman scattering is a adaptable and powerful spectroscopic method that has revolutionized the manner in which scientists investigate molecular vibrations and chemical composition. Its applications span a wide array of scientific disciplines providing researchers with invaluable insights into complex systems, from biological cells to materials and environmental samples. With the ongoing technological advancements, SRS is expected to play an even more significant role in driving scientific discovery and innovation, solidifying its status as an indispensable tool in the researcher's toolkit for the foreseeable future.

### 2.4.3 Soliton

In section 2.4.1, for the case that pulse laser operates under anomalous dispersion regime, lower frequency (longer wavelength) photons propagate slower than higher frequency (shorter wavelength) photons. Thus, it causes the leading edge of the pulse to slow down while the trailing edge propagates faster. Hence, SPM (Gu et al., 2019) compensates for the broadening of the pulse and reverses the dispersion induced by laser. If the laser pulse having a shape in which the effects of SPM and GVD (Malik et al., 2008) counterbalance each other, then the pulse retains its initial pulse width throughout the entire length of the fiber. Under such circumstances, the laser pulse would propagate without any distortion due to the mutual compensation of dispersion and SPM. This unique, undistorted pulse is commonly referred to as a soliton (Song et al., 2019). Since soliton pulse maintains their width during its propagation, it has tremendous potential for applications in super high bandwidth optical communication systems.

A typical soliton pulse laser exhibits narrow sidebands that are visible on both left and right sides of the central wavelength of the soliton spectrum as shown in Figure 2.19. These sidebands are often referred to as Kelly sidebands (Du et al., 2019) and are characterized by their lower intensity and the presence of sharp, narrow peaks. The wavelength separation between the Kelly sidebands and the center of the soliton spectrum can be described by the following equation:

$$\Delta\lambda = \frac{1.763\lambda^2}{2\pi c_0 \mathrm{r}} \sqrt{\frac{\mathrm{m}4\mathrm{r}^2}{\mathrm{L}|\beta 2|} - 1} \qquad (2.21)$$

where $\lambda$ is the center soliton wavelength, $r$ is the pulse width, $c$ is the speed of light, $m$ is the order of sidebands, and $\beta_2$ is the GVD with a cavity length of $L$ (Dennis & Duling, 1994; Nelson et al., 1997; Smith et al., 1992).

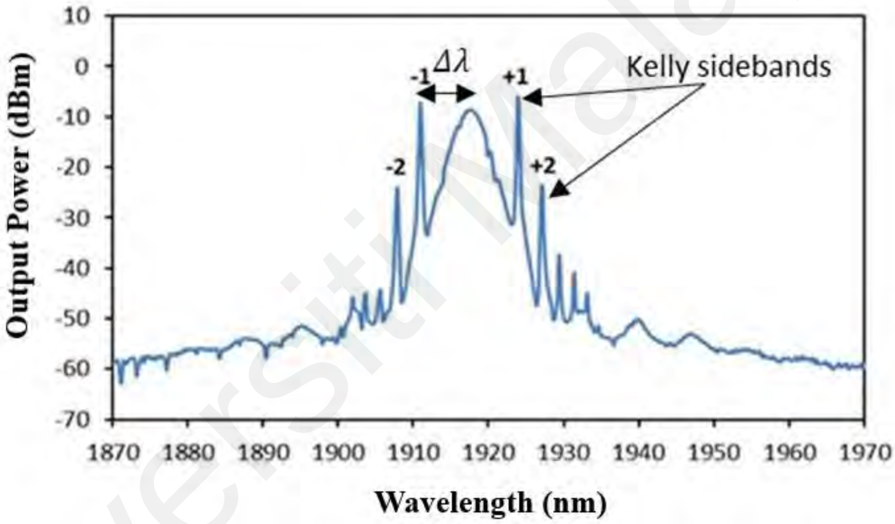

**Figure 2.19: Output spectrum of soliton pulse laser (Hasegawa, 2013)**

Soliton pulses require a delicate energy-mediated equilibrium between the nonlinearity and dispersion, which impose a constraint on the pulse energy $Q$ for a fundamental soliton.

$$Q = \frac{1.763 \text{ x } 2|\beta 2|}{\gamma \mathrm{r}} \qquad (2.22)$$

where $\gamma$ is the nonlinear coefficient of the optical fiber, $r$ is the pulse width, and $\beta_2$ is the GVD. One approach to gain a better understanding of the balanced interaction between nonlinearity and dispersion is through the concept of a characteristic length. The characteristics of nonlinear length $L_{nl}$ in the optical fiber can be described as follows:

$$L_{nl} = 1/\gamma P_p \qquad (2.23)$$

where $P_p$ is the peak power of the pulse, $\gamma$ is the nonlinear coefficient of the optical fiber.

The characteristic length of the optical fiber for dispersion $L_d$ is defined as:

$$L_d = (t/1.763)^2/\beta_2 \qquad (2.24)$$

When the characteristic length in fiber cavity is $L_{nl} > L_d$, nonlinearity becomes the dominant factor, leading to pulse distortion. Conversely, when $L_d > L_{nl}$, dispersion take place, causing the pulse to undergo temporal broadening. dispersion dominates and results in temporal broadening of the pulse. To establish a fundamental soliton, the characteristic nonlinear length $L_{nl}$ and the characteristic dispersion length $L_d$ must be equal (Agrawal, 2000).

## 2.5 Measurement of Pulsed Laser Performances

Fundamental parameters (Thiel & Wehr, 2004) such as the repetition rate, pulse duration, pulse energy, peak power, and slope efficiency are among the required measurement when dealing with laser pulses which including both their temporal and spectrum characteristic (Standard, 2005). Optical spectrum analyzer is used for observing the optical spectrum of the laser pulse while an optical power meter equipped with a thermal detector is utilized to quantify its average output power. Laser pulses in optical signal is first converted into electrical signal through a photodetector. This electrical signal can then be observed in both the time domain using an oscilloscope and in the frequency domain using an RF spectrum analyzer. In Figure 2.20, a regularly repeating sequence of optical pulses is depicted, with a repetition rate denoted as $f$, where $f = 1/T$.

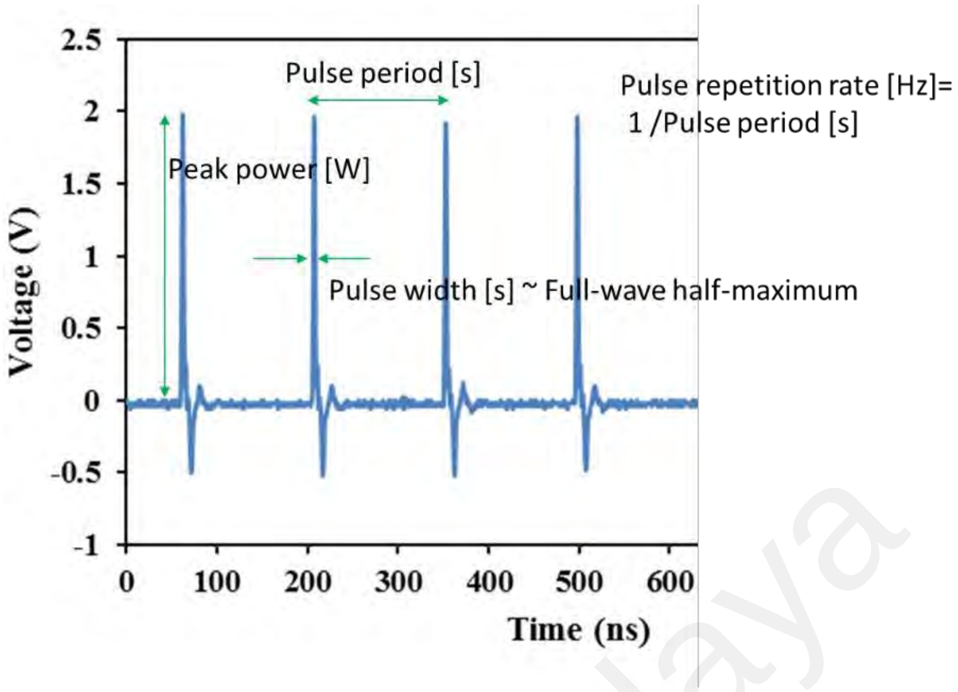

**Figure 2.20: Pulse train of pulsed lasers (J. C. Diels & W. Rudolph, 2006)**

### 2.5.1 Repetition Rate and its Stability

The Repetition Rate $f$ represents the quantity of pulses generated per second (Yu et al., 2021), which is illustrated as the inverse of the temporal pulse shaping demonstrated in Figure 2.20. The repetition rate is different for mode-locked and Q-switched fiber laser. In the context of mode-locking, the repetition rate is normally determined by the length of the fiber laser cavity and the frequency remains fixed. Conversely, for Q-switching, variations in the pump power are the main factor affecting the repetition rate. For both mode-locked and Q-switched laser pulses, the repetition rate is inversely proportional to the pulse width. As the repetition rate increases, the pulse width tends to decrease, and conversely, when the repetition rate decreases, the pulse width tends to increase. The stability of a laser pulse can be verified by examining its frequency domain parameter. In Figure 2.21, the RF spectrum of the pulse train is displayed, this spectrum has been recorded using an optical spectrum analyzer using a fast photodetector. The highlighted green area in the figure illustrates the first fundamental frequency which also corresponds to the repetition rate of the pulse train, while the subsequent frequencies are harmonics.

The variation in intensity between the peak and the signal floor within the spectrum is referred to as the signal-to-noise ratio (SNR). The SNR serves as a stability indicator of the laser pulse where an SNR exceeding 30 dB is generally considered a sign of stability.

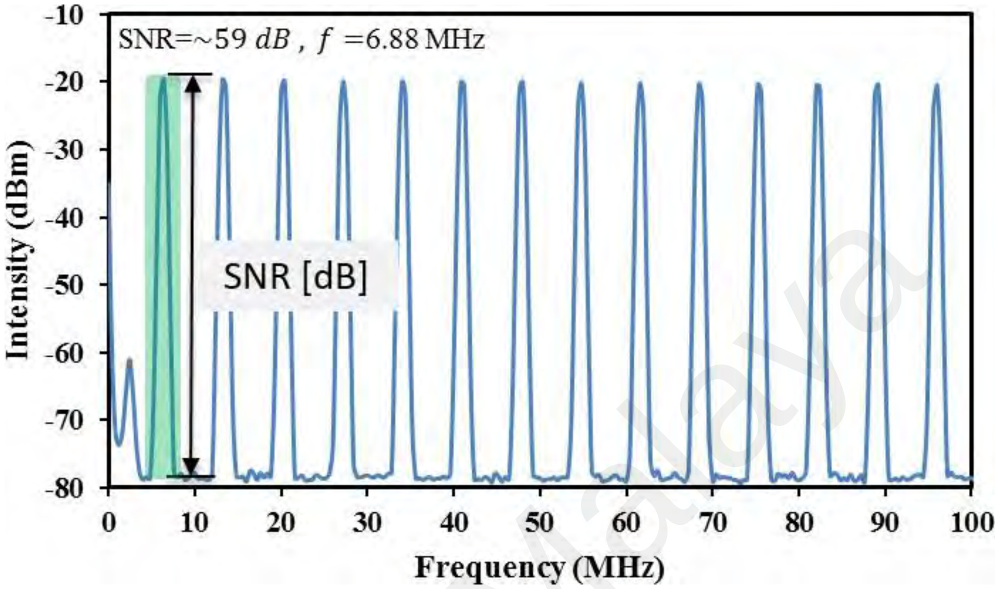

Figure 2.21: RF spectrum of pulsed lasers (Mustapha et al., 2022)

### 2.5.2 Pulse width or Pulse Duration

Pulse width $r$ is defined as the duration of the pulse during which the power is at half of its peak power (Luo et al., 2016). Alternatively, it is also commonly referred to as the full width at half maximum (FWHM). Conceptually, the laser pulse shape can be illustrated by a bell-shaped function, such as a Gaussian and Hyperbolic secant ($\mathrm{sech}^2$) function (Wu & Li, 2019). These mathematical functions are commonly used to describe the temporal profile of signal pulses, each function has its own unique characteristics and applications. As per Haus' master equation, anomalous dispersion regime used hyperbolic secant ($\mathrm{sech}^2$) pulse shapes such as soliton regime lasers. Conversely, the Gaussian pulse shape is typically employed in the normal dispersion regime. The specific parameters related to the pulse shape function can be found in Table 2.1. These functions fitting is used in the autocorrelation of the pulse to characterize the pulse shape and the full width at half maximum (FWHM) of the intensity autocorrelation pulse is denoted as $r_{AC}$. As mentioned in section 2.3.2 and 2.3.3, in the Q-switching method, the obtained pulse width typically fall within the range of nanoseconds to picoseconds whereas in mode-locking, the pulses are usually in the range of few picoseconds to femtoseconds.

**Table 2.1: Pulse characterization (Agrawal, 2007)**

| **Pulse shape** | $\boldsymbol{\tau}.\ \Delta\boldsymbol{\lambda}_{3dB}$ | $\boldsymbol{\tau}/\boldsymbol{\tau}_{AC}$ |
|---|---|---|
| **Gaussian** | 0.441 | 0.7071 |
| **Sech2** | 0.315 | 0.6482 |

Since actual half-maximum values are more experimentally accessible using an auto-correlator, the relationship between the pulse width and the 3-dB spectral bandwidth of a laser pulse can be expressed as follows:

$$r.\ \Delta\lambda_{3dB} \geq TBP \qquad (2.25)$$

where $r$ is the FWHM from single pulse temporal profile, $\Delta_{\lambda 3dB}$ recorded in Hz is the 3-dB spectral bandwidth measured from optical output spectrum and TBP is the time-bandwidth product which refer to Fourier-transform limit. TBP relates the duration and spectral width of a pulse and it signifies the trade-off between how short a pulse can be in time domain while simultaneously having a broad spectral bandwidth in frequency domain. If Equation 2.25 is satisfied, it indicates that the measured pulse width has reached its physical limit, known as the "transform limit." This is the smallest pulse width that can be achieved with the given laser parameters and spectral bandwidth ($\Delta\lambda$) and it represents the fundamental limitation imposed by the physics of the laser system. In other words, it's the shortest pulse duration attainable under those specific conditions. Thus, in order to achieve an ultrashort laser pulse in time domain, the developed laser must generate a broad spectral bandwidth. Alternatively, the minimum possible pulse width can be calculated given the spectrum $\Delta_{\lambda 3dB}$ (nm) at FWHM, central peak wavelength $\lambda_o$ (nm), and the speed of light (m/s) $c$ as follows:

$$r \geq TBP \frac{{\lambda_0}^2}{\Delta\lambda_{3\mathrm{dB}}.\mathrm{c}} \tag{2.26}$$

From Equation 2.26, the pulse width of mode-locked lasers for 2-micron region are mathematically obtained due to no available autocorrelator in the laboratory.

### 2.5.3 Pulse Energy and Peak Power

Figure 2.22 illustrates the autocorrelation pulse profile (Luo et al., 2016) which holds the energy of the pulse laser. Pulse Energy $Q$ represents the overall optical energy content within each individual pulse profile and it can be expressed as the integral of its optical power over time.

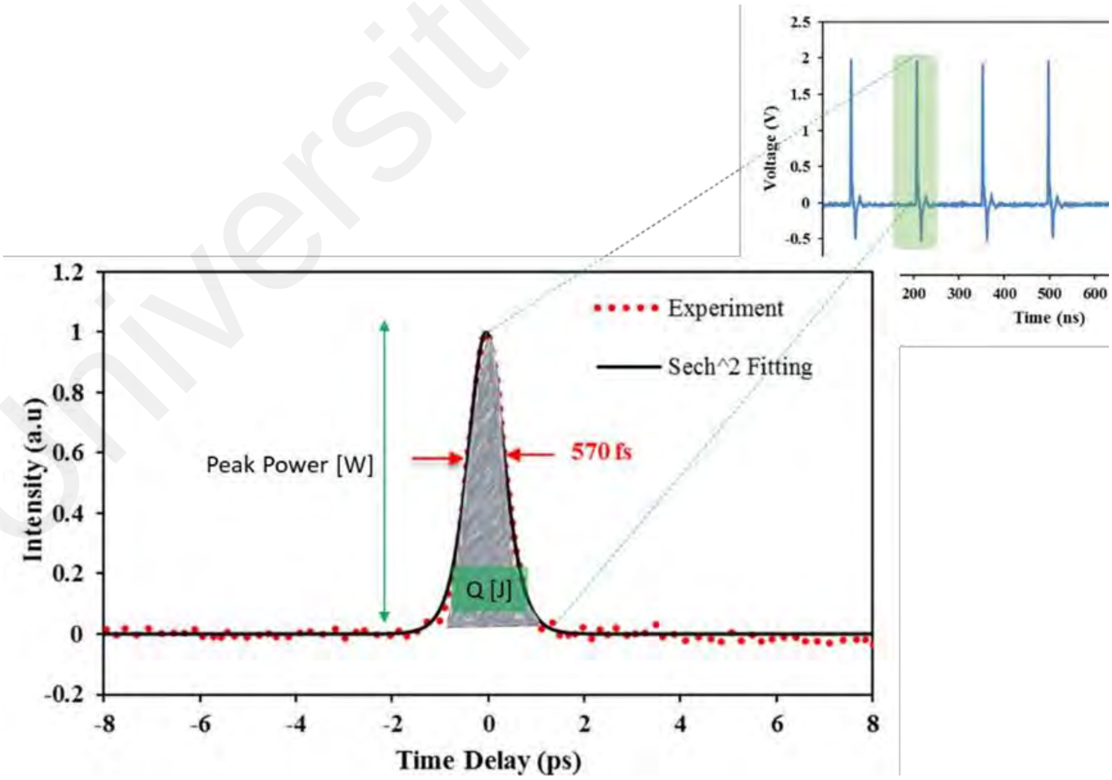

**Figure 2.22: Autocorrelation pulse profile of mode-locked lasers. The right hand corner inset is a train of oscilloscope waveforms. (Nolte et al., 2015)**

In Q-switching technique, the typical pulse energy falls within the range of microjoules uJ to millijoules mJ. While in mode-locking technique, the pulse energy is even lower, typically ranging from picojoules pJ to nanojoules nJ. Usually, the pulse energy Q is calculated based on dividing the average output power by the repetition rate, as follows:

$$Q[J] = \frac{P_{avg}}{f_r} \tag{2.27}$$

where $P$avg is the average output power and $fr$ is the repetition rate.

Peak power $Pp$ is the maximum instantaneous optical power within the pulses. In simpler terms, it represents the rate of energy transfer within each pulse profile as depicted in Figure 2.22. When the laser having very short pulse width, it can achieve very high peak power even though the pulse energy is moderate. By dividing the pulse energy Q by the pulse width r, the peak power can be written as

$$P_p[W] = 0.88\,\frac{Q}{r} \tag{2.28}$$

The transformation of peak power is dependent upon the temporal profile of the pulse. As mentioned previously, the single pulse profile transform limit is exclusively expressed by the Gaussian function or the Sech$^2$ function.

### 2.5.4 Time-Frequency Relationship

The temporal characteristics of a pulsed laser can be observed in both the time and frequency domains (Zou et al., 2016). The relationship between these time and frequency domains of a laser pulse can be clarified through the Fourier transform equation which is expressed as follows:

$$E(\omega) = \int_{-\infty}^{+\infty} E(\omega) e^{i\omega t} dt \tag{2.29}$$

where $E(\omega)$ represent the electric field of the pulse with angular frequency $\omega = 2\pi f$ and $f$ is the pulse frequency from output laser. Figure 2.23 illustrates the laser pulse in both the time and frequency domains.

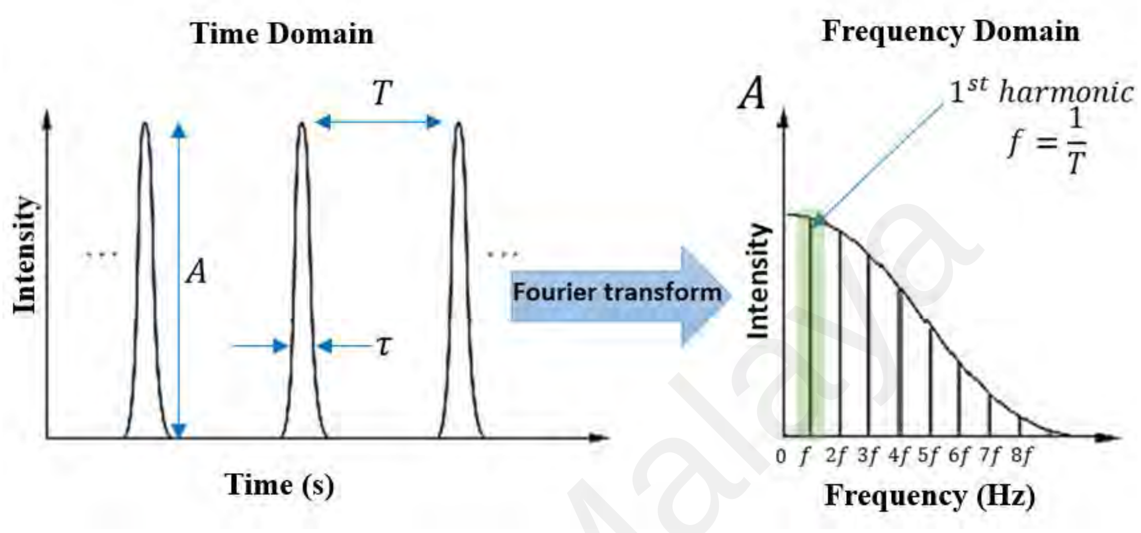

**Figure 2.23: Temporal characteristic of a pulsed laser in both time and frequency domain (Ratner, 2013)**

In the time domain, the initial step is to calculate the duty cycle of the pulse train. The duty cycle $d$ represents the proportion of time during which the laser is in the "on" state within a specific timeframe. The duty cycle d is calculated as below equation 2.30.

$$d = \frac{r}{T} \qquad (2.30)$$

where $r$ is the pulse width, and $T$ is the pulse period. The DC component $a_0$ in the Fourier series equation is calculated by assigning a value to amplitude $A$ at zero frequency and the duty cycle $d$ obtained in equation 2.30 give rise to the following:

$$a_0 = Ad \qquad (2.31)$$

Amplitude of the cosines wave $an$ and sine wave $bn$ are expressed as

$$a_n = \frac{2A}{n\pi}\sin(\frac{n\pi}{2}) \qquad (2.32)$$

$$b_n = 0 \qquad (2.33)$$

When $a_0$, $a_n$, $b_n$ are combined in the equation, this has formed a shape of the laser pulses in frequency domain as illustrated in Figure 2.23. The generation of shorter pulse widths in the time domain can be recognized by the formation of a constant amplitude in the frequency domain across an extensive range of frequencies, similar to an impulse waveform. Figure 2.24 illustrates a simulated RF spectrum derived from the Fourier transform equation with the time domain data obtained from experimental measurements. The simulation reveals that the pulse width determined from the simulated RF spectrum is 4.5*us* which is closely matches the pulse width 4.3*us* measured from the experimental pulse train in the time domain.

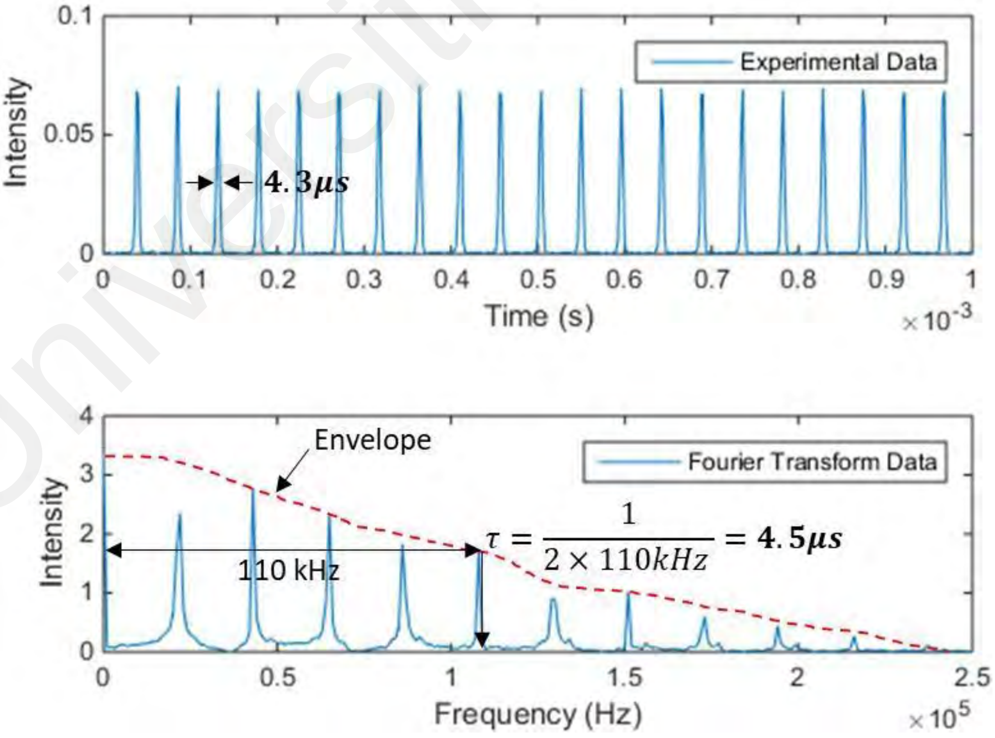

**Figure 2.24: Simulation of RF spectrum (Ghassemlooy et al., 2019)**

### 2.5.5 Slope efficiency / Laser efficiency

Slope efficiency or laser efficiency is a critical parameter for evaluating a laser's performance. This efficiency can be found by plotting the graph of output power against the input pump power. Typically, a balance between achieving higher slope efficiency and minimizing the threshold pump power is crucial to achieve the maximum laser output power efficiency for a given level of pump power. Laser efficiency refers to the conversion of input pump power into laser output power.

$$\eta = \frac{P_{out}}{P_{pump}} \tag{2.34}$$

where Pout is the laser output power and Ppump is the laser input pump power.

## 2.6 Passive Saturable Absorber (SA) with the principle of Saturable Absorption

The operation of pulse generation, Q-switching, and mode-locking in all-fiber lasers depends on the presence of an optical component known as a saturable absorber. Saturable absorber (SA) is a substance that exhibits varying levels of light absorption which depends on the optical intensity of the incident light. It demonstrates a high degree of absorption for low-intensity light, however, as the light intensity increases, reaches a point of saturated absorption, resulting in a lower degree of absorption for high-intensity light (Hercher, 1967). The advantageous characteristics of saturable absorbers include broad absorption bandwidth, low saturation intensity, ultrafast recovery time, and a high modulation depth. These properties make them valuable for a wide range of laser applications, including solid-state lasers, fiber lasers, and semiconductor lasers, operating at various wavelengths spanning from 500 nm to 2500 nm (Singh et al., 2012). Additionally, the desirable characteristics of saturable absorbers include achieving the highest pulse energy, with the modulation depth approximating one and a half times the initial gain, while minimizing the losses associated with non-saturable absorbers.

Moreover, a shallow depth is more suitable to achieve a lower pulse energy and a higher repetition rate. In order to ensure the rapid saturation of the saturable absorber and minimize the loss of pulse energy, the saturation energy of the saturable absorber should be lower than that of the gain medium. Furthermore, the recovery time of the saturable absorber should exceed the pulse duration, ensuring the time is sufficient to facilitate the recovery of losses before the gain is initiated following the pulse emission.

The saturable absorber SA is inserted into the fiber laser cavity to facilitate the generation of extremely short pulses. Most of the saturable absorbers (SAs) are fabricated using semiconductor materials in which resonant nonlinearities related to carrier transitions from the valence to conduction band resulted in the saturable absorption phenomenon. In order to illustrate this saturable absorption effect, people often use basic qualitative explanations based on a two-level electronic model where saturable absorption is similar and comparable to gain saturation. Figure 2.25 shows a visual representation of the entire saturable absorber process using a two-level model depicted in the form of photon particle. As depicted in the diagram, electrons situated on the ground state at lower energy valence band $E_1$ level are capable of absorbing photons when the photon energy matches the energy gap between the two levels. This absorption results in their transition to the higher energy conduction band $E_2$ level provided there are no electrons occupying the upper state. For wavelengths that is in close proximity to the bandgap energy in direct bandgap materials, there is a substantial increase in both absorption and the refractive index in response to changes in intensity. The main cause of saturable absorption is due to band-filling where with increasing intensity, intense photoexcitation leads to the saturation of states near the edges of the conduction and valence bands, effectively preventing further absorption. Band filling occurs because the Pauli Exclusion Principle dictates that no two electrons can occupy the same quantum state. The significant reduction in absorption is a result of fewer electrons remaining in the ground state $E_1$ and an increase in occupied states in the upper level $E_2$. state. When the material is exposed to sufficiently high intensity photons, it effectively becomes transparent to photon energies slightly above the band edge. This phenomenon is known as Pauli blocking or phase space filling and was initially theorized in 1969 (Zitter, 1969). Consequently, when the absorption become saturated, the photons can propagate through the transmission material without being absorbed. The electrons in the upper state $E_2$ decay back to the ground state $E_1$ once they reach a specific electron lifetime, and this process repeats continuously.

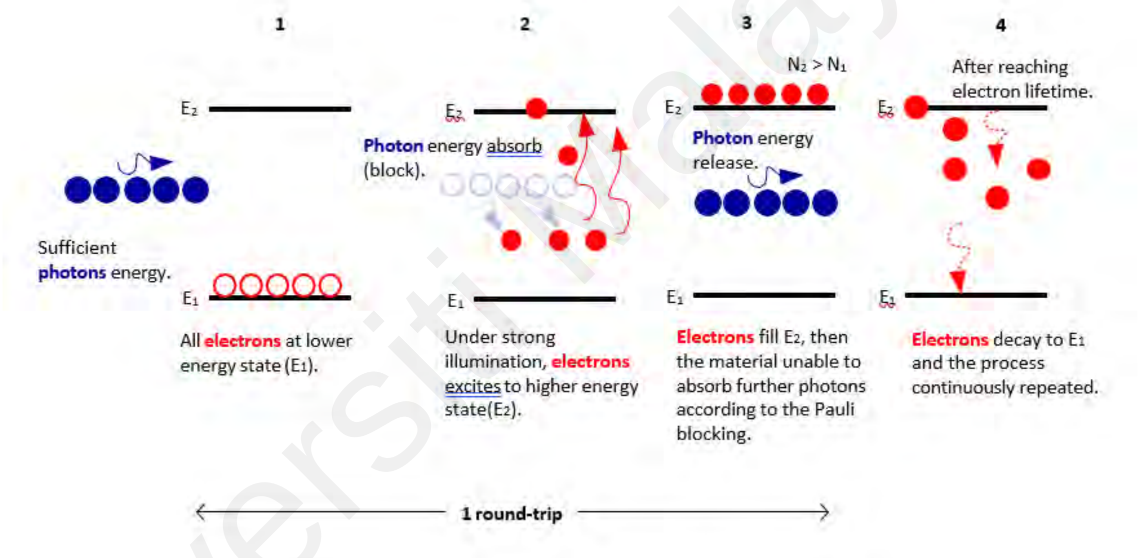

**Figure 2.25: Illustration of saturable absorber working mechanism based on a two-level model in particle form (Nayak, 2016)**

Based on this framework, the optical nonlinearities are directly related to the intensity of incident light as per the basic two-level saturable absorber model (Bao et al., 2009; Garmire, 2000; Zheng, Zhao et al., 2012):

$$\alpha(I) = \frac{\alpha_s}{(1 + I/I_{sat})} + \alpha_{ns} \qquad (2.35)$$

where $\alpha(I)$ is the absorption coefficient, $\alpha_s$ is the saturable absorption coefficient, $I$ is the incident light intensity, and $I_{sat}$ is the saturation intensity, $\alpha_{ns}$ is the non-saturable absorption coefficient. In the context of a saturable absorber, $\alpha_{ns}$ represents the constant background absorption of the material that remains the same regardless of the intensity of the incident light. The parameter at which $\alpha(I)$ decreases to half of its value at low incident light intensity ($\alpha(I_{sat}) = \alpha_s/2$) is known as the saturation intensity, denoted as $I_{sat}$. This is an important value that characterizes the intensity at which the saturable absorption effect becomes significant and leads to a reduction in the absorption coefficient to half of its value under low-intensity conditions. This nonlinear relationship between the absorption coefficient and the incident light intensity is shown in Figure 2.26. Certainly, the saturation intensity is a crucial parameter in evaluating and understanding the performance of a saturable absorber. It helps to determine the point at which the absorption behavior transitions from being dominated by linear processes to the saturable absorption effect, which is fundamental in various applications, such as pulse shaping and mode-locking for ultrashort pulse lasers.

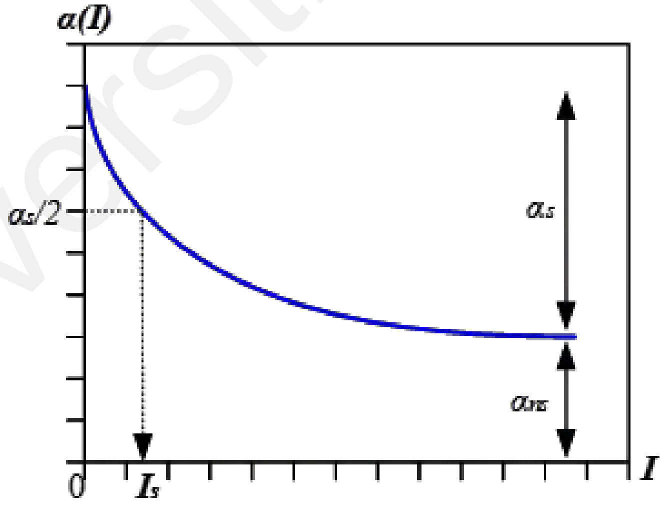

**Figure 2.26: Nonlinear optical profile of the absorption coefficient of a two-level system as a function of the incident light intensity $\alpha(I)$ (Ganeev, 2013)**

## 2.7 Two-dimensional Materials as Passive Saturable Absorber

The saturable absorber material employed in this thesis has two-dimensional (2D) atomic structure. Ever since the discovery of two-dimensional graphene material by Geim and Novoselov (Geim & Novoselov, 2007), the research exploration of 2D materials has broadened into diverse domains including electronics and optoelectronics (Li et al., 2017). Figure 2.27 illustrates the planar atomic arrangement of 2D materials delineating the area confined by the x- and y-axes. In general, the layered structure of 2D materials exhibits strong in-plane coupling and a weak Van der Waals coupling between layers. Hence, monolayer or few-layer samples of 2D materials can be easily fabricated through methods of mechanical exfoliation or chemical exfoliation (Luo et al., 2015; Sobon, 2015). Numerous promising functional applications of 2D materials are expected to be materialized in the near future. These applications span in various domains including optical modulators, photodetectors, logic transistors, high-frequency transistors, energy storage, and sensor devices (Butler et al., 2013).

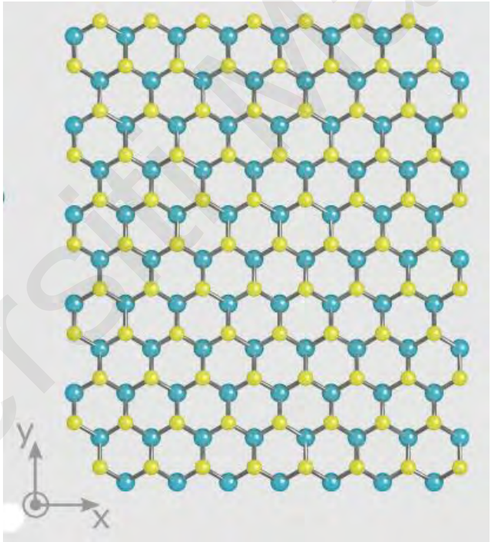

**Figure 2.27: Atomic structure of 2D materials (Shah, 2019)**

Thanks to an abundance of fascinating physics, a multitude of other groundbreaking 2D materials have been discovered and introduced to the public awareness. These 2D materials include graphene, topological insulators (TIs), black phosphorus (BP) and transition metal dichalcogenides (TMDs). This thesis focuses exclusively on a specific subset of 2D materials, namely transition metal dichalcogenides (TMD) group which include Molybdenum disulfide $MoS_2$, Molybdenum diselenide $MoSe_2$ and Molybdenum telluride $MoTe_2$. These 2D materials belong to the category of semiconductor materials.

Majority of 2D semiconductor materials exhibit a straightforward two-energy band structure which comprise the conduction band and the valence band. When the incident photons with energy higher than the bandgap energy, it can stimulate the transition of carriers from the valence band to the conduction band. In the existence of a more intense excitation such as a noise spike, all potential initial states are exhausted and the final states experience partial occupation due to the Pauli blocking effect. This results in saturation of absorption (Saraceno et al., 2011). In the field of applications involving saturable absorbers, the energy bandgap is one of the crucial properties in which photons with energy exceeding the bandgap energy of the materials can be easily absorbed. Hence, the bandgap energy of the saturable absorber should at least correspond to the photon energy generated within the laser cavity. In the case of a direct bandgap semiconductor materials, the photon absorption process is straightforward. This is because the excitation of electrons from the valence band to the conduction band does not demand a significant amount of momentum as these two bands share the same momentum value. In the case of indirect bandgap semiconductor materials, the efficiency of the photon absorption process is significantly lesser due to the need for additional absorption of phonons to compensate for the difference in momentum. The energy *E* of the photons in electronvolts $eV$ can be determined by using the following equation, which translated from the operating wavelength of the cavity.

$$E = h\frac{c}{\lambda} \tag{2.36}$$

where $\lambda$ is the operating wavelength, *h* is the Planck' constant, and *c* is speed of light. As per the equation in 2.36, a longer wavelength requires a smaller bandgap energy whereas a shorter wavelength requires a higher bandgap energy. The corresponding bandgap energies for wavelengths of 1550 nm ≈0.8eV and 2000 nm ≈0.62eV respectively. The bandgap of a semiconductor material determines its corresponding wavelength and each semiconductor material has its own distinctive bandgap. According to the photoelectric effect, semiconductors materials with a narrow bandgap exhibit broad ranges of responding wavelengths. However, for 2D materials with larger bandgaps, it is crucial to modulate the bandgap so that researchers and engineers can tailor the material's properties to suit specific requirements (Woodward & Kelleher, 2015) and $TiO_2$ (Tang et al., 1994). Another crucial property of a saturable absorber is its relaxation time. A shorter pulse width can be achieved with a faster relaxation time. On the other hand, the electron mobility of the 2D materials can also serve as an indicator of the relaxation time. Semiconductor materials with higher electron mobility often exhibit faster relaxation times which influence their performance in various applications. With a slow relaxation time, the pulse width formation will be in the range of nanoseconds to picoseconds. In order to obtain effective pulse shaping, the saturable absorber must rapidly recover to its initial state within a brief timeframe, typically ranging from picoseconds to femtoseconds (Keller, 2003; Woodward & Kelleher, 2015).

### 2.7.1 Graphene

Graphene is the first 2D material ever discovered (Luo et al., 2010) and was first suggested as a saturable absorber in 2009 (Bao et al., 2009). Ferrari et al. conducted an initial review on graphene focusing on its photonics and optoelectronics properties (Bonaccorso et al., 2010). This material is one-atom thick hybridized carbon and possesses a honeycomb lattice formed structure. The valance and conduction bands meet at high symmetry K points; thus, graphene is considered as zero-gap semiconductor material (Geim & Novoselov, 2007). The 2D honeycomb lattice formed structure has made graphene as saturable absorber with ultra-wide broadband operating wavelength spanning from terahertz THz to ultraviolet UV, ultrafast recovery time, low saturation intensity, ease of synthesis and flexibility of integration into fiber laser system(Bonaccorso et al., 2010; Sun et al., 2010). Few-layer graphene demonstrated a strong nonlinear refractive index of approximately $10^{-7}$ $cm^2/W$ surpassing other conventional bulk materials by seven orders of magnitude (Miao et al., 2015). This nonlinear refractive index resulted a significant nonlinear phase shifts, facilitating the creation of desired nonlinearity applications. Furthermore, the lower saturation absorption intensity of graphene in comparison to single walled carbon nanotube is advantageous for producing mode-locked fiber laser with a lower power threshold (Martinez & Sun, 2013). The measurement was taken for the thickness of monolayer graphene, yielding 0.33 ± 0.05 nm (Gupta et al., 2006) . Experiments were carried out to examine the impact of graphene layers from 1 to 15 layers (Chen et al., 2015), 3 to 12 layers (Sotor et al., 2015), and 9 to 48 layers (Sobon, 2015) on the modulation depth characteristic. According to these articles, higher modulation depth was achieved with greater thickness of graphene layers. Graphene is a saturable absorber with high crystalline quality (Peng et al., 2015) where even a minor structural defects in graphene can lead to phonon and electron scatterings and degrade the performance of saturable absorption (Banhart et al., 2011) such as causing higher non-saturable loss, higher saturation intensity, and lower modulation depth (Lin et al., 2013). Raman mapping characteristics can be used to examine defects in graphene where a higher level of defects is correlated with an increased number of graphene layers (Steinberg et al., 2017). While graphene is popularly used as a saturable absorber, it does have limitations. One example is the necessity for a hydrogen ambient environment during the synthesis of graphene through chemical vapor deposition where the process requirement stemming from the material's susceptibility to oxidation (Peng et al., 2015). Additionally, the absorption efficiency of graphene is relatively low with only 2.3% of incident light being absorbed per graphene layer. This results in a low carrier density and significantly impeding the ability of light modulation in strong-light interactions (Ge et al., 2018). Furthermore, the challenges in establishing an optical bandgap for graphene has constrained its integration into optoelectronic applications (Peng & Yan, 2021). Graphene has found extensive use in mode-locked erbium doped fiber lasers operating at the popular communication optical wavelength of 1550 nm. The parameters and performance of these fiber lasers are summarized in Table 2.2.

**Table 2.2: Erbium-doped fiber lasers Q-switched and Mode-locked by graphene at the wavelength of 1550 nm**

| **Laser type** | **Operational wavelength (nm)** | **Repetition rate** | **Pulse Width** | **SNR (dB)** | **Reference** |
|---|---|---|---|---|---|
| Mode-locked laser | 1550 nm | 18.67 MHz | 29 fs | 62 dB | (Purdie et al., 2015) |
| Mode-locked laser | 1564 nm | 19.30 MHz | 10.4 ps | 64 dB | (Fu et al., 2014) |
| Mode-locked laser | 1533.82 nm | 1.89 MHz | 1.21 ps | 71.6 dB | (Liu et al., 2016) |
| Q-switched fiber laser | 1566.2,<br>1566.4 nm | 65.9 kHz | 3.7µs | - | (Luo et al., 2010) |

### 2.7.2 Topological Insulator

A topological insulator is a material that has characteristic of an insulator in its inside interior but having conducting states on its surface (Sobon, 2015). Hence, only electrons can move along the surface of the material. Topological insulators have symmetry-protected topological order where the surface states are symmetry-protected Dirac fermions by particle number conservation and time-reversal symmetry. On the surface of a topological insulator there are special states that fall within the bulk energy gap and allow surface metallic conduction. Topological insulator TI such as bismuth telluride

$Bi_2Te_3$, bismuth selenide $Bi_2Se_3$, and antimony telluride $Sb_2Te_3$ have their band structure similar to graphene, hence, TI has been extensively researched and applied in the field of ultrafast photonics (Zhao et al., 2012). The field of research for topological insulators only focus on bismuth Bi and antimony Sb chalcogenide-based materials. The choice for chalcogenides-based material is due to the Van der Waals relaxation of the lattice matching strength which restricts the number of materials and substrates. Bismuth chalcogenides have been studied extensively for TIs and their applications in thermoelectric materials. In 2012, an initial investigation on the optical properties of bismuth telluride $Bi_2Te_3$ was conducted by employing this material as saturable absorber (SA) to achieve mode-locked fiber laser operation in the 1550nm wavelength range (Bernard et al., 2012). Inspired by this study, another mode-locked laser utilizing bismuth telluride $Bi_2Te_3$ has been successfully demonstrated through the hydrothermal intercalation/exfoliation method (Zhao et al., 2012). In 2013, a Q-switched operation is achieved with an erbium-doped yttrium aluminum garnet Er:YAG ceramic laser using bismuth telluride $Bi_2Te_3$ as saturable absorber. This Q-switched fiber laser operate at wavelength of 1645 nm and produce a maximum output power of 210 mW. This observation suggested that topological insulator TI as saturable absorber SA could be well-suited for high-power applications (Tang et al., 2013). During the same year, another topological insulator TI material bismuth selenide $Bi_2Se_3$ has successfully generated a dual-wavelength Q-switched fiber laser operating at 1545.85 and 1565.84 nm, as well as a wavelength-tunable Q-switched fiber laser spanning from 1510.9 to 1589.1 nm. Both of these Q-switched fiber lasers confirmed the potential of topological insulator TI as saturable absorber in facilitating broadband optical operations. Furthermore, despite the consistent performance of antimony telluride $Sb_2Te_3$ TI saturable absorbers in generating ultrashort and high-power pulses, the predominant emphasis in applications has been on the telecommunication band of 1550nm

(Boguslawski et al., 2014). Therefore, it is worthwhile to investigate additional operating wavelengths for antimony telluride $Sb_2Te_3$ saturable absorbers. Additionally, there is a need for exploring cost-effective and easier fabrication methods for topological insulator TI. Moreover, investigations into their applications in the higher wavelength band of the mid-infrared region should be further studied.

**Table 2.3: Summary of Topological Insulators SA-based Erbium-doped fiber lasers operating at 1.55 µm**

| Laser type/ TI material | Operational wavelength (nm) | Repetition rate | Pulse Width | SNR (dB) | Reference |
|---|---|---|---|---|---|
| Mode-locked laser/ Bismuth Selenide $Bi_2Se_3$ | 1557.5 nm | 12.5 MHz | 0.66 ps | 55 dB | (Liu, Zheng, et al., 2014) |
| Mode-locked laser/ Bismuth Selenide $Bi_2Se_3$ | 1558.3 nm | 5.1 MHz | 3.01 ps | 64 dB | (Chen et al., 2013) |
| Q-switched fiber laser/ Bismuth Selenide $Bi_2Se_3$ | 1559.8 nm | 87.03 kHz | 5.11 µs | 60 dB | (Harun et al., 2019) |
| Q-switched fiber laser/ Bismuth Selenide $Bi_2Se_3$ | 1560.33 nm | 12.9 kHz | 2.1µs | 40 dB | (Haris et al., 2017) |

### 2.7.3 Black Phosphorus (BP)

Black Phosphorus BP is a layered semiconductor material which is very similar in appearance to graphite. BP has numerous usages in optoelectronic, semiconductor, and photovoltaic applications. In a two-dimensional 2D form, black phosphorus is known as Phosphorene and has similar properties to other 2D semiconductor materials such as graphene in earlier section. Black phosphorus BP is the most thermodynamically stable allotrope of phosphorus which has gained the attention of the researchers (Churchill & Jarillo-Herrero, 2014). Even though there are plenty of findings on its unique electronic properties, however, its optical properties are less known and yet to explore further. BP has a layer-dependent direct band-gap which enable it to fill up the “blank space” between semi-metallic graphene and wide band-gap transition-metal dichalcogenides TMD. Since BP comprises only the elemental “phosphorus”, thus, it can be easily peeled off by mechanical exfoliation as graphene method above. Stimulated by the similarity between graphene and BP in terms of single elemental component and direct band-gap, BP could be used as a SA for Q-switched and mode-locked fiber laser generation.

Following the report on the broadband nonlinear optical response of black phosphorus (BP) (S. Lu et al., 2015), BP is utilized as a saturable absorber SA and manage to achieve both mode-locking at 1571.45 nm with a pulse duration as short as 946 fs and Q-switching at 1562.87 nm with a maximum pulse energy of 94.3 nJ (Chen et al., 2016). Subsequently, another mode-locked operation utilizing black phosphorus BP is achieved with a pulse duration of 786 fs and Q-switched operation with a maximum pulse energy of 18 nJ in the telecommunication band (Li et al., 2015b). The researchers also investigated the linear and nonlinear absorption properties of black phosphorus BP and observed that these properties were dependent on polarization and thickness. In 2016, a stable mode-locked soliton pulses were generated with a tunable wavelength extending from 1549 to 1575 nm by integrating black phosphorus BP using liquid-phase exfoliation

LPE method into an all-anomalous dispersion erbium doped cavity (Chen et al., 2016). In that same year, a new vector mode-locked soliton fiber laser utilizing black phosphorus was accomplished for the first time where the liquid-phase exfoliation (LPE) prepared black phosphorus nanoflakes were transferred onto the end facet of a fiber (Song et al., 2016). As per the findings, a stable 670 fs soliton pulses centered at 1550 nm were achieved with a fundamental repetition rate of 8.77 MHz and a signal-to-noise ratio (SNR) of 60 dB. Leveraging its layer-dependent direct bandgap, which can be significantly tuned from approximately 0.3 eV in bulk form to about 2 eV in monolayer form, black phosphorus (BP) emerges as a noteworthy intermediate material between zero bandgap graphene and wide-bandgap transition metal dichalcogenides (TMDs) (Tran et al., 2014). Despite the easier and cost-effective fabrication of black phosphorus (BP)(Qin et al., 2015), its instability in the presence of air and water molecules requires relatively strict conditions for both its preparation and operation thus restricts its application especially in high power regimes (Castellanos-Gomez et al., 2014; Island et al., 2015). Currently, there is a demand for further research not only on cost-effective fabrication methods for stable black phosphorus saturable absorbers but also on their application in specific types of ultrafast lasers. One prominent example is harmonic mode-locked lasers with high repetition rate pulses, which play a crucial role in optical communication applications (Mikulla et al., 1999), spectroscopy (Babu et al., 2007), and frequency bombing (McFerran, 2009). Table 2.4 outlines the performance metrics of both Q-switched fiber lasers and mode-locked fiber lasers utilizing black phosphorus as saturable absorbers.

**Table 2.4: Pulsed lasers utilizing black phosphorus as saturable absorbers**

| **Laser type** | **Operational wavelength (nm)** | **Repetition rate** | **Pulse Width** | **SNR (dB)** | **Reference** |
|---|---|---|---|---|---|
| Mode-locked laser | 1558.7 nm | 14.7 MHz | 786 fs | 56 dB | (Li et al., 2015a) |
| Mode-locked laser | 1555 nm | 23.9 MHz | 102 fs | 60 dB | (Jin et al., 2018) |
| Q-switched fiber laser | 1563 nm | 34.3 kHz | 2.96 µs | 53.2 dB | (Mu et al., 2015) |
| Q-switched fiber laser | 1550.9 nm | 28.57 kHz | 5.35 µs | - | (Fauziah et al., 2017) |

### 2.7.4 Transition Metal Dichalcogenide (TMD)

Transition metal dichalcogenide (TMD) is atomically thin semiconductors of the type $MX_2$ (Eftekhari, 2017). In $MX_2$ arrangement, M is the transition metal atom from the group IV, V, or VI columns of the periodic table such as Molybdenum (Mo) and Tungsten (W) while X is a chalcogen atom such as Sulfur (S), Selenium (Se) and Tellurium (Te) (Zhang et al., 2014). One layer of M atoms is paired with two layers of X atoms. Transition metal dichalcogenide (TMD) is part of the large family 2D materials due to their extraordinary thinness and TMD bulk crystals are formed of monolayers bound to each other by van-der-Waals attraction. The atoms within the layers of the transition metal dichalcogenide TMD are connected by a strong covalent bond while the stacked individual layers are held together by a comparatively weaker Van der Waals force (Mao et al., 2015; Wang et al., 2013). These weaker Van der Waals bonds has enable the TMD to undergo exfoliation, resulting in the formation of single or a few-layer structures. The characteristic of the bandgap in TMDs are highly influenced by the thickness of the material, for example, bulk TMDs and monolayer TMDs such as $WS_2$, exhibit characteristics of an indirect and direct bandgap, respectively (Mao et al., 2015). Furthermore, the electronic properties of TMDs are determined by the coordination and oxidation states of the M atoms, showcasing their potential to manifest as metals, semiconductors or insulators (Wang et al., 2012; Zhang et al., 2014). Hence, the speciality of TMDs lies in their thickness-dependent bandgap and electronic band structure, making them particularly attractive for optoelectronics applications in comparison with graphene, topological insulator TI and black phosphorus BP. TMD can be used as transistors in optical field to produce light emitters and photodetectors. Atomic layers of TMDs have been used as a phototransistor and ultrasensitive detectors as it shows very high efficiency of photoresponsivity. This high degree of electrostatic control is due to the thin active region of the monolayer. Its simplicity and the fact that it has only one semiconductor region, whereas the current generation of photodetectors is typically a p-n junction, makes possible industrial applications such as high-sensitivity and flexible photodetectors. Other than that, TMD has become an emerging research and development field due to its direct bandgap characteristic and this has created a vast potential application in optoelectronics devices such as solar cells, LEDs, photocatalytic and sensing devices. The emission efficiency of TMD monolayer is much higher than bulk material. The four most extensively studied TMDs are $MoS_2$, $WS_2$, $MoSe_2$ and $WSe_2$ (Bikorimana et al., 2016). The ultrafast carrier dynamics and strong third-order nonlinear optical NLO response in few-layer structures of $MoS_2$ and $WS_2$ have generated significant research interest as potential replacements for graphene (Shi et al., 2013). For example, $MoS_2$ demonstrated a faster saturation absorption for femtosecond pulse in 800 nm and showed a higher optical nonlinear response compared to graphene (Cui et al., 2016). However, $MoS_2$ has a lower optical damage threshold compared to graphene due to its weaker thermal conductivity and mechanical characteristics (Cui et al., 2016). Moreover, monolayer $MoS_2$ shares a comparable drawback with graphene concerning oxidation issues under high-energy laser irradiation and weak light-matter interaction, therefore reducing the generation of the laser pulse (Qin et al., 2016; Zhao et al., 2015). Consequently, multilayer $MoS_2$ is more appropriate than its monolayer $MoS_2$ for generating mode-locked fiber laser. A comprehensive review of the current status and future development of $MoS_2$ in mode-locked fiber laser was conducted (Woodward et al., 2015). When compared to $MoS_2$ and $WS_2$, $MoSe_2$ and $WSe_2$ shows similar molecular structures with a lower bandgap due to the larger mass of selenium (Se) than sulfur (S) chalcogenide atoms. Specifically, bulk $MoSe_2$ and $WSe_2$ have indirect bandgap of 1.09 eV and 1.20 eV (Du et al., 2014) while monolayer $MoSe_2$ and $WSe_2$ have direct bandgap of 1.57 eV and 1.67 eV respectively (Gusakova et al., 2017). The wider saturable absorption band for mode-locked fiber laser is facilitated by the reduced bandgap in monolayer compared to bulk

TMDs when incorporating selenium (Se) instead of sulfur (S) chalcogenide atoms (Luo et al., 2015). However, pairing a TMD with Se chalcogenide is limited by its weaker chemical reactivity compared to the S chalcogenide atom (Yin et al., 2017). Table 2.5 provides an overview of ultrafast Q-switched and mode-locked lasers by TMDs.

**Table 2.5: Laser pulses generation using Transition metal dichalcogenides TMDs SA at the wavelength of 1550 nm**

| **Laser type / type of TMD** | **Operational wavelength (nm)** | **Repetition rate** | **Pulse Width** | **SNR (dB)** | **Reference** |
|---|---|---|---|---|---|
| Mode-locked laser/ $MoS_2$ | 1569 nm | 8.3 MHz | 1.28 ps | 27 dB | (Xia et al., 2014) |
| Mode-locked laser / $MoS_2$ | 1570 nm | 12.1 MHz | 710 fs | 60 dB | (Liu, Luo, et al., 2014) |
| Q-switched fiber laser / $MoS_2$ | 1551.2 nm | 16.78 kHz | 5.7 µs | 50 dB | (Huang et al., 2014) |
| Q-switched fiber laser / $MoS_2$ | 1565 nm | 6.5–27.0 kHz | 5.4–23.2 µs | 54.5 dB | (Luo et al., 2014) |

## 2.8 Conventional way of fabrication of 2D SAs

The fabrication of two-dimensional saturable absorbers (2D SAs) has emerged as a crucial element in the domain of ultrafast optics and laser technology. These materials play a crucial role in generating ultrashort pulses especially in Q-switched and mode-locked fiber lasers due to their unique electronic and optical properties. The conventional methods employed for the fabrication of 2D saturable absorbers make use of a wide range of materials in which each exhibiting distinct characteristics that cater for specific applications. This section provides an overview of the conventional approaches used in the fabrication of 2D SAs including chemical vapor deposition CVD technique, optical deposition technique, drop cast technique, mechanical exfoliation technique and PVA thin film. The complex interaction between material science and laser technology in the context of 2D SA fabrication method highlights a continuous demand to improve performance metrics including faster response times, better saturation intensities and higher spectral tunability to fulfill the requirements of advanced applications in the field of ultrafast optics. Scientists continue in exploring, investigating and innovating with novel materials and techniques in the fabrication of saturable absorbers to address the evolving technological requirements. Every method has its own set of advantages and challenges, and the selection depends on factors such as the specific material, the required film thickness and the intended application. Researchers often optimize these fabrication processes to improve the effectiveness of passive saturable absorbers in generating ultrafast pulse laser.

### 2.8.1 Chemical vapor deposition CVD technique

Chemical Vapor Deposition (CVD) (Carlsson & Martin, 2010; Dobkin & Zuraw, 2003) serves as a fundamental approach in the domain of thin film deposition methods in providing a versatile and widely utilized method for cultivating films and coatings of superior quality. This section explores the fundamental principles, varied applications and advancements associated with CVD, showing its importance in material science, electronics, and other fields. Generally, CVD is a method in which a thin film is formed on the surface of a substrate through the chemical reaction of gaseous precursors. This method relies on the controlled and systematically introducing precursor molecules into a reaction chamber where those molecules undergo reactions to form a solid deposit on the substrate. The selection of precursors along with temperature and pressure conditions will govern the composition, structure, and properties of the film deposited. The CVD process starts with the volatile precursor gases such as organometallic compounds or metal halides introduced into a reaction chamber which these precursor gases undergo chemical reactions involving thermal decomposition or reduction and resulting in the formation of reactive species. These reactive species are then transported to the surface of the substrate where the actual film deposition occurs.

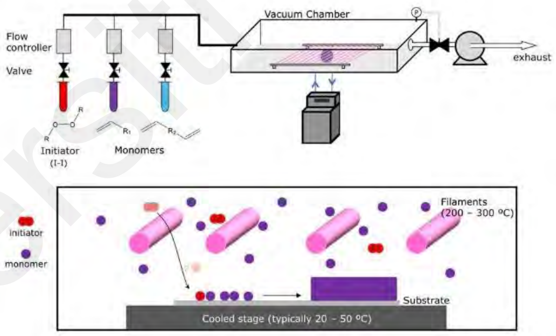

**Figure 2.28: Chemical vapor deposition CVD technique (Ovezmyradov et al., 2015)**

CVD is widely applied in diverse industries due to its capacity to deposit films with precise control over thickness, composition, and structure. In semiconductor manufacturing, CVD is utilized for the production of thin films for integrated circuits and other electronic devices. Additionally, innovations in precursor chemistry and reactor design have enabled the deposition of complex materials in manufacturing protective coatings, optical films, and advanced materials such as graphene and carbon nanotubes

(Cai et al., 2018; Dobkin & Zuraw, 2003). Although CVD technique has its advantages, however, it also faces some challenges where achieving precise control over film uniformity and minimizing impurity incorporation is very challenging and this makes CVD continues to be a focal point of ongoing research. With the evolution of technology, researchers are actively exploring and investigating novel precursors, refining reactor designs, and developing real-time monitoring techniques to tackle these challenges and unlock new possibilities. In summary, Chemical Vapor Deposition method stands as a popular technique in materials science and technology, making a substantial contribution to the production of advanced materials and devices. Its ongoing evolution and adaptability emphasize its crucial role in shaping the landscape of modern technological advancements.

### 2.8.2 Optical deposition technique

In optical deposition technique (Macleod, 2018), an intense light is injected from the fiber connector end into the saturable absorber (SA) solution to attract the SA particle to form onto the ferrule tip (Nicholson et al., 2007). There are typically two types of effects that lead to self-channeling of light in the fluid suspension. One is the optical gradient force and the other is the thermal effects that rely on the absorption. The optical gradient force is weak when the particle size is smaller than the optical wavelength, hence, a higher particle density is required to cause significant change in the refractive index to absorb the narrow beams. When the particle has higher density, multiple scattering of light dominates where the direction of the scattered light becomes random. This causes the particle moved toward the beam center. On the other hand, thermal effect can cause significant refractive index change, however, the refractive index typically decreases with increasing temperature in liquid. Thermophoresis is a thermal mechanism which uses a strong reaction of the suspended particles to temperature gradients which describes the ability of a macromolecule or particle to drift along passive Q-switched and Mode-locked

Fiber Lasers Using Saturable Absorbers temperature gradient. Although various methods are capable to deposit saturable absorber SA to the fiber core, thermophoresis is considered as the most likely process that is responsible for creating saturable absorber SA through optical deposition (Opiolka et al., 1994).

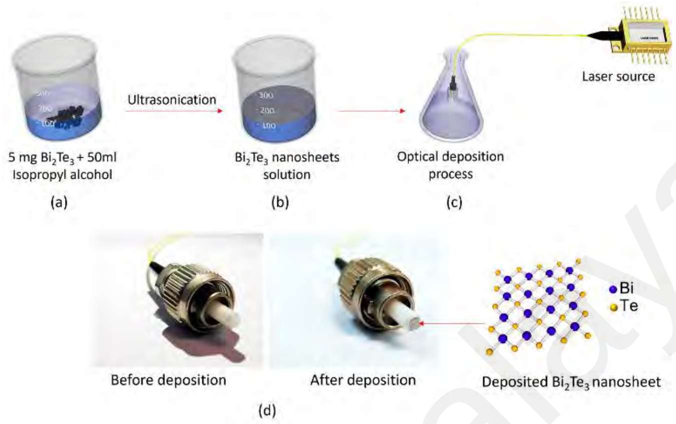

Figure 2.29: The process of optical deposition technique (Hazlihan, 2018)

When the laser source is switched on with the fiber ferrule in the solution, a strong convection current centered at the tips is observed, the induced current moves the SA particles toward the fiber ferrule. When fabricating a saturable absorber SA using optical deposition, it must be started with ultrasonification process (Soundeswaran et al., 2005). Centrifugation is also performed where only the homogeneous part of the solution is used for optical deposition process (El Ghazouani et al., 2023). For depositing the SA to the fiber ferrule, precise optical power is essential. Low optical power will not cause the SA particles to stick on the fiber ferrule while too high optical power will cause concentrated deposition around the fiber core. The optimum deposition is influenced by many factors such as optical power, the size of particles, solution temperature, concentration levels of the solution, and the optical wavelength used in the deposition process. To monitor the optical deposition process, a setup that involves optical circulator and power meters is needed. Furthermore, in order to control the insertion loss, the duration of the deposition has to be determined. Long deposition duration would create higher insertion loss. Optical deposition technique is highly efficient as it only uses a small amount of saturable absorber. However, the disadvantage of this optical deposition causes large scattering loss, and this process has too many factors that can influence the required optical power for the SA particles adhere to the fiber core.

### 2.8.3 Drop cast technique

The drop cast technique (Kumar et al., 2020) offers a straightforward and effective approach in depositing saturable absorber materials onto substrates to enable the formation of thin films with controlled thickness and homogeneity. In the field of saturable absorbers, this technique allows researchers to customize the properties of the thin film to achieve specific nonlinear optical effects. The procedure begins with preparing a solution containing saturable absorber materials and followed by the careful and precise deposition of a droplet of this solution onto a substrate. As the solvent gradually evaporates, a thin film is formed, and this gives rise to the creation of the passive saturable absorber (Razak et al., 2017). The insertion loss of the SA can be controlled through the concentration of the solution and the number of times this process is repeated. The dripping and drying process can also be repeated until the desired insertion loss is achieved.

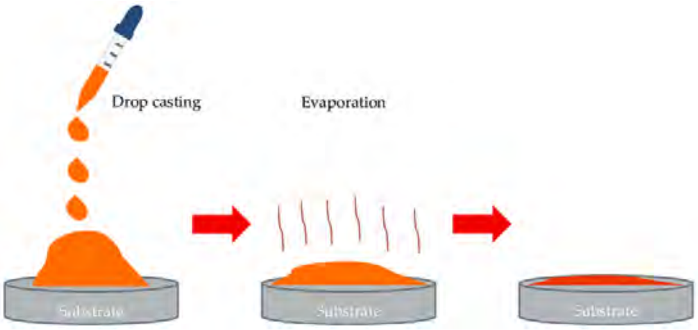

**Figure 2.30: The process of drop cast technique (Rodríguez-Hernández et al., 2020)**

Although the insertion loss is high through multiple dripping and drying, this high loss can be overcome by increasing the pulse energy. Since the pulse energy depends on the power and frequency, it can be solved by increasing the laser pump power or lengthen the fiber laser cavity. The simplicity of the drop cast technique is a key advantage as it requires minimal equipment and is easily accessible to researchers with different levels of expertise. This accessibility has contributed to its extensive adoption in academic as well as industrial environments. The drop cast technique is cost-effective compared to more complex deposition methods such as spin coating or chemical vapor deposition making it accessible to a broader range of researchers and laboratories as well as it can accommodates a variety of saturable absorber materials. Another advantage in this drop cast technique is that it allows researchers to easily control the thickness of the deposited film by adjusting the concentration of the solution and the volume of the droplet, thus making it possible for precise tuning of the saturable absorber's properties (Eng et al., 2015). While drop cast technique offers notable advantages, there are challenges in fine-tuning this technique for the fabrication of saturable absorbers. Achieving thickness uniformity in the deposited films can be a concern and the process is sensitive to factors such as substrate surface energy and drying conditions (Eng et al., 2015). Furthermore, understanding the correlation between film morphology and optical performance are important criteria in this technique. Another drawback of this technique is that it inevitably changes the repetition rate and pulse width of the mode-locked fiber laser when the pulse energy increases. Researchers have tackled these challenges through modifications to the technique such as implementing controlled drying environments or incorporating surfactants to improve the uniformity of the film. Future directions may include integrating the drop-cast technique with other fabrication methods such as laser-induced deposition or electrostatic assembly to achieve greater control over the structure and properties of saturable absorber films. The straightforward nature of the drop-cast technique proves beneficial as it enables the efficient exploration of various materials and configurations. Its simplicity combined with the capability to precisely control the thin film parameters has made it an invaluable asset in the development of advanced optical devices. As researchers refine and broaden the applications of the drop-cast technique, it stands ready to contribute significantly to the evolution of ultrafast laser technology and its diverse applications across scientific and technological domains.

### 2.8.4 Mechanical exfoliation technique

Mechanical exfoliation has become a popular and powerful technique in the field of materials science particularly for the fabrication of passive saturable absorbers (Eng et al., 2015). This approach involves mechanically extracting thin layers from a bulk material and often resulting in two-dimensional structures with unique properties. In the field of passive saturable absorbers, mechanical exfoliation offers a promising path for customizing materials to achieve specific nonlinear optical effects. In year 2004, Sir Andre Geim and Sir Konstantin Novoselov utilized this mechanical exfoliation method and managed to isolate graphene as a single layer of carbon atoms arranged in a hexagonal lattice (Tyutyunnik, 2021). This monolayer carbon is obtained by repetitive peeling of graphene layers from a graphite piece using adhesive tape (Hancock, 2011). The discovery of graphene and its unique properties such as remarkable strength and conductivity had contributed to their recognition with the Nobel Prize in Physics in 2010.

**Figure 2.31: The process of mechanical exfoliation technique (Demon et al., 2020)**

Mechanical exfoliation or commonly referred to as the Scotch tape method is based on the physical separation of atomic or molecular layers from a parent material. Usually, this process involves utilizing an adhesive tape to peel off thin layers of a bulk material due to its weak interlayer bonds. The resulting thin layers is commonly referred to as flakes and this flakes demonstrate unique electronic and optical properties that differ from those of the bulk material. This is clarified in section 2.7.4 where varying bandgaps are observed between monolayers and the bulk material. The unique electronic band structures and fast carrier dynamics of these thin layer materials make them as excellent candidates for applications in ultrafast optics including mode-locking lasers and pulse shaping. The pulse is generated using the peeled SA layer which is transferred to the fiber ferrule (Chang et al., 2010). A fiberscope is used to verify the successful transfer of the SA layer onto the core of the fiber ferrule. The advantage of mechanical exfoliation lies on its capability to produce monolayer and few-layer-thick sheets which enable precise control over the thickness of the saturable absorber. This degree of control is crucial in customizing the nonlinear optical response. Additionally, the resulting thin layers flakes demonstrate high crystallinity and minimal defects which contributes to superior optical properties in achieving high-performance saturable absorbers. Mechanical exfoliation is applicable to a wide range of materials beyond graphene including various TMDs, black phosphorus, and other two-dimensional 2D materials. This diversity allows researchers to explore and investigate different materials to fulfill specific application requirements. Despite its advantages, mechanical exfoliation comes with its own set of challenges where achieving large-area and scalable production is a significant concern. Moreover, the needs for manual manipulation in the exfoliation process may introduce variability and hinder reproducibility. Additionally, controlling the specific SA layers intended for transfer onto the core of the fiber ferrule poses a challenge. Therefore, researchers are actively addressing these challenges by developing automated exfoliation techniques and strategies to enable large-scale production. The adaptability and unique properties of two-dimensional 2D materials obtained through mechanical exfoliation open the way for innovations and advancements in ultrafast laser technology and beyond.

### 2.8.5 Saturable absorber (SA) PVA Thin film fabrication technique

The SA PVA film was fabricated by homogenously mixing the desired Saturable absorber nano powder into PVA solution (Al-Hiti et al., 2019; Kumar et al., 2004). The fabrication processes of the SA PVA film provided in Figure 2.31 below.

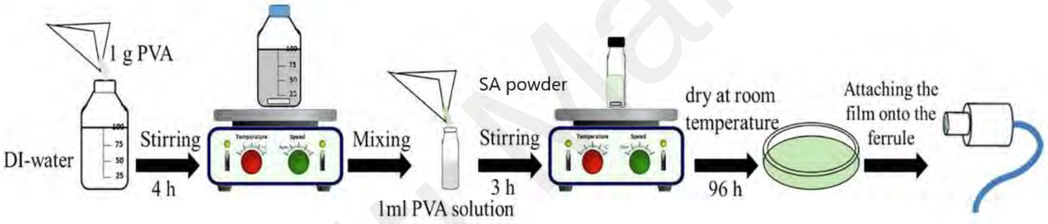

**Figure 2.32: The fabrication processes of the saturable absorber SA PVA thin film (Al-Hiti et al., 2019)**

Polyvinyl alcohol PVA thin films have become a promising materials for SA fabrication due to their unique optical and mechanical properties. Polyvinyl alcohol PVA is a synthetic polymer soluble in water and is well known for its biocompatibility, transparency and film-forming properties. These characteristics make PVA a compelling choice for the production of thin films in optical devices. The initiation process involves preparing a PVA solution with the desired concentration and this is usually done by dissolving PVA in distilled water under controlled conditions to achieve a homogenous solution. The PVA solution is continuously stirred using a magnetic stirrer for a specified duration at a constant speed. Subsequently, the well stirred PVA solution is blended with the saturable absorber SA powder. Once again, the PVA solution containing the SA powder is stirred at a constant speed using a magnetic stirrer for a specified duration. The homogenously dispersed SA PVA solution is subsequently transferred into a clean glass petri dish. The petri dish glass must be properly cleaned and treated to ensure maximum film adhesion. The SA PVA solution is allowed to dry and eventually evaporate at room temperature over a specific period to facilitate the formation of a dry SA polymer film. The amount of PVA solution poured onto the petri dish will influences the film thickness and quality. The target thickness of the desired SA film is around 40 µm. A small segment of the fabricated SA thin film measuring approximately 1 mm × 1 mm is extracted from the petri dish and is gently attached on a clean FC/PC fiber ferrule with the help of index matching gel as shown in Figure 2.31 above. Following the fabrication process, it is essential to characterize the PVA thin film to verify its suitability as a saturable absorber. The characterization techniques include UV-Vis spectroscopy, X-ray diffraction, and atomic force microscopy can provide insights into optical and structural properties of the fabricated thin film. The SA PVA film fabrication is s slightly more complex than mechanical exfoliation and drop cast techniques, however, it is much simpler compared to chemical vapor deposition method (Das, 2022). Despite its advantages, there are some challenges encountered during PVA thin film fabrication including the need to maintain uniformity and control the transfer of the SA layer.

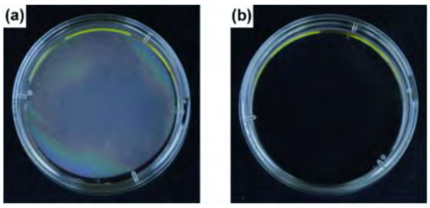

**Figure 2.33: PVA thin film on petri dish (Al-Hiti et al., 2019)**

In summary, the fabrication of PVA thin films for application as saturable absorbers offers promising prospects in the field of ultrafast optics by exploring ongoing research and potential advancements in the field, including the development of automated fabrication techniques and novel materials for enhanced SA performance. Advancements in material synthesis and deposition techniques continue to shape the landscape of SA technology and this create new way of innovative applications in laser systems and beyond.

## 2.9 Summary and Research Gap

The literature review emphasizes the significant advancements in the utilizing two-dimensional (2D) materials as passive saturable absorbers (SAs) with a focus on graphene, topological insulators, black phosphorus, and transition metal dichalcogenides. These materials have shown promising optical properties which make them suitable for various photonic applications. Furthermore, the review also covered conventional methods for fabricating 2D Sas including Chemical Vapor Deposition (CVD), optical deposition, drop casting, mechanical exfoliation and PVA thin film fabrication techniques.

However, despite the advancements in this field, a research gap still exists in optimizing fabrication methods to improve the consistency and reproducibility of the characteristics of 2D SAs. Moreover, the exploration of less commonly studied materials such as $MoS_2$, $MoSe_2$ and $MoTe_2$ using alternative fabrication techniques like electro-deposition offers a valuable opportunity for further research. This research aims to bridge these gaps by focusing on the fabrication of Molybdenum dichalcogenides as passive SAs using the electro-deposition method along with a comprehensive characterization of their structural, crystallographic, and optical properties. Additionally, the research will evaluate the practical application of the electro-deposited SAs in photonic devices including mode-locked and Q-switched lasers to demonstrate their viability and potential advantages over SAs fabricated by other methods.

# CHAPTER 3: MATERIAL FABRICATION AND CHARACTERIZATION OF TMD SATURABLE ABSORBER

## 3.1 Fabrication of TMD SA using electro-deposition method

This research work utilized two-dimensional (2D) materials with a specific focus on transition metal dichalcogenides (TMD) (Manzeli et al., 2017) such as molybdenum disulfide $MoS_2$, molybdenum diselenide $MoSe_2$ and molybdenum ditelluride $MoTe_2$ as saturable absorber to generate passive Q-switched and Mode-locked fiber lasers. This chapter provides detailed insight on the method used for preparing and charactering these TMDs materials. In this research, the electrodeposition method with a potentiostatic mode has been selected for synthesizing thin films among the various available methods. Hence, the experimental details on the electrodeposition method and substrates preparation will be further discussed in this chapter.

Furthermore, a comprehensive explanation regarding the characterization of the fabricated TMDs thin films properties is also presented in this chapter (Manzeli et al., 2017). The analytical techniques used to characterize this TMDs thin film are field emission scanning electron microscopy (FESEM), energy dispersive X-ray (EDX) spectroscopy, X-ray diffraction (XRD) including optical properties such as linear absorption and modulation depth.

Figure 3.1 shows the flow chart of preparation and characterization of these TMD thin films. This includes the raw materials preparation, substrate and electrolyte preparation, process of cyclic voltammetry and electrodeposition, followed by TMD thin film characterization. The results of Q-switched and mode-locked pulsed laser utilizing the fabricated TMD thin film will be further discussed in chapter 4 and chapter 5.

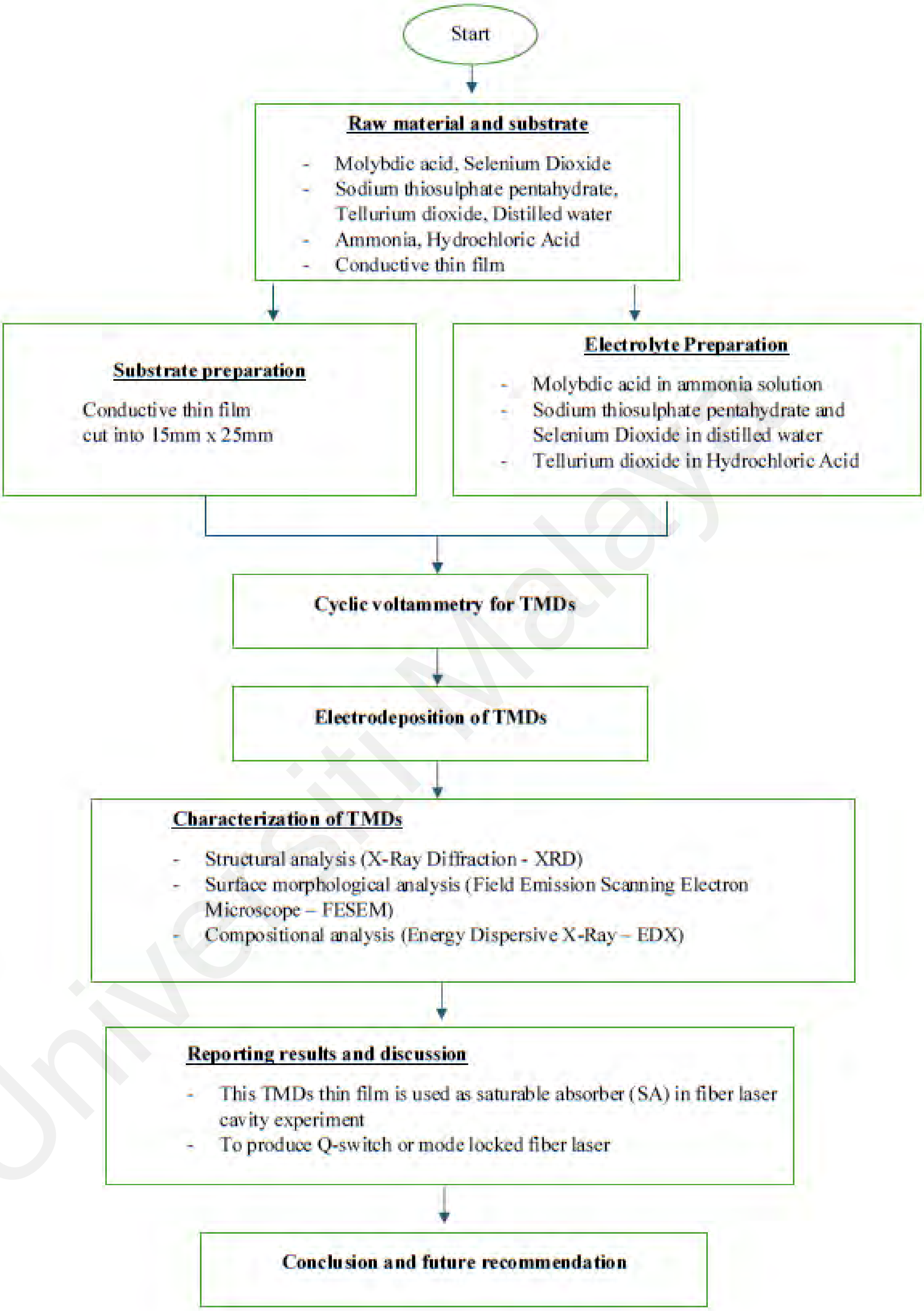

**Figure 3.1: Flow chart in preparation and characterization of the TMDs thin film**

### 3.1.1 Raw Materials

The following raw materials have been utilized in the fabrication of TMDs thin films.

**Table 3.1: Raw materials for fabrication of TMDs thin films.**

| No. | Materials | Purpose |
|---|---|---|
| 1. | Molybdic Acid<br>$H_2MoO_4$ | Molybdic acid can be ionized to produce molybdate ions $Mo^{4+}$ and these ions serves as a precursor for the synthesis of various molybdenum compounds. |
| 2. | Sodium Thiosulphate Pentahydrate<br>$Na_2S_2O_3 . 5H_2O$ | Sodium thiosulphate pentahydrate is used as a precursor for $S^{2-}$ ions |
| 3. | Selenium Dioxide<br>$SeO_2$ | Selenium dioxide powder is used as precursor for $Se^{2-}$ ions |
| 4. | Tellurium dioxide<br>$TeO_2$ | Tellurium dioxide is used as a precursor for $Te^{2-}$ ions |
| 5. | Ammonia Solution<br>$NH_3$ | Ammonia solution is used as solvent to dissolve molybdic acid. |
| 6. | Hydrochloric Acid<br>HCI | Hydrochloric acid is used as solvent to dissolve tellurium dioxide powder. |
| 7. | Distilled water<br>$H_2O$ | Distilled water is used as solvent to dissolve sodium thiosulphate pentahydrate crystal and selenium dioxide powder. |

### 3.1.2 Substrate Preparation

In the electro-deposition method, the common substrates typically used for the chemical deposition are conducting glass substrates and metal substrates. However, these substrates pose a challenge when it comes to fiber laser applications as they cannot be easily cut into small pieces for inserting them into fiber ferrules to generate laser pulse. While it may be possible to cut glass into smaller pieces, it is not feasible to insert the glass fragments between the fiber ferrule as it prevents the connectors from being securely tightened. On the other hand, metal substrates are unsuitable as the laser pulse is incapable of passing through the metallic medium. Additionally, the method of polyvinyl alcohol PVA thin films described in section 2.8.5 are unsuitable for use as they will dissolve in the chemical solution employed in the electrodeposition process. Recognizing this limitation, alternative solutions are needed to address the issue. One promising approach includes utilizing a thin conductive film as shown in Figure 3.11 below. This thin film is comprised of a plastic sheet coated with a thin layer of conductive material. This conductive layer has thickness of 10nm (Ren et al., 2022). This transparent-yet-conductive thin films is a crucial element in this electro-deposition process.

**Figure 3.2: Indium based coated conductive film substrate**

Unlike glass and metal substrates, this thin film offers the advantage of being easily cut into smaller pieces, capable of permitting the passage of laser light and allowing efficient integration into the fiber ferrules. This alternative approach not only addresses the limitations posed by rigid substrates requirement but also enhances the adaptability and versatility of the electro-deposition method in various applications. Being an electrically conductive film, this indium based coated conductive film has a surface resistivity of approximately 5 ohm/sqm. It has a thickness of only 0.125mm which can be easily cut into smaller size of of 15mm x 25mm as shown in Figure 3.12. Before the electrodeposition process, a protective layer of plastic cover is peeled off from the surface of the conductive film.

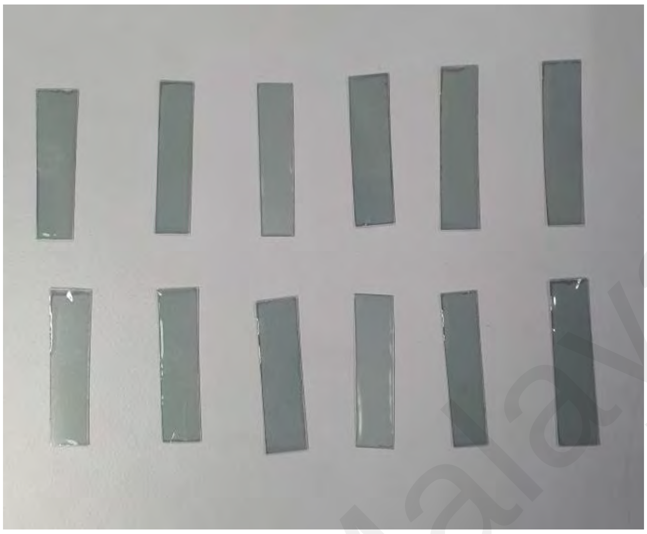

**Figure 3.3: 15mm x 25mm size of conductive film substrate**

### 3.1.3 Electrolyte Preparation

For the deposition of transition metal dichalcogenides (TMDs) thin films, a mixture of molybdic acid in ammoniacal solution of pH 9.3 ± 0.2 with chalcogenides elements such as sodium thiosulphate pentahydrate, selenium dioxide and tellurium dioxide are used as electrolyte ions precursors. The deposition of these TMDs thin film is carried out in specific time duration at temperature of 40±1 ºC.

In order to prepare the electrolyte solutions having concentration of 0.5M of molybdic acid $H_2MoO_4$, 0.5M sodium thiosulphate pentahydrate $Na_2S_2O_3.5H_2O$, 0.5M selenium dioxide, $SeO_2$ and 0.5M tellurium dioxide $TeO_2$, the proportion of solution is mix according to the Table 3.1 below.

**Table 3.2: 0.5M concentration electrolyte solutions**

| Raw Material | Ions | Mass added to 100ml of solvent (grams) | Solvent |
|---|---|---|---|
| Molybdic Acid – $H_2MoO_4$ | $Mo^{4+}$ | 8.10 | Ammonia |
| Sodium Thiosulphate Pentahydrate $Na_2S_2O_3 . 5H_2O$ | $S^{2-}$ | 12.40 | Distilled water |
| Selenium dioxide, SeO2 | $Se^{2-}$ | 5.55 | Distilled water |
| Tellurium dioxide $TeO_2$ | $Te^{2-}$ | 8.00 | Acid Hydrochloric |

According to Table 3.1 above, 8.10grams of molybdic acid powder $H_2MoO_4$ is added into 100ml of ammonia $NH_3$ solution to establish a concentration of 0.5M molybdic acid in the ammoniacal solution. As for sodium thiosulphate pentahydrate $Na_2S_2O_3.5H_2O$, a powder weighing 12.40 grams is mixed with 100ml of distilled water. On the other hand, 5.55g of selenium dioxide $SeO_2$ is combined with 100 ml of distilled water. Lastly 8g of tellurium dioxide $TeO_2$ is added to 100ml of hydrochloric acid to generate 0.5M concentration. These solutions were blended in proportionate amounts in accordance with the stoichiometry of the precursor electrolyte. For the synthesis of transition metal dichalcogenides (TMDs) thin films, the electrolyte mixture ratio between the precursor solution is selected to be 1:2 following its stoichiometry. For instance, 50ml of molybdic acid $H_2MoO_4$ is mixed with 100ml of sodium thiosulphate pentahydrate $Na_2S_2O_3 . 5H_2O$, 100ml selenium dioxide $SeO_2$ and 100ml tellurium dioxide $TeO_2$.

### 3.1.4 Thin Films Synthesis via Electrodeposition

In this research, transition metal dichalcogenides (TMDs) were electro-deposited onto indium based coated conductive films. Electro-deposition relies on fundamental principles of electrochemistry. Electro-deposition involves the controlled reduction of metal ions from an electrolyte onto a substrate under the influence of an electric field. The electro-deposition technique has been more extensively studied for the fabrication of thin films of metallic alloys. In comparison with other fabrication methods, electro-deposition is relatively more scalable and cost effective due to its non-vacuum nature and operation at room temperature (Ouerfelli et al., 2008). Furthermore, substrates with various sizes and shapes can be utilized without the requirement for toxic gaseous precursors with contrast to numerous gas-phase techniques. Electro-deposition processes are more easily controllable, since the film compositions are not very sensitive to small variations in the precursor concentrations and the precursor solutions are stable (Anand et al., 2013). Additionally, this technique offers simplicity and the ability to achieve precise control over film thickness and composition. The electro-deposition process is influenced by factors including voltage, current density, temperature and the composition of the electrolyte, Hence, through the manipulation of these parameters, the thickness, morphology and crystallographic structure of the deposited thin films can be controlled.

The electro-deposition of transition metal dichalcogenides (TMDs) thin film is conducted using Admiral Squidstat potentiostat. The deposition of thin film begins with cyclic voltammetry (CV) technique and then followed by synthesis of the chalcogenides through electro-deposition method. All the voltages are measured with reference to a saturated calomel electrode (SCE) known as reference electrode.

#### 3.1.4.1 Cyclic Voltammetry Measurements

Cyclic Voltammetry (CV) is a powerful electrochemical technique used for exploring the redox characteristics of substances dissolved in a solution. This cyclic and repetitive approach provides valuable insights into the electrochemical properties of a wide range of compounds including small organic molecules to complex biomolecules and nanomaterials (Heinze, 1984). Fundamentally, cyclic voltammetry involves systematically sweeping the potential of a working electrode linearly or in a stepwise manner over a specified duration. This potential sweep triggers redox reactions at the electrode interface. As the potential changes, the corresponding current response is recorded. The resultant voltammogram is a plot of graph showing the relationship between current and applied potential which provides a visual portrayal of the electro-chemical processes. The cyclical nature involves the iteration of the potential sweep in both forward and reverse directions. The generated cyclic voltammogram exhibits peaks and troughs in which these fluctuations corresponding to specific electrochemical events as shown in Figure 3.13. Peaks indicates oxidation or reduction processes while troughs denote the reverse reactions.

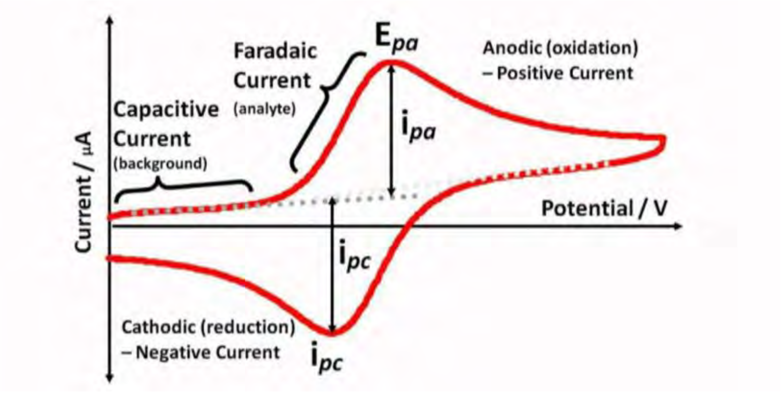

**Figure 3.4: Cyclic voltammogram of current and applied voltage**

The fundamental elements of a typical cyclic voltammetry setup consist of a working electrode, reference electrode and counter electrode submerged in an electrolyte solution. The working electrode facilitates electrochemical reactions by providing the necessary surface for chemical transformations to occur. The reference electrode maintains a consistent potential that serves as a reference for measuring the potential of the working electrode. Lasty, the counter electrode completes the circuit, allowing the flow of current. Modern cyclic voltammetry instruments often incorporate potentiostats which control the potential applied to the working electrode and galvanostats which govern the current flow within the system. This incorporation allows precise control of experimental conditions to facilitate the exploration of various electrochemical systems.

Before initiating the electro-deposition process, cyclic voltammetry procedure is conducted to better understand the reduction and growth dynamics in TMDs thin films. This cyclic voltammetry process can be considered as the most efficient and versatile electroanalytical technique employed for the mechanistic investigation of redox systems (Elgrishi et al., 2018). Typically, this is the initial experiment to be conducted when dealing with any electrochemically active sample. The objective of using cyclic voltammetry is to gauge the current response at the electrode surface on a specific range of potentials in the chemical solution (Anuar et al., 2007). It is carried out by establishing two potential limits on the prepared chemical solution to explore the potential ranges suitable for the deposition of thin films.

For this case of transition metal dichalcogenide (TMD) compounds, the potential ranges from -2.00V to +1.00V is deemed appropriate for conducting cyclic voltammetry (CV) measurements (Anuar et al., 2007; Zainal et al., 2005). The reduction and oxidation process of the electrochemical active ion specimen deposited on the metal substrate occurs within this potential range. However, employing the identical potential configuration of -2.00V to +1.00V on indium based coated conductive thin film may result in the peeling off this conductive layer during the oxidation cycle at positive voltage. Consequently, the graph will deviate from the representation of Figure 3.13 when the thin film experiences a disruption in current flow as the conductive layer peels off. To observe this occurrence, the Admiral Squidstat Cyclic Voltammetry Software is utilized for conducting this measurement and to monitor the current and voltage profiles. This scenario is evident in Figure 3.14 where the plots appear abnormal during the positive cycle of oxidation.

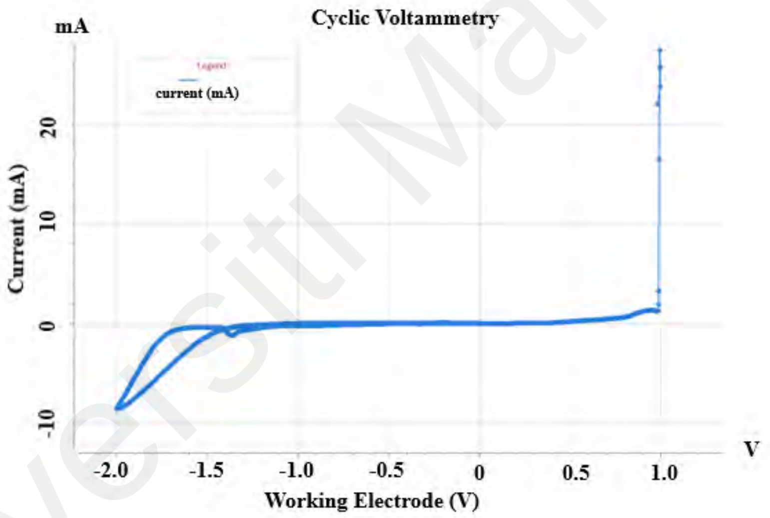

Figure 3.5: Cyclic voltammetry in oxidation cycle

Therefore, guided by this observation, cyclic voltammetry measurement within the negative potential ranges from 0V to -2.00V is performed as shown in Figure 3.15. In Figure 3.15, the forward scan initially started with a constant current until an increase in cathodic current occurred at around -0.60V indicating a reduction process. The increase of current is associated with the reduction of transition metal ions and dichalcogenides ions to form solid transition metal dichalcogenides TMDs compound on the thin film. Further increases in current at more negative potentials could be attributed to the hydrogen evolution reaction (Anuar et al., 2007; Zainal et al., 2005). The deposition of transition metal dichalcogenides (TMDs) compounds on the thin film continued until reaching the equilibrium potential at an interception between the forward and reverse scans occurring at approximately -0.60V versus the reference electrode. **Figure 3.15** shows the optimal deposition of TMDs materials at -1.30V during the reduction cycle in the cyclic voltammetry measurement.  In simpler terms, the deposition rate is highest at potential -1.30V compared to other negative potentials due to the uptick in the cyclic voltammetry graph. Hence, -1.30V is used to perform electro-deposition of TMDs on the conductive thin film in section 3.1.4.2.

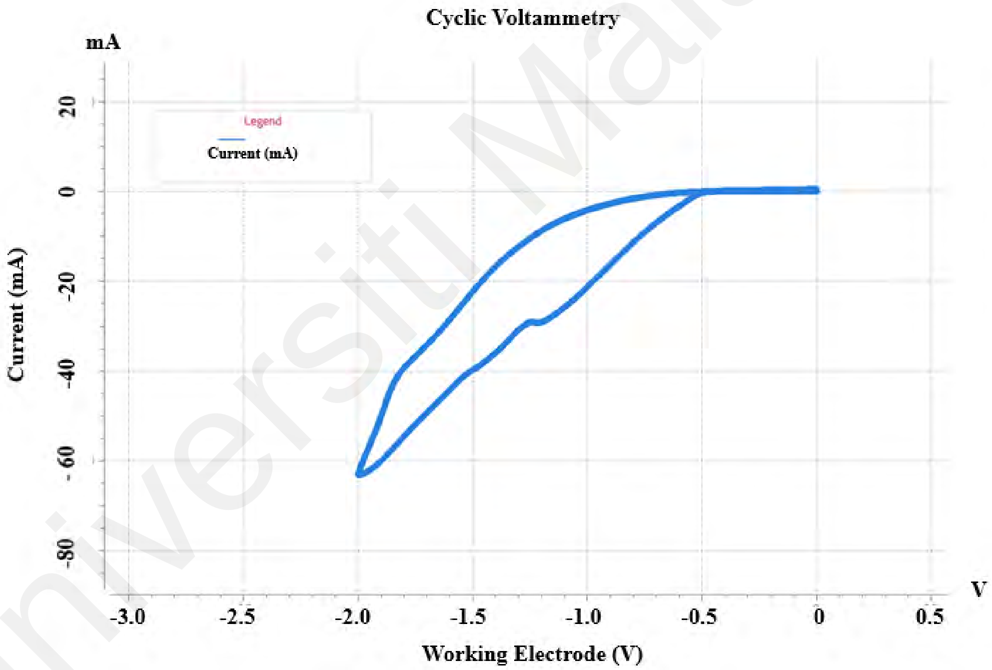

**Figure 3.6: Cyclic voltammetry in reduction cycle**

### 3.1.4.2 Electro-deposition of $MoS_2$, $MoSe_2$ and $MoTe_2$ Thin Films

A three-electrode configuration is used for both the cyclic voltammetry analysis (Chandra & Sahu, 1984) as well as the electro-deposition of the TMDs compounds onto the conductive thin film as discussed in section 3.1.4.1. The schematic diagram and experiment setup of this configuration are shown in Figure 3.16, Figure 3.17 and Figure

3.18 respectively. The electrolysis cell consists of a conductive film designated as the working electrode (WE) where the deposition of the TMD material takes place. On the contrary, the graphite rod serves as the counter electrode (CE) while a saturated calomel electrode (SCE) with an Ag/AgCl reference system functions as the reference electrode (Zainal et al., 2005).

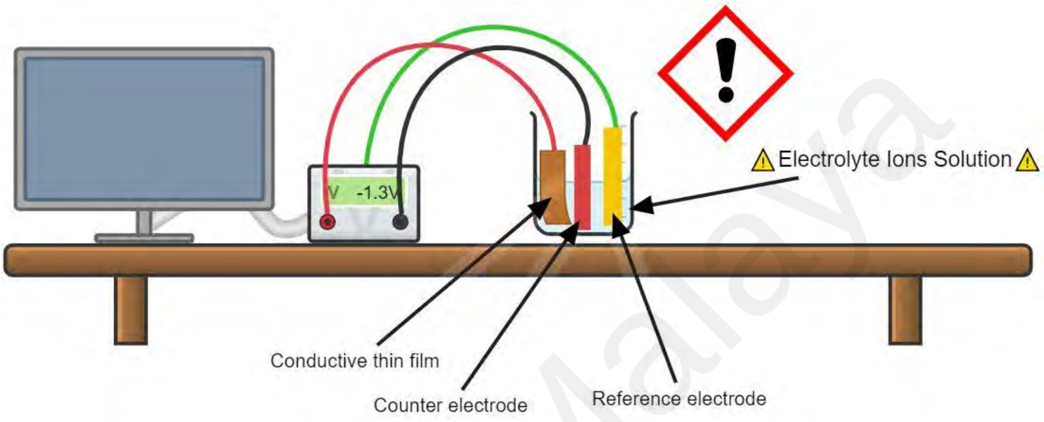

**Figure 3.7: Schematic diagram of experimental setup for TMDs thin film deposition**

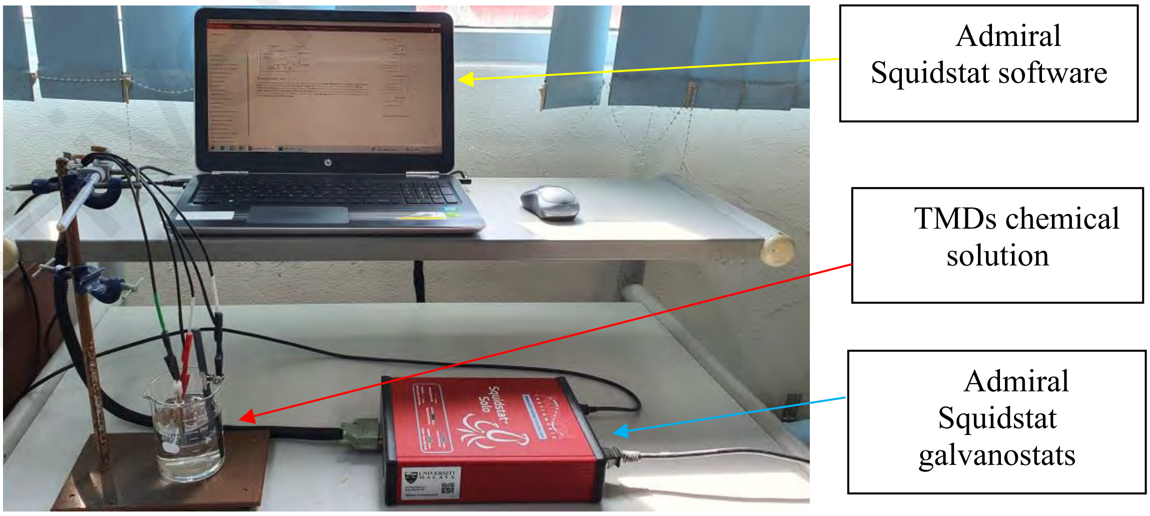

**Figure 3.8: Experiment setup for electro-deposition of TMDs**

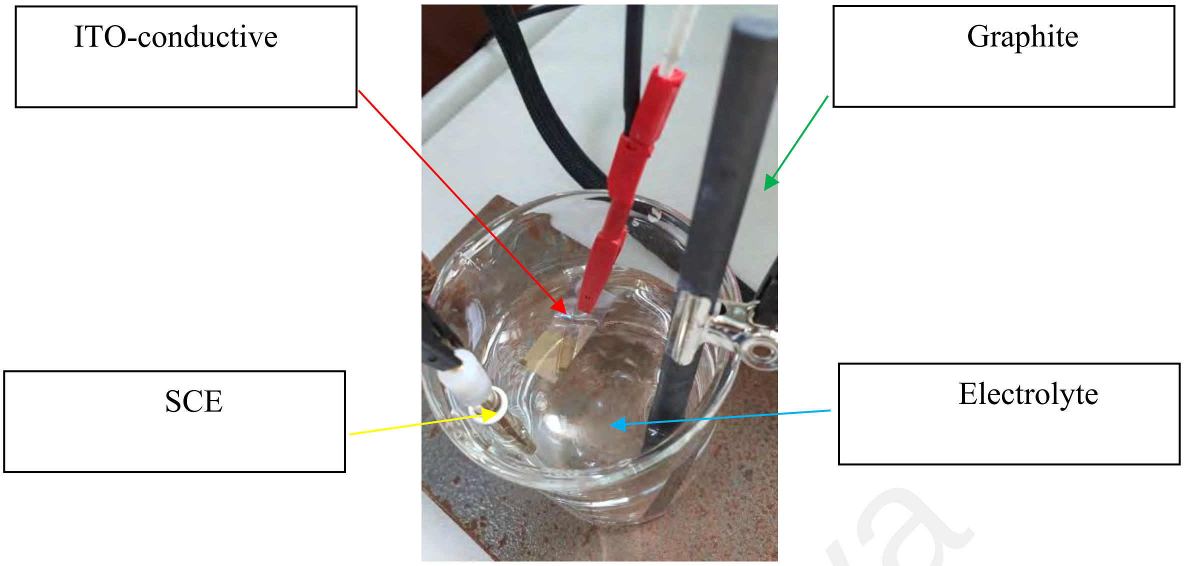

**Figure 3.9: Experiment setup for Electrolysis cell of TMDs thin film deposition**

As a precautionary measure, it is essential to precisely adjust the position and the spacing among these three electrodes to achieve optimal deposition. The working electrode and counter electrode are placed approximately 1 cm from each other with both surfaces facing each other maintained in parallel position. This arrangement ensures that the ions released are attracted and deposited in a precisely perpendicular manner to the surface of the substrate. The reference electrode (SCE) serves the purpose of measuring the potential of the working electrode. Therefore, it is positioned in very close to the working electrode to ensure that the precise potential at the surface is monitored and remains unaffected by the solution resistance (internal resistance of the cell).

For the deposition of molybdenum disulfide $MoS_2$ thin film, 0.5M of molybdic acid in 100ml ammoniacal solution with 0.5M sodium thiosulphate pentahydrate in 200ml distilled water is used as electrolyte ions precursors. The deposition of molybdenum disulfide $MoS_2$ thin film is carried out for 15 second at temperature of 40±1 ºC. After the completion of the deposition process, remove the thin film and allow it to dry by employing a spring clip, as illustrated in Figure 3.19 below.

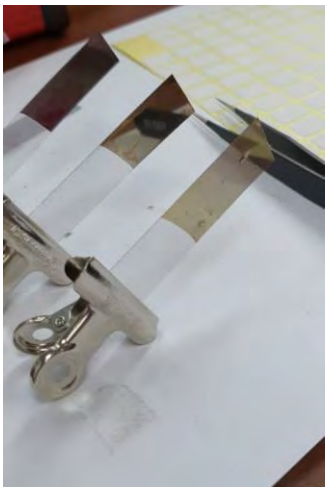

Figure 3.10: **Drying process using spring clip**

For the deposition of molybdenum diselenide $MoSe_2$ thin film, 0.5M of molybdic acid in 100ml ammoniacal solution with 0.5M selenium dioxide in 200ml distilled water is used as electrolyte ions precursors. The deposition of molybdenum diselenide $MoSe_2$ thin film is carried out in for 15 second at temperature of 40±1 ºC. Following the completion of the deposition process, extract the thin film and let it dry with the assistance of a spring clip, as depicted in Figure 3.19 above.

For the deposition of molybdenum ditelluride $MoTe_2$ thin film, 0.5M of molybdic acid in 100ml ammoniacal solution with 0.5M tellurium dioxide in 200ml hydrochloric acid is used as electrolyte ions precursors. The deposition of molybdenum ditelluride $MoTe_2$ thin film is carried out for 15 second at temperature of 40±1 ºC. Upon finishing the deposition process, extract the thin film and let it dry with the assistance of a spring clip, as depicted in Figure 3.19 above.

During the deposition of TMDs thin film, certain modifications were implemented in comparison to the deposition process utilized in the solar cell experiment. For solar cells application, the deposition time required ranges from a minimum of 10 minutes to a maximum of 30 minutes. This is essential to convert the solar photons energy into electron for efficient electricity generation. However, if the deposition approach employed in solar cells is applied in this research work, the resulting TMD layer becomes excessively thick which obstruct the penetration of the laser light. Therefore, when the laser is unable to penetrate, achieving Q-switch and mode-locked laser pulses becomes impossible. As a result, the deposition time is adjusted from minutes to seconds to overcome this challenge and ultimately enabling the attainment of an extremely thin layer of the TMD material. This modification allows light to propagate through and supporting the generation of the desired ultrashort laser pulse.

## 3.2 Characterization of Conductive Thin Film substrate

A comprehensive explanation of the thin film details has been extensively addressed in section 3.1.2 on substrate preparation. In this section, the FESEM and EDX analyses of the thin film will be discussed to provide information on the element composition. Therefore, based on this information, it is possible to identify the TMDs materials coated on the thin film by subtracting the substrate material initially. This thin film comprised of a plastic sheet coated with a thin layer of conductive material with thickness of 10nm. Being an electrically conductive film, this indium based coated conductive film has a surface resistivity of approximately 5 ohm/sqm. It has a thickness of only 0.125mm which can be easily cut into smaller sizes. Before the electrodeposition process, a protective layer of plastic cover is peeled off from the surface of the conductive film as shown in Figure 3.20.

**Figure 3.11: Clear surface of indium based coated conductive film substrate**

### 3.2.1 Field Emission Scanning Electron Microscopy (FESEM)

The surface morphology of this indium based coated conductive substrate thin films are shown in Figure 3.21 below.

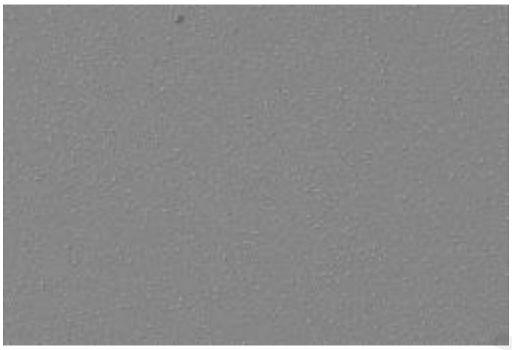

**Figure 3.12: FESEM of indium based coated conductive film substrate at 1000X magnification demonstrates an outstanding degree of consistency and uniformity**

Figure 3.21 illustrates the conductive thin film layer observed at magnifications of 1000 times. The surface morphology of this thin film exhibits an exceptional level of homogeneity and uniformity. Upon careful examination, it becomes apparent that the surface features are consistently distributed across the entire thin film which reveal an exceptional even topography. Each region of the surface appears to reflect the characteristics of its adjacent areas with a smooth and consistent pattern. The absence of noticeable irregularities or variations indicates a high degree of consistency, demonstrating that this thin film has been developed under a well-controlled and uniform manufacturing methodology. The homogeneous surface morphology not only highlights the precision of the fabrication process but also holds significant promise for applications where uniformity is crucial as demonstrated in the case of thin-film coatings.

### 3.2.2 Energy Dispersive X-Ray (EDX) Analysis

EDX is a technique used for elemental analysis and it is operated by capturing distinctive X-rays emitted by a sample when it is bombarded with high-energy electrons. Each element produces a unique set of X-ray energies and these X-ray energies are identified and quantified by the EDX system. Quantitative analysis of the thin film was conducted using the EDX technique in a nitrogen atmosphere to investigate the presence of indium and other conductive elements in the films' stoichiometry.

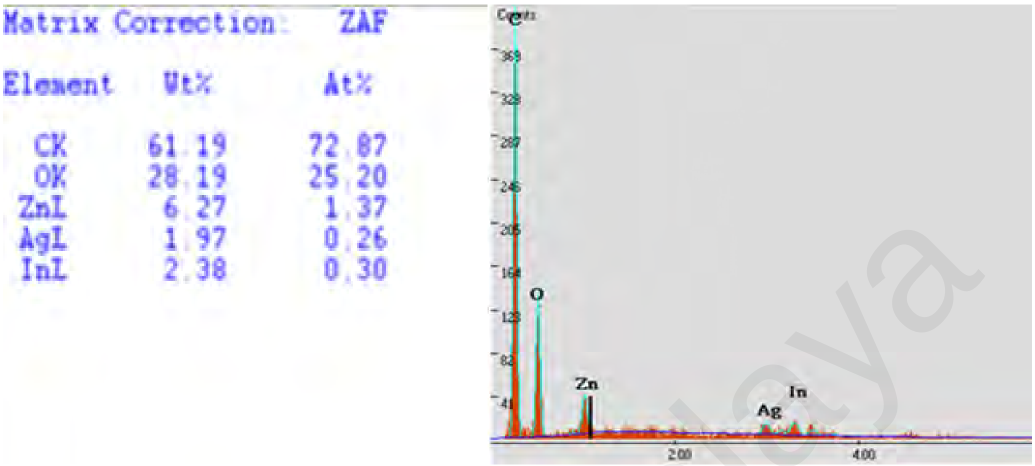

Matrix Correction ZAF

| Element | Wt% | At% |
|---|---|---|
| CK | 61.19 | 72.87 |
| OK | 28.19 | 25.20 |
| ZnL | 6.27 | 1.37 |
| AgL | 1.97 | 0.26 |
| InL | 2.38 | 0.30 |

Figure 3.13: The EDX of indium based coated conductive film substrate

The EDX results of this indium-based coated conductive substrate thin films are depicted in the above Figure 3.22. Upon analysis of the figure, it becomes apparent that the thin film contains not only indium (In) but also other elements such as silver (Ag) and zinc (Zn). This is acceptable as silver and zinc elements are additional conductive components incorporated into this thin film. The presence of silver and zinc elements into an indium-coated thin film is intended for specific functional purposes including enhanced conductivity and stability, corrosion resistance as well as improved adhesion and compatibility. Silver is a highly conductive metal, therefore, the incorporation of silver into the thin film can enhance the overall conductivity which lead to better electrical performance. Additional, silver is also corrosion-resistant which can enhance the stability and longevity of the thin film. On the other hand, zinc functions comparably to silver acting as both a good conductive metal and providing corrosion resistance. This significantly contributes to the durability of the film. Furthermore, silver and zinc can enhance the adhesion of the thin film to the substrate and improve compatibility between different layers and hence, promoting a more robust and reliable structure.

Apart from indium, silver and zinc, it is observed that the EDX analysis of this thin film reveals the presence of carbon (C) and oxygen (O) elements. The presence of carbon in this EDX analysis is associated with the thin film is made of plastic sheet. Carbon constitutes an essential element in various organic materials including plastics. Plastics are composed of long chains of carbon-based molecules with other additional elements depending on the specific type of plastic. During an EDX analysis of a plastic sheet, the spectrum may exhibit peaks that correspond to the elements within the material including carbon with the carbon signal in the EDX data reflecting the carbon content in the plastic sheet. On the other hand, despite oxygen (O) not contributing to the synthesis of the films, its peaks are consistently observable in the EDX analysis. This is due to the particular advantage of EDX in elemental analysis where it has the capability to detect low atomic number elements such as carbon and oxygen. This capability makes EDX valuable for analyzing materials that contain elements commonly found in the environment such as carbon and oxygen (Herguth & Nadeau, 2004). Furthermore, the presence of oxygen is observed in all the films as it is deemed unavoidable in the efforts of synthesizing transition metal chalcogenides thin films through chemical deposition (Lokhande et al., 2002; Srikanth et al., 2011). This is applicable to all the synthesized thin films in this research work.

## 3.3 Characterization of Electrodeposited Molybdenum Disulfide $MoS_2$ Thin Film

The characterization of electrodeposited molybdenum disulfide ($MoS_2$) thin films will be further explored in the following sub-section, covering techniques such as Field Emission Scanning Electron Microscopy (FESEM), Energy Dispersive X-Ray (EDX) spectroscopy, linear absorption, and modulation depth.

Molybdenum disulfide $MoS_2$ is a solid compound with a silvery-black appearance that resembles the mineral molybdenite and serves as the primary ore for molybdenum (Sebenik et al., 2000). Moreover, molybdenum disulfide $MoS_2$ share similarities with graphite in terms of appearance and feel. Both materials are layered structures with a slippery or lubricating quality. The colour of $MoS_2$ deposited on a thin film may change depending on factors such as thickness, purity and the specific deposition method used.

Typically, $MoS_2$ is known for its colour ranging from dark grey to black. While the thin film deposition process may influence the optical properties and appearance, the material often retains its characteristic dark colour. Moreover, the thickness of the film and its interaction with light can also impact its perceived colour. In the research work, the $MoS_2$ deposited on the conductive coated layer shows a dark grey colour while it appears gold on the reflective layer due to light interaction mentioned earlier.

### 3.3.1 Field Emission Scanning Electron Microscopy (FESEM) of Molybdenum Disulfide $MoS_2$ Thin Film

The electrodeposited molybdenum disulfide $MoS_2$ thin film is used for FESEM analysis. The sample was coated with a thin layer of gold to enhance conductivity and minimize charging effects during the imaging process. The FESEM analysis was performed using a state-of-the-art electron microscope Hitachi SU8700 fitted with 70mm$^2$ $Si_3$ $N_4$ SDD operated at 500V. The FESEM images provide a thorough representation of the surface morphology of $MoS_2$. The images taken at different magnifications showcased the well-defined layers and offered valuable insights into the surface roughness. Additionally, the observation of the distribution of $MoS_2$ compounds provides valuable information regarding the overall quality and uniformity of the sample.

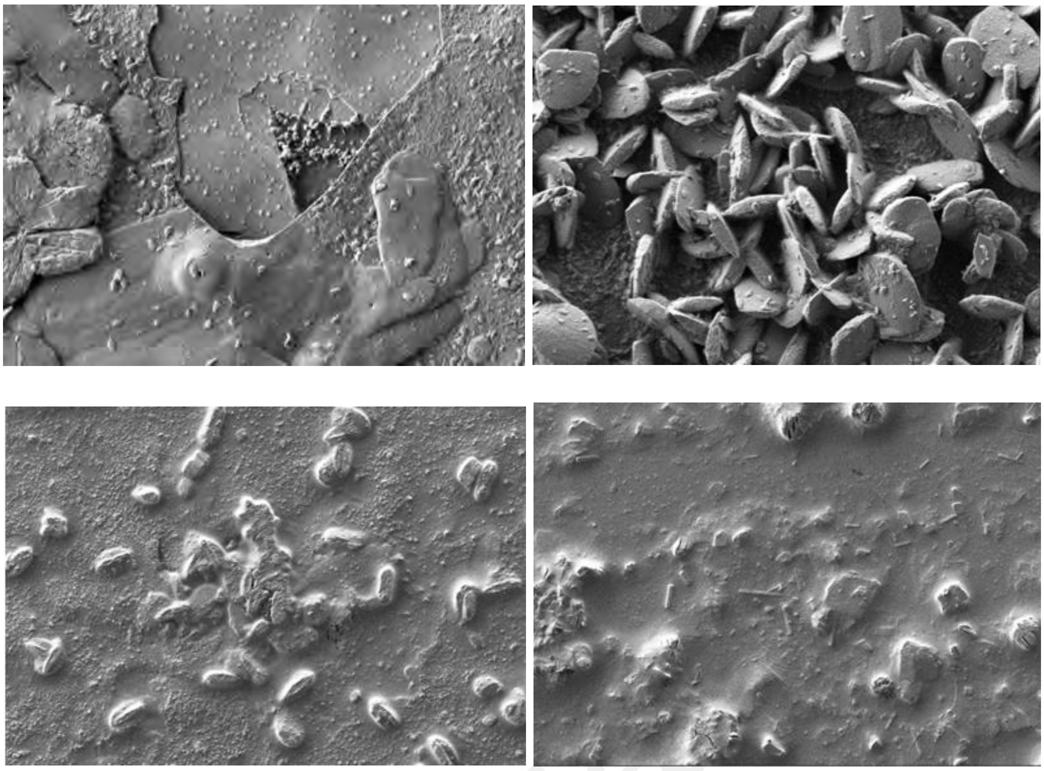

**Figure 3.14: FESEM of $MoS_2$ thin film at 1000X magnification**

The advanced high-resolution capabilities of FESEM enabled the detection of defects and imperfections in the structure of $MoS_2$. These defects may include vacancies, dislocations or other irregularities that might impact the material's performance. These specific defects within Mo or S in a suitable range can effectively decrease the bandgap (Martín-Palma et al., 2006; Wang et al., 2013). A reduced bandgap allows for the potential of broad-spectrum saturable absorption in defective $MoS_2$. The ability to visualize and characterize defects offers valuable insights for optimizing synthesis methods and enhancing material quality.

### 3.3.2 Energy Dispersive X-Ray (EDX) Analysis

Energy-Dispersive X-ray Spectroscopy (EDX) serves as a powerful analytical technique in the field of material science offering valuable insights into the elemental composition of diverse samples. This technique is frequently used in conjunction with field emission scanning electron microscopy FESEM utilizes the characteristic X-rays emitted by a sample under the impact of high-energy electrons. The resulting spectra not only disclose the present elements but also provide quantitative data on their concentrations that enables a detailed understanding of a material's composition. The core principle of EDX revolves around X-ray fluorescence. When a high-energy electron collides with an inner electron of an atom, it displaces the inner electron from its shell. The vacancy is filled by an electron from a higher energy level leading to the emission of X-ray photons. Each element exhibits individual X-rays with unique properties that enable their identification and quantification. The spectra obtained through EDX are based on the energy and intensity of these X-rays. Modern EDX systems are incorporated into FESEM platforms that merge the advantages of both techniques. The electron beam from the FESEM induces X-ray emissions after interacting with the sample. These X-rays are then captured by the EDX detector and the resulting spectrum is analyzed to identify the elements present. Advanced EDX systems provide enhanced spatial resolution which enables a detailed elemental analysis at the micro and nanoscale. EDX is widely used in the characterization of diverse materials including metals, ceramics, polymers and biological samples. The elemental data obtained assists in the identification of phases, evaluation of purity and understanding the composition of complex materials.

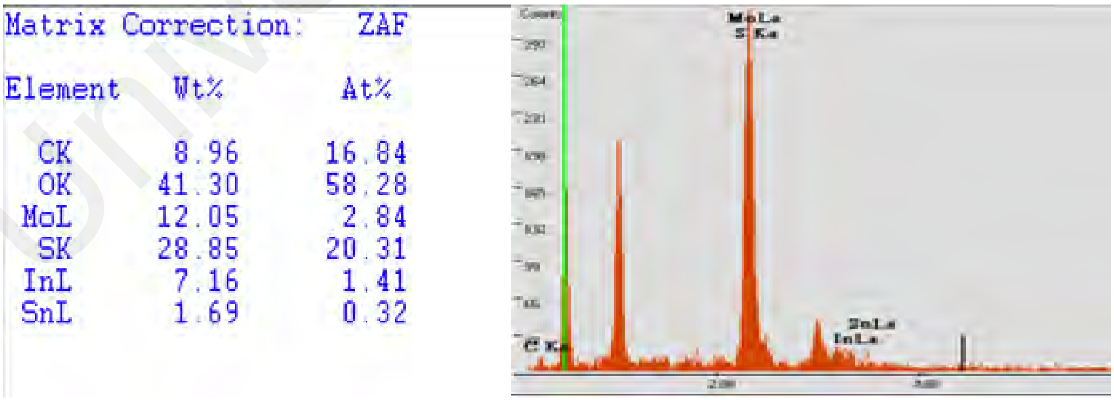

```
Matrix Correction:    ZAF

Element    Wt%        At%

  CK       8.96      16.84
  OK      41.30      58.28
 MoL      12.05       2.84
  SK      28.85      20.31
 InL       7.16       1.41
 SnL       1.69       0.32
```

Figure 3.15: EDX of $MoS_2$ thin film

$MoS_2$ sample is analyzed through energy-dispersive X-ray spectroscopy (EDX) coupled with FESEM to enable the mapping of elemental composition. This analysis confirmed the presence of molybdenum element at 12.05 wt% and sulfur element at

28.85wt% providing quantitative data regarding their distribution across the surface. Both Mo and S are tangibly appeared on the conductive film with the approximate ratio of 1:2. The elemental mapping results complemented the morphological observations contributing to a comprehensive understanding of the $MoS_2$ composition.

### 3.3.3 Linear Absorption

Another critical feature of saturable absorber involves the exploration of the linear optical response of the SA thin films. The linear saturable absorption property of $MoS_2$ was measured by linking the white light source (Ando, AQ4303B) to one end of the sandwiched $MoS_2$-SA with the other end connected to the Optical Spectrum Analyzer (OSA: Anritsu, MS97010C). The experimental setup for linear absorption of $MoS_2$-SA is illustrated in Figure 3.28. Linear saturable absorption of the $MoS_2$-SA was measured in the range of 1000 nm to 1600 nm as shown in Figure 3.29. At the wavelength of 1560 nm, the $MoS_2$-SA exhibited linear absorption of 2.5 dB.

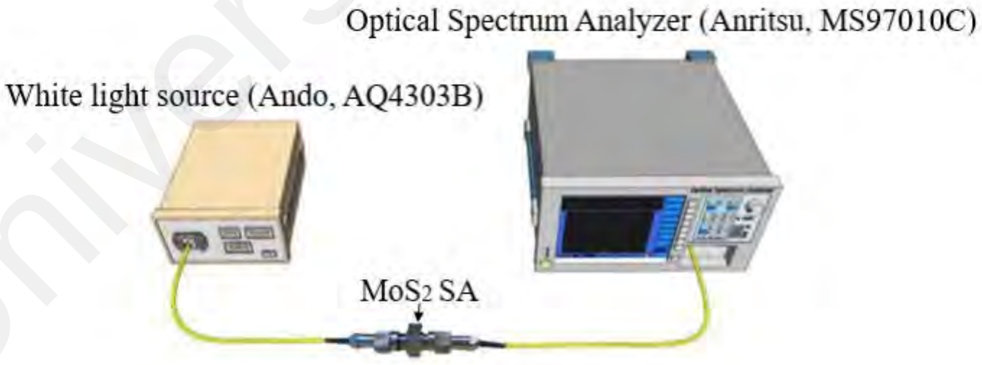

**Figure 3.16: The Experimental setup for linear absorption**

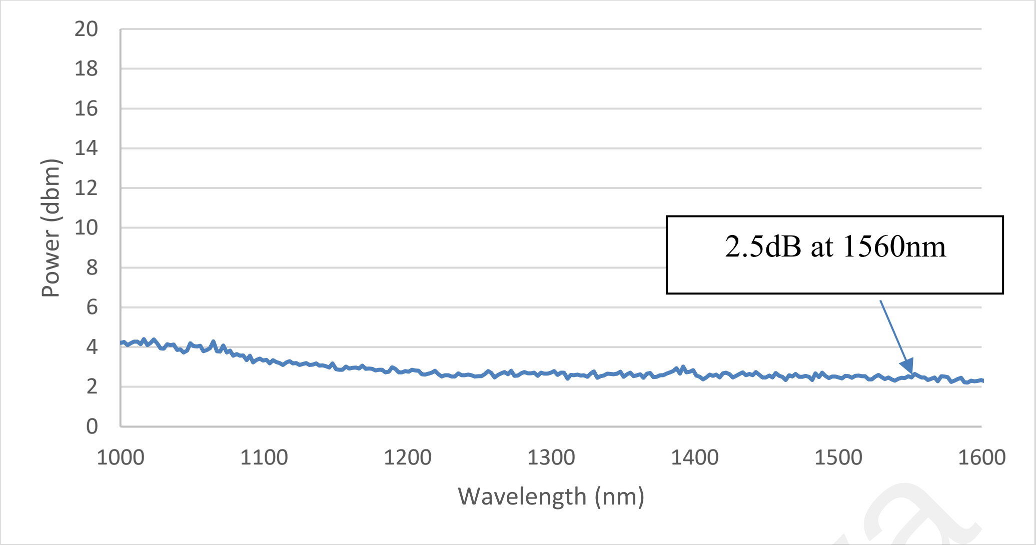

**Figure 3.17: Linear absorption spectrum from 1000 to 1600 nm of $MoS_2$-SA**

### 3.3.4 Modulation depth

Alternatively, the nonlinear optical profile of the $MoS_2$-SA was determined through experimental investigation using a balanced twin detector measurement technique to confirm the saturable absorption level. An in-house mode-locked fiber laser operating at a wavelength of 1567 nm with a 0.75 ps pulse width and a repetition rate of 21.75 MHz was used as the input pulsed laser source. The laser pulse was amplified through an erbium-doped fiber amplifier (EDFA) with the output power regulated by a variable optical attenuator (VOA). The output laser pulse from the variable optical attenuator was subsequently divided by a 50% coupler. One output is directed to the saturable absorber and measured by the optical power meter while the other is directly being measured by an optical power meter as illustrated in Figure 3.30.

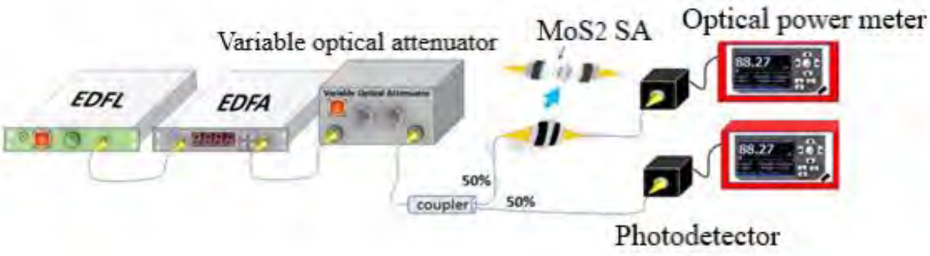

**Figure 3.18: The experimental setup for balanced twin-detector measurement**

By varying the input laser power through the balanced twin-detector measurement, the transmitted power is recorded as a function of incident intensity on the device. In order to obtain the result for saturation intensity, non-saturable absorption and modulation depth of the MoS2-SA, the experimental data for absorption are fitted according to a simple two-level SA model (Bao et al., 2009; Garmire, 2000; Zheng et al., 2012) in chapter 2 as equation 2.3 below:

$$\alpha(I) = \frac{\alpha_s}{1 + \frac{I}{I_{sat}}} + \alpha_{ns} \qquad (2.3)$$

where $\alpha(I)$ is the absorption coefficient, $\alpha_s$ is the saturable absorption coefficient, $I$ is the incident light intensity, and $I_{sat}$ is the saturation intensity, $\alpha_{ns}$ is the non-saturable absorption coefficient. Based on the equation 2.3, the saturation intensity of the $MoS_2$-SA was calculated as 0.3 MW/cm2. The saturable and non-saturable absorption values were identified at level of 3.4% and 62.7% respectively as illustrated in Figure 3.31. It is worth to mention that there is no optical damage on the thin film and the saturable absorber is reusable after the twin-detector measurement. Hence, this suggest that the $MoS_2$-SA thin film has a reasonably high optical damage threshold.

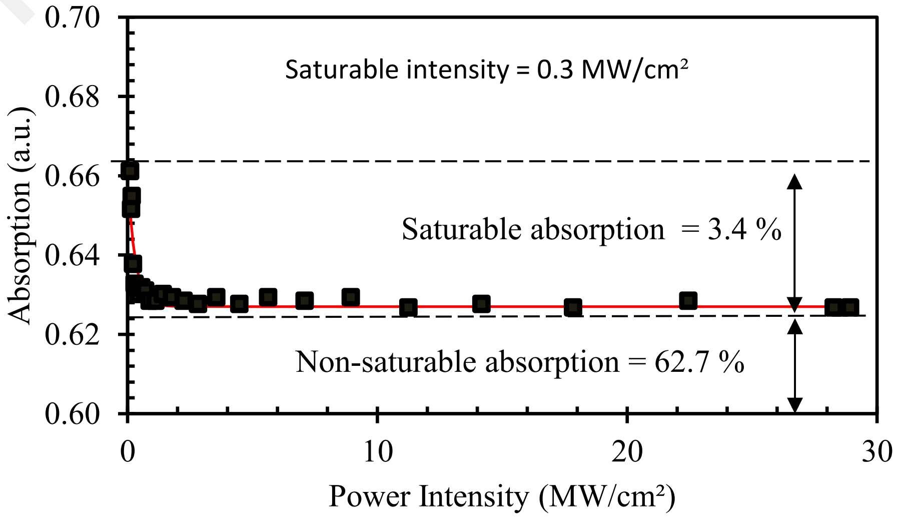

**Figure 3.19: Modulation depths of $MoS_2$ thin film**

### 3.4 Characterization of Electrodeposited Molybdenum Diselenide $MoSe_2$ Thin Film

Molybdenum diselenide $MoSe_2$ has emerged as a promising candidate in the exploration of two-dimensional (2D) materials paving the way for innovative applications in photonics in recent years. $MoSe_2$ stands out as an exceptional saturable absorber in the field of ultrafast photonics due to its unique electronic and optical properties. $MoSe_2$ is a member of the transition metal dichalcogenides (TMDs) family and this compound consists of layers of molybdenum atoms sandwiched between selenium atoms forming a unique hexagonal lattice structure as shown in Figure 3.32.

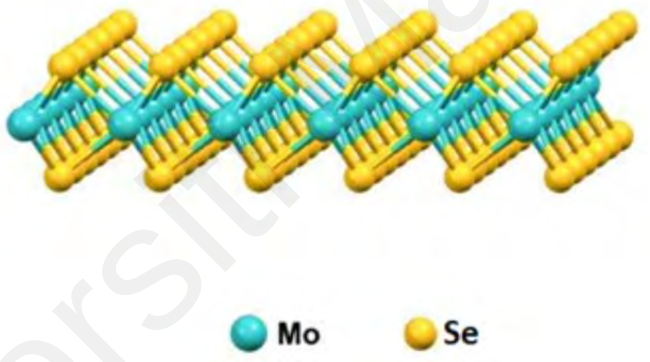

**Figure 3.20: Atomic structure of $MoSe_2$**

$MoSe_2$ shares a typical layered structure found in TMDs where weak van der Waals forces holding adjacent layers together. $MoSe_2$ exhibits excellent semiconducting properties with a moderate bandgap making it an ideal candidate for photonics applications. $MoSe_2$'s high carrier mobility and its ability to adjust its bandgap in response to external stimuli make it particularly attractive for ultrafast pulse generation. The unique optical properties of $MoSe_2$ especially its nonlinear saturable absorption behaviour which enable efficient modulation of light that allows selective absorption and passage of specific wavelengths that is essential for pulse generation in ultrafast lasers.

$MoSe_2$-based saturable absorbers find applications in various ultrafast photonics systems including material processing, telecommunications and medical applications.

Molybdenum diselenide $MoSe_2$ is a solid compound with a dark metallic grey appearance. The colour of deposited $MoSe_2$ on a thin film can vary based on factors including thickness and the type of deposition method employed. In this research work, the $MoSe_2$ thin film produced through electrodeposition technique exhibits a dark red colour. This is confirmed by the consistency observed in other selenide compounds which also exhibit a dark red colour (Hankare et al., 2003). The $MoS_2$ thin film produced in section 3.3 has dark grey to black colour which is different from $MoSe_2$. While the thin film deposition process may influence the optical properties and appearance, the material often retains its characteristic dark red colour due to selenium element. Furthermore, the thickness of the film and its interaction with light can also influence its apparent colour. Referring to Figure 3.33 above, the $MoSe_2$ deposited on the conductive coated layer shows a dark red colour while it appears dark grey on the reflective layer due to light interaction mentioned earlier.

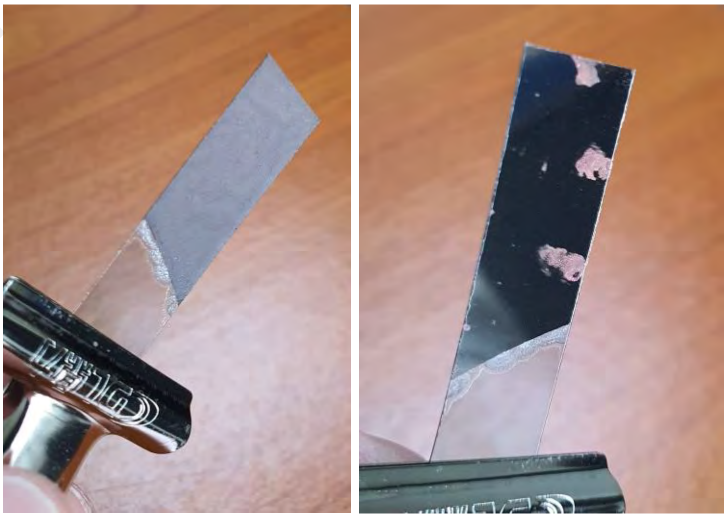

**Figure 3.21: Physical appearance of $MoSe_2$ thin film**

### 3.4.1 Field Emission Scanning Electron Microscopy (FESEM) of Molybdenum Diselenide MoSe$_2$ Thin Film

The thin film of electrodeposited molybdenum diselenide MoSe$_2$ is used for FESEM analysis. The sample was coated with a thin layer of gold to enhance conductivity and minimize charging effects during the imaging process. The FESEM analysis was performed using a state-of-the-art electron microscope Hitachi SU8700 fitted with 70mm$^2$ Si$_3$ N$_4$ SDD operated at 500V. The FESEM images provide a thorough representation of the surface morphology of MoSe$_2$. The images taken at different magnifications showcased the well-defined layers and offered valuable insights into the surface roughness. Additionally, the observation of the distribution of MoSe$_2$ compounds provides valuable information regarding the overall quality and uniformity of the sample.

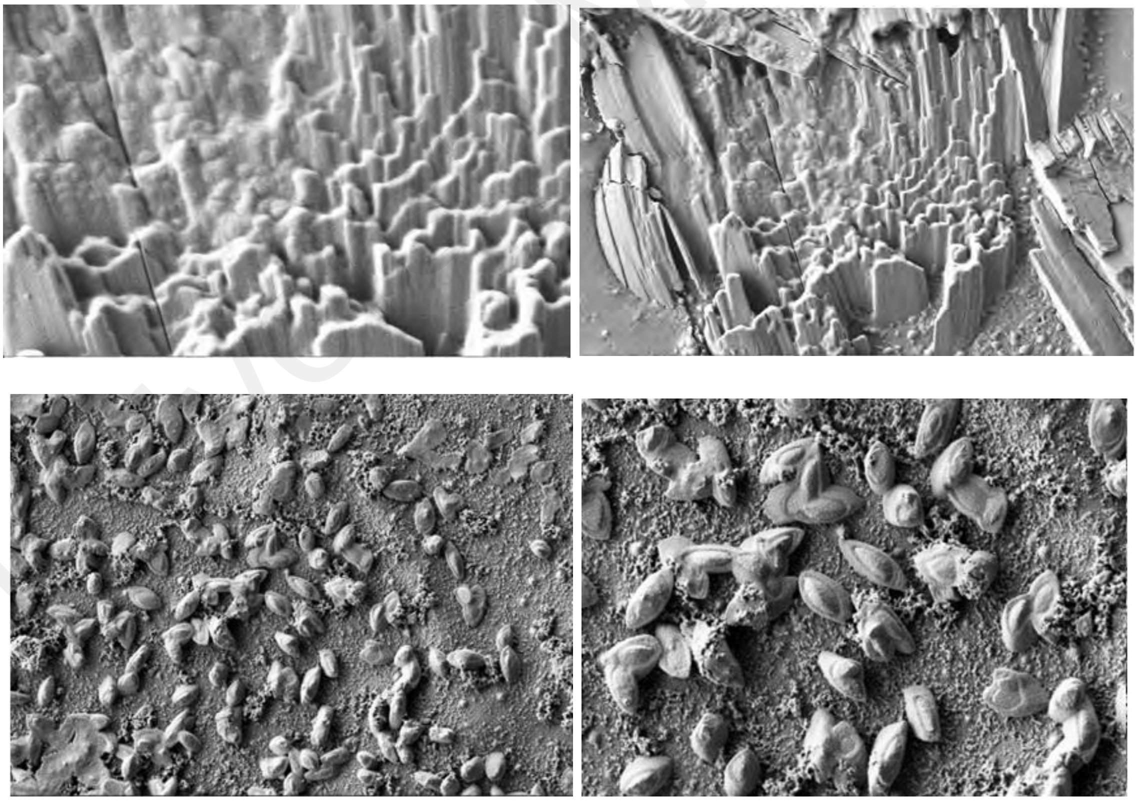

**Figure 3.22: FESEM of MoSe$_2$ thin film at 1000X magnification**

### 3.4.2 Energy Dispersive X-Ray (EDX) Analysis

$MoSe_2$ sample is analyzed through energy-dispersive X-ray spectroscopy (EDX) coupled with FESEM to enable the mapping of elemental composition. This analysis confirmed the presence of molybdenum element at 18.92 wt% and selenium element at 36.76 wt% providing quantitative data regarding their distribution across the surface. Both Mo and Se are visibly present on the conductive film in an approximate ratio of 1:2. The elemental mapping results complemented the morphological observations contributing to a comprehensive understanding of the $MoSe_2$ composition.

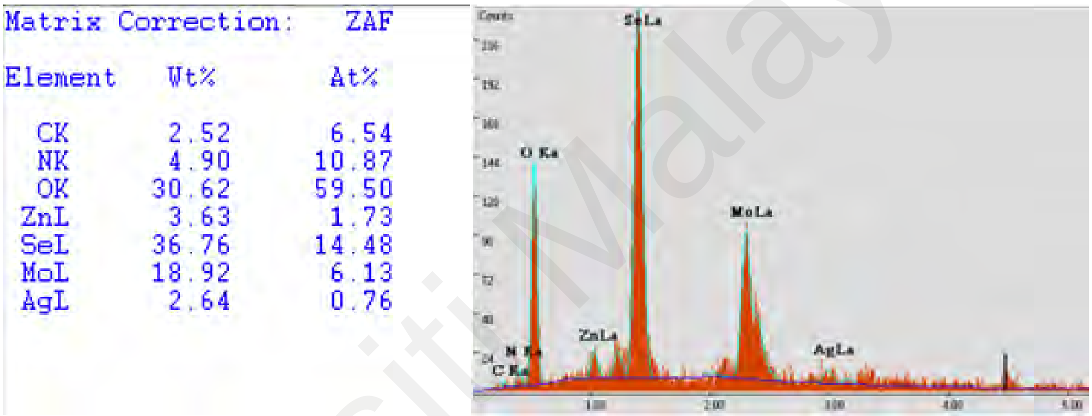

Matrix Correction: ZAF

| Element | Wt% | At% |
|---|---|---|
| CK | 2.52 | 6.54 |
| NK | 4.90 | 10.87 |
| OK | 30.62 | 59.50 |
| ZnL | 3.63 | 1.73 |
| SeL | 36.76 | 14.48 |
| MoL | 18.92 | 6.13 |
| AgL | 2.64 | 0.76 |

Figure 3.23: EDX of $MoSe_2$ thin film

### 3.4.3 Linear Absorption

Another critical feature of saturable absorber involves the exploration of the linear optical response of the SA thin films. The linear saturable absorption property of $MoSe_2$ was measured by linking the white light source (Ando, AQ4303B) to one end of the sandwiched $MoS_2$-SA with the other end connected to the Optical Spectrum Analyzer (OSA: Anritsu, MS97010C). The experimental setup for linear absorption of $MoSe_2$-SA is illustrated in Figure 3.28 in section 3.3.4. The only difference is the substitution of $MoS_2$ SA with $MoSe_2$ SA. Linear saturable absorption of the $MoSe_2$-SA was measured in the range of 1000 nm to 1600 nm as shown in Figure 3.36. At the wavelength of 1561 nm, the $MoSe_2$-SA exhibited linear absorption of 3.1 dB.

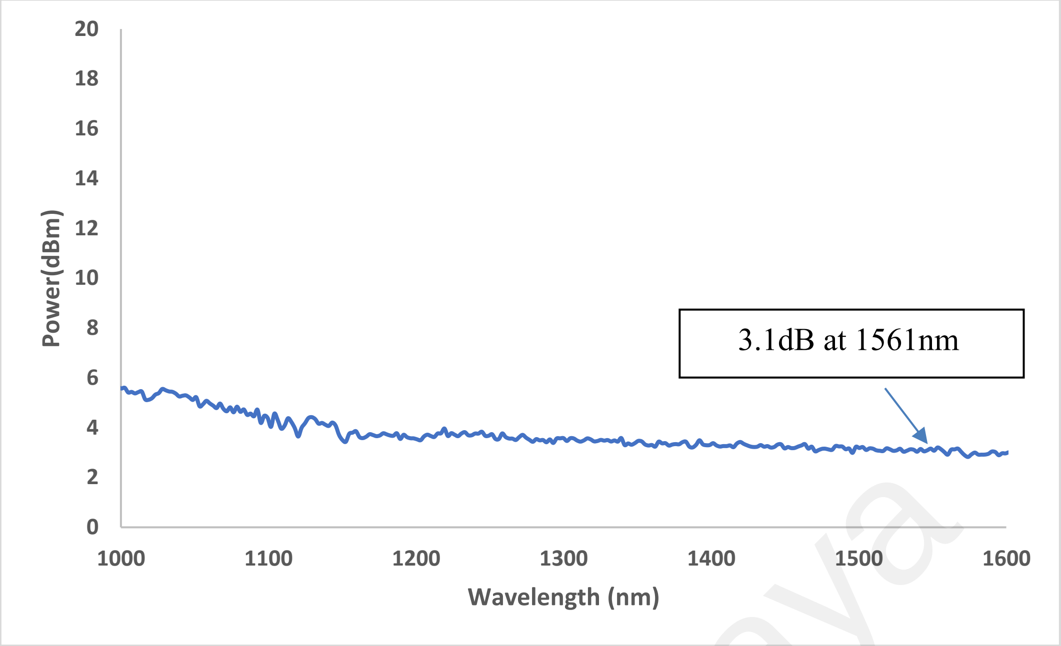

**Figure 3.24: Linear absorption spectrum from 1000 to 1600 nm of $MoSe_2$-SA**

### 3.4.4 Modulation depth

Alternatively, the nonlinear optical profile of the $MoSe_2$-SA was determined through experimental investigation using a balanced twin detector measurement technique to confirm the saturable absorption level. An in-house mode-locked fiber laser operating at a wavelength of 1567 nm with a 0.75 ps pulse width and a repetition rate of 21.73 MHz was used as the input pulsed laser source. The laser pulse was amplified through an erbium-doped fiber amplifier (EDFA) with the output power regulated by a variable optical attenuator (VOA). The output laser pulse from the variable optical attenuator was subsequently divided by a 50% coupler. One output is directed to the saturable absorber and measured by the optical power meter while the other is directly being measured by an optical power meter as illustrated in Figure 3.30 in section 3.3.5. The only difference is the substitution of $MoS_2$ SA with $MoSe_2$ SA. By varying the input laser power through the balanced twin-detector measurement, the transmitted power is recorded as a function of incident intensity on the device. Based on the equation 2.3, the saturation intensity of the $MoS_2$-SA was calculated as 0.25 MW/cm2. The saturable and non-saturable absorption values were identified at level of 5.0% and 19.1% respectively as illustrated in Figure 3.37. It is worth to mention that there is no optical damage on the thin film and the saturable absorber is reusable after the twin-detector measurement. Hence, this suggest that the $MoSe_2$-SA thin film has a reasonably high optical damage threshold.

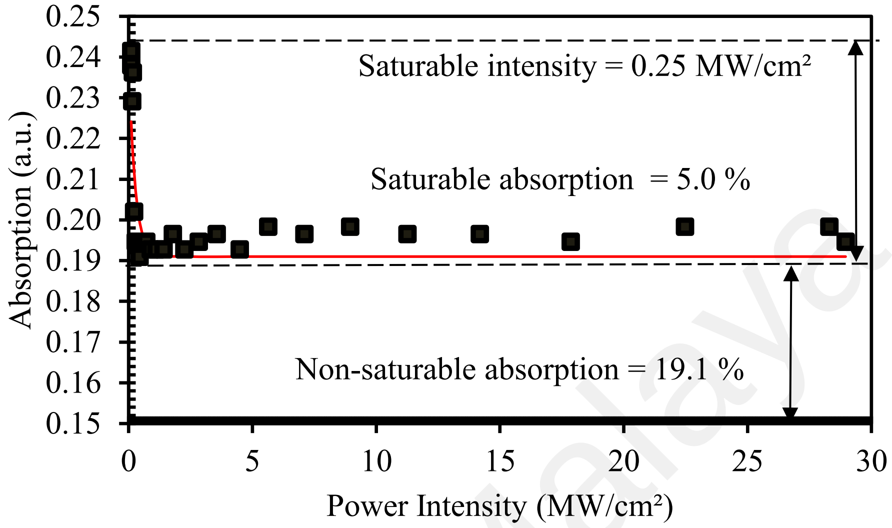

**Figure 3.25: Modulation depths of $MoSe_2$ thin film**

## 3.5 Characterization of Electrodeposited Molybdenum Ditelluride $MoTe_2$ Thin Film

The characterization of electrodeposited molybdenum ditelluride $MoTe_2$ thin films will be further explored in the following sub-section, covering techniques such as Field Emission Scanning Electron Microscopy (FESEM), Energy Dispersive X-Ray (EDX) spectroscopy, linear absorption, and modulation depth.

Molybdenum ditelluride $MoTe_2$ is a solid compound with a dark gray or black appearance that resembles the mineral molybdenite and serves as the primary ore for molybdenum (Sebenik et al., 2000). Moreover, molybdenum ditelluride $MoTe_2$ share some similarities with graphite in terms of appearance and feel. Both materials are part of the layered materials family and exhibit a lamellar structure. Both molybdenum ditelluride and graphite appear as dark gray or black solids and have a smooth or lubricious texture owing to their layered composition. The colour of $MoTe_2$ deposited on a thin film may change depending on factors such as thickness, purity and the specific deposition method used. While the thin film deposition process may influence the optical properties and appearance, the material often retains its characteristic dark colour. Moreover, the thickness of the film and its interaction with light can also impact its perceived colour. Referring to Figure 3.39 above, the $MoTe_2$ deposited on the conductive coated layer shows a dark colour while it appears silver on the reflective layer due to light interaction mentioned earlier.

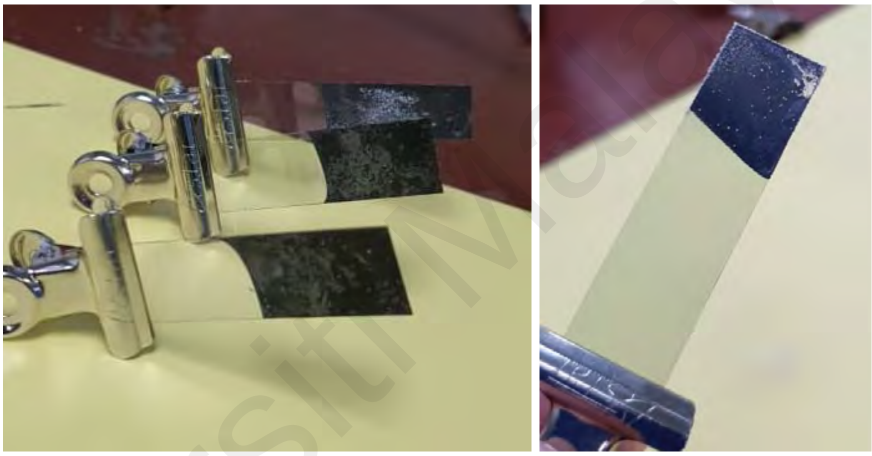

**Figure 3.26: Physical appearance of $MoTe_2$ thin film**

### 3.5.1 Field Emission Scanning Electron Microscopy (FESEM) of Molybdenum Ditelluride $MoTe_2$ Thin Film

The electrodeposited molybdenum ditelluride $MoTe_2$ thin films is used for FESEM analysis. The sample was coated with a thin layer of gold to enhance conductivity and minimize charging effects during the imaging process. The FESEM analysis was performed using a state-of-the-art electron microscope Hitachi SU8700 fitted with 70mm$^2$ $Si_3 N_4$ SDD operated at 500V. The FESEM images provide a thorough representation of the surface morphology of $MoTe_2$. The images taken at different magnifications showcased the well-defined layers and offered valuable insights into the surface roughness. Additionally, the observation of the distribution of $MoTe_2$ compounds provides valuable information regarding the overall quality and uniformity of the sample. The ability to visualize and characterize defects offers valuable insights for optimizing synthesis methods and enhancing material quality.

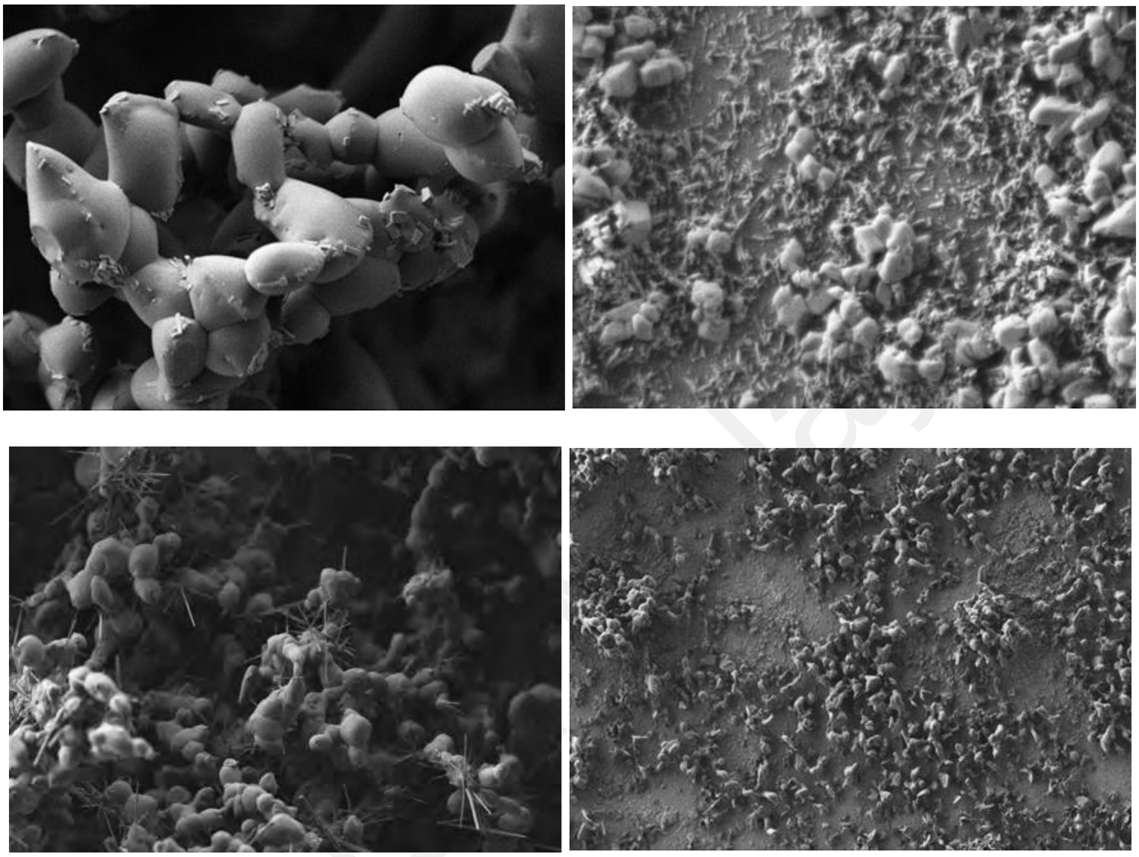

Figure 3.27: FESEM of $MoTe_2$ thin film at 1000X magnification

### 3.5.2 Energy Dispersive X-Ray (EDX) Analysis

$MoTe_2$ sample is analyzed through energy-dispersive X-ray spectroscopy (EDX) coupled with FESEM to enable the mapping of elemental composition. This analysis confirmed the presence of molybdenum element at 14.63 wt% and tellurium element at 36.61 wt% providing quantitative data regarding their distribution across the surface. The high concentration of chloride detected in the Energy Dispersive X-ray (EDX) analysis is attributed to the dissolution of tellurium in hydrochloric acid. Upon drying, the residual chloride is left on the surface of the thin film. The elemental mapping results complemented the morphological observations contributing to a comprehensive understanding of the $MoTe_2$ composition.

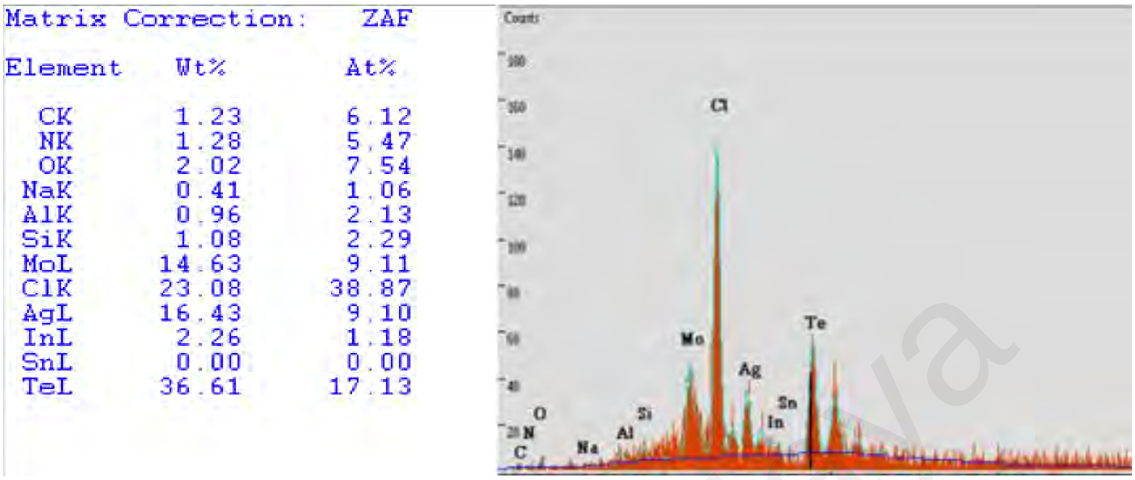
Matrix Correction: ZAF

| Element | Wt% | At% |
|---|---|---|
| CK | 1.23 | 6.12 |
| NK | 1.28 | 5.47 |
| OK | 2.02 | 7.54 |
| NaK | 0.41 | 1.06 |
| AlK | 0.96 | 2.13 |
| SiK | 1.08 | 2.29 |
| MoL | 14.63 | 9.11 |
| ClK | 23.08 | 38.87 |
| AgL | 16.43 | 9.10 |
| InL | 2.26 | 1.18 |
| SnL | 0.00 | 0.00 |
| TeL | 36.61 | 17.13 |

**Figure 3.28: EDX of $MoTe_2$ thin film**

### 3.5.3 Linear Absorption

Another critical feature of saturable absorber involves the exploration of the linear optical response of the SA thin films. The linear saturable absorption property of $MoTe_2$ was measured by linking the white light source (Ando, AQ4303B) to one end of the sandwiched $MoTe_2$-SA with the other end connected to the Optical Spectrum Analyzer (OSA: Anritsu, MS97010C). The experimental setup for linear absorption of $MoTe_2$-SA is illustrated in Figure 3.28 in section 3.3.4. The only difference is the substitution of $MoS_2$ SA with $MoTe_2$ SA. Linear saturable absorption of the $MoTe_2$-SA was measured in the range of 1000 nm to 1600 nm as shown in Figure 3.42. At the wavelength of 1558 nm, the $MoTe_2$-SA exhibited linear absorption of 4.54 dB.

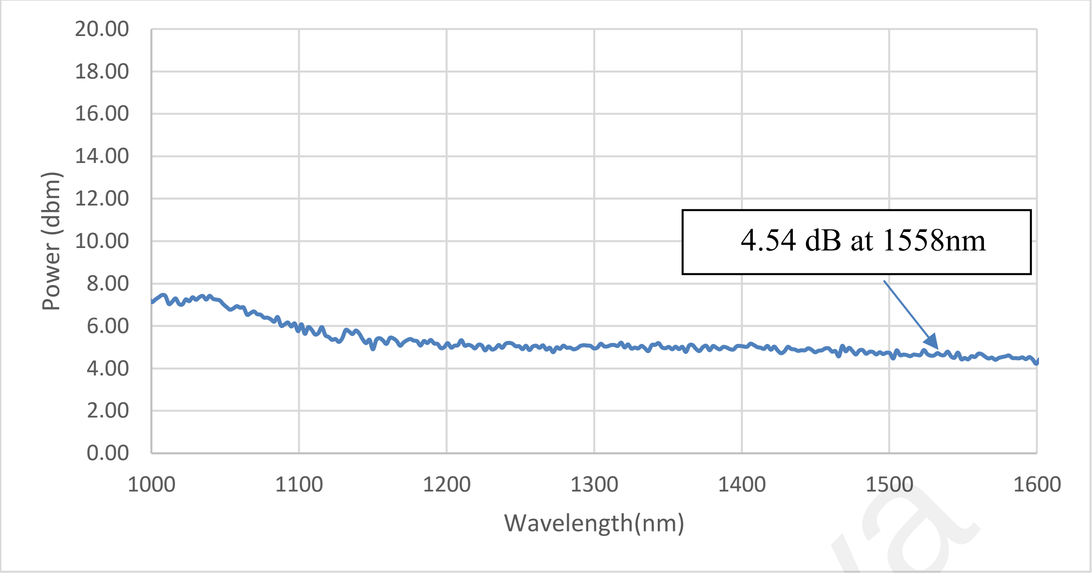

**Figure 3.29: Linear absorption spectrum from 1000 to 1600 nm of $MoTe_2$-SA**

### 3.5.4 Modulation depth

Alternatively, the nonlinear optical profile of the $MoTe_2$-SA was determined through experimental investigation using a balanced twin detector measurement technique to confirm the saturable absorption level. An in-house mode-locked fiber laser operating at a wavelength of 1531 nm with a 1.34 ps pulse width and a repetition rate of 0.9681 MHz was used as the input pulsed laser source. The laser pulse was amplified through an erbium-doped fiber amplifier (EDFA) with the output power regulated by a variable optical attenuator (VOA). The output laser pulse from the variable optical attenuator was subsequently divided by a 50% coupler. One output is directed to the saturable absorber and measured by the optical power meter while the other is directly being measured by an optical power meter as illustrated in Figure 3.30 in section 3.3.5.

By varying the input laser power through the balanced twin-detector measurement, the transmitted power is recorded as a function of incident intensity on the device. Based on the equation 2.3, the saturation intensity of the $MoTe_2$-SA was calculated as 6 MW/cm2. The saturable and non-saturable absorption values were identified at level of 1.7 % and 64.3 % respectively as illustrated in Figure 3.43**.** It is worth to mention that there is no optical damage on the thin film and the saturable absorber is reusable after the twin-detector measurement. Hence, this suggest that the $MoTe_2$-SA thin film has a reasonably high optical damage threshold.

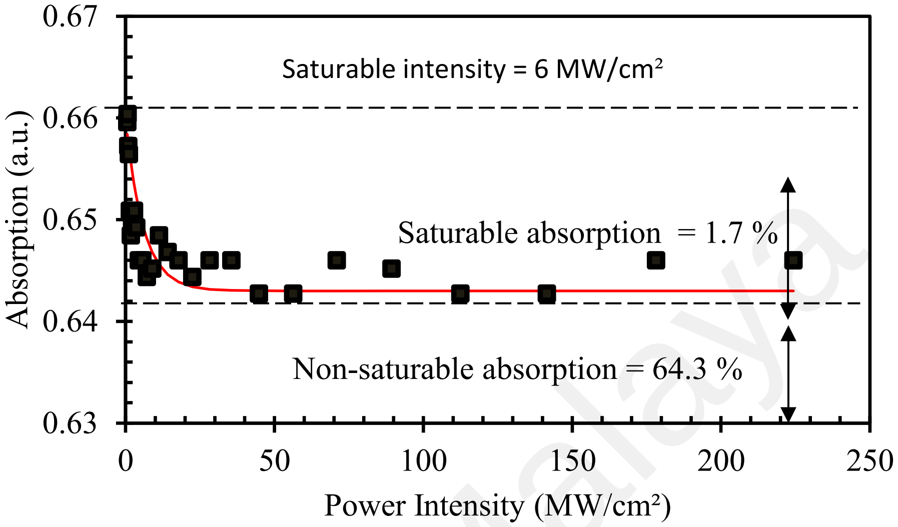

**Figure 3.30: Modulation depths of $MoTe_2$ thin film**

## 3.6 Summary

In Chapter 3, we addressed the fabrication of thin films of $MoS_2$, $MoSe_2$ and $MoTe_2$ using the electro-deposition method for use as saturable absorbers. We also discussed the material utilized in the fabrication process along with an examination of electrolyte preparation. Last but not least, we conducted characterizations of the fabricated thin films of $MoS_2$, $MoSe_2$, and $MoTe_2$ using FESEM, EDX, linear absorption, and modulation depth.

# CHAPTER 4: Q-SWITCHING PULSE GENERATION OF FABRICATED SATURABLE ABSORBER

## 4.1 Experimental setup for Q-switched fiber laser

Figure 4.1 shows the experimental setup used to generate passive Q-switched fiber lasers. The fiber laser ring cavity was assembled using a wavelength division multiplexer (WDM), an erbium-doped fiber (EDF), a polarization-independent isolator (PI-ISO), a polarization controller, output couplers and single-mode fiber (SMF). A gain medium was deployed using a 2-meter-long erbium-doped fiber (EDF) with specific parameters including a numerical aperture of 0.16, a core diameter of 4 μm, a group velocity dispersion (GVD) of 27.6 ps$^2$/km and a peak absorption of 23 dB/m. Subsequently, the 980 nm laser diode power-pumps the Erbium-doped fiber (EDF) gain medium through a 980/1550 wavelength division multiplexer (WDM). A polarization controller in the cavity is used to adjust the polarization state of light circulation that is favorable for pulse optimization. Following that, the laser is directed into a polarization-independent optical isolator (PI-ISO). The purpose of employing this optical isolator is to prevent back reflections of light into the laser source and to maintain the unidirectional propagation of the laser beam within the cavity. After the polarization-independent optical isolator (PI-ISO), the fabricated TMDs saturable absorber SA is incorporated into the laser cavity to modulate intracavity loss and consequently transforming the continuous wave (CW) laser into Q-switched pulsed lasers. The saturable absorber (SA) is placed between two fiber connectors through a fiber adaptor. The saturable absorber (SA) is securely positioned with the assistance of index matching gel to ensure its adhesion to the fiber ferrule. Following that, the laser is directed into the coupler which divides the output laser for performance investigations. Two different output couplers (OC) with coupling ratios of 50:50 and 95:5 were employed to examine the quality of Q-switched formation. The 95:5

coupler is utilized to enable more pump power to be returned to the cavity through which 95% laser light is circulated back into the cavity through the 1550 nm port of the WDM.

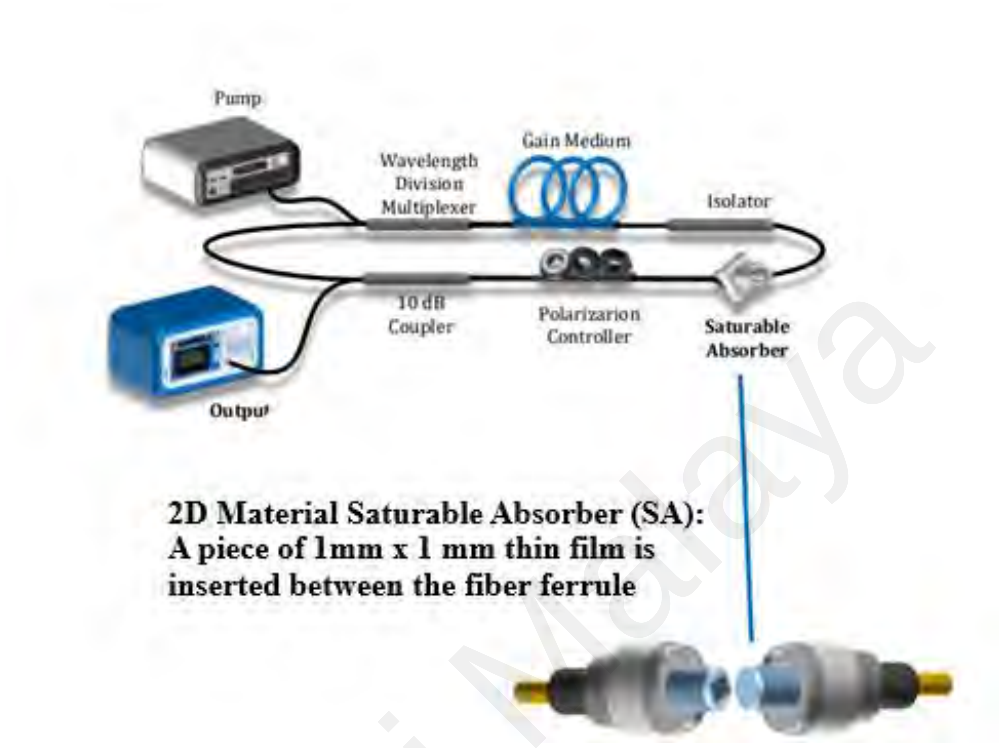

**Figure 4.1: Experiment setup for producing Q-switched fiber lasers (Jeon, 2021)**

To observe the laser performance on the 5% output coupler, the 50:50 coupler is introduced to concurrently split the output laser for real-time data measurements using two different measuring devices. The overall length of the cavity used for Q-switched operation is approximately 6 meters including all standard single-mode fiber (SMF-28). The performance of the Q-switched pulsed laser was measured using an optical spectrum analyzer OSA (Anritsu, MS97010C), a digital oscilloscope (OSC) with 3GHz bandwidth (Gwinstek, GSP-9300B), a radio frequency spectrum analyzer (RFSA) (Anritsu, MS2803A), an InGaAs photodetector (Thorlabs: DET10D/M) and optical power meter (OPM) (Thorlabs, PM100D). The combination of these devices is utilized to collect the required data.

## 4.2 Q-switching Pulse Generation at 1.55-micron region for Molybdenum Disulfide $MoS_2$ Saturable Absorber

The molybdenum disulfide saturable absorber $MoS_2$-SA used in this experiment was prepared through the electro-deposition method as described in section 3.1.4.2 while the experiment setup is presented in section 4.1. The observation of the continuous-wave (CW) laser operation occurs at a pump power of 10 mW and at the wavelength of 1561.9 nm. The Q-switch pulses emerge when reaching the threshold pump power of 51.67mW and the pump power is gradually increases up to 105.27mW. A stable self-starting Q-switched pulse is observed in this pump power range. As the pump power further increases beyond 130mW, the Q-switch pulse train becomes unstable and vanishes. On the other hand, the absence of Q-switching operation is observed when the $MoS_2$-SA is removed from the cavity thereby confirming the role of $MoS_2$-SA as a Q-switcher.

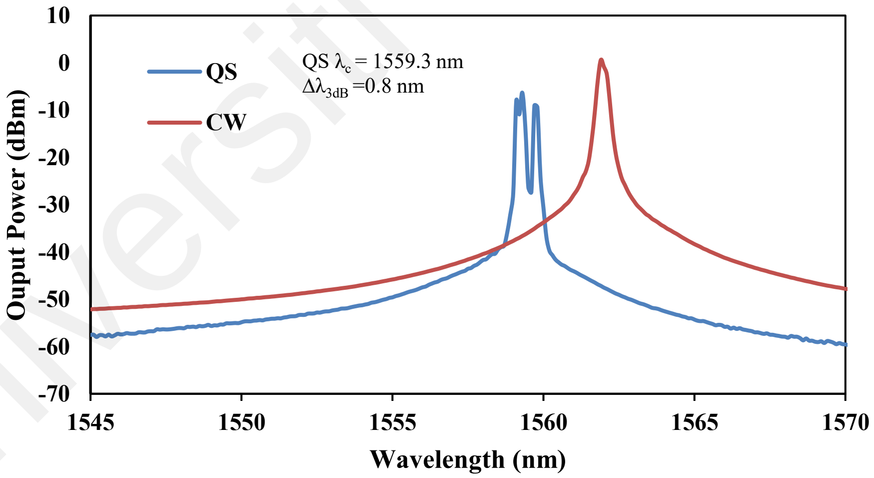

**Figure 4.2: Output spectrum of continuous wave (CW) and Q-switched (QS) pulse at threshold pump power of 105.27 mW.**

Figure 4.2 above illustrates the optical spectrum wavelength of Q-switched and continuous-wave operation which were obtained with and without SA at the maximum pump power of 105.27 mW. The peak laser wavelength was blue-shifted from 1561.9 nm to 1559.3 nm after the $MoS_2$-SA was incorporated into the cavity. It is observed that the optical spectrum slightly broadens during Q-switching operation compared to continuous-wave (CW) operation. The Q-switched laser exhibits a 3 dB spectral bandwidth of 0.8 nm which is broader than the 0.2 nm bandwidth observed in the continuous-wave (CW) laser. The shift towards shorter wavelengths is induced by the loss increment within the cavity. Consequently, lasing occurs at lower wavelengths to achieve higher amplification gain and to compensate for the additional losses.

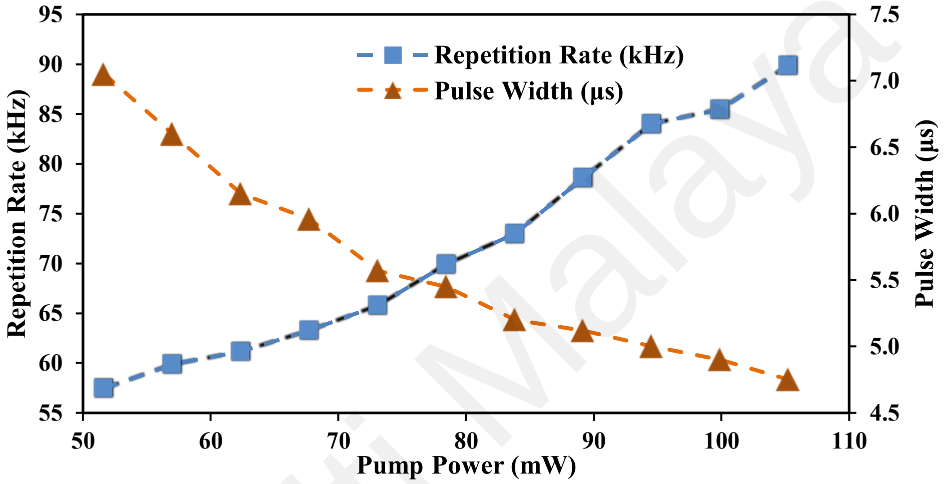

**Figure 4.3: Repetition rate and pulse width of Q-switched EDFL within 51.67mW – 105.27mW**

Figure 4.3 shows the repetition rate and pulse width against pump power. The pulse repetition rate increased almost linearly against the pump power whereas the pulse width decreases almost linearly against the pump power. In this scenario, the pulse repetition rate of the Q-switched fiber laser increases from 57.47kHz to 89.89kHz through varying the pump power from 51.67mW to 105.27mW whereas the pulse width reduces from 7.05 µs to 4.75 µs. By increasing the pump power within the laser cavity, it accelerates the gain population excitation process which ultimately leads to the achievement of the saturation state. Hence, a higher pulse repetition rate with narrower pulse width is achieved. The trend of increasing pulse repetition rate with increased pump power while decreasing pulse width aligns with the principles of passive Q-switching theory. The pulse train becomes unstable and vanishes as the pump power increases beyond 130 mW which potentially due to the limitation of MoS2 SA recovery time.

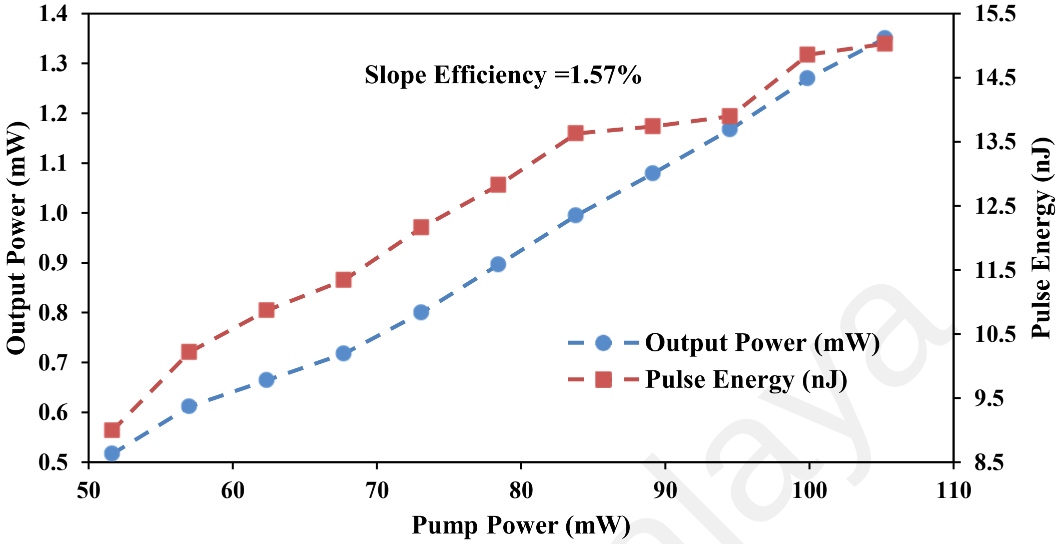

**Figure 4.4: Output power and pulse energy of Q-switched EDFL within 51.67mW – 105.27mW**

Figure 4.4 illustrates the correlation between the average output power and pulse energy of the Q-switched fiber laser in relation to pump power. The output power rises from 0.517mW to 1.351mW when the pump power increases from 51.67mW to 105.27mW. The slope efficiency of this Q-switched fiber laser is 1.57% calculated from the gradient of the output power with respect to pump power. Additionally, the pulse energy increased from 8.99 nJ to 15.03 nJ and started to reach saturation state at pump power of 130mW. This indicated that the $MoS_2$ saturable absorber has reached the damage threshold of Q-switching operation. When the pump power exceeds 130 mW, MoS2 is unable to fully recover leading to its inability to perform saturable absorption and become transparent within the cavity.

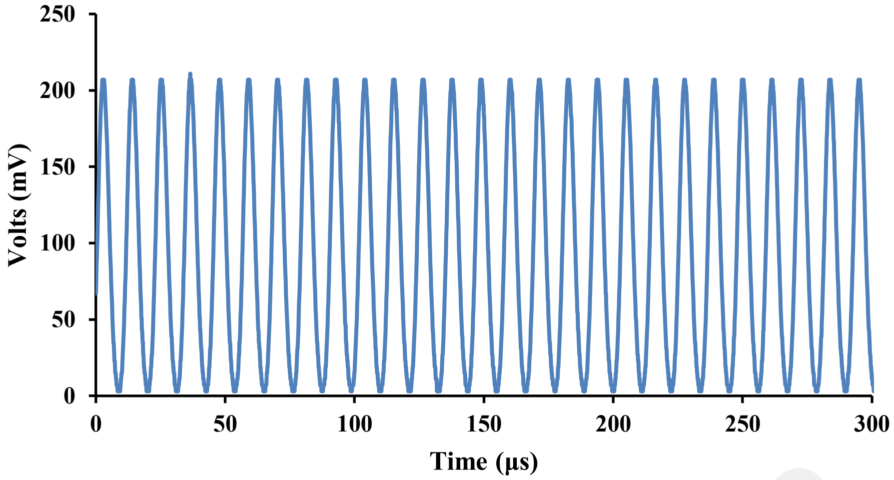

Figure 4.5: Oscilloscope pulse train at pump power of 105.27 mW

Figure 4.5 illustrates the oscilloscope trace of Q-switched pulses at pump power of 105.27 mW. At this pump power, the pulse duration is measured at 4.75 µs corresponding to a frequency of 89.89 kHz. The oscilloscope trace shows that the Q-switching operation is highly consistent throughout the observed time span. To assess the stability of the pulse, an RF spectrum is obtained for evaluation as shown in Figure 4.6. The RF spectrum of the Q-switched pulse demonstrates remarkable stability featuring a signal-to-noise ratio (SNR) of approximately 62.28 dB at the fundamental frequency of 89.89 kHz.

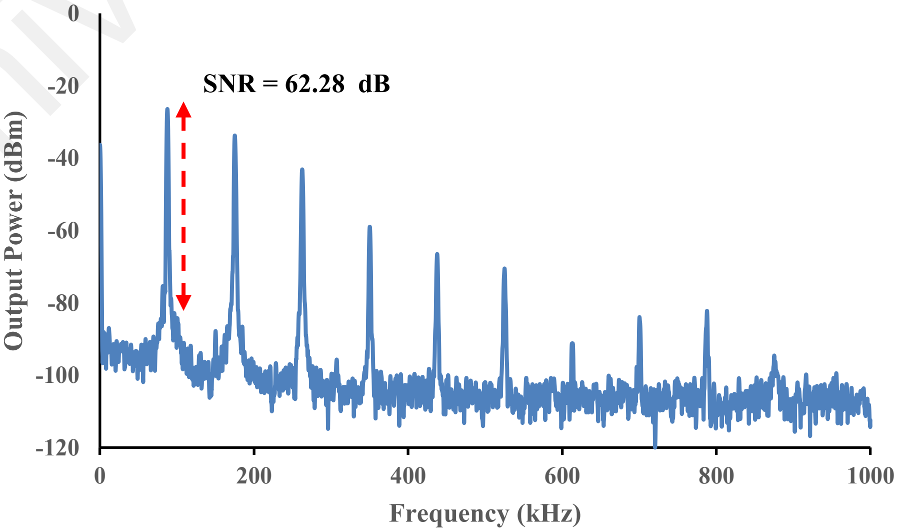

Figure 4.6: RF spectrum at 89.89 kHz

Ultimately, the output spectrum was examined over time to investigate the long-term stability of the Q-switched laser as depicted in Figure 4.7. The laser pulse was recorded at intervals of 30 minutes covering a total duration of 210 minutes. All the pulses operated around the wavelength of 1559.3nm with optical power intensity fluctuating about -8dBm. All samples closely resembled each other thereby confirming the stability of the pulsed laser. Furthermore, this demonstrates that the proposed $MoS_2$ saturable absorber can operate for an extended duration without experiencing any pulse disturbance.

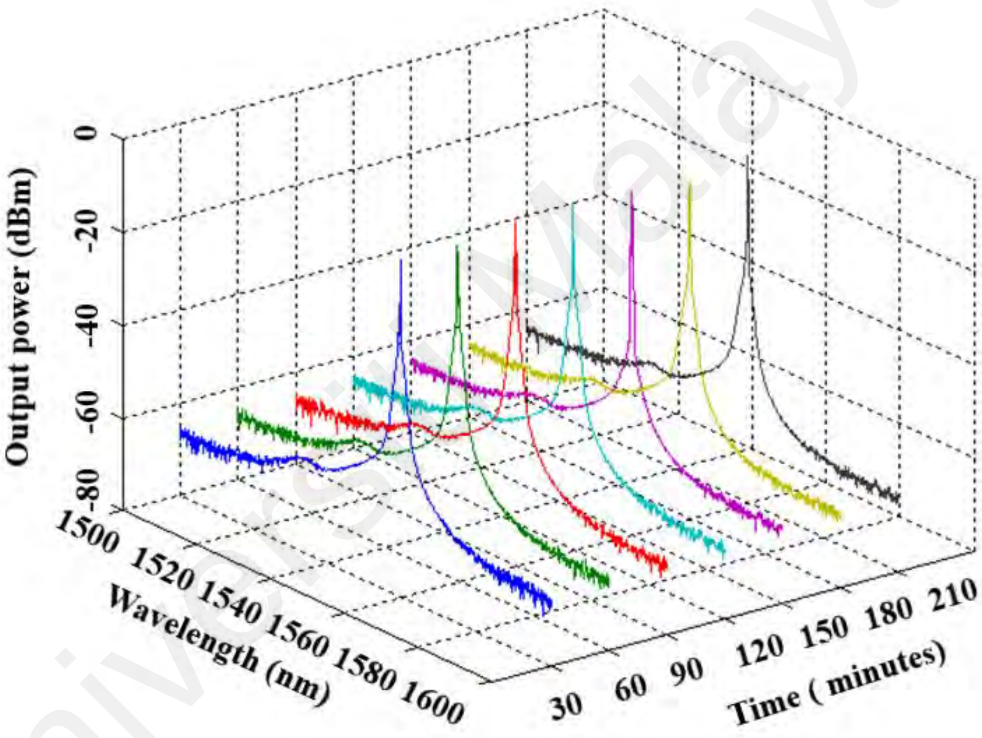

Figure 4.7: Sustained performance of the Q-switched fiber laser over a duration of 210 minutes with intervals of 30 minutes

## 4.3 Q-switching Pulse Generation at 1.55-micron region for Molybdenum Diselenide $MoSe_2$ Saturable Absorber

The molybdenum diselenide saturable absorber $MoSe_2$-SA used in this experiment was prepared through the electro-deposition method as described in section 3.1.4.2 while the experiment setup is presented in section 4.1. The observation of the continuous-wave (CW) laser operation occurs at a pump power of 20 mW and at the wavelength of 1563 nm. The Q-switch pulses emerge when reaching the threshold pump power of 76.75 mW and the pump power is gradually increases up to 108.05 mW. A stable self-starting Q-switched pulse is observed in this pump power range. As the pump power further increases beyond 120mW, the Q-switch pulse train becomes unstable and vanishes. On the other hand, the absence of Q-switching operation is observed when the $MoSe_2$-SA is removed from the cavity thereby confirming the role of $MoSe_2$-SA as a Q-switcher.

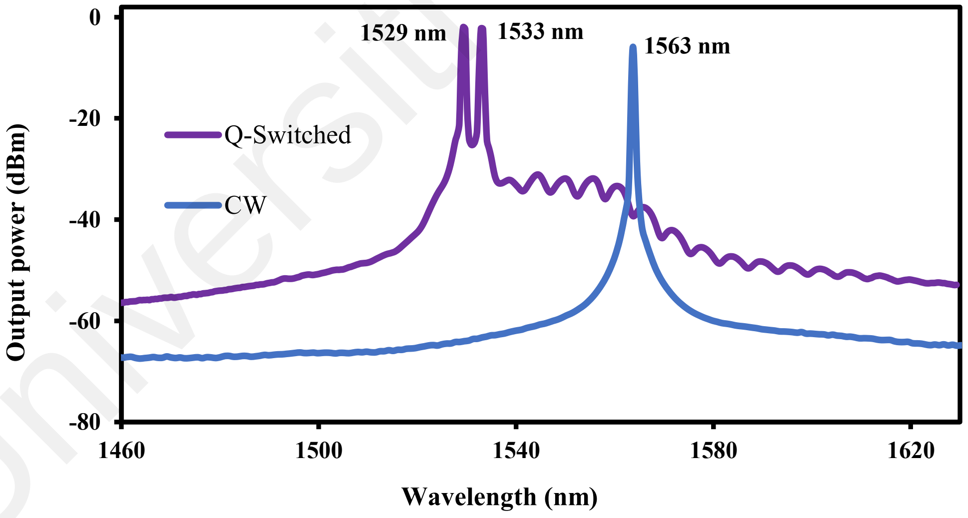

**Figure 4.8: Output spectrum of continuous wave (CW) and Q-switched (QS) pulse at threshold pump power of 108.05 mW**

Figure 4.8 above illustrates the optical spectrum wavelength of Q-switched and continuous-wave operation which were obtained with and without SA at the maximum pump power of 108.05 mW. The peak laser wavelength was blue-shifted from 1563 nm to 1533 nm and 1529 nm after the $MoSe_2$-SA was incorporated into the cavity. It is observed that the optical spectrum has two peak wavelengths during Q-switching operation. The shift towards shorter wavelengths is induced by the loss increment within the cavity. Consequently, lasing occurs at lower wavelengths to achieve higher amplification gain and to compensate for the additional losses.

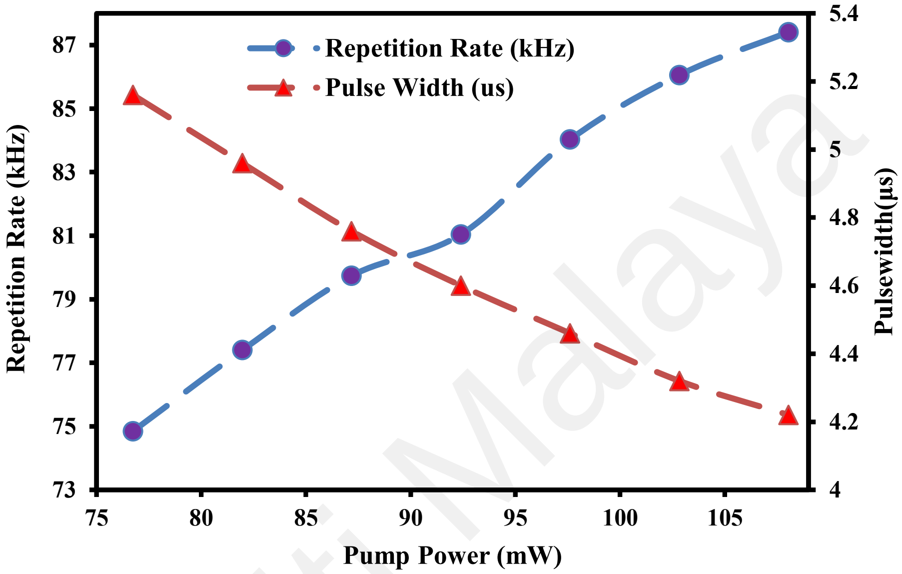

**Figure 4.9: Repetition rate and pulse width of Q-switched EDFL within 76.75mW – 108.05mW**

Figure 4.9 shows the repetition rate and pulse width against pump power. The pulse repetition rate increased almost linearly against the pump power whereas the pulse width decreases almost linearly against the pump power. In this scenario, the pulse repetition rate of the Q-switched fiber laser increases from 74.85 kHz to 87.41 kHz through varying the pump power from 76.75 mW to 108.05 mW whereas the pulse width reduces from 5.16 µs to 4.22 µs. By increasing the pump power within the laser cavity, it accelerates the gain population excitation process which ultimately leads to the achievement of the saturation state. Hence, a higher pulse repetition rate with narrower pulse width is achieved. The trend of increasing pulse repetition rate with increased pump power while decreasing pulse width aligns with the principles of passive Q-switching theory. The pulse train becomes unstable and vanishes as the pump power increases beyond 120 mW which potentially due to the limitation of $MoSe_2$ SA recovery time.

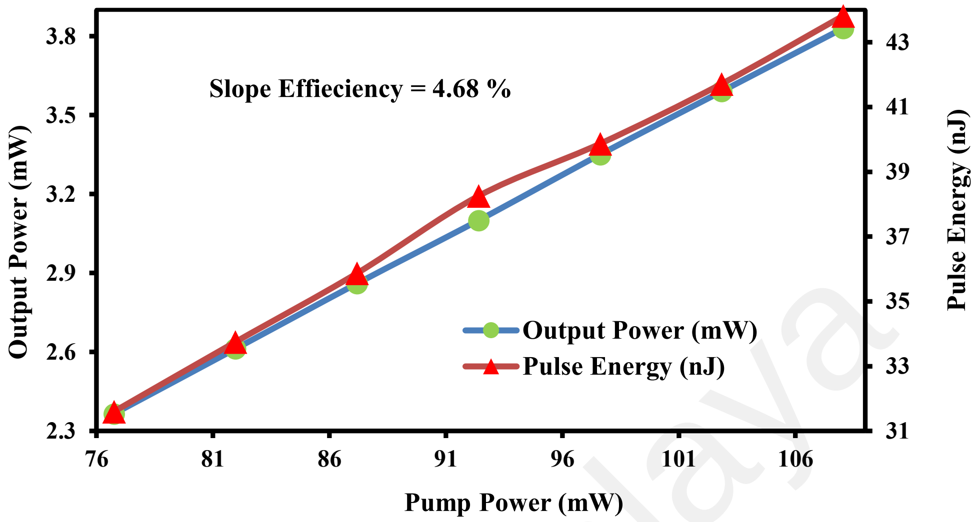

**Figure 4.10: Output power and pulse energy of Q-switched EDFL within 76.75mW – 108.05mW**

Figure 4.10 illustrates the correlation between the average output power and pulse energy of the Q-switched fiber laser in relation to pump power. The output power rises from 2.365 mW to 3.83 mW when the pump power increases from 76.75 mW to 108.05 mW. The slope efficiency of this Q-switched fiber laser is 4.68 % calculated from the gradient of the output power with respect to pump power. Additionally, the pulse energy increased from 31.6 nJ to 43.8 nJ and started to reach saturation state at pump power of 120mW. This indicated that the $MoSe_2$ saturable absorber has reached the damage threshold of Q-switching operation. When the pump power exceeds 120 mW, $MoSe_2$ is unable to fully recover leading to its inability to perform saturable absorption and become transparent within the cavity.

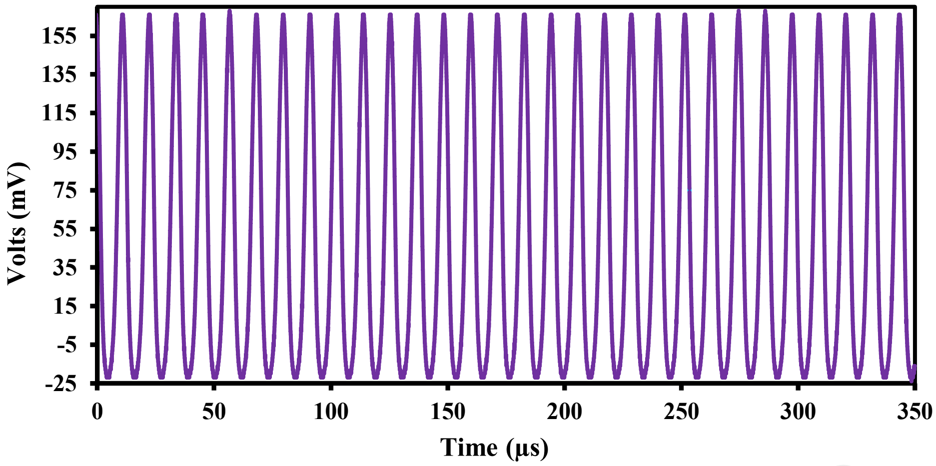

**Figure 4.11: Oscilloscope pulse train at pump power of 108.05 mW**

Figure 4.11 illustrates the oscilloscope trace of Q-switched pulses at pump power of 108.05 mW. At this pump power, the pulse duration is measured at 4.22 µs corresponding to a frequency of 87.41 kHz. The oscilloscope trace shows that the Q-switching operation is highly consistent throughout the observed time span. To assess the stability of the pulse, an RF spectrum is obtained for evaluation as shown in Figure 4.12. The RF spectrum of the Q-switched pulse demonstrates remarkable stability featuring a signal-to-noise ratio (SNR) of approximately 39.99 dB at the fundamental frequency of 87.41 kHz.

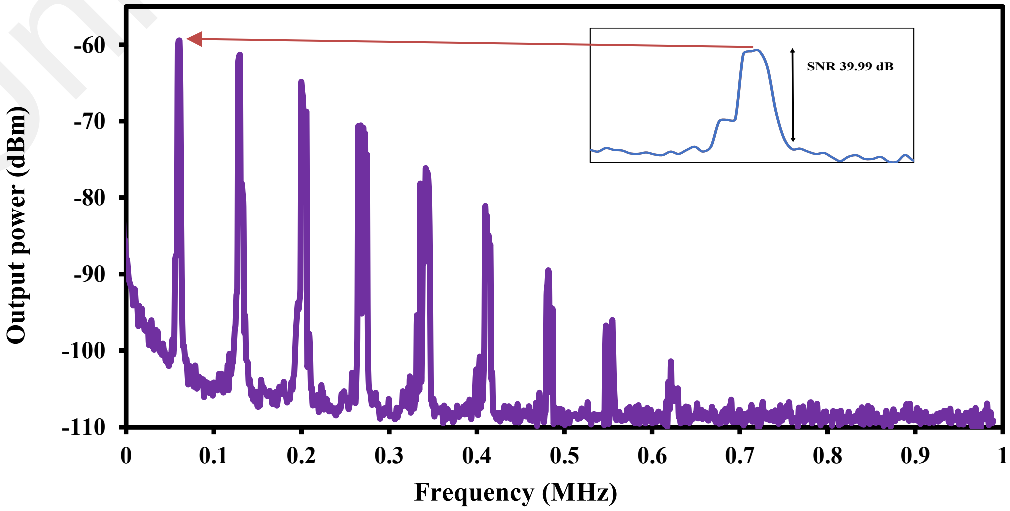

**Figure 4.12: RF spectrum at 87.41 kHz**

## 4.4 Q-switching Pulse Generation at 1.55-micron region for Molybdenum Ditelluride $MoTe_2$ Saturable Absorber

The molybdenum ditelluride saturable absorber $MoTe_2$-SA used in this experiment was prepared through the electro-deposition method as described in section 3.1.4.2 while the experiment setup is presented in section 4.1. The observation of the continuous-wave (CW) laser operation occurs at a pump power of 10 mW and at the wavelength of 1562 nm. The Q-switch pulses emerge when reaching the threshold pump power of 51.67mW and the pump power is gradually increases up to 89.19 mW. A stable self-starting Q-switched pulse is observed in this pump power range. As the pump power further increases beyond 100mW, the Q-switch pulse train becomes unstable and vanishes. On the other hand, the absence of Q-switching operation is observed when the $MoTe_2$-SA is removed from the cavity thereby confirming the role of $MoTe_2$-SA as a Q-switcher.

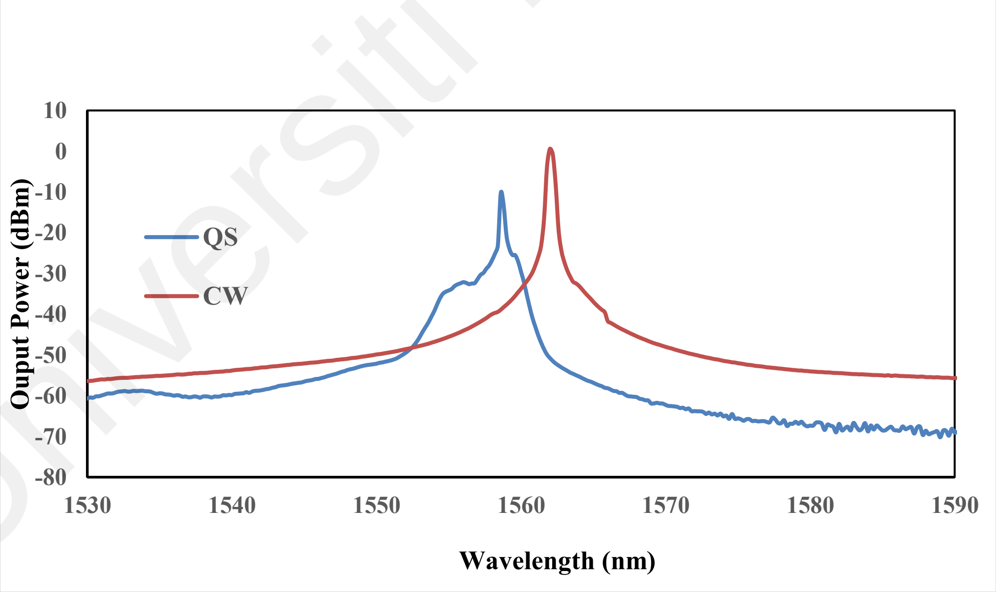

**Figure 4.13: Output spectrum of continuous wave (CW) and Q-switched (QS) pulse at threshold pump power of 89.19 mW**

Figure 4.13 above illustrates the optical spectrum wavelength of Q-switched and continuous-wave operation which were obtained with and without SA at the maximum pump power of 89.19 mW. The peak laser wavelength was blue-shifted from 1562 nm to

1558.6 nm after the $MoTe_2$-SA was incorporated into the cavity. It is observed that the optical spectrum slightly broadens during Q-switching operation compared to continuous-wave (CW) operation. The shift towards shorter wavelengths is induced by the loss increment within the cavity. Consequently, lasing occurs at lower wavelengths to achieve higher amplification gain and to compensate for the additional losses.

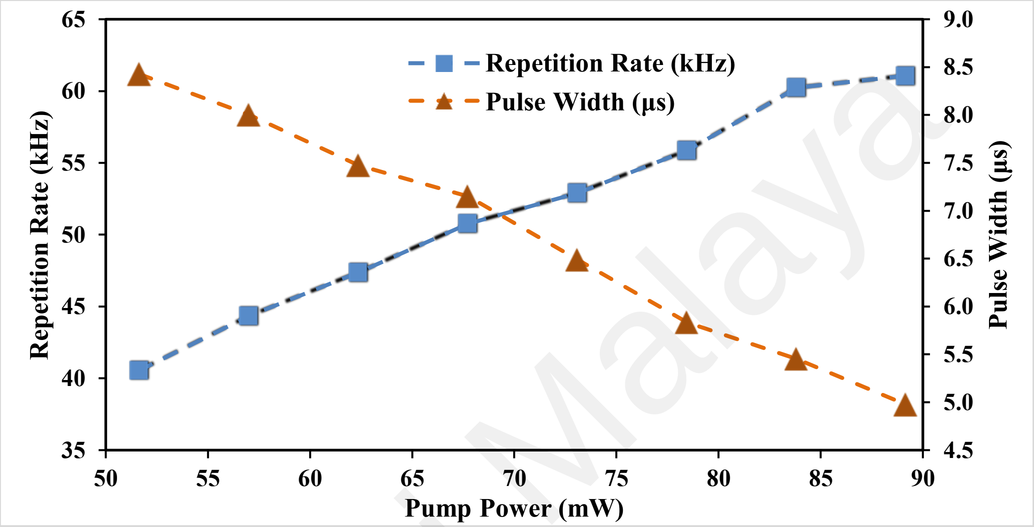

**Figure 4.14: Repetition rate and pulse width of Q-switched EDFL within 51.67mW – 89.19mW**

Figure 4.14 shows the repetition rate and pulse width against pump power. The pulse repetition rate increased almost linearly against the pump power whereas the pulse width decreases almost linearly against the pump power. In this scenario, the pulse repetition rate of the Q-switched fiber laser increases from 40.57 kHz to 61.07 kHz through varying the pump power from 51.67 mW to 89.19 mW whereas the pulse width reduces from 8.43 μs to 4.98 μs. By increasing the pump power within the laser cavity, it accelerates the gain population excitation process which ultimately leads to the achievement of the saturation state. Hence, a higher pulse repetition rate with narrower pulse width is achieved. The trend of increasing pulse repetition rate with increased pump power while decreasing pulse width aligns with the principles of passive Q-switching theory. The pulse train becomes unstable and vanishes as the pump power increases beyond 100 mW which potentially due to the limitation of $MoTe_2$ SA recovery time.

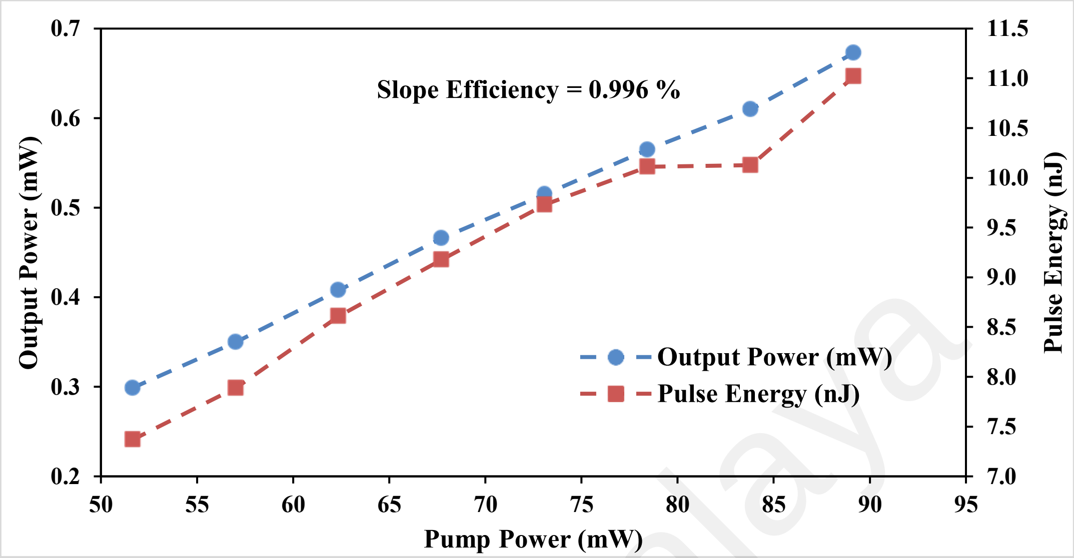

**Figure 4.15: Output power and pulse energy of Q-switched EDFL within 51.67mW – 89.19mW**

Figure 4.15 illustrates the correlation between the average output power and pulse energy of the Q-switched fiber laser in relation to pump power. The output power rises from 0.299 mW to 0.673 mW when the pump power increases from 51.67 mW to 89.19 mW. The slope efficiency of this Q-switched fiber laser is 0.996 % calculated from the gradient of the output power with respect to pump power. Additionally, the pulse energy increased from 7.37 nJ to 11.02 nJ and started to reach saturation state at pump power of 100mW. This indicated that the $MoTe_2$ saturable absorber has reached the damage threshold of Q-switching operation. When the pump power exceeds 100 mW, $MoTe_2$ is unable to fully recover leading to its inability to perform saturable absorption and become transparent within the cavity.

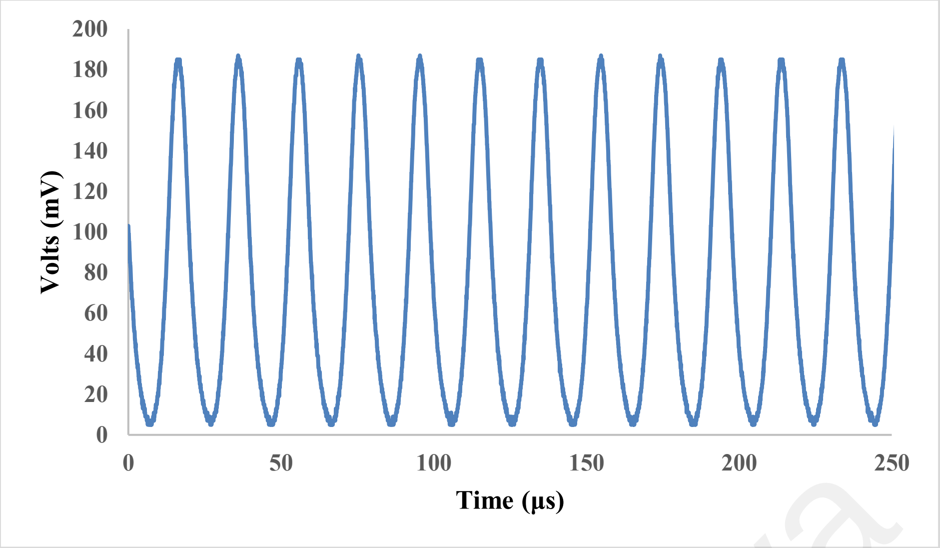

Figure 4.16: Oscilloscope pulse train at pump power of 89.19 mW

Figure 4.16 illustrates the oscilloscope trace of Q-switched pulses at pump power of 89.19 mW. At this pump power, the pulse duration is measured at 4.98 µs corresponding to a frequency of 61.07 kHz. The oscilloscope trace shows that the Q-switching operation is highly consistent throughout the observed time span. To assess the stability of the pulse, an RF spectrum is obtained for evaluation as shown in Figure 4.17. The RF spectrum of the Q-switched pulse demonstrates remarkable stability featuring a signal-to-noise ratio (SNR) of approximately 57.52 dB at the fundamental frequency of 61.07 kHz.

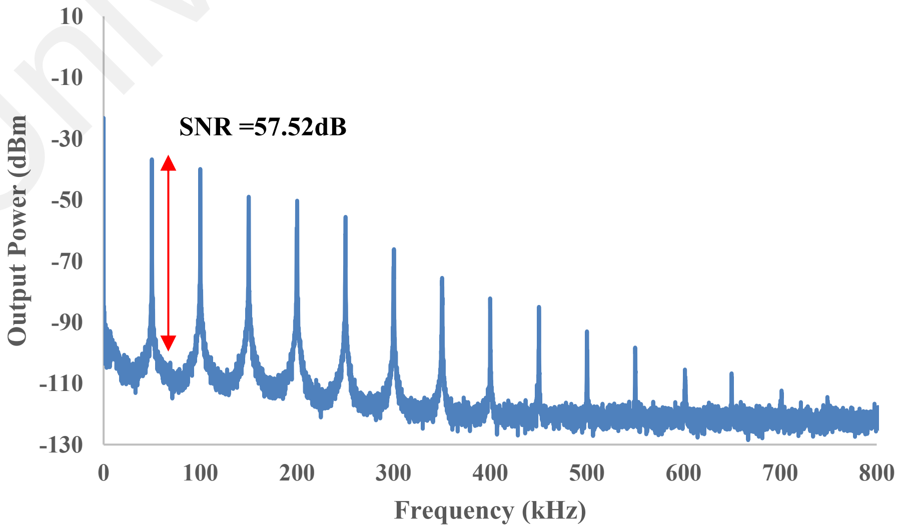

Figure 4.17: RF spectrum at 61.07 kHz

Ultimately, the output spectrum was examined over time to investigate the long-term stability of the Q-switched laser as depicted in Figure 4.18. The laser pulse was recorded at intervals of 30 minutes covering a total duration of 210 minutes. All the pulses operated around the wavelength of 1558.6 nm with optical power intensity fluctuating about -10dBm. All samples closely resembled each other thereby confirming the stability of the pulsed laser. Furthermore, this demonstrates that the proposed $MoTe_2$ saturable absorber can operate for an extended duration without experiencing any pulse disturbance.

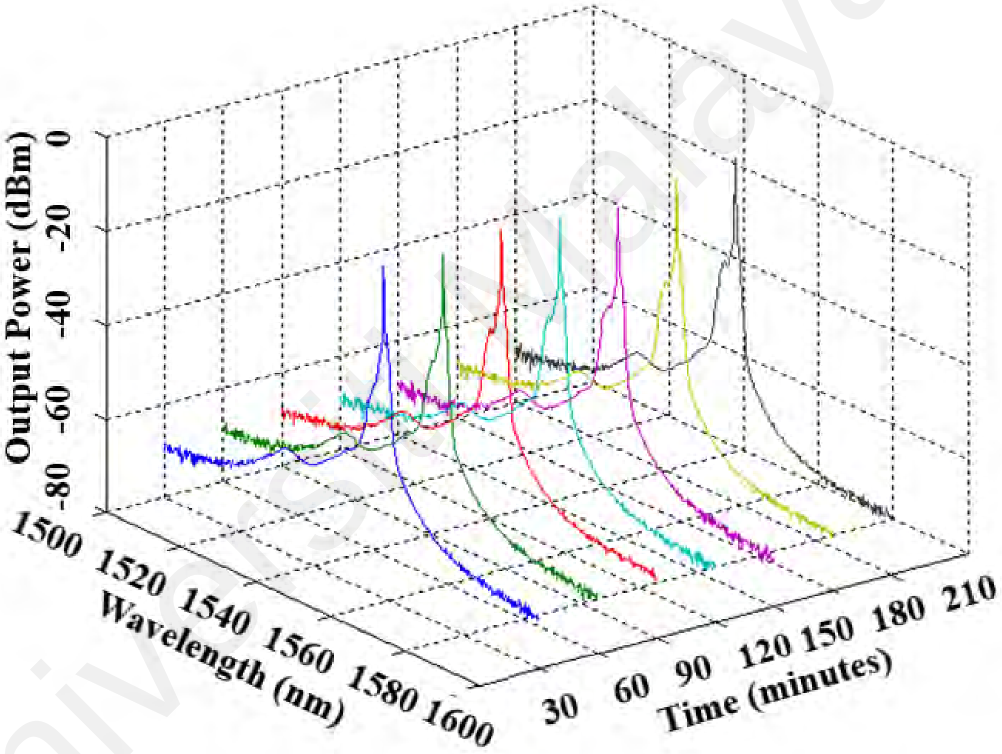

**Figure 4.18: Sustained performance of the Q-switched fiber laser over a duration of 210 minutes with intervals of 30 minutes**

### 4.5 Q-switching Pulse Generation at 2 -micron region for Molybdenum Ditelluride $MoTe_2$ Saturable Absorber

The molybdenum ditelluride saturable absorber $MoTe_2$-SA used in this experiment was prepared through the electro-deposition method as detailed in section 3.1.4.2. The experimental setup is presented in section 4.1 with slight modifications. The original setup was designed for 1.5 µm fiber laser while this modification accommodates 2 µm region.

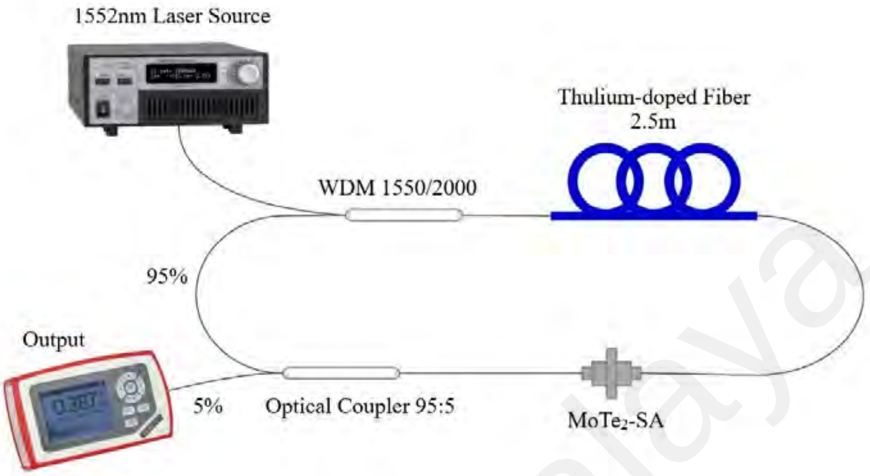

**Figure 4.19: Modified experiment setup for producing Q-switched fiber lasers in 2 µm region**

The modified experimental setup of the thulium-doped fiber ring laser with the $MoTe_2$-SA is illustrated in Figure 4.19. The laser cavity is replaced with a pump source which is a homemade Erbium-Ytterbium-doped fiber operating at 1552 nm. The laser source has a peak power of 997.26 mW and the power can be adjusted using a laser diode controller (Arroyo Instruments: 4320). Similar to the prior experimental configuration outlined in section 4.1, the 980/1550 wavelength division multiplexer (WDM) has been replaced with a 1550nm/2000nm wavelength division multiplexer (WDM). Subsequently, the 2-meter-long erbium-doped fiber (EDF) is also replaced by a 2.5 m thulium-doped fiber. Initially, the laser source is connected to a 1550nm/2000nm wavelength division multiplexer (WDM). The output from the wavelength division multiplexer WDM is connected to the 5 m thulium-doped fiber which functions as the linear gain medium within the cavity. The output of the thulium-doped fiber is connected to the $MoTe_2$-SA which is securely positioned between two fiber connectors through a fiber adaptor with the assistance of index matching gel to ensure its adhesion to the fiber ferrule. Finally, the connection is linked to a 95:5 output coupler with the 95% port of the output coupler connected to the 2000 nm port of the WDM to complete the laser ring cavity. The 95:5 coupler is employed to facilitate the return of a greater amount of pump power back to the cavity. Ultimately, the 5% portion of the laser output was extracted for measurements. The output signal was analyzed using a mid-infrared spectrometer (Miriad S3) for spectral analysis. To conduct measurements in both the time domain and frequency domain, an oscilloscope equipped with a built-in 1 GHz radio frequency spectrum analyzer (GWINSTEK: MDO-2302AG) is utilized. In order to monitor the laser pulse in time domain, the oscilloscope was coupled with a 12.5 GHz 2 μm InGaAs photodetector (EOT: ET-5000F). For measuring the output power, an optical power meter (Thorlabs: PM100D) is employed. The combination of these devices is utilized to collect the required data. The Q-switched laser pulse was immediately generated upon inserting the $MoTe_2$-SA into the laser cavity thereby eliminating the need for a polarization controller in the setup. The overall length of the cavity used for Q-switched operation is approximately 6 meters including all standard single-mode fiber (SMF-28).

The observation of the continuous-wave (CW) laser operation occurs at a pump power of 415.57 mW and at the wavelength of 1966.1 nm. The Q-switch pulses emerge when reaching the threshold pump power of 570.3 mW and the pump power is gradually increases up to 677.04 mW. A stable self-starting Q-switched pulse is observed in this pump power range. As the pump power further increases beyond 700 mW, the Q-switch pulse train becomes unstable and vanishes. On the other hand, the absence of Q-switching operation is observed when the $MoTe_2$-SA is removed from the cavity thereby confirming the role of $MoTe_2$-SA as a Q-switcher.

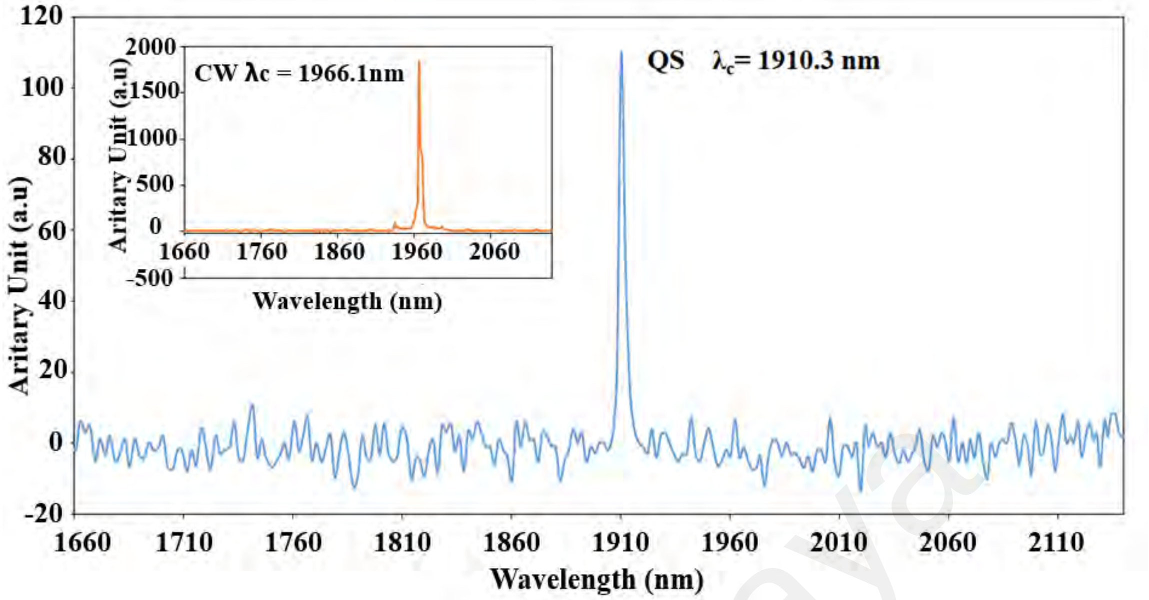

**Figure 4.20: Output spectrum of continuous wave (CW) and Q-switched (QS) pulse at threshold pump power of 677.04 mW**

Figure 4.20 above illustrates the optical spectrum wavelength of Q-switched and continuous-wave operation which were obtained with and without SA at the maximum pump power of 677.04 mW. The peak laser wavelength was blue-shifted from 1966.1 nm to 1910.3 nm after the $MoTe_2$-SA was incorporated into the cavity. The shift towards shorter wavelengths is induced by the loss increment within the cavity. Consequently, lasing occurs at lower wavelengths to achieve higher amplification gain and to compensate for the additional losses.

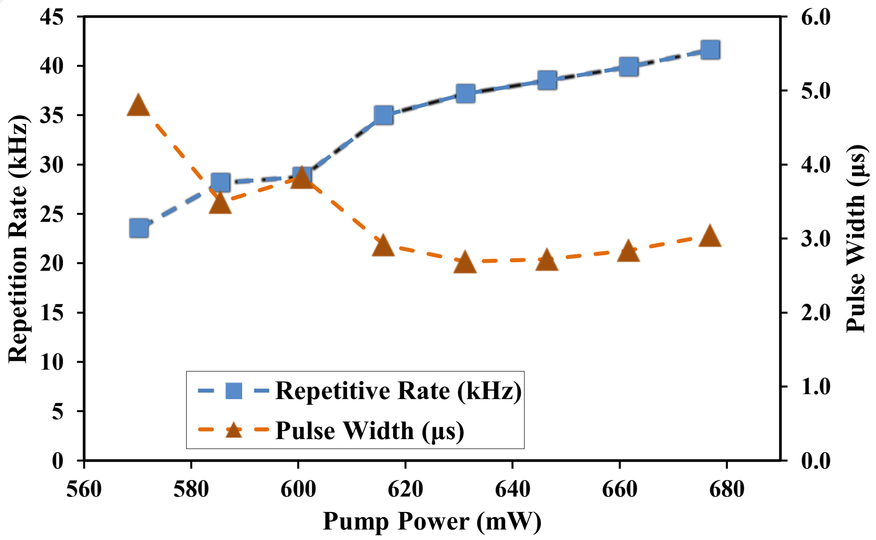

**Figure 4.21: Repetition rate and pulse width of Q-switched TDFL within 570.30mW – 677.04mW**

Figure 4.21 shows the repetition rate and pulse width against pump power. The pulse repetition rate increased almost linearly against the pump power whereas the pulse width decreases almost linearly against the pump power. However, the pulse width reduction becomes stagnant above pump power of 650 mW due to saturation of the saturable absorber. In this scenario, the pulse repetition rate of the Q-switched fiber laser increases from 23.53 kHz to 41.61 kHz through varying the pump power from 570.30 mW to 677.04 mW whereas the pulse width reduces from 4.82 μs to 3.05 μs. By increasing the pump power within the laser cavity, it accelerates the gain population excitation process which ultimately leads to the achievement of the saturation state. Hence, a higher pulse repetition rate with narrower pulse width is achieved. The trend of increasing pulse repetition rate with increased pump power while decreasing pulse width aligns with the principles of passive Q-switching theory. The pulse train becomes unstable and vanishes as the pump power increases beyond 700 mW which potentially due to the limitation of $MoTe_2$ SA recovery time.

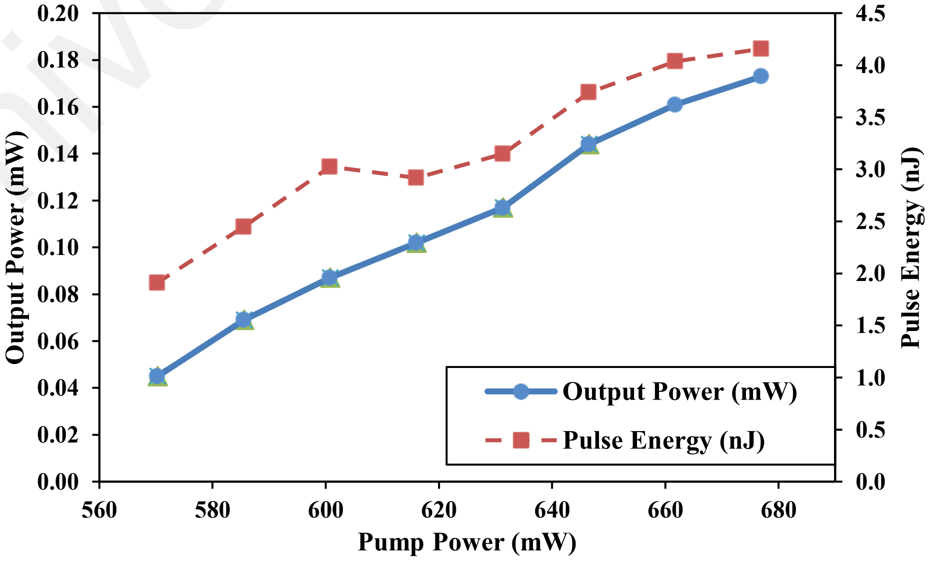

**Figure 4.22: Output power and pulse energy of Q-switched TDFL within 570.30mW – 677.04mW**

Figure 4.22 illustrates the correlation between the average output power and pulse energy of the Q-switched fiber laser in relation to pump power. The output power rises from 0.05 mW to 0.173 mW when the pump power increases from 570.30 mW to 677.04 mW. The slope efficiency of this Q-switched fiber laser is 0.12 % calculated from the gradient of the output power with respect to pump power. Additionally, the pulse energy increased from 1.912 nJ to 4.158 nJ and started to reach saturation state at pump power of 700 mW. This indicated that the $MoTe_2$ saturable absorber has reached the damage threshold of Q-switching operation. When the pump power exceeds 700 mW, $MoTe_2$ is unable to fully recover leading to its inability to perform saturable absorption and become transparent within the cavity.

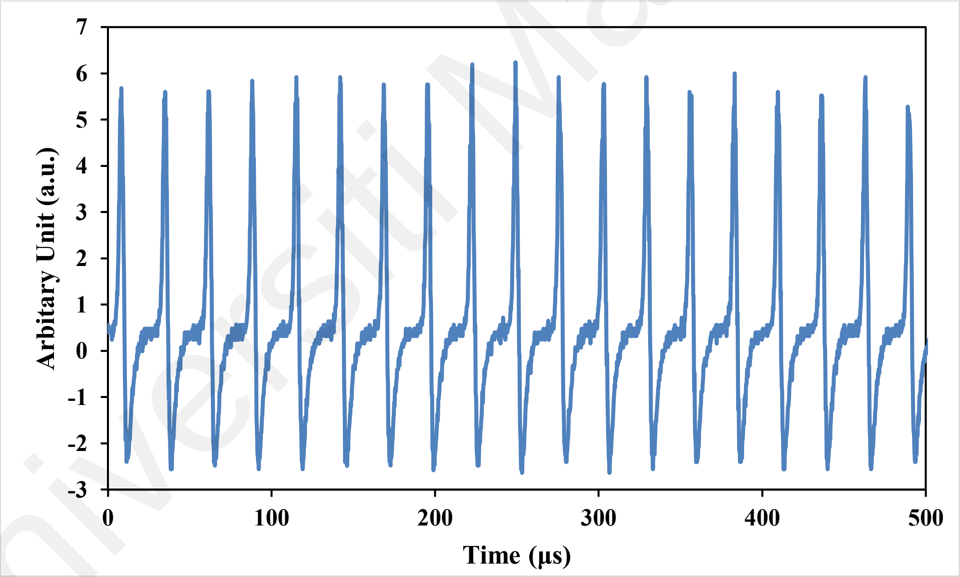

**Figure 4.23: Oscilloscope pulse train at pump power of 677.04 mW**

Figure 4.23 illustrates the oscilloscope trace of Q-switched pulses at pump power of 677.04 mW. At this pump power, the pulse duration is measured at 3.05 µs corresponding to a frequency of 41.61 kHz. The oscilloscope trace shows that the Q-switching operation is highly consistent throughout the observed time span. To assess the stability of the pulse, an RF spectrum is obtained for evaluation as shown in Figure 4.24. The RF spectrum of the Q-switched pulse demonstrates remarkable stability featuring a signal-to-noise ratio (SNR) of approximately 47.60 dB at the fundamental frequency of 41.61 kHz.

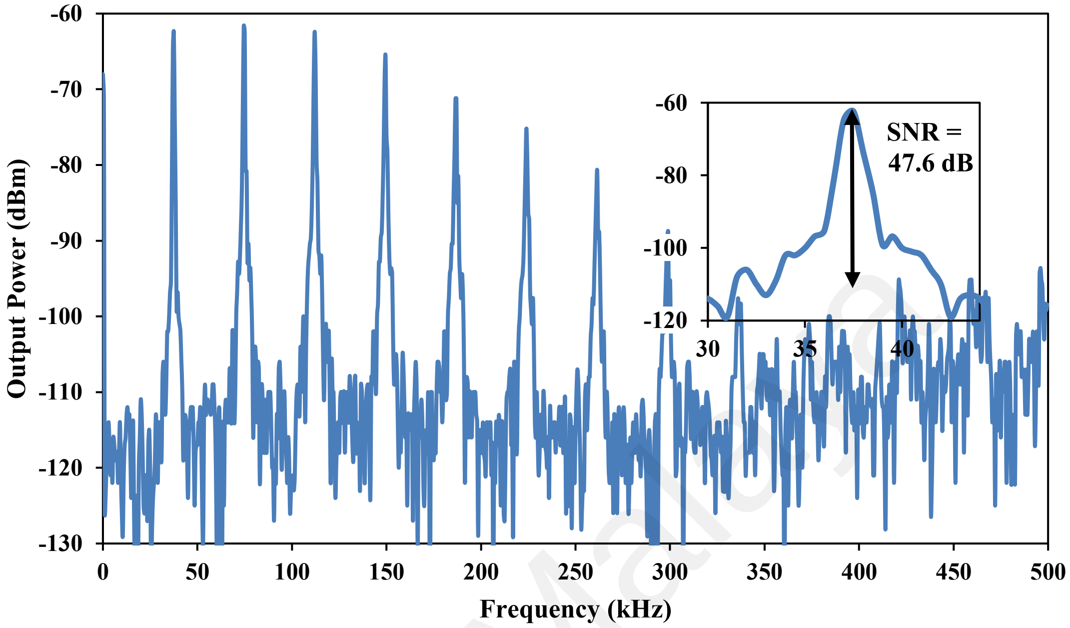

Figure 4.24: RF spectrum at 41.61 kHz

## 4.6 Summary

Table 4.1 presents the performance of electro-deposited TMDs -MoS$_2$, MoSe$_2$ and MoTe$_2$ as saturable absorbers in the generation of Q-switched pulse lasers.

**Table 4.1: Performance of TMDs saturable absorber (SA) for Q-switched operation**

| No. | SA | Region **µm** | Q-switched wavelength **nm** | Frequency **kHz** | Input pump power **mW** | Output power **mW** | Pulse Energy **nJ** | SNR **dB** |
|---|---|---|---|---|---|---|---|---|
| 1. | MoS$_2$ | 1.55 | 1559.3 | 57.47–89.89 | 51.67–105.27 | 0.517–1.351 | 8.99-15.03 | 62.28 |
| 2. | MoSe$_2$ | 1.55 | 1529;1533 | 74.85-87.41 | 76.75-108.05 | 2.365-3.83 | 31.6-43.8 | 39.99 |
| 3. | MoTe$_2$ | 1.55 | 1558.6 | 40.57–61.07 | 51.67–89.89 | 0.299-0.673 | 7.37-11.02 | 57.52 |
| 4. | MoTe$_2$ | 2.00 | 1910.3 | 23.53-41.61 | 570.30-677.04 | 0.05-0.173 | 1.912-4.158 | 47.60 |

|  |  |  |  |  |  |  |  |  |
|---|---|---|---|---|---|---|---|---|

The above Table 4.1 indicates that 2D transition metal dichalcogenides TMDs saturable absorbers are capable of generating Q-switched fiber lasers. However, the table above also demonstrates that various TMD materials exhibit different performance characteristics. Factors such as the choice of a chemical compound can influence the performance of these 2D TMD saturable absorbers in generating Q-switched pulses. During the experimental process, using selenium to generate Q-switched pulses proves to be more challenging when compared to sulfur and tellurium. Furthermore, the fabrication time in this research will also impact the performance of these 2D TMDs saturable absorbers. Certain TMD material may require a shorter fabrication time (thinner layer) compared to other TMD material. Some thinner SAs may easily generate Q-switched pulses whereas certain Q-switched pulses required a thicker SA for higher damage threshold. Therefore, the fabrication of these TMDs saturable absorber is guided by the experience gained through testing these SAs in the cavity. Moreover, the frequency of Q-switched pulses is heavily dependent on both the compound material and the fabrication time. For example, using the same material with varying fabrication times will result in different frequency outputs. Thus, we cannot definitively determine which saturable absorbers outperform others in any given situation.

# CHAPTER 5: MODE-LOCKED PULSE GENERATION OF FABRICATED SATURABLE ABSORBER

## 5.1 Experimental setup for mode-locked fiber laser

Figure 5.1 shows the experimental setup used to generate passive mode-locked fiber lasers. The experimental arrangement closely resembles the one detailed in section 4.1 with minor adjustments made to incorporate an additional component. The initial configuration outlined in section 4.1 was designed for the generation of Q-switched pulse lasers. To achieve mode-locking operation, an additional fiber length is necessary to interplay with both the normal cavity dispersion and the nonlinear effect within the fiber ring cavity. Balancing the dispersion and nonlinearity is crucial for generating mode-locked laser pulses. Thus, a stable mode-locking regime can be generated only with the appropriate cavity length with the addition of 100m SMF-28 to the cavity. The combination of dispersion and nonlinear effect can lead to the formation of an optical pulse where the wave is stable and unchanged during its propagation through the fiber. Under these conditions, the pulse would propagate undistorted due to the mutual compensation of dispersion and self-phase modulation and hence this solitary wave pulse is referred to as a soliton. The dispersion and nonlinearity characteristics of the EDFL cavity were schematically designed to evaluate the ability of TMDs SA in generating mode-locking pulses at a wavelength of 1.55 µm. Further reducing the additional SMF length may result in decreased cavity dispersion which leads to an imbalance in compensation thereby hindering the generation of mode-locked pulses. The remaining aspects of the experimental design closely resemble the configuration used for Q-switch generation. The fiber laser ring cavity was assembled using a wavelength division multiplexer (WDM), an erbium-doped fiber (EDF), a polarization-independent isolator (PI-ISO), a polarization controller, output couplers and single-mode fiber (SMF). A gain medium was deployed using a 2-meter-long erbium-doped fiber (EDF) with specific parameters including a numerical aperture of 0.16, a core diameter of 4 μm, a group velocity dispersion (GVD) of 27.6 $ps^2$/km and a peak absorption of 23 dB/m. Subsequently, the 980 nm laser diode power-pumps the Erbium-doped fiber (EDF) gain medium through a 980/1550 wavelength division multiplexer (WDM). A polarization controller in the cavity is used to adjust the polarization state of light circulation that is favorable for pulse optimization. Following that, the laser is directed into a polarization-independent optical isolator (PI-ISO). The purpose of employing this optical isolator is to prevent back reflections of light into the laser source and to maintain the unidirectional propagation of the laser beam within the cavity. After the polarization-independent optical isolator (PI-ISO), the fabricated TMDs saturable absorber SA is incorporated into the laser cavity to modulate intracavity loss and consequently transforming the continuous wave (CW) laser into mode-locked pulsed lasers. The saturable absorber (SA) is placed between two fiber connectors through a fiber adaptor. The saturable absorber (SA) is securely positioned with the assistance of index matching gel to ensure its adhesion to the fiber ferrule. Following that, the laser is directed into the coupler which divides the output laser for performance investigations. Two different output couplers (OC) with coupling ratios of 50:50 and 95:5 were employed to examine the quality of Q-switched formation. The 95:5 coupler is utilized to enable more pump power to be returned to the cavity through which 95% laser light is circulated back into the cavity through the 1550 nm port of the WDM. To observe the laser performance on the 5% output coupler, the 50:50 coupler is introduced to concurrently split the output laser for real-time data measurements using two different measuring devices. The overall length of the cavity used for mode-locked operation is approximately 106 meters including the additional of standard single-mode fiber (SMF-28).

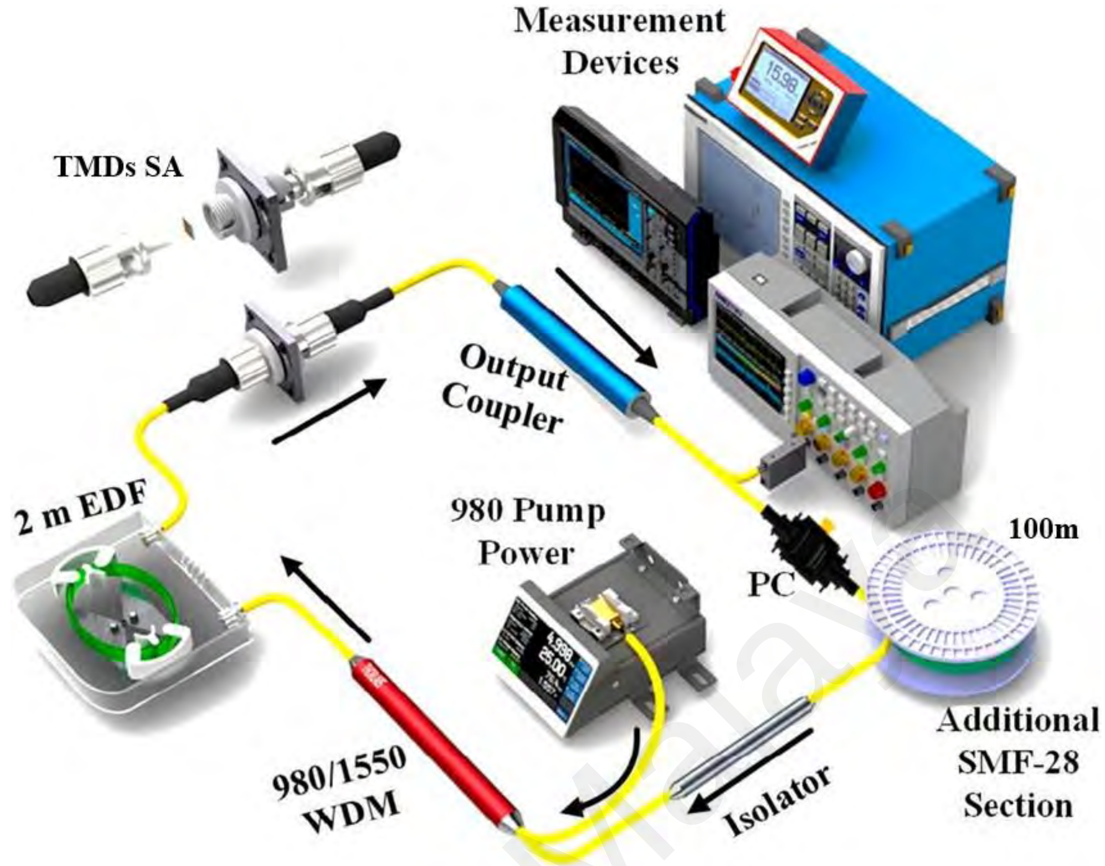

**Figure 5.1: Experiment setup for producing Mode-locked fiber lasers (Dutta, 2024)**

The performance of the mode-locked pulsed laser was measured using an optical spectrum analyzer OSA (Anritsu, MS97010C), a digital oscilloscope (OSC) with 3GHz bandwidth (GW Instek, GSP-9300B), a radio frequency spectrum analyzer (RFSA) (Anritsu, MS2803A), an InGaAs photodetector (Thorlabs: DET10D/M) and optical power meter (OPM) (Thorlabs, PM100D). Due to the constrain of the oscilloscope, an additional piece of equipment called an autocorrelator (Alnair Labs HAC- 200) is needed in mode-locked pulse measurement to investigate the pulse width in picosecond or even in femtosecond region. Since the pulse width is extremely narrow, the oscilloscope is incapable of measuring such small resolutions. Therefore, an auto-correlator is employed to accurately determine the pulse width. Alternatively, the pulse width can be mathematically calculated based on time-bandwidth-product (TBP). These devices are employed in combination to gather the necessary data.

## 5.2 Mode-Locked Pulse Generation at 1.55-micron region for Molybdenum Disulfide $MoS_2$ Saturable Absorber SA thin film

The molybdenum disulfide saturable absorber $MoS_2$-SA used in this experiment was prepared through the electro-deposition method as described in section 3.1.4.2 while the experiment procedure is presented in section 5.1. The experimental visualization of the ultrafast laser is depicted in a standard ring Erbium-doped fiber laser (EDFL) as illustrated in Figure 5.1. The $MoS_2$ thin film with an insertion loss of 2.86 dB is incorporated into the ring cavity using a sandwiching technique. Initially, the ring laser cavity is operated in continuous wave (CW) region at the wavelength of 1564.65 nm at a pump power of 20 mW. By precisely tuning the sandwiched fiber ferrule and gradually increasing the pump power, the laser cavity self-started into the mode-locking operation at pump power of 78.5 mW. The cavity maintains stable mode-locking operation as the pump power increases within the range of 78.5 mW to 142.8 mW. The mode-locked laser spectrum is centered at 1560.8 nm with a 3 dB spectral bandwidth of 2.5 nm as depicted in Figure 5.2. The high net cavity dispersion and minimal nonlinearity induced by the laser pump had caused the narrow spectrum in the mode-lock operation. The spectrum reveals the observable presence of obvious Kelly spectral sidebands indicating that the fiber laser is operating in the soliton regime.

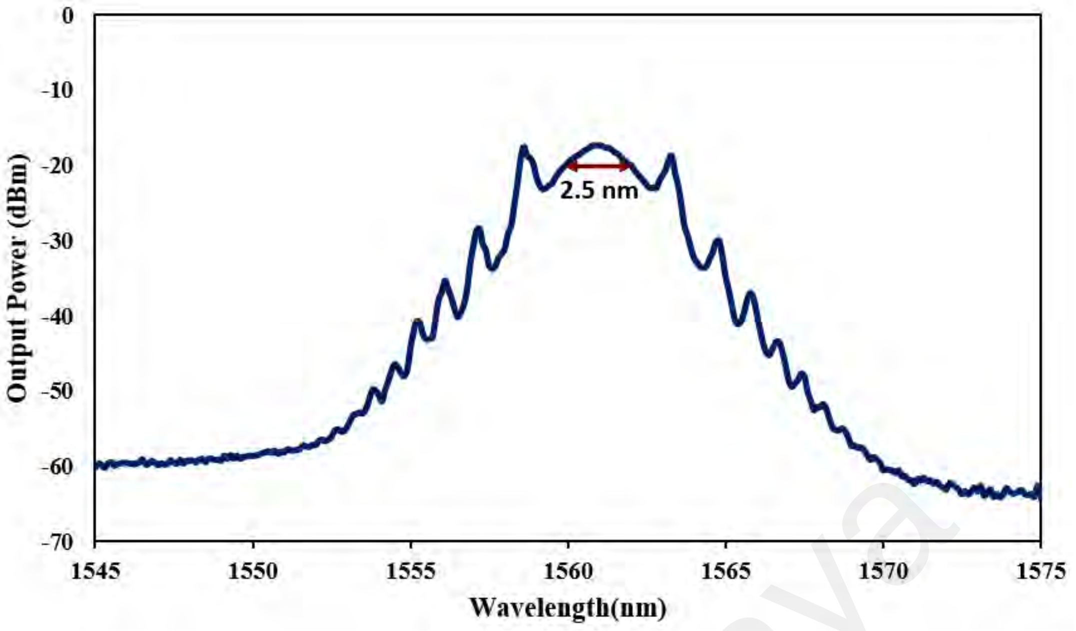

**Figure 5.2: Optical spectrum of mode-locked EDFL at pump power of 142.8mW**

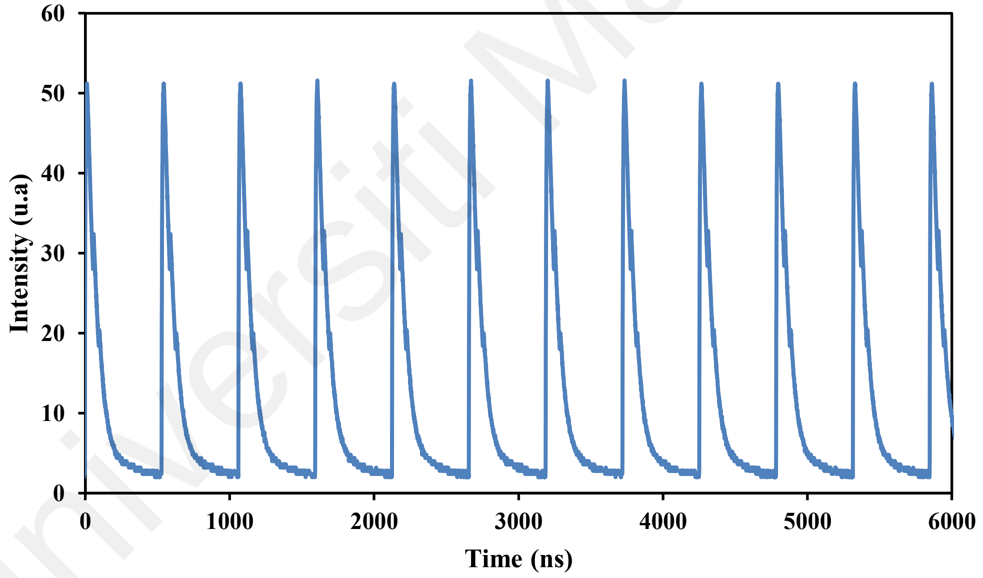

**Figure 5.3: Mode-locked pulse train**

The mode-locking operation is more observable in time domain as depicted in Figure 5.3. The oscilloscope captures a repetitive pulse train with a pulse repetition rate of 1.88 MHz. The round-trip time of 532 ns aligns well with the cavity length of 106 m. The accurate measurement of the pulse width was not realized due to the limitations of the oscilloscope. Therefore, an autocorrelator is used to perform the autocorrelation based on

Sech$^2$ fitting to determine the pulse width. As depicted in Figure 5.4, the measured pulse is accurately fitted by the hyperbolic Sech$^2$ function with a full width at half maximum (FWHM) yielding a pulse width of 1.47 ps which suggests that the fiber laser operates in a high stable regime.

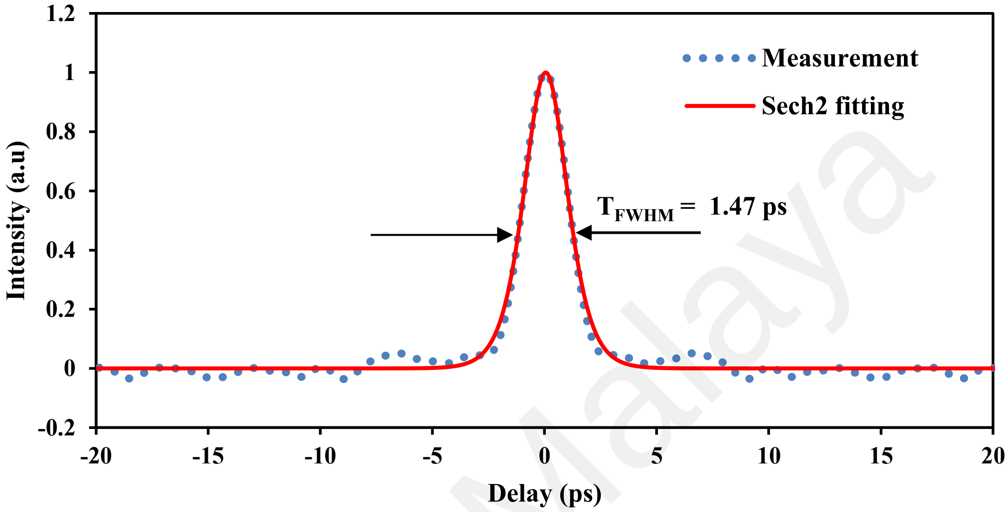

Figure 5.4: Autocorrection trace for mode-locked pulse width

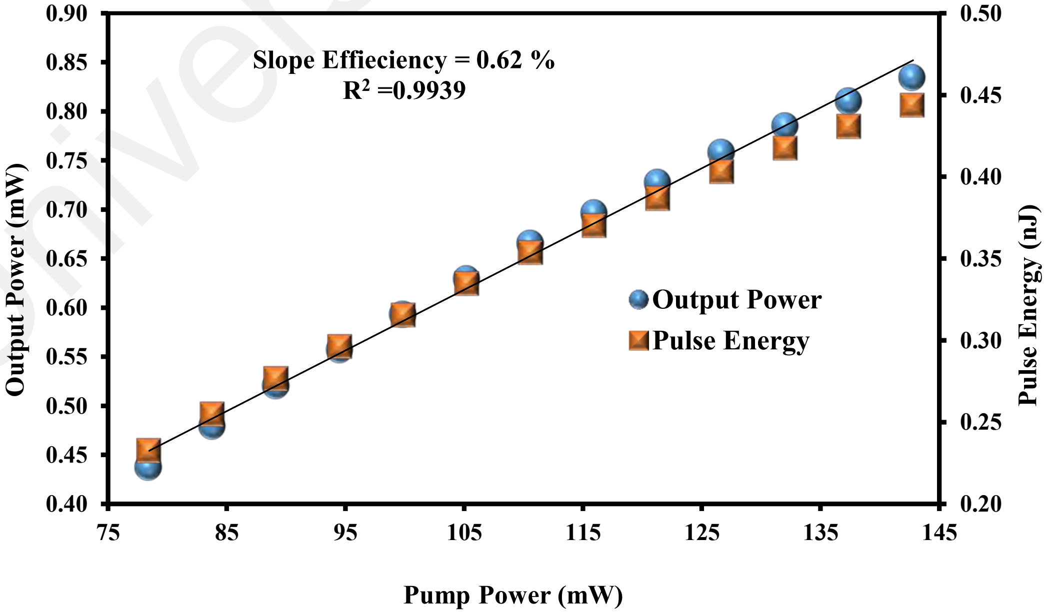

Figure 5.5: Output power and average pulse energy analysis with the increase of pump power

The analysis of the output power and average pulse energy is further presented in Figure 5.5. As the pump power rises from 78.5 mW to 142.8 mW, both the output power and average pulse energy exhibit a linear increase with an $R^2$ value of 0.9939. Within the tuning range of pump power, the recorded output power ranges from 0.44 mW to 0.83 mW resulting in a laser efficiency of 0.62%. Additionally, the maximum recorded average pulse energy is 0.44 nJ at a pump power of 142.8 mW. The mode-locking operation is restricted by the maximum power of the pump laser diode, nevertheless, this $MoS_2$ saturable absorbers exhibit a high potential to operate at pump powers beyond 142.8 mW.

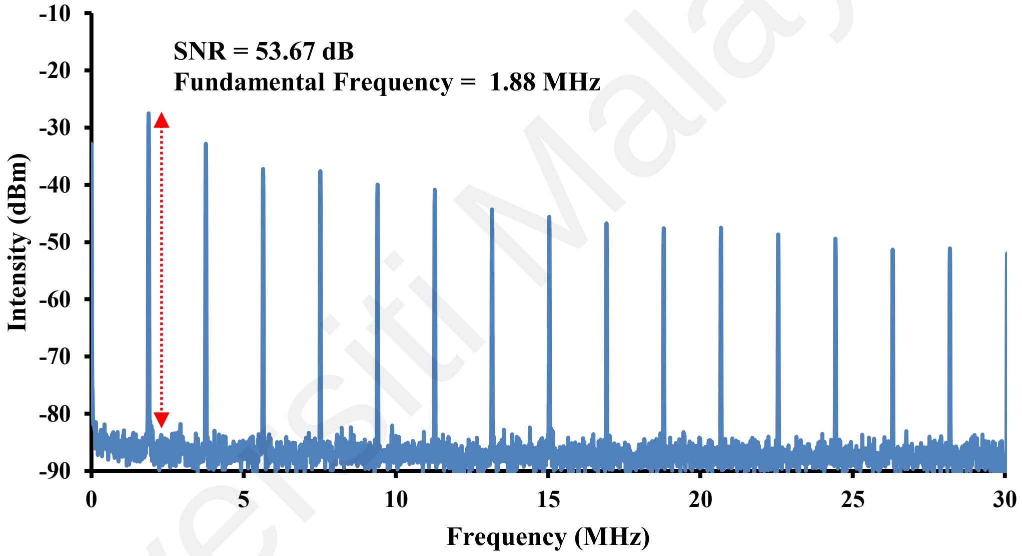

Figure 5.6: RF spectrum of the mode-locked laser

Alternatively, the stability of the mode-locked laser is examined in the frequency domain as depicted in Figure 5.6. The fundamental frequency is measured at 1.88 MHz which aligns well with the pulse repetition rate observed in the time domain depicted in Figure 5.3. The signal-to-noise ratio is recorded at 53.67 dB signifying high stability of the mode-locked laser. The mode-locked laser has been continuously operational in the laboratory environment for approximately 8 hours with no noticeable wavelength shift or intensity degradation observed throughout the operation period as illustrated in Figure 5.7. On the other hand, the absence of mode-locking operation is observed when the

$MoS_2$-SA is removed from the cavity thereby confirming the role of $MoS_2$-SA as a mode-locker.

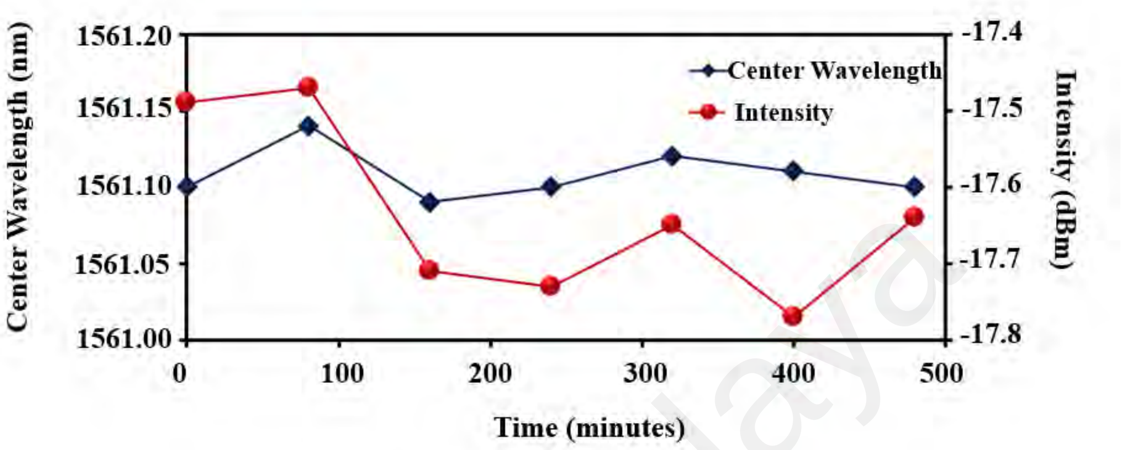

**Figure 5.7: Stability test based on optical spectrum**

### 5.3 Mode-Locked Pulse Generation at 1.55-micron region for Molybdenum Ditelluride $MoTe_2$ Saturable Absorber SA thin film

The molybdenum ditelluride saturable absorber $MoTe_2$-SA used in this experiment was prepared through the electro-deposition method as described in section 3.1.4.2 while the experiment procedure is presented in section 5.1. The experimental visualization of the ultrafast laser is depicted in a standard ring Erbium-doped fiber laser (EDFL) as illustrated in Figure 5.1. The $MoTe_2$ thin film with an insertion loss of 4.54 dB is incorporated into the ring cavity using a sandwiching technique. Initially, the ring laser cavity is operated in continuous wave (CW) region at the wavelength of 1564.65 nm at a pump power of 20 mW. By precisely tuning the sandwiched fiber ferrule and gradually increasing the pump power, the laser cavity self-started into the mode-locking operation at pump power of 94.55 mW. The cavity maintains stable mode-locking operation as the pump power increases within the range of 94.55 mW to 158.87 mW. Figure 5.8 shows the typical bell-shape mode-locking optical spectrum centered at 1558nm with 3-dB spectral bandwidth of 0.3 nm. The high net cavity dispersion and minimal nonlinearity induced by the laser pump had caused the narrow spectrum in the mode-lock operation.

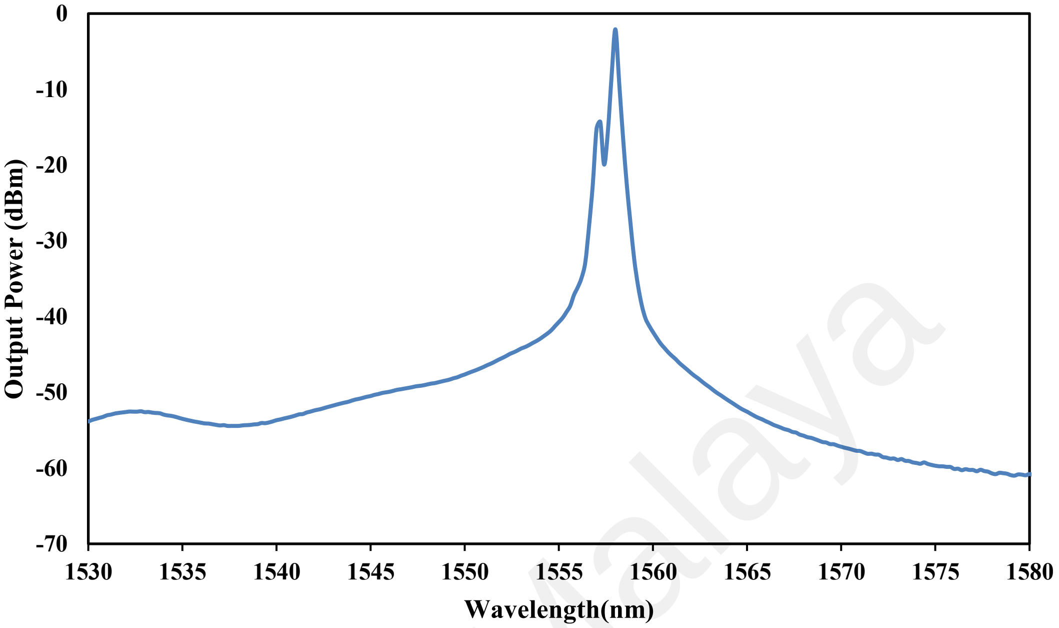

**Figure 5.8: Output optical spectrum of conventional mode-locked using $MoTe_2$ SA with a pump power of 158.87mW**

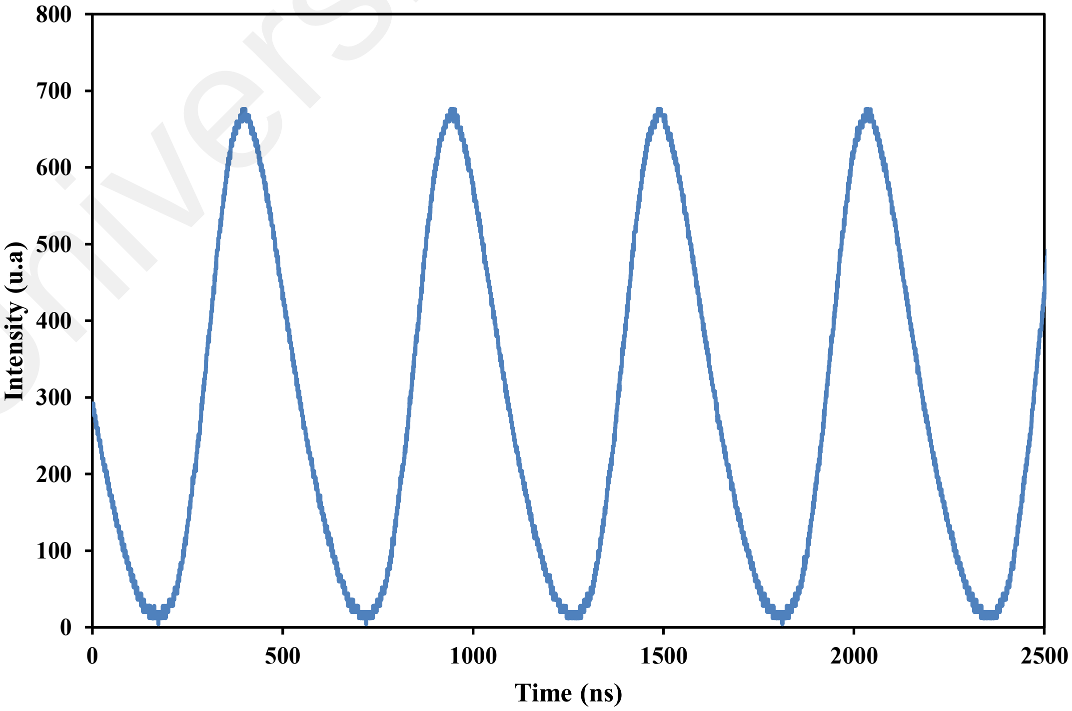

**Figure 5.9: Oscilloscope trace of conventional mode-locked using $MoTe_2$ SA with a pump power of 158.87mW**

The mode-locking operation is more observable in time domain as depicted in Figure 5.9. The oscilloscope captures a repetitive pulse train with a pulse repetition rate of 1.83 MHz. The oscilloscope pulse trace displays a consistently uniform intensity with a pulse-to-pulse interval of 547 ns that corresponds with the cavity's roundtrip time. The round-trip time aligns well with the cavity length of 106 m. As the pulse width falls within the nanosecond range, the oscilloscope can measure the output signal without requiring an autocorrelator in this scenario. Even when employing an autocorrelator for this pulse measurement, it proves unsuccessful because of the broader pulse width. The autocorrelator is utilized to execute autocorrelation employing a $Sech^2$ fitting method to ascertain the pulse width typically measured in picoseconds (ps) or femtoseconds (fs).

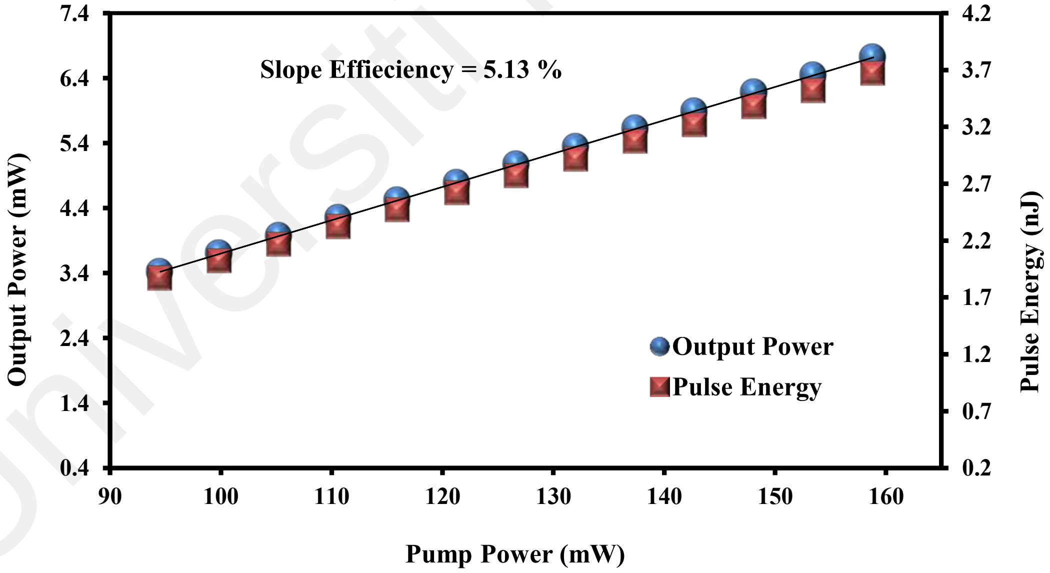

**Figure 5.10: Output power and pulse energy of mode-locked EDF within 94.55mW – 158.87mW pump power**

The analysis of the output power and average pulse energy is further presented in Figure 5.10. As the pump power rises from 94.55.5 mW to 158.87 mW, both the output power and average pulse energy exhibit a linear increase. Within the tuning range of pump power, the recorded output power ranges from 3.42 mW to 6.72 mW resulting in a laser efficiency of 5.13%. Additionally, the maximum recorded average pulse energy is 3.67 nJ at a pump power of 158.87 mW. When the input pump power exceeds 200mW, the stability of the mode-locking operation is compromised leading to observable fluctuations in the spectrum. Nevertheless, mode-locked pulses reappear upon reducing the pump power to 160 mW.

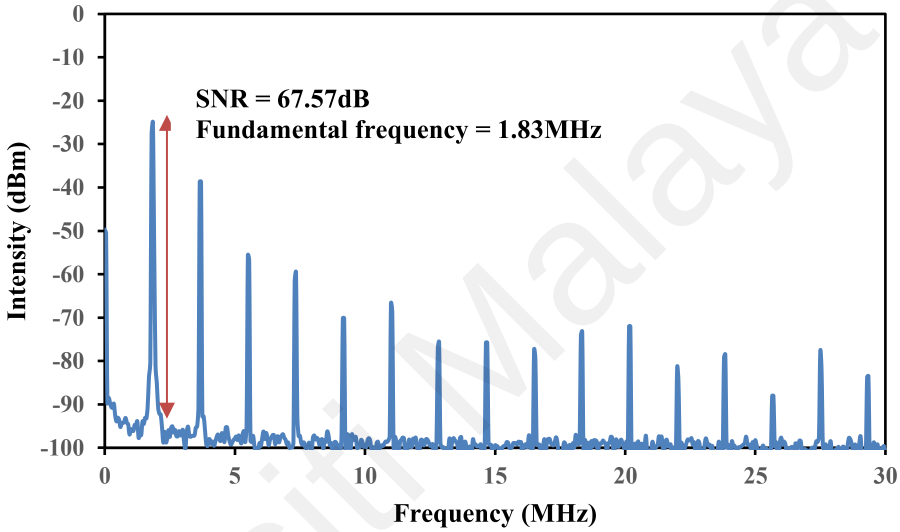

**Figure 5.11: RF of Conventional mode-locked using $MoTe_2$ SA with a pump power of 158.87 mW**

Alternatively, the stability of the mode-locked laser is examined in the frequency domain as depicted in Figure 5.11. The fundamental frequency is measured at 1.83 MHz which aligns well with the pulse repetition rate observed in the time domain depicted in Figure 5.9. The signal-to-noise ratio is recorded at 67.57 dB signifying high stability of the mode-locked laser. In the mode-locking operation, a stable pulse is achieved at 1.83 MHz as depicted in Figure 5.12 where the graphs plot the repetition rate against the pump power. In the figure, the repetition rate remains consistently stable, and there is no observable significant fluctuation in the line. With further improvement, this developed device has the potential to become commercially viable.

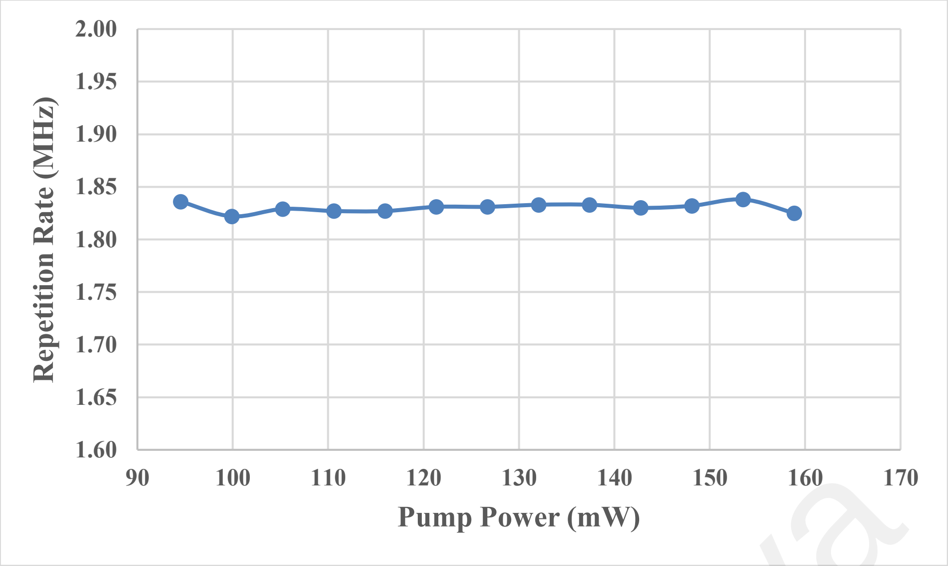

**Figure 5.12: Repetition rate as a function of pump power**

Furthermore, the mode-locked laser has been continuously operational in the laboratory environment for approximately 8 hours with no noticeable wavelength shift or intensity degradation observed throughout the operation period as illustrated in Figure 5.13. To validate the mode-locked state of this fiber laser, the $MoTe_2$-SA is removed from the laser cavity. Despite adjusting the input pump power and polarization controller across their entire ranges, mode-locked operation is not detected. Therefore, this confirms that the mode-locking operation is contributed by the $MoTe_2$ saturable absorber.

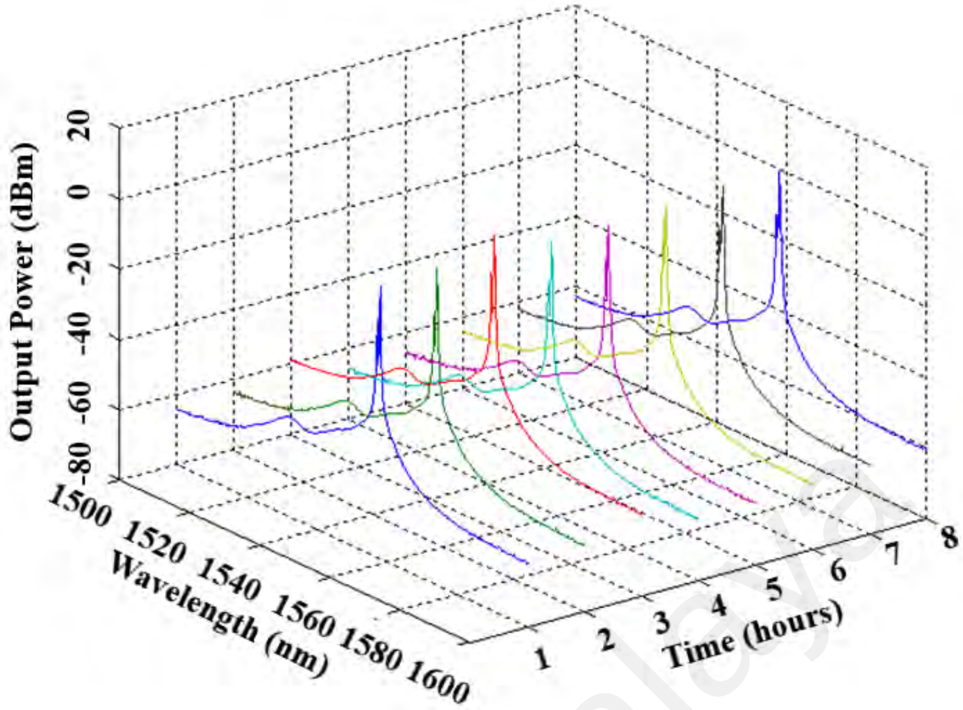

**Figure 5.13: Stability test based on optical spectrum**

## 5.4 Summary

Table 5.1 presents the performance of electro-deposited TMDs -$MoS_2$ and $MoTe_2$ as saturable absorbers in the generation of passive mode-locked fiber lasers.

**Table 5.1: Performance of TMDs saturable absorber (SA) for mode-locked operation**

| No. | SA | Region **µm** | Mode-locked wavelength **nm** | Frequency **MHz** | Pulse Width | Input pump power **mW** | Output power **mW** | Pulse Energy **nJ** | SNR **dB** |
|---|---|---|---|---|---|---|---|---|---|
| 1. | $MoS_2$ | 1.55 | 1560.8 | 1.88 | 1.47 ps | 78.5–142.8 | 0.44 – 0.834 | 0.23-0.44 | 53.67 |
| 2. | $MoSe_2$ | NA | NA | NA | NA | NA | NA | NA | NA |
| 3. | $MoTe_2$ | 1.55 | 1558 | 1.83 | 225 ns | 94.55 – 158.87 | 3.42 – 6.72 | 1.87-3.67 | 67.57 |

The above Table 5.1 indicates that 2D transition metal dichalcogenides TMDs saturable absorbers are capable of generating mode-locked fiber lasers. However, the table above also demonstrates that various TMD materials exhibit different performance characteristics. Factors such as the choice of a chemical compound can influence the performance of these 2D TMD saturable absorbers in generating mode-locked pulses. During the experimental process, using selenium to generate mode-locked pulses proves to be more challenging when compared to sulfur and tellurium. Therefore, we are unable to achieve mode-locked pulses for $MoSe_2$. Furthermore, the fabrication time in this research will also impact the performance of these 2D TMDs saturable absorbers. Certain TMD material may require a shorter fabrication time (thinner layer) compared to other TMD material. Some thinner SAs may easily generate mode-locked pulses whereas certain mode-locked pulses required a thicker SA for higher damage threshold. Therefore, the fabrication of these TMDs saturable absorber is guided by the experience gained through testing these SAs in the cavity. Moreover, the frequency of mode-locked pulses is heavily dependent on both the compound material and the fabrication time. For example, using the same material with varying fabrication times will result in different frequency outputs. Thus, we cannot definitively determine which saturable absorbers outperform others in any given situation.

# CHAPTER 6: CONCLUSION AND FUTURE DIRECTION

This chapter concludes the research by presenting a comprehensive summary of all the successful work done in this thesis. In overview, this thesis discloses the experimental validation of Q-switched and mode-locked fiber lasers through the implementation of an innovative fabrication technique for transition metal dichalcogenides (TMDs) incorporating $MoS_2$, $MoSe_2$ and $MoTe_2$ as saturable absorbers. The crucial findings and implications of the research are deliberated upon and concisely outlined. Furthermore, this thesis also explores the potential paths for future research aimed at improving the performance of the pulsed lasers.

## 6.1 Conclusion

This thesis showcases the demonstration of Q-switched and mode-locked fiber lasers in the generation of short pulses with minimal jitter in the 1.55- and 2-micron regions. The successful generation of this ultrashort pulse laser is contributed by both the passive saturable absorber and an optimized laser cavity. By thoroughly executing these four workflows in section 1.4, this research successfully achieves the three predefined objectives. Chapters 3, 4 and 5 address all of these objectives.

The saturable absorber utilized in this study was fabricated and prepared using 2D materials. These 2D materials from the transition metal dichalcogenide group serve as the fundamental material for the saturable absorber specifically $MoS_2$, $MoSe_2$ and $MoTe_2$. The preparation of these transition metal dichalcogenides in this study employs a bottom-up method in contrast to the conventional top-down approach. This innovative approach is known as electro-deposition method. While this method has found application in other research fields, it has not been utilized in the domain of Q-switched and mode-locked fiber lasers.

The first objective was accomplished with the successful fabrication of $MoS_2$, $MoSe_2$, and $MoTe_2$. Subsequently, the second objective of this research was addressed by conducting physical and optical characterizations of these SAs. Surface morphology and the elemental composition of the prepared SAs were characterized using Field Emission Scanning Electron Microscopy (FESEM) and Energy-dispersive X-ray Spectroscopy (EDS). The analysis of the optical properties of the SAs are conducted using in-house setups for linear and nonlinear absorption. The setup for linear absorption involved connecting a white light source to the SA and the output was channeled to an optical spectrum analyzer (OSA). Meanwhile, a twin balance detector technique was used to investigate nonlinear absorption. The electro-deposited $MoS_2$, $MoSe_2$ and $MoTe_2$ thin film exhibit modulation depths of 3.4 %, 5.0 % and 1.7 % respectively. This makes them well-suited for applications of Q-switching and mode-locking. Chapter 3 details the fabrication and characterization of these SAs.

The third objective is to demonstrate various Q-switched and mode-locked pulse generations in various fiber laser cavities using the fabricated SAs. As outlined in Chapter 4, the performances of the SAs have been duly verified through the successful generation of stable Q-switched pulsed lasers in both the 1.5 and 2.0 μm regions as indicated in Table 6.1. This concludes that all transition metal dichalcogenides (TMDs) SAs effectively converted continuous-wave (CW) lasing into Q-switching operation. As detailed in Chapter 5, the successful demonstration of mode-locked pulse generation was achieved using the same fabricated SAs as illustrated in Table 6.2. These findings indicate that electro-deposited TMDs have the capability to generate mode-locked pulses and show significant potential for various photonics applications. With the successful generation of Q-switched and mode-locked pulses using electro-deposited TMDs SAs, this thesis has successfully fulfilled its overall objectives based on the experimental results. These findings collectively indicate the potential of passive devices to inspire further advancements in laser technology. The performance of the pulsed laser aligns with recent studies that highlight the significant potential of electro-deposited TMDs SAs as promising candidates for both Q-switching and mode-locking applications.

**Table 6.1: Performance of TMDs saturable absorber (SA) for Q-switched operation**

| No. | SA | Region **µm** | Q-switched wavelength **nm** | Frequency **kHz** | Input pump power **mW** | Output power **mW** | Pulse Energy **nJ** | SNR **dB** |
|---|---|---|---|---|---|---|---|---|
| 1. | MoS$_2$ | 1.55 | 1559.3 | 57.47–89.89 | 51.67 – 105.27 | 0.517–1.351 | 8.99-15.03 | 62.28 |
| 2. | MoSe$_2$ | 1.55 | 1529;1533 | 74.85-87.41 | 76.75-108.05 | 2.365-3.83 | 31.6-43.8 | 39.99 |
| 3. | MoTe$_2$ | 1.55 | 1558.6 | 40.57–61.07 | 51.67–89.89 | 0.299-0.673 | 7.37-11.02 | 57.52 |
| 4. | MoTe$_2$ | 2.00 | 1910.3 | 23.53-41.61 | 570.30-677.04 | 0.05-0.173 | 1.912-4.158 | 47.60 |

**Table 6.2: Performance of TMDs saturable absorber (SA) for mode-locked operation**

| No. | SA | Region **µm** | Mode-locked wavelength **nm** | Frequency **MHz** | Pulse Width | Input pump power **mW** | Output power **mW** | Pulse Energy **nJ** | SNR **dB** |
|---|---|---|---|---|---|---|---|---|---|
| 1. | MoS$_2$ | 1.55 | 1560.8 | 1.88 | 1.47 ps | 78.5–142.8 | 0.44 – 0.834 | 0.23-0.44 | 53.67 |
| 2. | MoTe$_2$ | 1.55 | 1558 | 1.83 | 225 ns | 94.55 – 158.87 | 3.42 – 6.72 | 1.87-3.67 | 67.57 |

Different 2D TMDs materials exhibit diverse performance characteristics as indicated in the tables above. Several factors can influence the performance of these 2D TMDs material SAs in producing Q-switched or mode-locked pulses including the choice of chemical compound. The conducted experiment revealed that producing Q-switched or mode-locked pulses with Selenium (Se) is more challenging compared to sulfur and tellurium. Therefore, we are unable to achieve mode-locked pulses for $MoSe_2$. On the other hand, the fabrication time of the electrodeposition process in this study will also impact the performance of these 2D SAs. For instance, certain 2D TMDs materials may require less fabrication time which results in thinner layers compared to other TMD materials. Some thinner SA will easily produce Q-switch pulses while some thicker SA will produce mode-lock pulses. Therefore, the experience gained from testing the SAs in the cavity influences the variation in fabricating the new SA. Moreover, the frequency of Q-switched and mode-locked pulses is highly dependent on both the compound material and fabrication time. As an illustration, employing the same material but varying the fabrication time will result in different frequency outputs. Therefore, it is not possible to definitively determine which SAs outperform others in any given situation.

### 6.2 Future Direction

Although all the outlined objectives have been successfully accomplished, there is room for further exploration in demonstrating Q-switched and mode-locked fiber lasers based on TMDs SAs. Additional efforts should be directed towards improving the performance of the proposed fiber laser specifically in terms of reducing pulse width, increasing repetition rate, enhancing output power and improving the pulse energy. Achieving this involves addressing a shorter cavity length and utilizing an improved gain medium. Furthermore, future efforts should concentrate on investigating the electro-deposited TMDs SAs from this study for operation in different wavelength regions specifically in 1 μm and 3.0 μm region respectively. Exploring Q-switched and mode-locked fiber lasers operating in the 3.0 μm region would be a highly interesting area for investigation. On the other hand, exploring the development of new materials for fiber laser applications would be an interesting research area. As electro-deposition has not been attempted in fabricating SAs for pulse laser generation previously, this method can be extended to other TMDs materials groups including $WS_2$, $WSe_2$, $WTe_2$ and so on. In addition, alternative conductive thin films such as ITO thin film and silver nanofilm can be used as substrates for depositing TMDs materials SAs. Furthermore, this electro-deposition method can be extended for the production of topological insulators including materials like Bismuth Telluride ($Bi_2Te_3$), Bismuth Selenide ($Bi_2Se_3$) and Antimony Telluride ($Sb_2Te_3$). Another aspect of improvement includes enhancing the nonlinear properties of the SAs particularly the modulation depth, absorption characteristics, recovery time, damage threshold and wideband absorption. The modulation depth shows a strong correlation with incident power density or thickness ratio which increases in proportion to the density. A higher modulation depth is preferable as it results in a more significant pulse shortening compared to a lower modulation depth. Moreover, the incorporation of a saturable absorber into a well-balanced dispersion optical cavity can lead to the generation of high-quality soliton pulses. Future improvements in the fabrication of saturable absorbers can enhance the quality of the output pulse by employing a thinner layer and ensuring a more uniform surface for the SAs film which can minimize beam divergence and scattering effects. Ultrafast fiber lasers with broad bandwidth, adjustability and high repetition rates are desirable for applications in high-capacity telecommunication systems and photonic fields. At present, harmonic mode-locking stands out as the most promising method for generating this type of pulsed laser. Hence, future research should concentrate on advancing both the theory of high-repetition-rate mode-locked cavities which is  commonly referred to as harmonic mode-locking and the experimental development of a highly stable passive harmonic mode-locked erbium-doped fiber laser through cavity manipulation.

## 6.3 Novelty and Significance of the Research Contribution

This research introduces significant novelty by exploring innovative fabrication techniques and materials in the field of 2D saturable absorbers (SAs). By using electro-deposition methods to produce molybdenum dichalcogenides of $MoS_2$, $MoSe_2$, and $MoTe_2$ as passive saturable absorbers, this study addresses the current challenges related to the consistency and reproducibility of material properties. The exploration into less commonly studied materials and innovative fabrication approaches contributes valuable insights and paves the way for new research opportunities. Moreover, the comprehensive characterization and practical assessment of these electro-deposited SAs in photonic devices including mode-locked and Q-switched fiber lasers have highlighted their potential benefits and enhance the reliability and performance of photonic technologies. This research represents a meaningful advancement in the optimization and application of 2D SAs, highlighting its importance and impact on the field. This research marks a significant advancement in optimizing and applying 2D SAs, highlighting its importance and impact on the field of photonics and material science.

# REFERENCES

Adel, P. (2004). *Pulsed Fiber Lasers*. Cuvillier. https://books.google.com.my/books?id=xJoFPWAacC0C

Agostini, P., & DiMauro, L. F. (2004). The physics of attosecond light pulses. *Reports on progress in physics*, *67*(6), 813.

Agrawal, G. P. (1987). Modulation instability induced by cross-phase modulation. *Physical review letters*, *59*(8), 880.

Agrawal, G. P. (2000). Nonlinear fiber optics. In *Nonlinear Science at the Dawn of the 21st Century* (pp. 195-211). Springer.

Agrawal, G. P. (2007). *Nonlinear Fiber Optics*. Elsevier Science. https://books.google.com.my/books?id=b5S0JqHMoxAC

Ahmed, J., Hussain, A., Siyal, M., Manzoor, H., & Masood, A. (2014). Parametric analysis of four wave mixing in DWDM systems. *Optik*, *125*(7), 1853-1859.

Al-Hiti, A. S., Al-Masoodi, A. H., Wong, W. R., Yasin, M., Al-Masoodi, A. H., & Harun, S. (2021). Nanosecond passively Q-switched fiber laser in the 1.5 µm region using turmeric saturable absorber. *Optics & Laser Technology*, *139*, 106971.

Al-Hiti, A. S., Rahman, M. F. A., Harun, S. W., Yupapin, P., & Yasin, M. (2019). Holmium oxide thin film as a saturable absorber for generating Q-switched and mode-locked erbium-doped fiber lasers. *Optical fiber technology*, *52*, 101996.

Alfano, R. R., Shen, Y., & Yang, G.-Z. (2016). Theory of self-phase modulation and spectral broadening. *The Supercontinuum Laser Source: The Ultimate White Light*, 1-32.

Anand, J. S., Rajan, R. K., & Zaidan, A. A. M. (2013). Electrosynthesized NiS2 thin films and their optical and semiconductor studies. *Reports in Electrochemistry*, *3*, 25.

Anderson, P., Aranas, E. B., Assaf, Y., Behrendt, R., Black, R., Caballero, M., Cameron, P., Canakci, B., De Carvalho, T., & Chatzieleftheriou, A. (2023). Project Silica: towards sustainable cloud archival storage in glass. Proceedings of the 29th Symposium on Operating Systems Principles,

Anderson, P., Black, R., Cerkauskaite, A., Chatzieleftheriou, A., Clegg, J., Dainty, C., Diaconu, R., Drevinskas, R., Donnelly, A., & Gaunt, A. L. (2018). Glass: A new media for a new era? 10th USENIX Workshop on Hot Topics in Storage and File Systems (HotStorage 18),

Anuar, K., Tan, W., Atan, M., Dzulkefly, K., Ho, S., Jelas, H. M., & Saravanan, N. (2007). Cyclic voltammetry study of copper tin sulfide compounds. *Pacific J. Sci. Technol*, *8*(2), 252-260.

Aso, O., Tadakuma, M., & Namiki, S. (1999). Four-wave mixing in optical fibers and its applications. *dEp*, *1*(2).

Babu, P., Seo, H. J., Jang, K. H., Balakrishnaiah, R., Jayasankar, C., Lim, K.-S., & Lavín, V. (2007). Optical spectroscopy, 1.5 μm emission, and upconversion properties of Er 3+-doped metaphosphate laser glasses. *JOSA B*, *24*(9), 2218-2228.

Banhart, F., Kotakoski, J., & Krasheninnikov, A. V. (2011). Structural defects in graphene. *ACS nano*, *5*(1), 26-41.

Bao, Q., Zhang, H., Ni, Z., Wang, Y., Polavarapu, L., Shen, Z., Xu, Q.-H., Tang, D., & Loh, K. P. (2011). Monolayer graphene as a saturable absorber in a mode-locked laser. *Nano Research*, *4*, 297-307.

Bao, Q., Zhang, H., Wang, Y., Ni, Z., Yan, Y., Shen, Z. X., Loh, K. P., & Tang, D. Y. (2009). Atomic‐layer graphene as a saturable absorber for ultrafast pulsed lasers. *Advanced Functional Materials*, *19*(19), 3077-3083.

Basiev, T., Sobol, A., Zverev, P., Ivleva, L., Osiko, V., & Powell, R. (1999). Raman spectroscopy of crystals for stimulated Raman scattering. *Optical materials*, *11*(4), 307-314.

Becker, R. (2000). Produced and process water recycling using two highly efficient systems to make distilled water. SPE Annual Technical Conference and Exhibition?,

Behrens, R. G., Lemons, R. S., & Rosenblatt, G. M. (1974). Vapor pressure and thermodynamics of selenium dioxide. The enthalpy of atomization of SeO2 (g). *The Journal of Chemical Thermodynamics*, *6*(5), 457-466.

Bernard, F., Zhang, H., Gorza, S.-P., & Emplit, P. (2012). Towards mode-locked fiber laser using topological insulators. Nonlinear Photonics,

Bikorimana, S., Lama, P., Walser, A., Dorsinville, R., Anghel, S., Mitioglu, A., Micu, A., & Kulyuk, L. (2016). Nonlinear optical responses in two-dimensional transition metal dichalcogenide multilayer: WS 2, WSe 2, MoS 2 and Mo 0.5 W 0.5 S 2. *Optics express*, *24*(18), 20685-20695.

Blackmon, R. L., Hutchens, T. C., Hardy, L. A., Wilson, C. R., Irby, P. B., & Fried, N. M. (2015). Thulium fiber laser ablation of kidney stones using a 50-μ m-core silica optical fiber. *Optical Engineering*, *54*(1), 011004-011004.

Boguslawski, J., Sotor, J., Sobon, G., Tarka, J., Jagiello, J., Macherzynski, W., Lipinska, L., & Abramski, K. (2014). Mode-locked Er-doped fiber laser based on liquid phase exfoliated Sb2Te3 topological insulator. *Laser Physics*, *24*(10), 105111.

Bonaccorso, F., Sun, Z., Hasan, T., & Ferrari, A. (2010). Graphene photonics and optoelectronics. *Nature photonics*, *4*(9), 611-622.

Bret, G., & Gires, F. (1964). Giant‐pulse laser and light amplifier using variable transmission coefficient glasses as light switches. *Applied Physics Letters*, *4*(10), 175-176.

Butler, S. Z., Hollen, S. M., Cao, L., Cui, Y., Gupta, J. A., Gutiérrez, H. R., Heinz, T. F., Hong, S. S., Huang, J., & Ismach, A. F. (2013). Progress, challenges, and opportunities in two-dimensional materials beyond graphene. *ACS nano*, *7*(4), 2898-2926.

Cai, Y., Feng, J., Wang, H., Ferrini, G., Xu, X., Jing, J., & Treps, N. (2015). Quantum-network generation based on four-wave mixing. *Physical Review A*, *91*(1), 013843.

Cai, Z., Liu, B., Zou, X., & Cheng, H.-M. (2018). Chemical vapor deposition growth and applications of two-dimensional materials and their heterostructures. *Chemical reviews*, *118*(13), 6091-6133.

Carlsson, J.-O., & Martin, P. M. (2010). Chemical vapor deposition. In *Handbook of Deposition Technologies for films and coatings* (pp. 314-363). Elsevier.

Castellanos-Gomez, A., Vicarelli, L., Prada, E., Island, J. O., Narasimha-Acharya, K., Blanter, S. I., Groenendijk, D. J., Buscema, M., Steele, G. A., & Alvarez, J. (2014). Isolation and characterization of few-layer black phosphorus. *2D Materials*, *1*(2), 025001.

Chandra, S., & Sahu, S. (1984). Electrodeposited semiconducting molybdenum selenide films. I. Preparatory technique and structural characterisation. *Journal of Physics D: Applied Physics*, *17*(10), 2115.

Chang, Y. M., Kim, H., Lee, J. H., & Song, Y.-W. (2010). Multilayered graphene efficiently formed by mechanical exfoliation for nonlinear saturable absorbers in fiber mode-locked lasers. *Applied Physics Letters*, *97*(21).

Chen, Y., Chen, S., Liu, J., Gao, Y., & Zhang, W. (2016). Sub-300 femtosecond soliton tunable fiber laser with all-anomalous dispersion passively mode locked by black phosphorus. *Optics Express*, *24*(12), 13316-13324.

Chen, Y., Jiang, G., Chen, S., Guo, Z., Yu, X., Zhao, C., Zhang, H., Bao, Q., Wen, S., & Tang, D. (2015). Mechanically exfoliated black phosphorus as a new saturable absorber for both Q-switching and mode-locking laser operation. *Optics express*, *23*(10), 12823-12833.

Chen, Y., Zhao, C., Huang, H., Chen, S., Tang, P., Wang, Z., Lu, S., Zhang, H., Wen, S., & Tang, D. (2013). Self-assembled topological insulator: Bi $ _ {2} $ Se $ _ {3} $ membrane as a passive Q-switcher in an Erbium-doped fiber laser. *Journal of lightwave technology*, *31*(17), 2857-2863.

Cheng, J.-X., Min, W., Ozeki, Y., & Polli, D. (2021). *Stimulated Raman scattering microscopy: Techniques and applications*. Elsevier.

Cheng, Q., Miao, Y., Wild, J., Min, W., & Yang, Y. (2021). Emerging applications of stimulated Raman scattering microscopy in materials science. *Matter*, *4*(5), 1460-1483.

Choi, D. S., Kim, C. H., Lee, T., Nah, S., Rhee, H., & Cho, M. (2019). Vibrational spectroscopy and imaging with non-resonant coherent anti-Stokes Raman scattering: double stimulated Raman scattering scheme. *Optics express*, *27*(16), 23558-23575.

Churchill, H. O., & Jarillo-Herrero, P. (2014). Phosphorus joins the family. *Nature nanotechnology*, *9*(5), 330-331.

Cui, Y., Lu, F., & Liu, X. (2016). MoS2-clad microfibre laser delivering conventional, dispersion-managed and dissipative solitons. *Scientific reports*, *6*(1), 1-8.

Das, K. (2022). Spin coating of sacrificial Polyvinyl Alcohol thin film on Silicon Substrate. *Materials Science*.

Demon, S. Z. N., Kamisan, A. I., Abdullah, N., Noor, S. A. M., Khim, O. K., Kasim, N. A. M., Yahya, M. Z. A., Manaf, N. A. A., Azmi, A. F. M., & Halim, N. A. (2020). Graphene-based Materials in Gas Sensor Applications: A Review. *Sensors & Materials*, *32*.

Dennis, M. L., & Duling, I. N. (1994). Experimental study of sideband generation in femtosecond fiber lasers. *IEEE Journal of Quantum electronics*, *30*(6), 1469-1477.

Desurvire, E., Simpson, J. R., & Becker, P. (1987). High-gain erbium-doped traveling-wave fiber amplifier. *Optics letters*, *12*(11), 888-890.

Dickey, F. M. (2018). *Laser beam shaping: theory and techniques*. CRC press.

Diels, J.-C., & Rudolph, W. (2006). *Ultrashort laser pulse phenomena*. Elsevier.

Diels, J. C., & Rudolph, W. (2006). *Ultrashort Laser Pulse Phenomena*. Elsevier Science. https://books.google.com.my/books?id=rDQe81K0d3kC

Dobkin, D., & Zuraw, M. K. (2003). *Principles of chemical vapor deposition*. Springer Science & Business Media.

Du, J., Wang, Q., Jiang, G., Xu, C., Zhao, C., Xiang, Y., Chen, Y., Wen, S., & Zhang, H. (2014). Ytterbium-doped fiber laser passively mode locked by few-layer Molybdenum Disulfide (MoS2) saturable absorber functioned with evanescent field interaction. *Scientific reports*, *4*(1), 1-7.

Du, Y., Han, M., Cheng, P., & Shu, X. (2019). Pulsating soliton with broadened Kelly sidebands in an ultrafast fiber laser. *Optics letters*, *44*(16), 4087-4090.

Dutta, N. K. (2024). *Mode-locked Lasers: Introduction To Ultrafast Semiconductor And Fiber Lasers*. World Scientific Publishing Company. https://books.google.com.my/books?id=umMOEQAAQBAJ

Dzhibladze, M. I., Esiashvili, Z., Teplitskiĭ, É. S., Isaev, S. K., & Sagaradze, V. (1983). Mode locking in a fiber laser. *Soviet Journal of Quantum Electronics*, *13*(2), 245.

Ebnali-Heidari, M., Monat, C., Grillet, C., & Moravvej-Farshi, M. (2009). A proposal for enhancing four-wave mixing in slow light engineered photonic crystal waveguides and its application to optical regeneration. *Optics express*, *17*(20), 18340-18353.

Eftekhari, A. (2017). Tungsten dichalcogenides (WS 2, WSe 2, and WTe 2): materials chemistry and applications. *Journal of Materials Chemistry A*, *5*(35), 18299-18325.

Einstein, A. (1916). Zur quantentheorie der strahlung. *Physikalische Gesellschaft Zürich*, *18*, 47-62.

El Ghazouani, J., Saidoun, M., Tort, F., & Daridon, J.-L. (2023). Experimental Evaluation Method of Asphaltene Deposition Inhibitor's Efficacity at Atmospheric Pressure Using a Fully Immersed Quartz Crystal Resonator, Centrifugation, and Optical Microscopy Techniques. *Energy & Fuels*, *37*(8), 5895-5904.

Elgrishi, N., Rountree, K. J., McCarthy, B. D., Rountree, E. S., Eisenhart, T. T., & Dempsey, J. L. (2018). A practical beginner's guide to cyclic voltammetry. *Journal of chemical education*, *95*(2), 197-206.

Eng, A. Y. S., Chua, C. K., & Pumera, M. (2015). Intrinsic electrochemical performance and precise control of surface porosity of graphene-modified electrodes using the drop-casting technique. *Electrochemistry Communications*, *59*, 86-90.

Evans, C. D., Monteith, D. T., Fowler, D., Cape, J. N., & Brayshaw, S. (2011). Hydrochloric acid: an overlooked driver of environmental change. *Environmental Science & Technology*, *45*(5), 1887-1894.

Faubert, D., & Chin, S. (1982). Short laser pulse generation: Part one. *Optics & Laser Technology*, *14*(4), 197-206.

Fauziah, C., Rosol, A., Latiff, A., & Harun, S. (2017). The generation of q-switched erbium-doped fiber laser using black phosphorus saturable absorber with 8% modulation depth. IOP Conference Series: Materials Science and Engineering,

Fermann, M. E., & Hartl, I. (2013). Ultrafast fibre lasers. *Nature photonics*, *7*(11), 868-874.

Ferreira, M. F. S., & Paul, M. C. (2024). *Specialty Optical Fibers: Materials, Fabrication Technology, and Applications*. Elsevier Science. https://books.google.com.my/books?id=UdPKEAAAQBAJ

Fox, A. M. (2001). *Optical Properties of Solids*. Oxford University Press. https://books.google.com.my/books?id=-5bVBbAoaGoC

Franken, e. P., Hill, A. E., Peters, C., & Weinreich, G. (1961). Generation of optical harmonics. *Physical review letters*, *7*(4), 118.

Freudiger, C. W., Yang, W., Holtom, G. R., Peyghambarian, N., Xie, X. S., & Kieu, K. Q. (2014). Stimulated Raman scattering microscopy with a robust fibre laser source. *Nature photonics*, *8*(2), 153-159.

Fu, B., Hua, Y., Xiao, X., Zhu, H., Sun, Z., & Yang, C. (2014). Broadband graphene saturable absorber for pulsed fiber lasers at 1, 1.5, and 2 μm. *IEEE Journal of Selected Topics in Quantum Electronics*, *20*(5), 411-415.

Ganeev, R. A. (2013). *Nonlinear Optical Properties of Materials*. Springer Netherlands. https://books.google.com.my/books?id=r6G5BQAAQBAJ

Gapontsev, V., Fomin, V., & Yusim, A. (2009). Recent progress in scaling of high-power fiber lasers at IPG photonics. *22nd Annual Solid State and Diode Laser Technology Review*.

Garmire, E. (2000). Resonant optical nonlinearities in semiconductors. *IEEE Journal of Selected Topics in Quantum Electronics*, *6*(6), 1094-1110.

Gattass, R. R., & Mazur, E. (2008). Femtosecond laser micromachining in transparent materials. *Nature photonics*, *2*(4), 219-225.

Ge, Y., Zhao, F., & Wei, J. (2018). A high order compact ADI method for solving 3D unsteady convection diffusion problems. *Applied and Computational Mathematics*, *7*(1), 1-10.

Geim, A. K., & Grigorieva, I. V. (2013). Van der Waals heterostructures. *Nature*, *499*(7459), 419-425.

Geim, A. K., & Novoselov, K. S. (2007). The rise of graphene. *Nature materials*, *6*(3), 183-191.

Ghassemlooy, Z., Popoola, W., & Rajbhandari, S. (2019). *Optical Wireless Communications: System and Channel Modelling with MATLAB®, Second Edition*. CRC Press. https://books.google.com.my/books?id=v02WDwAAQBAJ

Gordon, J. P., Zeiger, H. J., & Townes, C. H. (1954). Molecular microwave oscillator and new hyperfine structure in the microwave spectrum of N H 3. *Physical Review*, *95*(1), 282.

Grudinin, A. (2013). Fibre laser directions. *Nature Photonics*, *7*(11), 846-847.

Gu, M., Satija, A., & Lucht, R. P. (2019). Effects of self-phase modulation (SPM) on femtosecond coherent anti-Stokes Raman scattering spectroscopy. *Optics express*, *27*(23), 33954-33966.

Guerreiro, P., Ten, S., Borrelli, N., Butty, J., Jabbour, G., & Peyghambarian, N. (1997). PbS quantum-dot doped glasses as saturable absorbers for mode locking of a Cr: forsterite laser. *Applied Physics Letters*, *71*(12), 1595-1597.

Gupta, A., Chen, G., Joshi, P., Tadigadapa, S., & Eklund. (2006). Raman scattering from high-frequency phonons in supported n-graphene layer films. *Nano letters*, *6*(12), 2667-2673.

Gusakova, J., Wang, X., Shiau, L. L., Krivosheeva, A., Shaposhnikov, V., Borisenko, V., Gusakov, V., & Tay, B. K. (2017). Electronic properties of bulk and monolayer TMDs: theoretical study within DFT framework (GVJ‐2e method). *physica status solidi (a)*, *214*(12), 1700218.

Hancock, Y. (2011). The 2010 Nobel Prize in physics—ground-breaking experiments on graphene. *Journal of Physics D: Applied Physics*, *44*(47), 473001.

Hankare, P., Bhuse, V., Garadkar, K., Delekar, S., & Mulla, I. (2003). Low temperature route to grow polycrystalline cadmium selenide and mercury selenide thin films. *Materials chemistry and physics*, *82*(3), 711-717.

Haris, H., Harun, S., Muhammad, A., Anyi, C., Tan, S., Ahmad, F., Nor, R., Zulkepely, N., & Arof, H. (2017). Passively Q-switched Erbium-doped and Ytterbium-doped fibre lasers with topological insulator bismuth selenide (Bi2Se3) as saturable absorber. *Optics & Laser Technology*, *88*, 121-127.

Harun, S. W., & Arof, H. (2013). *Current Developments in Optical Fiber Technology*. IntechOpen. https://books.google.com.my/books?id=GHafDwAAQBAJ

Harun, S. W., Zulkipli, N., Muhammad, A. R., & Latiff, A. A. (2019). Q‐Switching Pulses Generation Using Topology Insulators as Saturable Absorber. *Advanced Topological Insulators*, 207-238.

Hasan, T., Sun, Z., Wang, F., Bonaccorso, F., Tan, P. H., Rozhin, A. G., & Ferrari, A. C. (2009). Nanotube–polymer composites for ultrafast photonics. *Advanced materials*, *21*(38‐39), 3874-3899.

Hasegawa, A. (2013). *Optical Solitons in Fibers*. Springer Berlin Heidelberg. https://books.google.com.my/books?id=Nl7_CAAAQBAJ

Haus, H. A. (2000). Mode-locking of lasers. *IEEE Journal of Selected Topics in Quantum Electronics*, *6*(6), 1173-1185.

Hazlihan, H. (2018). *Generation of ultra-short pulse lasers using graphene and topological insulator based 2D nanomaterials/Hazlihan Haris* Universiti Malaya].

Hecht, J. (2010). Short history of laser development. *Optical engineering*, *49*(9), 091002-091002-091023.

Heinze, J. (1984). Cyclic voltammetry—"electrochemical spectroscopy". New analytical methods (25). *Angewandte Chemie International Edition in English*, *23*(11), 831-847.

Hercher, M. (1967). An analysis of saturable absorbers. *Applied Optics*, *6*(5), 947-954.

Herguth, W. R., & Nadeau, G. (2004). Applications of scanning electron microscopy and energy dispersive spectroscopy (SEM/EDS) to practical tribology problems. *Herguth Lab Inc CA*, *94590*.

Huang, Y., Luo, Z., Li, Y., Zhong, M., Xu, B., Che, K., Xu, H., Cai, Z., Peng, J., & Weng, J. (2014). Widely-tunable, passively Q-switched erbium-doped fiber laser with few-layer MoS 2 saturable absorber. *Optics express*, *22*(21), 25258-25266.

Ippen, E., Shank, C., & Dienes, A. (1972). Passive mode locking of the cw dye laser. *Applied Physics Letters*, *21*(8), 348-350.

Islam, M. N., Mollenauer, L. F., Stolen, R. H., Simpson, J. R., & Shang, H.-T. (1987). Cross-phase modulation in optical fibers. *Optics letters*, *12*(8), 625-627.

Island, J. O., Steele, G. A., van der Zant, H. S., & Castellanos-Gomez, A. (2015). Environmental instability of few-layer black phosphorus. *2D Materials*, *2*(1), 011002.

Ismail, M. A., Harun, S. W., Zulkepely, N. R., Nor, R. M., Ahmad, F., & Ahmad, H. (2012). Nanosecond soliton pulse generation by mode-locked erbium-doped fiber laser using single-walled carbon-nanotube-based saturable absorber. *Applied optics*, *51*(36), 8621-8624.

Javan, A., Bennett Jr, W. R., & Herriott, D. R. (1961). Population inversion and continuous optical maser oscillation in a gas discharge containing a He-Ne mixture. *Physical Review Letters*, *6*(3), 106.

Jeon, M. Y. (2021). *Fiber Optic Sensors and Fiber Lasers*. MDPI AG. https://books.google.com.my/books?id=C91BEAAAQBAJ

Jin, X., Hu, G., Zhang, M., Hu, Y., Albrow-Owen, T., Howe, R. C., Wu, T.-C., Wu, Q., Zheng, Z., & Hasan, T. (2018). 102 fs pulse generation from a long-term stable, inkjet-printed black phosphorus-mode-locked fiber laser. *Optics express*, *26*(10), 12506-12513.

Johnson, L., Geusic, J., & Van Uitert, L. (1965). Coherent oscillations from Tm3+, Ho3+, Yb3+ and Er3+ ions in yttrium aluminum garnet. *Applied Physics Letters*, *7*(5), 127-129.

Jones, D. J., Diddams, S. A., Taubman, M. S., Cundiff, S. T., Ma, L.-S., & Hall, J. L. (2000). Frequency comb generation using femtosecond pulses and cross-phase modulation in optical fiber at arbitrary center frequencies. *Optics letters*, *25*(5), 308-310.

Kalisky, Y. (2004). Cr4+-doped crystals: their use as lasers and passive Q-switches. *Progress in Quantum Electronics*, *28*(5), 249-303.

Keller, U. (2003). Recent developments in compact ultrafast lasers. *nature*, *424*(6950), 831-838.

Keller, U., Miller, D., Boyd, G., Chiu, T., Ferguson, J., & Asom, M. (1992). Solid-state low-loss intracavity saturable absorber for Nd: YLF lasers: an antiresonant semiconductor Fabry–Perot saturable absorber. *Optics letters*, *17*(7), 505-507.

Koester, C. J., & Snitzer, E. (1964). Amplification in a fiber laser. *Applied optics*, *3*(10), 1182-1186.

Kumar, A. K. S., Zhang, Y., Li, D., & Compton, R. G. (2020). A mini-review: How reliable is the drop casting technique? *Electrochemistry Communications*, *121*, 106867.

Kumar, R., Singh, A. P., Kapoor, A., & Tripathi, K. N. (2004). Fabrication and characterization of polyvinyl-alcohol-based thin-film optical waveguides. *Optical Engineering*, *43*(9), 2134-2142.

Lamb Jr, W. E. (1964). Theory of an optical maser. *Physical Review*, *134*(6A), A1429.

Leciejewicz, J. (1961). The crystal structure of tellurium dioxide. A redetermination by neutron diffraction. *Zeitschrift für Kristallographie*, *116*(3-6), 345-353.

Lee, E. J., Choi, S. Y., Jeong, H., Park, N. H., Yim, W., Kim, M. H., Park, J.-K., Son, S., Bae, S., & Kim, S. J. (2015). Active control of all-fibre graphene devices with electrical gating. *Nature communications*, *6*(1), 6851.

Lefrancois, S., Fu, D., Holtom, G. R., Kong, L., Wadsworth, W. J., Schneider, P., Herda, R., Zach, A., Xie, X. S., & Wise, F. W. (2012). Fiber four-wave mixing source for coherent anti-Stokes Raman scattering microscopy. *Optics letters*, *37*(10), 1652-1654.

Li, D., Jussila, H., Karvonen, L., Ye, G., Lipsanen, H., Chen, X., & Sun, Z. (2015a). Polarization and thickness dependent absorption properties of black phosphorus: new saturable absorber for ultrafast pulse generation. *Scientific reports*, *5*(1), 1-9.

Li, D., Jussila, H., Karvonen, L., Ye, G., Lipsanen, H., Chen, X., & Sun, Z. (2015b). Ultrafast pulse generation with black phosphorus. *arXiv preprint arXiv:1505.00480*.

Li, X., Tao, L., Chen, Z., Fang, H., Li, X., Wang, X., Xu, J.-B., & Zhu, H. (2017). Graphene and related two-dimensional materials: Structure-property relationships for electronics and optoelectronics. *Applied Physics Reviews*, *4*(2).

Li, Y., Shen, B., Li, S., Zhao, Y., Qu, J., & Liu, L. (2021). Review of stimulated Raman scattering microscopy techniques and applications in the biosciences. *Advanced Biology*, *5*(1), 2000184.

Liang, X., Kumar, S., Shao, J., Malekiha, M., & Plant, D. V. (2014). Digital compensation of cross-phase modulation distortions using perturbation technique for dispersion-managed fiber-optic systems. *Optics Express*, *22*(17), 20634-20645.

Lin, Y.-H., Yang, C.-Y., Liou, J.-H., Yu, C.-P., & Lin, G.-R. (2013). Using graphene nano-particle embedded in photonic crystal fiber for evanescent wave mode-locking of fiber laser. *Optics express*, *21*(14), 16763-16776.

Ling, S. J., Moebs, W., & Sanny, J. (2016). 16.5 The Electromagnetic Spectrum. *University Physics Volume 2*.

Liu, H., Luo, A.-P., Wang, F.-Z., Tang, R., Liu, M., Luo, Z.-C., Xu, W.-C., Zhao, C.-J., & Zhang, H. (2014). Femtosecond pulse erbium-doped fiber laser by a few-layer MoS 2 saturable absorber. *Optics letters*, *39*(15), 4591-4594.

Liu, H., Zheng, X.-W., Liu, M., Zhao, N., Luo, A.-P., Luo, Z.-C., Xu, W.-C., Zhang, H., Zhao, C.-J., & Wen, S.-C. (2014). Femtosecond pulse generation from a topological insulator mode-locked fiber laser. *Optics express*, *22*(6), 6868-6873.

Liu, J. M. (2016). *Principles of Photonics*. Cambridge University Press. https://books.google.com.my/books?id=lbXDDAAAQBAJ

Liu, X., Yang, H., Cui, Y., Chen, G., Yang, Y., Wu, X., Yao, X., Han, D., Han, X., & Zeng, C. (2016). Graphene-clad microfibre saturable absorber for ultrafast fibre lasers. *Scientific reports*, *6*(1), 1-8.

Lokhande, C., Sankapal, B., Mane, R., Pathan, H., Muller, M., Giersig, M., & Ganesan, V. (2002). XRD, SEM, AFM, HRTEM, EDAX and RBS studies of chemically deposited Sb2S3 and Sb2Se3 thin films. *Applied Surface Science*, *193*(1-4), 1-10.

Lu, F.-K., Basu, S., Igras, V., Hoang, M. P., Ji, M., Fu, D., Holtom, G. R., Neel, V. A., Freudiger, C. W., & Fisher, D. E. (2015). Label-free DNA imaging in vivo with stimulated Raman scattering microscopy. *Proceedings of the National Academy of Sciences*, *112*(37), 11624-11629.

Lu, S., Miao, L., Guo, Z., Qi, X., Zhao, C., Zhang, H., Wen, S., Tang, D., & Fan, D. (2015). Broadband nonlinear optical response in multi-layer black phosphorus: an emerging infrared and mid-infrared optical material. *Optics express*, *23*(9), 11183-11194.

Luo, Z., Huang, Y., Zhong, M., Li, Y., Wu, J., Xu, B., Xu, H., Cai, Z., Peng, J., & Weng, J. (2014). 1-, 1.5-, and 2-μm fiber lasers Q-switched by a broadband few-layer MoS 2 saturable absorber. *Journal of lightwave Technology*, *32*(24), 4077-4084.

Luo, Z., Li, Y., Zhong, M., Huang, Y., Wan, X., Peng, J., & Weng, J. (2015). Nonlinear optical absorption of few-layer molybdenum diselenide (MoSe 2) for passively mode-locked soliton fiber laser. *Photonics Research*, *3*(3), A79-A86.

Luo, Z., Wu, D., Xu, B., Xu, H., Cai, Z., Peng, J., Weng, J., Xu, S., Zhu, C., & Wang, F. (2016). Two-dimensional material-based saturable absorbers: towards compact visible-wavelength all-fiber pulsed lasers. *Nanoscale*, *8*(2), 1066-1072.

Luo, Z., Zhou, M., Weng, J., Huang, G., Xu, H., Ye, C., & Cai, Z. (2010). Graphene-based passively Q-switched dual-wavelength erbium-doped fiber laser. *Optics letters*, *35*(21), 3709-3711.

Macleod, H. A. (2018). Recent developments in deposition techniques for optical thin films and coatings. *Optical Thin Films and Coatings*, 3-23.

Maiman, T. (1960). Optical and microwave-optical experiments in ruby. *Physical review letters*, *4*(11), 564.

Malik, A. H., Azeem, M., Hamza, M. Y., & Tariq, S. (2008). Comparison of interaction of GVD and SPM between normal and anomalous dispersion regimes of single mode fiber. 2008 Second International Conference on Electrical Engineering,

Mamalis, N. (2011). Femtosecond laser: the future of cataract surgery? *Journal of Cataract & Refractive Surgery*, *37*(7), 1177-1178.

Manassah, J. T. (1989). Simple models of self-phase and induced-phase modulation. In *The Supercontinuum Laser Source: Fundamentals with Updated References* (pp. 184-294). Springer.

Manzeli, S., Ovchinnikov, D., Pasquier, D., Yazyev, O. V., & Kis, A. (2017). 2D transition metal dichalcogenides. *Nature Reviews Materials*, *2*(8), 1-15.

Mao, D., Wang, Y., Ma, C., Han, L., Jiang, B., Gan, X., Hua, S., Zhang, W., Mei, T., & Zhao, J. (2015). WS2 mode-locked ultrafast fiber laser. *Scientific Reports*, *5*(1), 7965.

Martín-Palma, R. J., Martínez-Duart, J., & Agulló-Rueda, F. (2006). *Nanotechnology for microelectronics and optoelectronics*. Elsevier.

Martinez, A., & Sun, Z. (2013). Nanotube and graphene saturable absorbers for fibre lasers. *Nature photonics*, *7*(11), 842-845.

McCullough, J. D. (1937). The crystal structure of selenium dioxide. *Journal of the American Chemical Society*, *59*(5), 789-794.

McFerran, J. (2009). Échelle spectrograph calibration with a frequency comb based on a harmonically mode-locked fiber laser: a proposal. *Applied optics*, *48*(14), 2752-2759.

Mears, R., Reekie, L., Jauncey, I., & PAYNE, D. N. (1987). High-gain rare-earth-doped fiber amplifier at 1.54 µm. Optical Fiber Communication Conference,

Mears, R., Reekie, L., Poole, S., & Payne, D. (1985). Neodymium-doped silica single-mode fibre lasers. *Electronics letters*, *21*, 738-740.

Miao, L., Jiang, Y., Lu, S., Shi, B., Zhao, C., Zhang, H., & Wen, S. (2015). Broadband ultrafast nonlinear optical response of few-layers graphene: toward the mid-infrared regime. *Photonics Research*, *3*(5), 214-219.

Mikulla, B., Leng, L., Sears, S., Collings, B., Arend, M., & Bergman, K. (1999). Broad-band high-repetition-rate source for spectrally sliced WDM. *IEEE Photonics Technology Letters*, *11*(4), 418-420.

Milonni, P. W., & Eberly, J. H. (2010). *Laser physics*. John Wiley & Sons.

Mu, H., Lin, S., Wang, Z., Xiao, S., Li, P., Chen, Y., Zhang, H., Bao, H., Lau, S. P., & Pan, C. (2015). Black phosphorus–polymer composites for pulsed lasers. *Advanced Optical Materials*, *3*(10), 1447-1453.

Mustapha, A. B., Shamsuddin, S., Rizvi, S. Z. H., Asman, S. B., & Jamaian, S. S. (2022). *Proceedings of the 7th International Conference on the Applications of Science and Mathematics 2021: Sciemathic 2021*. Springer Nature Singapore. https://books.google.com.my/books?id=5qd3EAAAQBAJ

Nayak, P. K. (2016). *Two-dimensional Materials: Synthesis, Characterization and Potential Applications*. IntechOpen. https://books.google.com.my/books?id=lnCPDwAAQBAJ

Nelson, L. E., Jones, D., Tamura, K., Haus, H. A., & Ippen, E. (1997). Ultrashort-pulse fiber ring lasers. *Applied Physics B: Lasers & Optics*, *65*(2).

Nicholson, J., Windeler, R., & DiGiovanni, D. (2007). Optically driven deposition of single-walled carbon-nanotube saturable absorbers on optical fiber end-faces. *Optics express*, *15*(15), 9176-9183.

Nikoloski, A. N., & Ang, K.-L. (2014). Review of the application of ion exchange resins for the recovery of platinum-group metals from hydrochloric acid solutions. *Mineral Processing and Extractive Metallurgy Review*, *35*(6), 369-389.

Nolte, S., Schrempel, F., & Dausinger, F. (2015). *Ultrashort Pulse Laser Technology: Laser Sources and Applications*. Springer International Publishing. https://books.google.com.my/books?id=AN_HCgAAQBAJ

Okamoto, K. (2021). *Fundamentals of optical waveguides*. Elsevier.

Opiolka, S., Schmidt, F., & Fissan, H. (1994). Combined effects of electrophoresis and thermophoresis on particle deposition onto flat surfaces. *Journal of Aerosol Science*, *25*(4), 665-671.

Ouerfelli, J., Srivastava, S., Bernède, J., & Belgacem, S. (2008). Effect of microwaves on synthesis of MoS2 and WS2. *Vacuum*, *83*(2), 308-312.

Ovezmyradov, M., Magedov, I. V., Frolova, L. V., Chandler, G., Garcia, J., Bethke, D., Shaner, E. A., & Kalugin, N. G. (2015). Chemical vapor deposition of phosphorous-and boron-doped graphene using phenyl-containing molecules. *Journal of Nanoscience and Nanotechnology*, *15*(7), 4883-4886.

Oyerinde, O. F., Weeks, C. L., Anbar, A. D., & Spiro, T. G. (2008). Solution structure of molybdic acid from Raman spectroscopy and DFT analysis. *Inorganica Chimica Acta*, *361*(4), 1000-1007.

Paschotta, D. (2022). Ytterbium-doped laser gain media. In: Ytterbium-doped laser gain media, explained by RP Photonics Encyclopedia.

Paschotta, R. (2008). *Field guide to laser pulse generation* (Vol. 14). SPIE press Bellingham.

Peng, K.-J., Lin, Y.-H., Wu, C.-L., Lin, S.-F., Yang, C.-Y., Lin, S.-M., Tsai, D.-P., & Lin, G.-R. (2015). Dissolution-and-reduction CVD synthesis of few-layer graphene on ultra-thin nickel film lifted off for mode-locking fiber lasers. *Scientific Reports*, *5*(1), 13689.

Peng, X., & Yan, Y. (2021). Graphene saturable absorbers applications in fiber lasers. *Journal of the European Optical Society-Rapid Publications*, *17*(1), 16.

Purdie, D., Popa, D., Wittwer, V., Jiang, Z., Bonacchini, G., Torrisi, F., Milana, S., Lidorikis, E., & Ferrari, A. (2015). Few-cycle pulses from a graphene mode-locked all-fiber laser. *Applied Physics Letters*, *106*(25), 253101.

Qin, C., Gao, Y., Qiao, Z., Xiao, L., & Jia, S. (2016). Atomic‐Layered MoS2 as a Tunable Optical Platform. *Advanced Optical Materials*, *4*(10), 1429-1456.

Qin, Z., Xie, G., Zhang, H., Zhao, C., Yuan, P., Wen, S., & Qian, L. (2015). Black phosphorus as saturable absorber for the Q-switched Er: ZBLAN fiber laser at 2.8 µm. *Optics Express*, *23*(19), 24713-24718.

Rashed, A. N. Z., Altahan, B. R., Manasavenna, T., Ahammad, S. H., Priya, P. P., Krishna, M. R., Amzad, H. M., Smirani, L. K., & Said Abdelhamid, H. (2022). High-speed passive optical networks performance signature in downstream direction based on the engagement of both nonlinear cross-phase modulation (XPM) and cross-gain modulation (XGM) techniques. *Journal of Optical Communications*(0).

Ratner, A. (2013). *Spectral, Spatial, and Temporal Properties of Lasers*. Springer US. https://books.google.com.my/books?id=HORmoAEACAAJ

Razak, N. N., Yasin, M., Zakaria, Z., Latiff, A. A., & Harun, S. W. (2017). Q-switched fiber laser with tungsten disulfide saturable absorber prepared by drop casting method. *Photonics Letters of Poland*, *9*(3), 103-105.

Reekie, L., Mears, R., Poole, S., & Payne, D. (1986). Tunable single-mode fiber lasers. *Journal of lightwave technology*, *4*(7), 956-960.

Ren, Y., Liu, P., Liu, R., Wang, Y., Wei, Y., Jin, L., & Zhao, G. (2022). The key of ITO films with high transparency and conductivity: Grain size and surface chemical composition. *Journal of Alloys and Compounds*, *893*, 162304.

Rodríguez-Hernández, J., Bormashenko, E., Rodríguez-Hernández, J., & Bormashenko, E. (2020). Methodologies Involved in Manufacturing Self-assembled Breath-figures Patterns: Drop-casting and Spin-and dip-Coating–Characterization of Microporous Surfaces. *Breath Figures: Mechanisms of Multi-scale Patterning and Strategies for Fabrication and Applications of Microstructured Functional Porous Surfaces*, 111-148.

Rostami, A., & Andalib, A. (2007). A principal investigation of the group velocity dispersion (GVD) profile for optimum dispersion compensation in optical fibers: A theoretical study. *Progress In Electromagnetics Research*, *75*, 209-224.

Rüdiger, P. (2008). Encyclopedia of laser physics and technology. *Handbook/Reference Book*.

Sanger, M. J., & Danner, M. (2010). Aqueous ammonia or ammonium hydroxide? Identifying a base as strong or weak. *Journal of chemical education*, *87*(11), 1213-1216.

Saraceno, C. J., Schriber, C., Mangold, M., Hoffmann, M., Heckl, O. H., Baer, C. R., Golling, M., Südmeyer, T., & Keller, U. (2011). SESAMs for high-power oscillators: design guidelines and damage thresholds. *IEEE Journal of Selected Topics in Quantum Electronics*, *18*(1), 29-41.

Schawlow, A., & Townes, C. (2002). Infrared and optical masers. *SPIE milestone series*(173), 24-33.

Sebenik, R. F., Burkin, A. R., Dorfler, R. R., Laferty, J. M., Leichtfried, G., Meyer‐Grünow, H., Mitchell, P. C., Vukasovich, M. S., Church, D. A., & Van Riper, G. G. (2000). Molybdenum and molybdenum compounds. *Ullmann's Encyclopedia of Industrial Chemistry*.

Senior, J. M., & Jamro, M. Y. (2009). *Optical fiber communications: principles and practice*. Pearson Education.

Set, S. Y., Yaguchi, H., Tanaka, Y., & Jablonski, M. (2004). Laser mode locking using a saturable absorber incorporating carbon nanotubes. *Journal of lightwave Technology*, *22*(1), 51.

Seto, K., Kobayashi, T., & Tokunaga, E. (2023). Theoretical description for Nonlinear Dynamic Light Scattering Based on Stimulated Raman Effect (NLDLS‐SRS). *Journal of Raman Spectroscopy*.

Shah, J. (2019). *Atomic and electronic structures of two-dimensional layers on noble metals*. Linkopings Universitet. https://books.google.com.my/books?id=cuf_DwAAQBAJ

Shcherbakov, E., Fomin, V., Abramov, A., Ferin, A., Mochalov, D., & Gapontsev, V. P. (2013). Industrial grade 100 kW power CW fiber laser. Advanced Solid State Lasers,

Shi, H., Yan, R., Bertolazzi, S., Brivio, J., Gao, B., Kis, A., Jena, D., Xing, H. G., & Huang, L. (2013). Exciton dynamics in suspended monolayer and few-layer MoS2 2D crystals. *ACS nano*, *7*(2), 1072-1080.

Singh, S., & Singh, N. (2007). Nonlinear effects in optical fibers: origin, management and applications. *progress in Electromagnetics Research*, *73*, 249-275.

Singh, S. C., Zeng, H., Guo, C., & Cai, W. (2012). *Nanomaterials: processing and characterization with lasers*. John Wiley & Sons.

Sirleto, L., & Ferrara, M. A. (2020). Fiber amplifiers and fiber lasers based on stimulated Raman scattering: a review. *Micromachines*, *11*(3), 247.

Smith, N. J., Blow, K., & Andonovic, I. (1992). Sideband generation through perturbations to the average soliton model. *Journal of lightwave technology*, *10*(10), 1329-1333.

Snitzer, E. (1961). Optical maser action of Nd+ 3 in a barium crown glass. *Physical Review Letters*, *7*(12), 444.

Sobon, G. (2015). Mode-locking of fiber lasers using novel two-dimensional nanomaterials: graphene and topological insulators. *Photonics Research*, *3*(2), A56-A63.

Sobon, G., Klimczak, M., Sotor, J., Krzempek, K., Pysz, D., Stepien, R., Martynkien, T., Abramski, K. M., & Buczynski, R. (2014). Infrared supercontinuum generation in soft-glass photonic crystal fibers pumped at 1560 nm. *Optical Materials Express*, *4*(1), 7-15.

Soffer, B. (1964). Giant pulse laser operation by a passive, reversibly bleachable absorber. *Journal of applied physics*, *35*(8), 2551-2551.

Song, Y., Chen, S., Zhang, Q., Li, L., Zhao, L., Zhang, H., & Tang, D. (2016). Vector soliton fiber laser passively mode locked by few layer black phosphorus-based optical saturable absorber. *Optics express*, *24*(23), 25933-25942.

Song, Y., Shi, X., Wu, C., Tang, D., & Zhang, H. (2019). Recent progress of study on optical solitons in fiber lasers. *Applied Physics Reviews*, *6*(2).

Sotor, J., Sobon, G., Kowalczyk, M., Macherzynski, W., Paletko, P., & Abramski, K. M. (2015). Ultrafast thulium-doped fiber laser mode locked with black phosphorus. *Optics letters*, *40*(16), 3885-3888.

Soundeswaran, S., Kumar, O. S., Babu, S. M., Ramasamy, P., & Dhanasekaran, R. (2005). Influence of ultrsonification in CdS thin film deposition in PCD technique. *Materials Letters*, *59*(14-15), 1795-1800.

Srikanth, S., Suriyanarayanan, N., Prabahar, S., Balasubramanian, V., & Kathirvel, D. (2011). Structural and optical properties of chemical bath deposited Sb2S3 thin films. *Adv. Appl. Sci. Res*, *2*(1), 95-104.

Standard, I. (2005). Lasers and laser-related equipment-test methods for laser beam widths, divergence angles and beam propagation ratios. *ISO Standard*, 11146-11142.

Stehr, D., Morris, C. M., Schmidt, C., & Sherwin, M. S. (2010). High-performance fiber-laser-based terahertz spectrometer. *Optics letters*, *35*(22), 3799-3801.

Steinberg, D., Rosa, H. G., & de Souza, E. A. T. (2017). Influence of carbon nanotubes saturable absorbers diameter on mode-locking erbium-doped fiber laser performance. *Journal of Lightwave Technology*, *35*(21), 4804-4808.

Straumann, N., & Zürich, U. (2013). History of Physics (8). *COMMUNICATIONS DE LA SSP*, 48.

Stumpf, M., Pekarek, S., Oehler, A. E. H., Südmeyer, T., Dudley, J. M., & Keller, U. (2010). Self-referencable frequency comb from a 170-fs, 1.5-µm solid-state laser oscillator. *Applied Physics B*, *99*, 401-408.

Sun, Z., Hasan, T., Torrisi, F., Popa, D., Privitera, G., Wang, F., Bonaccorso, F., Basko, D. M., & Ferrari, A. C. (2010). Graphene mode-locked ultrafast laser. *ACS nano*, *4*(2), 803-810.

Sun, Z., Rozhin, A., Wang, F., Hasan, T., Popa, D., O'neill, W., & Ferrari, A. (2009). A compact, high power, ultrafast laser mode-locked by carbon nanotubes. *Applied Physics Letters*, *95*(25).

Svelto, O., & Hanna, D. C. (2010). *Principles of lasers* (Vol. 1). Springer.

Swader, J., Stocking, C., & Lin, C. H. (1975). Light - stimulated absorption of nitrate by Wolffia arrhiza. *Physiologia Plantarum*, *34*(4), 335-341.

Tang, H., Prasad, K., Sanjines, R., Schmid, P., & Levy, F. (1994). Electrical and optical properties of TiO2 anatase thin films. *Journal of applied physics*, *75*(4), 2042-2047.

Tang, P., Zhang, X., Zhao, C., Wang, Y., Zhang, H., Shen, D., Wen, S., Tang, D., & Fan, D. (2013). Topological insulator: $\hbox {Bi} _ {2}\hbox {Te} _ {3} $ saturable absorber for the passive Q-switching operation of an in-band pumped 1645-nm Er: YAG ceramic laser. *IEEE Photonics Journal*, *5*(2), 1500707-1500707.

Tang, S., Liu, J., Krasieva, T. B., Chen, Z., & Tromberg, B. J. (2009). Developing compact multiphoton systems using femtosecond fiber lasers. *Journal of biomedical optics*, *14*(3), 030508-030508-030503.

Taylor, P., & Beevers, C. (1952). The crystal structure of sodium thiosulphate pentahydrate. *Acta Crystallographica*, *5*(3), 341-344.

Thiel, K., & Wehr, A. (2004). Performance capabilities of laser scanners–an overview and measurement principle analysis. *International Archives of Photogrammetry, Remote Sensing and Spatial Information Sciences*, *36*(8), 14-18.

Tran, V., Soklaski, R., Liang, Y., & Yang, L. (2014). Layer-controlled band gap and anisotropic excitons in few-layer black phosphorus. *Physical Review B*, *89*(23), 235319.

Trebino, R. (2000). *Frequency-Resolved Optical Gating: The Measurement of Ultrashort Laser Pulses: The Measurement of Ultrashort Laser Pulses*. Springer Science & Business Media.

Tyutyunnik, V. M. (2021). Graphene breakthrough into future technology: the 2010 Nobel Prize in Physics Laureate Sir Konstantin Sergeevich Novoselov. *Journal of Advanced Materials and Technologies*, *6*(1), 6-9.

Verma, R., & Garg, P. (2012). Comparative analysis of self phase modulation (SPM) and cross phase modulation (CPM). *Int. J. Adv. Res, Comp. Sci. Electron. Eng*, *1*, 97-102.

Wallace, J. (2015). Ultrafast scientific lasers expand on their legacy. In (Vol. 51, pp. 42-46): PENNWELL PUBL CO 98 SPIT BROOK RD, NASHUA, NH 03062-2801 USA.

Wang, K., Wang, J., Fan, J., Lotya, M., O'Neill, A., Fox, D., Feng, Y., Zhang, X., Jiang, B., & Zhao, Q. (2013). Ultrafast saturable absorption of two-dimensional MoS2 nanosheets. *ACS nano*, *7*(10), 9260-9267.

Wang, Q. H., Kalantar-Zadeh, K., Kis, A., Coleman, J. N., & Strano, M. S. (2012). Electronics and optoelectronics of two-dimensional transition metal dichalcogenides. *Nature nanotechnology*, *7*(11), 699-712.

Wei, H., Yan, X., Niu, Y., Li, Q., Jia, Z., & Xu, H. (2021). Plasmon–exciton interactions: Spontaneous emission and strong coupling. *Advanced Functional Materials*, *31*(51), 2100889.

Welford, D. (2003). Passively Q-switched lasers. *IEEE circuits and devices magazine*, *19*(4), 31-36.

Woodward, R., Howe, R., Hu, G., Torrisi, F., Zhang, M., Hasan, T., & Kelleher, E. (2015). Few-layer MoS 2 saturable absorbers for short-pulse laser technology: current status and future perspectives. *Photonics Research*, *3*(2), A30-A42.

Woodward, R. I., & Kelleher, E. J. (2015). 2D saturable absorbers for fibre lasers. *Applied Sciences*, *5*(4), 1440-1456.

Wu, J., & Li, Q. (2019). Highly efficient self-similar spectral compression of hyperbolic secant pulses enhanced by pre-chirping in nonlinear fibres. *Journal of Optics*, *21*(8), 085503.

Xia, H., Li, H., Lan, C., Li, C., Zhang, X., Zhang, S., & Liu, Y. (2014). Ultrafast erbium-doped fiber laser mode-locked by a CVD-grown molybdenum disulfide (MoS 2) saturable absorber. *Optics express*, *22*(14), 17341-17348.

Xiao, G., & Bass, M. (1997). A generalized model for passively Q-switched lasers including excited state absorption in the saturable absorber. *IEEE Journal of Quantum Electronics*, *33*(1), 41-44.

Yakovlev, V. V., Petrov, G. I., Zhang, H. F., Noojin, G. D., Denton, M. L., Thomas, R. J., & Scully, M. O. (2009). Stimulated Raman scattering: old physics, new applications. *Journal of modern optics*, *56*(18-19), 1970-1973.

Yin, J., Li, J., Chen, H., Wang, J., Yan, P., Liu, M., Liu, W., Lu, W., Xu, Z., & Zhang, W. (2017). Large-area highly crystalline WSe 2 atomic layers for ultrafast pulsed lasers. *Optics express*, *25*(24), 30020-30031.

Yu, T., Fang, J., Hao, Q., Yang, K., Yan, M., Huang, K., & Zeng, H. (2021). High-precision passive stabilization of repetition rate for a mode-locked fiber laser based on optical pulse injection. *Optics Express*, *29*(13), 20930-20940.

Zainal, Z., Saravanan, N., & Mien, H. (2005). Electrodeposition of nickel selenide thin films in the presence of triethanolamine as a complexing agent. *Journal of Materials Science: Materials in Electronics*, *16*, 111-117.

Zeller, P., & Peuser, P. (2000). Efficient, multiwatt, continuous-wave laser operation on the 4 F 3/2–4 I 9/2 transitions of Nd: YVO 4 and Nd: YAG. *Optics Letters*, *25*(1), 34-36.

Zhang, H., Bao, Q., Tang, D., Zhao, L., & Loh, K. (2009). Large energy soliton erbium-doped fiber laser with a graphene-polymer composite mode locker. *Applied Physics Letters*, *95*(14).

Zhang, H., Lu, S., Zheng, J.-l., Du, J., Wen, S., Tang, D., & Loh, K. (2014). Molybdenum disulfide (MoS 2) as a broadband saturable absorber for ultra-fast photonics. *Optics express*, *22*(6), 7249-7260.

Zhang, M. (2019). *Handbook of Graphene, Volume 3: Graphene-like 2D Materials*. Wiley. https://books.google.com.my/books?id=tRWdDwAAQBAJ

Zhao, C., Zou, Y., Chen, Y., Wang, Z., Lu, S., Zhang, H., Wen, S., & Tang, D. (2012). Wavelength-tunable picosecond soliton fiber laser with topological insulator: Bi 2 Se 3 as a mode locker. *Optics express*, *20*(25), 27888-27895.

Zhao, G., Hou, J., Wu, Y., He, J., & Hao, X. (2015). Preparation of 2D MoS2/graphene heterostructure through a monolayer intercalation method and its application as an optical modulator in pulsed laser generation. *Advanced Optical Materials*, *3*(7), 937-942.

Zheng, Z., Zhao, C., Lu, S., Chen, Y., Li, Y., Zhang, H., & Wen, S. (2012). Microwave and optical saturable absorption in graphene. *Optics Express*, *20*(21), 23201-23214.

Zirngibl, M., Stulz, L., Stone, J., Hugi, J., DiGiovanni, D., & Hansen, P. (1991). 1.2 ps pulses from passively mode-locked laser diode pumped Er-doped fibre ring laser. *Electronics Letters*, *19*(27), 1734-1735.

Zitter, R. N. (1969). Saturated optical absorption through band filling in semiconductors. *Applied Physics Letters*, *14*(2), 73-74.

Zou, X., Lu, B., Pan, W., Yan, L., Stöhr, A., & Yao, J. (2016). Photonics for microwave measurements. *Laser & Photonics Reviews*, *10*(5), 711-734.